

# Strategies for Incorporating Functional Block copolymers into Polyelectrolyte Multilayer Coatings

by

WUI SIEW TAN

B.Sc., Materials Science and Engineering  
University of Illinois at Urbana Champaign, 2005

Submitted to the Department of Materials Science and Engineering  
in partial fulfillment of the requirements for the degree of

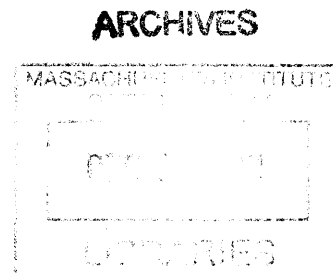
DOCTOR OF PHILOSOPHY IN MATERIALS SCIENCE AND ENGINEERING

at the

MASSACHUSETTS INSTITUTE OF TECHNOLOGY

SEPTEMBER 2011

© 2011 Massachusetts Institute of Technology.  
All rights reserved



Signature of author: .....

.....  
Department of Materials Science and Engineering  
Program in Polymer Science and Technology  
August 10<sup>th</sup>, 2011

Certified by: .....

.....  
Michael F. Rubner  
TDK Professor of Materials Science and Engineering  
Thesis Advisor

Certified by: .....

.....  
Robert E. Cohen  
St. Laurent Professor of Chemical Engineering  
Thesis Advisor

Accepted by: .....

.....  
Christopher Schuh  
Chair, Departmental Committee on Graduate Students



# **Strategies for Incorporating Functional Block copolymers into Polyelectrolyte Multilayer Coatings**

by

Wui Siew Tan

Submitted to the Department of Materials Science and Engineering on August 10<sup>th</sup>, 2011  
in partial fulfillment of the requirements for the degree of  
Doctor of Philosophy in Materials Science and Engineering

## **ABSTRACT**

This thesis explores the creation of thin film responsive hydrogel coatings via Layer-by Layer assembly (LbL) of temperature (T) responsive block copolymer – polyelectrolyte multilayers (PEMs). First, the LbL conditions that allow for temperature driven, large, reversible swelling transitions of multilayer constructs are determined. Use of weak polyelectrolyte components and selection of an appropriate deposition pH were found to be the critical factors that allowed large scale reversible swelling. These factors were the missing pieces that explain the lack of temperature response reported in prior literature. A series of block copolymer (BCP) molecules were subsequently synthesized to expose the influence of BCP architecture on the temperature responses of these micelle-PEMs. Diblock architectures that lack connectivity in the T-responsive poly(propylene oxide) block disintegrate quickly at low temperature. Triblock copolymers on the other hand allow access to a wide range of reversible swelling behavior. The dynamic interplay of various pH, salt concentration and T effects on the swelling and stability of these hydrogels are also further explored. In particular a critical ratio of charged block to T-responsive block length is necessary for film stability at low temperature. As a whole these systems can be customized to either swell reversibly (by up to 6 times their dry thickness) or disintegrate under specific sets of pH, time, temperature, and salt conditions, making them useful for a wide range of smart applications. The application of these conformal temperature responsive coatings to T-gating of membranes; creation of nanotube structures; T-enabled loading and release of proteins; as well as their tunable disintegration, useful for triggered release, is discussed and demonstrated. On a separate note, the utility of inorganic nanoparticle LbL assembly in creating conformal thin UV anti-reflection coatings for PMMA Fresnel lenses is demonstrated. Key features of thin porous nanoparticle coating assembly via LbL is discussed, including how particle size and deposition pH can tune the coating porosity and refractive index. In addition, we develop several strategies for stabilization of these inherently weak systems largely composed of air. In particular, a novel means to generate stable inversely structured surface nanoporosity in thermoplastic materials is developed.

Thesis advisors: Prof. Michael F. Rubner, TDK Professor of Materials Science and Engineering  
Prof. Robert E. Cohen, St. Laurent Professor of Chemical Engineering

## ~ Acknowledgements ~

My time here at MIT has been one full of growth in life's multitude of facets. Undoubtedly, I would not have managed to accomplish any of the things I have done, without the support of numerous other people.

First and foremost, I would like to thank my thesis advisors **Prof. Michael F. Rubner** and **Prof. Robert E. Cohen**, both amazing people and academics. I have benefited immensely from their dynamic partnership in co-advising students and from my projects that have components at the intersection of their pet interests. Thank You **Prof Rubner** for always being there, without fail, with support and solid advice; and Thank You, **Prof Cohen** for your continued enthusiasm, interest and support of this work. In addition, I thank you, both, for all that I have learnt from you as excellent experimentalists with a sharp eye for opportunity. Your passion in science has been a constant inspiration. Above all, I thank you for your open, honest communication at all times and how you have taught me that there is no wrong result in science. On a similar level, I would like to thank a very special 'third advisor', **Prof Svetlana A. Sukhishvili** from Steven's Institute of Technology. **Svetlana**, I cannot thank you enough for your unwavering support of my research and abilities. This project would never have been possible without your presence at its conception, and continued support through its development. It was most fortunate that I had a chance to work alongside and learn from an excellent scientist like you during your time here at MIT. Through all my good times and bad, thank you for being there for me with encouragement and good cheer. You have been an inspirational role model in juggling the responsibilities as a Professor with genuine concern for all of your students. I also thank my committee members, **Prof Darrell J. Irvine** and **Prof Krystyn J. Van Vliet** for their insightful feedback and comments on my work. Their academic paths and pursuit for scientific excellence, has too, been inspirational. In addition, would also like to thank **Prof Patrick S. Doyle**, (another scientist I have great respect for) for the time in his lab. It was a fantastic learning experience on several levels.

Next, I want to thank all the members of the Rubner & Cohen labs as well as members of the Sukhishvili lab and also the Dolye lab. It was a pleasure to have had the chance to meet and work with you. In particular I need to thank **Jonathan DeRocher**, **Erik Williamson** and **Daniel Pregibon**. It's funny how each lab has this one grad student that shines out above with their infinite generosity, helpfulness and *Amazing* ability to fix almost anything and everything in the lab. Things would not have run half as smoothly without each of you. I would also like to extend a special 'Thank You!' to **Yi Du**. Thank you for your friendship and for doing an amazing job at taking over the AR project and bringing it from strength to strength. It was an absolute pleasure knowing & working with you! I would also like to thank fellow grad students, **Gary Chia**, **Zhichen Zhu**, **Christina Lewis**, **Andrew Miller**, **Zekeriya Gemici** and **Jonathan Gilbert** for being great collaborators.

I thank staff: **Steve Kooi, Amy Tatem, Bill** and friends: **Zhiyong Poon, Amanda Engler** and **Abbey Oelker** for all their help at ISN, and for sharing their synthesis experiences. I would also like to thank **Tim Mclure, Libby Shaw, Yong Zhang, Patrick** and **Shianh Chen** of CMSE for all their technical support.

**Nathan** and **Asye**, thank you, for your friendship and transfer of membrane knowhow. ☺

Also I would like to thank the Hatton lab, for their generosity in letting me use their mDSC. Thank you **Nate** and **Mike** for facilitating that.

Especially, I thank my *parents*, **Tan Teck Poh** and **Margarte Yuen**, without whom I would not be the person I am today. Their constant love and support has been a constant stabilizing force in my life. For that, all pain however *unbearable* is endured.

A very special thank you has to go out to some of friends: **Xiao Qing, Bing-ru, Catherine, Tiffany, Erica, Yi, Zhiyong, Trina** and **Charmaine** who have, without fail, provided me tremendous physical/emotional support in my times of need:- from phone calls, to providing roofs over my head, to midnight trips to the hospital. Thank you all for being such *amazing* friends. I could not imagine how it might have been without you.

*While I really want to thank everyone I have gotten to know here individually, I can't, so... ..*

Here's a shout out to all of **friends07**; R & C lab: **Shree, Pinar, Adam, Hiro, Patrick, Grinia, Al, Siddarth, Hyomin, Justin, Nurxat**; **Chem. E. batch of 2008** (*sorry it was hard to keep in touch*); Doyle lab: **Dhananjaya, Rilla, Jason, Panda and Bong**; Svetlana's lab: **Swapnali, Li, Alex, Yun, Polina, Svetlana Jr, Yiming**; Japanese-English exchange: **Yasu and Co. Keiko, Akiko, Nic, Hiro, Shinya, Arik...** Sports meetup; **NH trippers**; **Wine and cheese eaters**; **SMITE 2007**; **DMSE year 2011 +/- x**; PPST crew: Thanks **Greg!** & fellow PPST students; **MIT Chinese Choral Society**; Singaporeans: **Kenneth, Lynette, Daryl, Xiaojuan, Winnie, Kongjie, Jit, Vincent ... ..**; **Imperial-MIT Global Fellows Program**: **Ellan, Tempest, Atun, Marta, Adam, Leon ... ..** and my previous apt mates: **Cynthia, Susan, Jessie, Kiyoko, Leah, Indira, Becca.**

***Life would not have quite been the same without each and every one of you.***

*Since I MUST have missed out some people (sorry!) whom I would have wanted to thank, I will end with this:*

Words simply **cannot** express how *deeply* grateful I am for all that I have learnt, simply in having the opportunity to be around the all amazing *driven, creative, people*. To me, MIT and Cambridge, MA, has been an amazing place in my pursuit of Science and Life, *solely*, because of the **PEOPLE** that exist at the heart of it all. With this I would like to thank all the people who have been part of my life and education over these years. The inspiration and growth in learning from all walks of brilliant and motivated, yet humble and constantly inquisitive minds is an education I *cannot* be more thankful for. **THANK YOU!**

*~This thesis is dedicated to those who choose to struggle in the pursuit of truth and perfection. ~  
Never give up! ☺*

A very special thank you goes to my brother, **Tan Wui Siang**, who is so different, yet so similar to me and *definitely* falls in the category above.

*Thank you kor for being the best big brother I could ever ask for.  
You are a constant inspiration.*

## TABLE OF CONTENTS

<b>ABSTRACT .....</b>	<b>3</b>
<b>ACKNOWLEDGEMENTS .....</b>	<b>4</b>
<b>LIST OF FIGURES.....</b>	<b>10</b>
<b>LIST OF TABLES.....</b>	<b>19</b>
<b>CHAPTER 1: INTRODUCTION &amp; BACKGROUND.....</b>	<b>21</b>
1.1 INTRODUCTION.....	21
1.2 RESPONSIVE HYDROGELS.....	21
1.2.1 Controlling gel dimensions through polymer chain configurations .....	25
1.2.2 Temperature responsive hydrogels .....	29
1.2.3 Relationship between gel swelling and functional gel properties .....	29
1.2.4 Kinetic Factors .....	31
1.3 POLYELECTROLYTES.....	32
1.4 BLOCK COPOLYMERS & MICELLIZATION.....	36
1.4.1 Block copolymers .....	36
1.4.2 Micellization of block copolymers in solution .....	38
1.5 LAYER-BY-LAYER ASSEMBLY & MULTILAYER FILMS.....	41
1.6 THESIS OUTLINE.....	44
<b>CHAPTER 2: SWELLING TRANSITIONS IN MULTILAYERS OF A CATIONIC TRIBLOCK COPOLYMER AND A POLYACID.....</b>	<b>49</b>
2.1 Abstract .....	50
2.2 Introduction .....	51
2.3 Materials and methods .....	53
2.4 Results and discussion .....	56
2.4.1 Temperature-triggered micellization of PD-PP-PD in solution .....	56
2.4.2 Multilayers of PD-PP-PD with polyanions .....	60
2.4.3 Effect of pH on the assembly of the PD-PP-PD/PAA system .....	63
2.4.4 Temperature response of PD-PP-PD containing multilayers .....	64
2.5 Conclusions .....	72
<b>CHAPTER 3: SYNTHESIS OF PDMAEMA CONTAINING BLOCK COPOLYMERS BY ATOM TRANSFER RADICAL POLYMERIZATION.....</b>	<b>77</b>
3.1 Abstract .....	78
3.2 Introduction and background .....	78
3.3 Materials .....	79
3.4 Synthesis Methods .....	80

3.4.1 Synthesis of macroinitiators .....	80
3.4.2 Synthesis of diblock and triblock copolymers .....	83
3.4.3 Block copolymer characterization .....	87
3.5 Conclusions .....	90
<b>CHAPTER 4: EFFECTS OF BLOCK COPOLYMER ARCHITECTURE ON THE THERMALLY-INDUCED SWELLING OF MICELLE-CONTAINING MULTILAYER THIN FILMS.....</b>	<b>91</b>
4.1 Abstract .....	92
4.2 Introduction .....	94
4.3 Materials and methods .....	96
4.4 Results and discussion .....	97
4.4.1 BCP composition and polydispersity .....	97
4.4.2 BCP solution self assembly.....	97
4.4.3 Surface morphology of BCP micelle LbL assemblies .....	101
4.4.4 Thin film mPEM temperature swelling responses in aqueous media .....	104
4.5 Conclusions .....	111
<b>CHAPTER 5: APPLICATIONS AND FUTURE PERSPECTIVES FOR TEMPERATURE RESPONSIVE MICELLE MULTILAYER COATINGS.....</b>	<b>115</b>
5.1 Abstract .....	115
5.2 Introduction .....	116
5.3 Materials and methods .....	118
5.4 Results and discussion .....	122
5.4.1 Temperature Gating of TEPC Membranes .....	122
5.4.2 Freestanding Nanotubes made of Temperature Responsive Multilayers .....	127
5.4.3 Protein Trapping and Release for Controlled Delivery .....	136
5.4.4 Tunable Disintegration of Multilayers for Triggered Release .....	140
5.5 Conclusions .....	150
<b>CHAPTER 6: LAYER BY LAYER ASSEMBLY FOR ANTI-REFLECTION ON THERMOPLASTIC SUBSTRATES.....</b>	<b>153</b>
6.1 Abstract .....	153
6.2 Introduction .....	154
6.3 Materials and methods .....	157
6.4 Results and discussion .....	159
6.4.1 Theoretical design of AR coatings on PMMA for 300 – 400 nm UV wavelengths .....	159
6.4.2 Creating single layer AR coatings using LbL assembly .....	160
6.4.3 Improving the mechanical stability of nanoparticle multilayers .....	169
6.5 Conclusions .....	180



<b>CHAPTER 7: CONCLUSIONS .....</b>	<b>183</b>
7.1 Summary of thesis contributions .....	183
7.2 Recommendations for future studies .....	185

## **APPENDICES**

APPENDIX A: Studies of PDMAEMA and PAA containing BCPs in solution .....	189
APPENDIX B: Morphology of BCP multilayers, additional AFM insights .....	199
APPENDIX C: Additional data related to LbL assembly for AR coatings on PMMA .....	213
APPENDIX D: Hierarchical Assembly of Viral Nanotemplates with Encoded Microparticles via Nucleic Acid Hybridization .....	217

## LIST OF FIGURES

- Figure 1-1.** Diagram showing the evolution of polymer chain dimension with degree of polymerization,  $N$ . Solvents of different quality give different size dependences on  $N$  and the effect of these different scaling regimes is reflected along a vertical where a polymer of fixed  $N$  increases in size when transiting from a poor, to a theta, to a good solvent ..... 28
- Figure 1-2.** Scheme showing how molecular level architecture of gels on the left hand side affects gel properties, a list of which is found on the right hand side ..... 29
- Figure 1-3.** Schematic diagram illustrating the molecular level architecture of network chains within a hydrogel in a poorly hydrated state (on the leftmost) and in a highly swollen state (in the middle). The mesh size,  $\xi$  of the network is indicated. The inset in the top right corner illustrates how the mesh size of gels determines the size cut off for the passage of various species (e.g. drugs, proteins, or even cells) through gel networks ..... 30
- Figure 1-4.** Chemical structures of various polyelectrolytes used in this thesis, grouped according to their classification as strong or weak polyelectrolytes: poly(dimethyldiallylammonium chloride) (PDAC), poly(sodium 4-styrenesulfonate) (PSS), poly(acrylic acid) (PAA), poly(allylamine hydrochloride) (PAH) and poly(dimethylamino ethylmethacrylate) (PDMAEMA). 'n' is the number of repeat units in the polymer chain (= degree of polymerization 'N') and varies linearly with molecular weight ..... 32
- Figure 1-5.** Idealized evolution of ionization degree with pH expected for a strong polyelectrolyte (PSS), a weak polyacid (PAA) and a weak polybase (PDMAEMA) ..... 34
- Figure 1-6.** Schematic illustrating the effect of pH induced changes in  $\alpha$  on polymer chain configurations for weak polyelectrolytes. Grey dotted downward arrows illustrate the effect of added salt that can associate to the fixed charges on the polyelectrolyte backbone and through charge screening lead to more collapsed chain configuration ..... 35
- Figure 1-7.** Drawings to illustrate some block copolymer architectures. A-B diblock, A-B-A triblock and  $(A-B)_n$  star block copolymers in particular are of interest in this thesis ..... 36
- Figure 1-8.** Schematic illustrating key features of block copolymer micellization.  $x$  is the aggregation number,  $A$  is the block copolymer in a single molecule (unimer) unaggregated state and  $A_x$  is a micelle composed of  $x$  unimers.  $\Delta G_m$  is the Gibbs free energy of micellization..... 38
- Figure 1-9.** Typical phase diagram of LCST polymers. The inset shows how polymer molecular weight and other factors that can affect solvent quality like the addition of salt to water can shift the LCST..... 40
- Figure 1-10.** Schematic of Layer-by-Layer (LbL) assembly process ..... 42

<b>Figure 2-1.</b> pH dependence of the micellization temperature in 3.3 mg/ml PD-PP-PD solutions with no added salt. The MT was determined from the peak exotherm observed during cooling from 65 to 6 °C in micro-DSC experiments.....	57
<b>Figure 2-2.</b> Thickness of multilayer assemblies as a function of the number of bilayers deposited from solutions without added salt at 24 °C. Inset shows the line fit to linear regions of each curve as well as the slope of the curve and standard error of the fit. ....	60
<b>Figure 2-3.</b> Growth curves obtained for (PD-PP-PD/PAA4.0), (PD-PP-PD/PAA6.0), (PD-PP-PD/PAA7.0), and (PD-PP-PD/PAA8.0) systems. ....	63
<b>Figure 2-4.</b> Temperature-dependent swelling of PD-PP-PD-containing multilayers deposited from solutions, with no added salt, at ~24 °C and subsequently exposed to DI water adjusted to pH 7. Multilayers of PD-PP-PD were constructed at pH 4 or 7 using PAA or PSS as polyanions.....	65
<b>Figure 2-5.</b> Temperature dependence of swelling of PD-PP-PD/PAA multilayers assembled from salt free solutions at pH 4, 5, 6, 7, or 8 submerged in DI adjusted to pH7.....	67
<b>Figure 2-6.</b> Plot of swelling ratio of (PD-PP-PD/PAA7.0) <sub>40</sub> multilayer as a function of immersion cycles in pH7 DI at 20°C, 6°C and dried in between.....	68
<b>Figure 2-7.</b> Reversible swelling of (PD-PP-PD/PAA7.0) <sub>24</sub> multilayers in 0.15 M NaCl solutions at pH 7 and temperatures, 6 °C (open squares) and 20 °C (filled squares).....	69
<b>Figure 2-8.</b> Effect of pH on the swelling of (PD-PP-PD/PAA7.0) <sub>24</sub> at 20 °C and 6 °C. At 20 °C obtained by <i>in situ</i> ellipsometric thickness measurements.....	70
<b>Figure 3-1.</b> Chemical reaction schemes for end functionalization via esterification of hydroxyl groups on mono-hydroxy methoxy-P <sub>65</sub> -OH (a) and di-hydroxy HO-P <sub>127</sub> - OH (b).....	80
<b>Figure 3-2.</b> Drawing illustration of set-up used for azeotropic distillation drying of PPO before esterification .....	81
<b>Figure 3-3.</b> Schematic showing the general mechanism of atom transfer radical polymerization .....	83
<b>Figure 3-4.</b> Illustration of how CuBr/Bpy complex should be added to a deoxygenated ATRP reaction mixture.....	86
<b>Figure 3-5.</b> <sup>1</sup> H NMR spectra of the commercial short D-P-D triblock copolymer (STB) and synthesized block copolymers: long D-P-D triblock copolymer (LTB) and P-D diblock copolymer (DB) in CDCl <sub>3</sub> ..	87
<b>Figure 3-6.</b> Gel Permeation Chromatography curves of synthesized block copolymers LTB, DB, and their respective macroinitiators in dimethylformamide and GPC curves of commercially obtained TB and its macroinitiator obtained from Polymer Source.....	89
<b>Figure 4-1.</b> Cryo-SEM images of freeze fractured surfaces of flash frozen BCP solutions, taken after sublimation to expose micelles. STB (a), LTB (b), and DB (c) solutions were of 0.1 mg/ml concentration in DI water, adjusted to pH 7. The white scale bars at the bottom right of each image represents 150 nm.	

Size distributions of micelles obtained by measurements from at least 4 images are shown on the right hand side of each representative image. .... 99

**Figure 4-2.** 1  $\mu\text{m} \times 1 \mu\text{m}$  atomic force microscope (AFM) images of BCP or homopolymer, poly (N,N dimethyl amino ethyl methacrylate) (D), multilayers assembled with PAA. The left column consists of height images while the right column consists of phase images. Rows a, b, c and d correspond to multilayers of (STB/PAA)<sub>30</sub>, (DB/PAA)<sub>35</sub>, (LTB/PAA)<sub>35</sub> and control (D/PAA)<sub>40</sub> respectively..... 102

**Figure 4-3.** AFM images of BIEE shell cross-linked BCPs: STB (a), LTB (b) and DB (c), dip coated onto the surface of silicon wafers. The inset in (b) shows the height profile along the dotted line..... 104

**Figure 4-4.** Drawings depicting the molecular configurations of BCPs within the mPEMs studied. The blue region surrounding the micelle cores are composed of D corona blocks ionically cross-linked to PAA chains (PAA not drawn for simplicity). The top row represents the multilayers in pH 7 DI water at 20 °C where the P domains are poorly hydrated while the bottom row represents the multilayers at 6 °C where micelle cores of all BCPs become highly swollen with water..... 105

**Figure 4-5.** Graphs showing the time-dependent evolution of the swelling degree ( $\tau = \text{wet film thickness}/\text{dry film thickness}$ ) of mPEMs, (a) (STB/PAA), (b) (DB/PAA) and (c) (LTB/PAA) held at various temperatures. All films studied were of similar thicknesses between 150 and 250 nm. The swelling degrees at 2 minutes of low temperature exposure are circled as they correspond to points subsequently discussed in Figure 4-7..... 106

**Figure 4-6.** Isochronous swelling degree,  $\tau = \text{wet thickness}/\text{dry thickness}$ , of mPEM films held at various temperatures for 10 min (hollow symbols with dotted lines) or 20 min (solid symbols and lines). Legend indicates the BCP component of the mPEMs for convenient identification of curves..... 107

**Figure 4-7.** Changes in swelling degree,  $\tau$ , of mPEMs: (a) (DB/PAA), (b) (STB/PAA) and (c) (LTB/PAA), upon cycling between the dry state at room temperature (20 °C), wet state in cold DI water adjusted to pH 7 at 2 min immersion times, and de-swollen and dried at (20 °C)..... 108

**Figure 4-8.** 1  $\mu\text{m} \times 1 \mu\text{m}$  atomic force microscope (AFM) images of dried mPEM multilayers after 7 cycles of swelling (at  $\Delta T = 6 \text{ }^\circ\text{C}$ ) and deswelling (at 20 °C) in pH 7 DI water. The left column consists of height images while the right column consists of phase images. Rows a, b, and c correspond to multilayers of (STB/PAA)<sub>30</sub> (swollen at 9 °C), (DB/PAA)<sub>35</sub> (swollen at 9 °C) and (LTB/PAA)<sub>35</sub> (swollen at 4 °C) respectively..... 110

**Figure 5-1.** Scanning electron microscope(SEM) image of the top down overview of a typical track etched polycarbonate (TEPC) membrane and cartoon illustrations of TEPC membrane gating using temperature responsive LbL coatings..... 122

**Figure 5-2.** Plot showing the changes in normalized membrane flux,  $\frac{J_{exp}(T)}{J_o(T)}$ , through TEPC membranes with 200 nm pores coated with (PD-PP-PD/PAA 7.0)<sub>15</sub>, as the temperature, T, is cycled between 20 and 0 °C. .... 125

**Figure 5-3.** SEM image of a TEPC membrane ( $d_o = 200 \text{ nm}$ ) coated with (PD-PP-PD/PAA 7.0)<sub>15</sub>..... 126

**Figure 5-4.** SEM images of TEPC membranes ( $d_o = 800$  nm) coated with increasing numbers of bilayers of (LTB/PAA 7.0). Images of the same coated membrane at different magnifications are shown in each row; (a) (LTB/PAA 7.0)<sub>5</sub>, (b) (LTB/PAA 7.0)<sub>10</sub> and (c) (LTB/PAA 7.0)<sub>15</sub>. The insets in row (b) and (c) are of the membranes after plasma etching of the top surface..... 128

**Figure 5-5.** SEM images of TEPC membranes ( $d_o = 3$   $\mu$ m) coated with increasing numbers of bilayers of (LTB/PAA 7.0). Images shown in each row are of the same coated membrane at different magnifications. Coatings are as follows, row (a) (LTB/PAA 7.0)<sub>10</sub>, (b) (LTB/PAA 7.0)<sub>20</sub>, (c) (LTB/PAA 7.0)<sub>25</sub>, and (d) (LTB/PAA 7.0)<sub>30</sub>..... 129

**Figure 5-6.** SEM images of TEPC membranes ( $d_o = 3$   $\mu$ m) coated with increasing numbers of bilayers of (PD-PP-PD/PAA 7.0). Images shown in each row are of the same coated membrane at different magnifications. Coatings are as follows, row (a) (PD-PP-PD /PAA 7.0)<sub>10</sub>, (b) (PD-PP-PD /PAA 7.0)<sub>20</sub>, (c) (PD-PP-PD /PAA 7.0)<sub>25</sub>, and (d) (PD-PP-PD /PAA 7.0)<sub>30</sub>. .... 130

**Figure 5-7.** SEM images demonstrating the various possible pitfalls possible in nanotube creation..... 132

**Figure 5-8.** SEM images of nanotube forests made from TEPC membranes ( $d_o = 800$  nm) coated with (LTB/PAA 7.0)<sub>10</sub> at different magnifications are shown in (a) and (b), while nanotube forests made from TEPC membranes ( $d_o = 3$   $\mu$ m) coated with (LTB/PAA 7.0)<sub>10</sub> at different magnifications are shown in (c) and (d)..... 134

**Figure 5-9.** High resolution SEM images<sup>1</sup> of nanotube forests made from TEPC membranes ( $d_o = 800$  nm) coated with (PD-PP-PD/PAA 7.0)<sub>10</sub> at different magnifications are shown in (a) and (b), while nanotubes made from TEPC membranes ( $d_o = 3$   $\mu$ m) coated with (PD-PP-PD/PAA 7.0)<sub>10</sub> at different magnifications are shown in (c) and (d). .... 135

**Figure 5-10.** Schematic diagram illustrating the nanocomposite nature of block copolymer micelle/polyanion multilayers. Typical length scales of the nanostructure, as well as the two distinct types of crosslinks operative in holding the network together are depicted..... 136

**Figure 5-11.** Cumulative FTIC-BSA released into 0.01 M PBS buffered solution (at 37 °C) as a function of time..... 138

**Figure 5-12.** Relative amount of FTIC-BSA released,  $M(t)/M_f$ , as a function of time. Curves labeled (a) corresponding to the data in Figure 5-11, while curves labeled (b) are data from a separate set of samples and separate release trial..... 138

**Figure 5-13.** The swelling of (D/PAA 7.0)<sub>40</sub> and (PD-PP-PD/PAA 7.0)<sub>40</sub> multilayers at room temperature, RT, of 22 °C is plotted as a function of NaCl salt concentration. The swelling ratio is defined as the  $\frac{\text{wet (swollen) film thickness}}{\text{dry film thickness}}$ . Solid points are stable to the salt solution in which swelling is reversible. Hollow points at 0.6 M salt concentration indicate film instability where film loss starts to occur..... 141

<sup>1</sup> High resolution images of nanotube forests made from membranes shown in Figure 5-9 are courtesy of my collaborator, Gary, Khok Khiang Chia.

**Figure 5-14.** The swelling of (PD-PP-PD/PSS 7.0) multilayers at room temperature (~22 °C) and cold temperature (6 °C) is plotted as a function of NaCl concentration. The swelling ratio in PBS is the same as the swelling in solutions with 0.2 M NaCl, as indicated by the labeled arrow. The cross indicates the points of film instability where the multilayer dissolves. .... 142

**Figure 5-15.** Fraction of multilayer films remaining ( $\frac{T_f}{T_i}$ ) for (D/PAA 4.0)<sub>20</sub> (squares), (D/PAA 7.0)<sub>20</sub> (triangles), (PD-PP-PD/PAA 7.0)<sub>40</sub> (circles) post annealing for 20 hours in DI water, adjusted to various pH values, at either 20 °C (solid symbols and lines) or 5 °C (hollow symbols and dotted lines)..... 144

**Figure 5-16.** Fraction of multilayer film thickness remaining,  $\frac{T_f}{T_i}$ , after 20 hours of immersion in DI water, adjusted to various pH, at 5 °C. All multilayers studied were assembled at pH 7 but contain block copolymers of different architecture, where PD is the PDMAEMA block, PP the PPO block and the numbers following each abbreviation being the degree of polymerization of the block. Block copolymer components used include triblocks (solid symbols and lines): PD7-PP127-PD7, PD20-PP127-PD20 and D20-PP127-PD20 as well as diblocks (hollow symbols; dotted lines): PP65-PD58 and PP65-PD65..... 146

**Figure 5-17.** Variation in the fraction of (DB/PAA 7.0) film thickness remaining,  $\frac{T_f}{T_i}$ , with time of annealing in pH 7 adjusted DI water at different degrees of undercooling,  $\Delta T = 3, 6$  or  $5$  °C ..... 147

**Figure 5-18.** Variation of the fraction of multilayer film thickness remaining,  $\frac{T_f}{T_i}$ , with time of annealing in pH 7 adjusted DI water at  $\Delta T = 6$  °C for different multilayer systems: (STB/PAA 7.0) (squares), (LTB/PAA 7.0) (circles) and (DB/PAA 7.0) (diamonds)..... 148

**Figure 5-19.** Variation of the fraction of (LTB/PAA 7.0) film thickness remaining,  $\frac{T_f}{T_i}$ , with time of annealing in pH 7 adjusted DI water at  $\Delta T = 10$  °C..... 149

**Figure 6-1.** Sensitivity of single index coatings to changes in refractive index: (a) reflectance from single index coatings of various refractive indices; (b) integrated total reflectance (area under curve) between 300-400nm for coatings of the different refractive indices..... 159

**Figure 6-2.** AFM images of (PAH(3)/SiO2(9b))<sub>1</sub>. The height image is shown on the left and the corresponding phase image, followed by the vertical scale bar is shown on the right. White scale bars in the images represent 300 nm..... 162

**Figure 6-3.** AFM height images of (PAH(6)/SiO2(9b))<sub>1</sub> ((a) and (d)), (PAH(6)/SiO2(9b))<sub>2</sub> ((b) and (e)) and (PAH(6)/SiO2(9b))<sub>3</sub> ((c) and (f)). The top row consist of  $2 \mu\text{m} \times 2 \mu\text{m}$  images while the bottom row consists of  $5 \mu\text{m} \times 5 \mu\text{m}$  images. Lateral scale bars shown in the bottom right represent 200 nm in the top row and 500 nm in the bottom row. The height scales for all images are the same and shown on the top right corner of (c)..... 163

**Figure 6-4.** Effective refractive index (RI) of porous silica nanoparticle layers, (PAH(6)/SiO2(9b)), on PMMA, determined by spectroscopic ellipsometry, as a function of the number of bilayers (i.e. number of LbL deposition cycles). Inset shows the RI variation for 2 bilayers of SiO2(9b) assembled with PAH at different pH..... 164

<b>Figure 6-5.</b> Reflectance from 1.5 mm thick PMMA samples coated on both sides with (PAH(6)/SiO <sub>2</sub> (9b)) <sub>2</sub> (yellow) contrasted with the bare uncoated native PMMA substrate (blue) over wavelengths of 200 – 800 nm. Reflectance was determined by UV-Vis spectroscopy in reflectance mode. On the right is a zoom into the reflectance from the coated sample over the 300 – 400 nm wavelength region of interest.....	165
<b>Figure 6-6.</b> Transmittance of native uncoated PMMA (blue) and PMMA coated with (PAH(6)/SiO <sub>2</sub> (9b)) <sub>2</sub> (yellow) determined by UV-Vis spectroscopy in transmission mode.....	166
<b>Figure 6-7.</b> The wavelength dependent scattering and absorptive losses (100 - Reflectance (%) – Transmittance (%)) of native (uncoated) PMMA substrates used in our studies.....	166
<b>Figure 6-8.</b> SEM images of a PMMA Fresnel lens coated with (PAH(6)/SiO <sub>2</sub> (9b)) <sub>3</sub> shows conformal coating by the LbL assembly method. (a) is an overview of the grooved saw-toothed edged surface of the coated, freeze fractured PMMA Fresnel lens; (b) is an enlarged image of one of the grooves and (c) is a higher magnification of the boxed region in (b). (d) is a higher resolution magnified image of the boxed region in (c). The inset in(c) shows a magnified view of the flat, sloping coated surface of the nanoparticle coated groove.....	168
<b>Figure 6-9.</b> Schematic illustration of the method developed to modify the PMMA substrate with an anchoring layer of PMMA-PAA.....	170
<b>Figure 6-10.</b> Static (diamonds), advancing (squares) and receding (triangles) contact angles of water: on uncoated PMMA substrates (points on the y-axis) and on PMMA substrates with PMMA-PAA adsorbed from solutions of 1 mg/ml 50% methanol 50% DI water, under various conditions.....	171
<b>Figure 6-11.</b> Transmission spectra of stained native PMMA and BCP coated PMMA (a). Staining was done by 1.5 hr immersion in 0.1 M methylene blue (MB) solution. Staining and absorption at 550 nm indicates presence of acid groups. (b) shows a photograph of the uniformly coated and MB stained vs uncoated, MB stained regions of a PMMA sample. (c) shows the transmission spectrum before and after vigorous wiping with kimwipes.....	172
<b>Figure 6-12.</b> Reflectance from PMMA coated with (PAH(6)/SiO <sub>2</sub> -COOH(9b)) multilayers showing the effects of thermal dehydration crosslinking at 70 °C for 72 hrs and the stability of the films to typical lens cleaning procedures (labeled wiped in the legend).....	173
<b>Figure 6-13.</b> Drawings to illustrate the evolution of the PMMA wetting of the silica nanoparticles and the sinking of (PAH(6)/SiO <sub>2</sub> (9b)) <sub>2</sub> coating into the PMMA surface with time and heat treatment ((a) to (d)), and the etching away of the silica nanoparticles at different stages to obtain a nanoporous surface layer in the PMMA substrate ((e) and (f)).....	175
<b>Figure 6-14.</b> (PAH(6)/SiO <sub>2</sub> (9b)) <sub>2</sub> (a) as assembled, (b) after annealing for 1 hr at 90°C and (c) after annealing for 2 hrs at 90°C. The images on the left are height images while the images on the right are corresponding phase images. Vertical scale bars are shown to the right of each row. Scale bars in the bottom right corner of images represent 100 nm.....	176

**Figure 6-15.** AFM height images of NaOH etched (PAH(6)/SiO<sub>2</sub>(9b))<sub>2</sub> on PMMA, (a) annealed at 120°C for 1 hr (b) annealed at 140 °C for 1 hr (c) annealed at 80°C for 5 hr, (d) annealed at 100°C for 1 hr and (e) annealed at 140°C for 1 hr (f) is the phase image corresponding to (e). Scale bars at the bottom right of each image represent 300 nm and the vertical scales of images are shown on the right of each row... 177

**Figure 6-16.** Reflectance from uncoated PMMA substrates (denoted ‘pristine’), PMMA coated with as assembled (PAH(6)/SiO<sub>2</sub>(9b))<sub>2</sub> (denoted ‘aa’), PMMA coated with (PAH(6)/SiO<sub>2</sub>(9b))<sub>2</sub> and heated at 140 °C for 1 hr (denoted ‘heated’) and PMMA coated with (PAH(6)/SiO<sub>2</sub>(9))<sub>2</sub> and heated at 140 °C for 1 hr and etched in 5 M NaOH for 2 days (denoted ‘hed’)..... 179

**Figure 6-17.** Reflectance from PMMA coated with as assembled (PAH(6)/SiO<sub>2</sub>(9b))<sub>2</sub> (aa), PMMA coated with (PAH(6)/SiO<sub>2</sub>(9b))<sub>2</sub> and heated at 140 °C for 1 hr and etched in 5 M NaOH for 2 days (hed) and the reflectance of each sample after wiping once and after wiping five times..... 179

**Figure A-1.** Heat flow as a function of temperature during representative heating (a) and cooling (b) cycles of 3.3 mg/ml PD-PP-PD solution in DI adjusted to pH 7..... 189

**Figure A-2.** Absorbance, of PD-PP-PD solutions with 0.004 mM DPH, at 356 nm as a function of solution temperature for 1 mg/ml PD-PP-PD solutions adjusted to different pH..... 190

**Figure A-3.** Number average hydrodynamic diameter in 0.1 mg/ml PD-PP-PD solutions at pH 4 and pH 7, as determined by dynamic light scattering..... 190

**Figure A-4.** Heat flow as a function of solution temperature during cooling for 3.3 mg/ml PD-PP-PD solution in DI adjusted to pH 4 with and without 0.2 M NaCl added..... 191

**Figure A-5.** Temperature dependent evolution of effective hydrodynamic diameter of 0.1 mg/ml BCP solutions at pH 7, obtained from dynamic light scattering..... 192

**Figure A-6.** Cryogenic scanning electron microscopy images of 0.1 mg/ml, pH 7 DB solution upon over sublimation and removal of too much water which results in heaping together of micelles..... 192

**Figure A-7.** Cryo-SEM images of freeze fractured surfaces of flash frozen STB BCP solutions, concentration 2 mg/ml and adjusted to pH 7, taken after sublimation to expose BCP structure.....193

**Figure A-8.** Cryo-SEM images of freeze fractured surfaces of flash frozen LTB BCP solutions, concentration 2 mg/ml and adjusted to pH 7, taken after sublimation to expose BCP structure..... 194

**Figure A-9.** Cryo-SEM images of freeze fractured surfaces of flash frozen DB BCP solutions, concentration 2 mg/ml and adjusted to pH 7, taken after sublimation to expose BCP structure..... 195

**Figure A-10.** Cryo-SEM images of freeze fractured LTB BCP solutions, concentration 5 mg/ml adjusted to pH 7..... 196

**Figure A-11.** Cryo-SEM images of freeze fractured surfaces of flash frozen DB BCP solutions at 2 mg/ml concentration with 0.2 M of NaCl added and adjusted to pH 7, taken after sublimation to expose BCP structure..... 197



<b>Figure A-12.</b> Variation of 0.004 mM DPH fluorescence ( $\lambda_{\text{ex}} = 350$ nm, $\lambda_{\text{em}} = 457$ nm) with BCP concentration, determined after allowing 5h for DPH solubilization. Lines illustrate the procedure used to determine the critical micelle concentration at 22 °C.....	198
<b>Figure B-1.</b> AFM of PD-PP-PD assembled with PAA or PSS at pH 4 or pH 7 after the 1st bilayer deposition reveal different initial film growth mechanisms. Confluent films are formed for assembly with both PAA or PSS at pH 7 but assembly at pH 4 shows the tendency for blob formation on the surface, more toward island type growth.....	199
<b>Figure B-2.</b> The morphological evolution of PD-PP-PD/PAA multilayers assembled at pH 4; AFM images of 1, 2, 5, 10 and 15 bilayer films, reveal an island growth mechanism of initial film formation during LbL assembly, where islands nucleate, grow and merge to form a conformal film during the first 15 bilayer deposition cycles.....	200
<b>Figure B-3.</b> AFM tapping mode images of dry (PD-PP-PD/PAA 4.0) <sub>15</sub> shows fully conformal films are formed after 15 bilayers of deposition. PP-PD-PP in pH 4, 0.1mg/ml solutions used for LbL assembly exist in a unimeric state as opposed to micelles at pH 7. The dry film surface morphology of multilayers of PP-PD-PP assembled with PAA at pH 4 is starkly different from films assembled from the same constituents at pH 7 seen in Figure B.3.....	201
<b>Figure B-4.</b> AFM tapping mode images of dry (PD-PP-PD/PAA 7.0) <sub>15</sub> reveals interesting dimpled structures that originate from micelle deposition.....	202
<b>Figure B-5.</b> AFM tapping mode images of dry (PD-PP-PD/PSS 7.0) <sub>10</sub> shows that the dry film surface morphology of multilayers of PP-PD-PP assembled with PSS at pH 7 also show evidence of dimple-type structure but have a different (more granular) surface as compared to PP-PD-PP assembled with PAA at the same pH of 7.....	203
<b>Figure B-6.</b> AFM tapping mode images of dry (PD-PP-PD/PSS 4.0) <sub>2</sub> shows rather unique the dry film surface morphology. It is interesting to recall from Chapter 1 that (PD-PP-PD/PSS 4.0) grows extremely slowly with less than 30 nm of film formed after 60 bilayer deposition cycles, the morphology shown here of a 2 bilayer film does not vary much from that of a 60 bilayer one.....	204
<b>Figure B-7.</b> AFM tapping mode images of dry (PD-PP-PD/PSS 4.0) <sub>41</sub> .....	205
<b>Figure B-8.</b> AFM tapping mode images of dry (PD-PP-PD/PAA) <sub>1</sub> assembled from PBS buffer.....	206
<b>Figure B-9.</b> Effect of assembly pH on PD-PP-PD/PAA surface morphology. AFM images of PD-PP-PD/PAA assembled at pH 4, pH 6, pH 7 and pH 8.....	207
<b>Figure B-10.</b> (PD-PP-PD/PAA 7.0) <sub>9</sub> assembled at room temperature dried at (a) 6 °C (b) 24 °C and (c) 40 °C. ....	208
<b>Figure B-11.</b> AFM tapping mode images of dry (PD-PP-PD/PAA 7.0) <sub>16</sub> multilayer films before ((a) and (c)) and after more than 5 swelling and deswelling cycles between 6 and 20 °C in DI water adjusted to pH 7. Images (a) and (b) are 500 nm X 500 nm while (c) and (d) are 1 $\mu\text{m}$ X 1 $\mu\text{m}$ .....	209

**Figure B-12.** AFM  $5\ \mu\text{m} \times 5\ \mu\text{m}$  height image (a) and corresponding phase image (b) of a dried DB/PAA multilayer post swelling in pH 7 DI water for 30 mins at  $6\ ^\circ\text{C}$ . White scale bars on the bottom right of each image represent 250 nm and the height and phase scales are shown on the right. An optical micrograph (c) is included to provide a large scale overview..... 210

**Figure B-13.**  $1\ \mu\text{m} \times 1\ \mu\text{m}$  (a) and  $3\ \mu\text{m} \times 3\ \mu\text{m}$  (b) atomic force microscope (AFM) images of dried (DB/PAA 7.0)<sub>35</sub> after 2 min swelling ( $T = 6\ ^\circ\text{C}$ ) and deswelling ( $T = 20\ ^\circ\text{C}$ ) cycles in pH 7 DI water. The left column consists of height images while the right column consists of phase images. This image reveals the beginning of instability and defect formation in the diblock copolymer multilayers when cycled at  $\Delta T = 9\ ^\circ\text{C}$  as opposed to reversible cycling at  $\Delta T = 6\ ^\circ\text{C}$  as seen in Chapter 4 Fig. 4-8..... 211

**Figure C-1.** AFM height images of uncoated PMMA substrate surfaces showing nanometer to micron scaled surface defects like potholes and scratches that can scatter light incident on these substrates..... 214

**Figure D-1.** Hierarchical assembly of fluorescein-labeled TMV1cys nanotemplates onto encoded and capture DNA embedded PEG-based microparticles. (a) Schematic diagram depicting the labeling, disassembly, and programming of TMV1cys. (b) AFM topographical image of TMV1cys. (c) Sucrose gradient containing fluorescently labeled TMVs as a discrete band (boxed) separated from unreacted fluorescein dye at the top of the sucrose gradient. (d) Brightfield micrograph of encoded microparticles. (e) Schematic diagram of stop-flow lithography (SFL) for production of encoded and DNA embedded microparticles. (f) Formation of nanobio-synthetic hybrid microentities following hybridization based assembly of TMVs with microparticles..... 220

**Figure D-2.** Hierarchical assembly of fluorescein-labeled TMV1cys nanotemplates onto microparticles via nucleic acid hybridization. (a) Overlay fluorescence image of fluorescein-labeled TMV1cys onto Rhodamine B labeled and encoded microparticles. Three regions define the  $180 \times 90 \times 30\ \mu\text{m}$  microparticles: an encoded region containing Rhodamine B, a middle negative control region, and a capture DNA region. (b) Fluorescence intensity plot across the TMV assembled region shown by the yellow line. .... 224

**Figure D-3.** TMV templates hybridized with a mixture of three different microparticle types. (a) Three microparticle types, all differing by the barcode and capture DNA sequence embedded within the microparticles. (b) Fluorescence overlay image showing fluorescein-labeled TMV1cys assembled onto only the microparticles containing the matching DNA sequence, C2..... 225

**Figure D-4.** AFM phase contrast image of TMV assembled onto encoded microparticles..... 226

**Figure D-5.** One-pot assembly of fluorescein-labeled TMV and ssDNA onto discrete regions of multifunctional microparticles: (a) Schematic diagram showing the three regions of the multifunctional microparticles: the TMV-complimentary (round edge) and ssDNA-complimentary (straight edge) regions are separated by a middle negative control region. (b) Brightfield image of the multifunctional microparticles. The yellow bar represents  $50\ \mu\text{m}$ . (c) Reconstituted 3-D confocal image of a multifunctional microparticle following hybridization with the fluorescein-labeled TMV and ssDNA. (d-f) Confocal z-scan images of TMV and ssDNA hybridized microparticles at the surface (d) several micrometers below the surface (e), and center (f)..... 227

## LIST OF TABLES

<b>Table 2-1.</b> Micellization temperatures of PD-PP-PD solutions at different pH obtained using microDSC and DPH-solubilization techniques.....	58
<b>Table 2-2.</b> Average thickness increment per bilayer for (PD-PP-PD/PAA4.0), (PD-PP-PD/PSS4.0), (PD-PP-PD/PAA7.0), and (PD-PP-PD/PSS7.0).....	61
<b>Table 4-1.</b> Composition and polydispersity of block copolymers.....	97
<b>Table 4-2.</b> BCP solution micellization characteristics, including micelle diameter, micellization temperature and critical micelle concentration.....	100
<b>Table 5-1.</b> Pore wall coating thickness, $t_p$ , at the different temperatures (T) as inferred from the transmembrane flux using Equation 5-3.....	126
<b>Table 6-1.</b> Refractive index and thickness of various nanoparticle/nanoparticle and nanoparticle/polymer components used in LbL assembly of coatings on PMMA.....	161
<b>Table C-1.</b> List of refractive index, thickness and thickness/bilayers(bL) values of a variety of LbL coatings deposited on unmodified and modified PMMA substrate surfaces.....	213
<b>Table C-2.</b> List of refractive index and thickness values of a variety of LbL coatings before and after hydrothermal treatment (HT) at 90 °C in saturated water vapor for 4 hours.....	215



# CHAPTER 1: INTRODUCTION & BACKGROUND

## 1.1 INTRODUCTION

This chapter introduces several concepts and ideas surrounding responsive hydrogels, polyelectrolytes, block copolymer micellization and Layer-by-Layer assembly. The fundamental concepts outlined in this chapter are included to provide readers with a common foundational framework for understanding the subsequent interpretation and discussion of results presented in this thesis. The aim of this introduction is to provide relevant background knowledge. While not included here, detailed literature reviews of work relevant to each chapter are presented in the individual introduction sections of the chapters to follow.

## 1.2 RESPONSIVE HYDROGELS

Stimuli responsive hydrogels are able to reversibly uptake large amounts of water and in doing so exhibit large changes in volume, mechanical compliance<sup>1,2</sup>, solute permeability<sup>3</sup>, and chemical affinity<sup>4</sup>. As a result, they are of interest for controlled drug delivery<sup>5</sup>, mechanical actuation<sup>6</sup>, molecular separations<sup>4</sup> and sensing<sup>7</sup> amongst several other applications.

Put simply, gels are polymer networks (held together by physical or chemical crosslinks) that are able to hold a large amount of solvent, the solvent being water in the case of hydrogels. Key material properties of interest in gel materials are tuned, namely, by a few interrelated parameters: the crosslink density or molecular weight between crosslinks (also related to the ‘mesh size’ of a gel), polymer solvent affinity, and the nature of the crosslinks.

Since the swelling of thin film hydrogels is a recurring topic in this thesis, a brief theoretical background relating to the swelling and elastic properties of gels in general is provided here.

Based on the Flory-Rehner theory<sup>8</sup>, the thermodynamic drive toward solvent polymer mixing and gel swelling is opposed by entropically derived retractive forces of polymer chains that resist chain extension during swelling. The changes in total Gibbs free energy of a neutral gel,  $\Delta G$ , can be expressed as a sum of the change in free energy due to mixing,  $\Delta G_{mix}$ , and the change in free

energy of polymer chains as a result of chain deformation,  $\Delta G_{el}$ , as shown in black in Equation (1).

$$\text{Equation (1),} \quad \Delta G = \Delta G_{mix} + \Delta G_{el} \quad (+\Delta G_{ion})$$

In the case of an ionic hydrogel where the polymer chains in the network carry charged groups, an additional term  $\Delta G_{ion}$  (added to Equation (1) in grey) needs to be considered<sup>9</sup>.  $\Delta G_{ion}$  deals with the energetic changes that arise from electrostatic interactions between the charged groups as well as the mixing of solvent molecules and counterions.<sup>10</sup> Counterions are oppositely charged ions attracted to the vicinity of charged groups on the polymer backbone that maintain overall charge neutrality of the system.

According to the Flory-Rehner theory, equilibrium swelling of a neutral gel is achieved when the chemical potential of solvent molecules ( $\mu_1$ ) within the gel network is equal to that in the bulk solvent ( $\mu_1^o$ ).

$$\text{Equation (2),} \quad \mu_1 - \mu_1^o = (\Delta\mu_1)_{mix} + (\Delta\mu_1)_{el} = 0$$

Using Flory-Huggins theory<sup>11</sup>, the change in solvent chemical potential due to mixing of solvent molecules with polymer chains of high degree of polymerization,  $N$ , can be expressed as<sup>12 13</sup>

$$\text{Equation (3),} \quad (\Delta\mu_1)_{mix} = RT[\ln(1 - v_{p,s}) + v_{p,s} + \chi v_{p,s}^2]$$

Where  $R$  is the universal gas constant, 8.314 J/mol/K,  $T$  is the temperature of the solution,  $v_{p,s}$  is the volume fraction of polymer chains in the swollen gel (thus subscripts  $p$  and  $s$ ) and  $\chi$  is the Flory-Huggins interaction parameter that is a measure of solvent polymer affinity (described further in Section 1.2.1).

The change in solvent chemical potential due to polymer chain deformation is given by<sup>11,13</sup>

$$\text{Equation (4),} \quad (\Delta\mu_1)_{el} = RT \left[ \frac{V_1}{\bar{v}\bar{M}_c} \right] \left[ 1 - \frac{2\bar{M}_c}{\bar{M}_n} \right] v_{p,r} \left[ \left( \frac{v_{p,s}}{v_{p,r}} \right)^{1/3} - \frac{1}{2} \left( \frac{v_{p,s}}{v_{p,r}} \right) \right]$$

Where  $V_1$  is the molar volume of the solvent,  $\bar{v}$  is the specific volume of the polymer,  $\bar{M}_c$  is the molecular weight between crosslinks in the polymer network,  $\bar{M}_n$  is the molecular weight of the component polymer chains in their uncrosslinked state and  $v_{p,r}$  is the volume fraction of polymer chains in their relaxed state in an unswollen gel.

Since the polymer chains in a gel are crosslinked and held fixed within the gel, while solvent molecules can diffuse into and out of the gel, the physical boundary of the gel can be thought of as a semi-permeable membrane that sustains an osmotic pressure,  $\pi_{os}$ , across the gel surface due to the presence of polymer chains within the gel. Thinking in terms of the energetic changes per unit change in gel dimension, equilibrium gel swelling involves a force balance between the osmotic pressure  $\pi_{os}$  acting to swell the network and the elastic pressure that arises from entropic cost of extending polymer network chains. The theory of rubber elasticity assumes the latter to be the sum of contributions resulting from the changes in the distribution of individual network chain configurations during swelling. For a perfect tetrafunctional network with no trapped entanglements, the elastic pressure,  $\pi_{el}$ , is given by Equation (5)<sup>2,8</sup>.

Equation (5), 
$$\pi_{el}/k_B T = A \frac{\varphi R^2}{NR_o^2}$$

Where  $N$  is the number of statistical units between crosslinks,  $R$  and  $R_o$  are the root mean-squared end-to-end distance of a network chain in the stretched state at concentration  $\varphi$  and in its unperturbed state respectively. The prefactor  $A$  is related to assumptions made with respect to fluctuations of interchain junctions.

Here, it is straightforward to see that the equilibrium swollen state of a polymer gel, where the osmotic pressure,  $\pi_{os}$ , is exactly balanced by the elastic pressure,  $\pi_{el}$ , generated by the stretched network chains, is related to the ratio of the stretched to un-stretched polymer dimensions,  $\frac{R^2}{R_o^2}$ , as shown in Equation (5). Factors that affect chain dimensions thus affect the swelling of gels. These factors are discussed below, in Section 1.2.1.

Written in an alternative form more useful to experimentalists (who can often have control over  $\bar{M}_c$  during gel formation), the equilibrium swelling of a gel is related to the molecular weight between crosslinks,  $\bar{M}_c$ , by Equation (6)<sup>8</sup>.

Equation (6), 
$$\bar{M}_c = -V_1 \rho_p (c^{1/3} - 0.5c) / [\ln(1 - c) + c + \chi c^2]$$

Where  $\rho_p$  is the polymer density,  $c$  is the relative concentration of polymer,  $1 + \frac{\rho_p(W - W_o)}{\rho_s W_o}$  in which  $\rho_s$  is the solvent density,  $W_o$  is the dry weight of the gel and  $W$  is the equilibrium weight of the swollen gel.

From Equation (6), it is clear that increasing the molecular weight between crosslinks by decreasing the crosslink density is a straightforward synthetic means to create gels with higher equilibrium fractions of solvent.

It is also important to note that the osmotic pressure  $\pi_{os}$  that acts to swell gel networks can take on additional twists. For example when charged polymers like polyelectrolytes in aqueous media are considered and the  $\Delta G_{ion}$  term in Eqn. (1) becomes active. The osmotic pressure in such cases takes on an additional dependence on the ionization state of the polymers<sup>2,9,10</sup>. Ionized groups on the polymer backbone of polyelectrolyte network chains carry charge and attract counterions that contribute to generation of additional osmotic pressure within the gel. Further, like charges along the polymer backbone experience electrostatic repulsion away from one another and act to stretch the chains further. As such the degree of swelling of polyelectrolyte gels is highly dependent on the charged state of network chains as well as charge screening effects of added salt<sup>10,13</sup>. With weak polyelectrolytes (discussed in Section 1.3), pH dependent ionization is possible and allows for the creation of pH responsive hydrogels.

Since the temperature responsive polymer networks studied in this thesis involve weak polyelectrolytes, the effects of temperature, pH and salt concentration interplay and influence the degree of hydrogel swelling observed.



### 1.2.1 Controlling gel properties through changes in polymeric chain configurations.

In order to understand the changes in gel swelling, we first consider the basic unit of a swelling gel: the network polymer chain between crosslinks. The dimensions of a polymer chain can be characterized by a vector  $\mathbf{R}$  that points from one end of the chain to the other. Assuming a freely jointed chain, a polymer of  $N$  bonds of length  $\mathbf{b}$ , takes on the trace of a random walk of  $N$  steps of length  $\mathbf{b}$ . Consequently, the probability distribution of  $\mathbf{R}$  is Gaussian. With one end of the chain at the origin, we have the probability of  $\mathbf{R}$  as a function of  $N$  and  $\mathbf{b}$  given by<sup>14</sup>

Equation (7), 
$$P(\mathbf{R}, N) = \left(\frac{3}{2\pi N\mathbf{b}^2}\right)^{3/2} \exp\left(-\frac{3\mathbf{R}^2}{2N\mathbf{b}^2}\right)$$

Unlike a random walk however, polymer chains cannot fold back onto themselves as it is not physically possible for distinct portions of a polymer chain to occupy the same point in space. Despite this fact, under certain conditions, real polymer chains can be modeled well by this ‘random walk model’, where, following from Eqn. (7), the mean squared end-to-end distance of the chain,  $\overline{r_o^2}$ , has a linear dependence on  $N$ .  $\overline{r_o^2}$  can be written in terms of an effective bond length  $\mathbf{b}_{\text{eff}}$  as follows:

Equation (8), 
$$\left(\overline{r_o^2}\right) = N\mathbf{b}_{\text{eff}}^2$$

Commonly,  $\left(\overline{r_o^2}\right)$  is also be expressed as  $\left(\overline{r_o^2}\right) = C_{\infty}Nl^2$  where  $C_{\infty}$  is a measure of chain flexibility. The important take home point is that in these models,  $\left(\overline{r_o^2}\right) \propto N$ .

Polymer chains, with  $\left(\overline{r_o^2}\right) \propto N$  are called ‘ideal chains’. Related to the random walk model above is the Gaussian chain model. While the Gaussian model is purely mathematical in nature and very simple, it is perhaps one of the most powerful models for the qualitative understanding of polymer physics. The Gaussian chain model assumes the polymer chain to be composed of  $N$  segments where the bond vector,  $\mathbf{r}$ , possesses some flexibility (unrelated to physical bond lengths) and follows a Gaussian distribution.

Gaussian distribution: 
$$P(\mathbf{r}) = \left(\frac{3}{2\pi\mathbf{b}^2}\right)^{3/2} \exp\left(-\frac{3\mathbf{r}^2}{2\mathbf{b}^2}\right)$$

Writing the position vector of the  $n^{\text{th}}$  segment as  $\mathbf{R}_n$ , the distribution of the bond vector  $\mathbf{r}_n = \mathbf{R}_n - \mathbf{R}_{n-1}$  is given by Equation (9). The chain configuration is thus described by the set of

position vectors  $\{\mathbf{R}_n\} \equiv (\mathbf{R}_0, \mathbf{R}_1, \dots, \mathbf{R}_N)$  and the probability distribution of the chain configuration is described by the probability distribution of this set of vectors and given by<sup>14</sup>:

$$\text{Equation (9),} \quad P(\{\mathbf{R}_n\}) = \left(\frac{3}{2\pi b^2}\right)^{3N/2} \exp\left(-\frac{3}{2b^2} \sum_{n=1}^N (\mathbf{R}_n - \mathbf{R}_{n-1})^2\right)$$

Thinking of the Gaussian chain as segments connected by harmonic springs with spring constant  $k$ , the energy of the chain can be written as<sup>14</sup>

$$\text{Equation (10),} \quad U = \frac{1}{2} k \sum_{n=1}^N (\mathbf{R}_n - \mathbf{R}_{n-1})^2$$

Where the equilibrium state of the chain is then described by a distribution function proportional to  $\exp\left(-\frac{U}{k_B T}\right)$ . Using a spring constant  $k = \frac{3k_B T}{b^2}$ , the mathematical description of the chain's equilibrium distribution becomes equivalent to Equation (9). Owing to this connection to spring-like behavior, the Gaussian chain model is often called the bead-spring model.

While polymer chains can be thought of to occupy a roughly spherical volume with diameter

$O\left(\overline{r_o^2}^{1/2} = \sqrt{N}b\right)$ , the radius of gyration  $\mathbf{R}_g$  is often a more convenient way to express the size of a polymer chain because it can be directly measured (e.g. by light or small angle X-ray scattering) and can be defined for polymers with non linear, branched structures. Put simply,  $\mathbf{R}_g$  is related to the polymer center of mass,  $\mathbf{R}_G = \frac{1}{N} \sum_{n=1}^N \mathbf{R}_n$  by<sup>14</sup>,

$$\text{Equation (11),} \quad \mathbf{R}_g^2 = \frac{1}{N} \sum_{n=1}^N \langle (\mathbf{R}_n - \mathbf{R}_G)^2 \rangle$$

For an ideal chain with large  $N$ ,  $\mathbf{R}_g$  is related to the average square of the end-to-end distance of a chain given by the random walk model (in Equation (8)) by<sup>14</sup>:

$$\text{Equation (12),} \quad \mathbf{R}_g^2 = \frac{1}{6} \overline{r_o^2}$$

While the ideal chain model simplistically takes into account only short range interactions, extensive investigations into the statistical properties of polymer chains that take account for excluded volume effects (related to the fact that polymer chain segments cannot exist at locations already occupied by another segment), has shown that for large  $N$ , the following holds<sup>14</sup>:

$$\text{Equation (13),} \quad \mathbf{R}_g \sim N^\nu b$$

Where the exponent  $\nu$  is approximately 0.588 (or 3/5) when excluded volume is accounted for. We see that the characteristic size of excluded volume chains is proportional to  $N^{3/5}$  rather than  $N^{1/2}$  for an ideal chain. This difference indicates that the average size of an excluded volume chain is greater than an ideal chain of the same  $N$ . This follows logically from the fact that segment overlap is more probable in compact chain configurations as compared to expanded ones. In the excluded volume model, elimination of configurations in which chain overlap occurs shifts the size distribution to larger values.

While the above models do not take into explicit account the influence of solvent, the dimensions of polymer chains in solutions depend on solvent quality. Chain dimensions will be expanded to maximize the number of polymer solvent contacts in a ‘good’ solvent and chain dimensions will be collapsed in a ‘poor’ solvent, where polymer segments prefer to be in contact with other polymer segments.

In representing real polymer chains in bulk or solvent, the chain dimension dependence on  $N$  can generally be described by  $R_g \sim N^\nu$  with specific solvent effects included in the parameter  $\nu$ .

To describe the effects of solvent polymer interactions, it is useful to discuss  $\chi$  in more detail.  $\chi$  is theoretically defined for a polymer-solvent pair as  $\chi = \frac{z\Delta\epsilon}{k_B T}$ , where  $\Delta\epsilon$  is  $1/2$  the energetic cost of replacing a polymer-polymer contact and a solvent-solvent contact with 2 polymer-solvent interactions<sup>11</sup>. When the average of the polymer-polymer and solvent-solvent interaction energies is equal to the polymer-solvent interaction energy,  $\Delta\epsilon = 0$ , representing the lowest possible value of  $\chi$  in the absence of specific bonding. The greater the value of  $\chi$  the higher the energetic cost of polymer-solvent contacts; the less the polymer wants to mix with the solvent, and the more compact the polymer chain conformation. Higher values of  $\chi$  ( $\chi > 1/2$ ) reflect a poor (or non)solvent-polymer pair, while low values of  $\chi$  ( $\chi < 1/2$ ) reflect a good solvent-polymer pair. In the case where  $\chi = 1/2$ , polymer chains exhibit ‘ideal chain’ behavior described by Eqns. (7, 8, 9 and 10)<sup>11</sup>. While experimentally, the concept of  $\chi$  is qualitative in nature,  $\chi$  is one of the most important parameters involved in interpreting the behavior of polymer mixtures and block copolymer behavior.

The changes in polymer chain dimension with solvent quality can be simplistically captured by the different scaling dependencies of  $R_g$  on  $N$  as the solvent quality is varied.

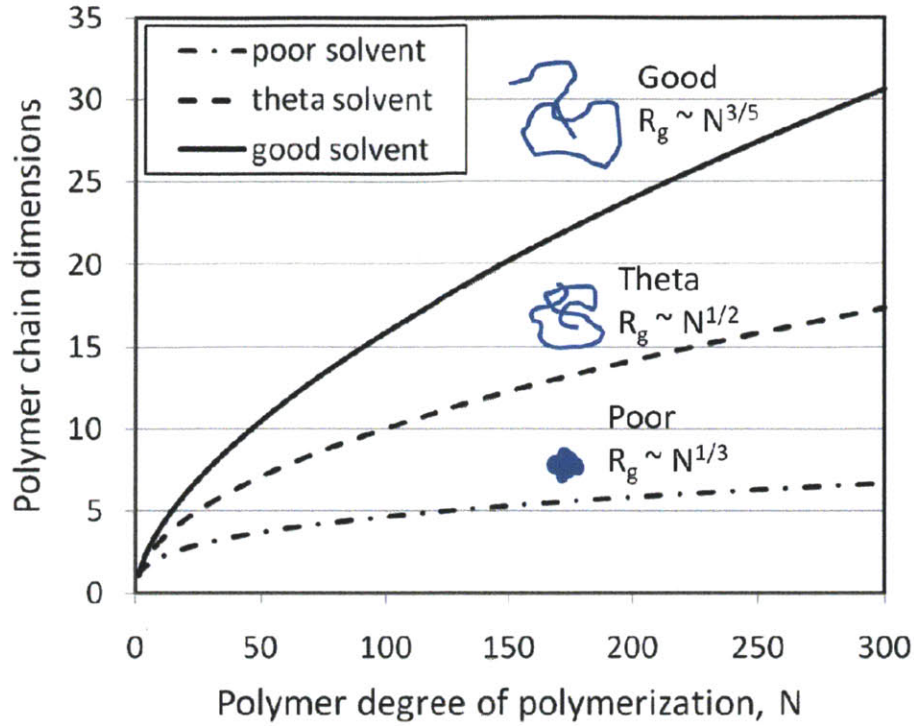


**Figure 1-1.** Diagram showing the evolution of polymer chain dimension with degree of polymerization,  $N$ . Solvents of different quality give different size dependences on  $N$  and the effect of these different scaling regimes is reflected along a vertical where a polymer of fixed  $N$  increases in size when transiting from a poor, to a theta, to a good solvent.

As seen in Figure 1-1, polymer chain dimensions increase with the degree of polymerization,  $N$ , and increase with increasing solvent quality. In the context of gels, swollen gel dimensions increase with increasing molecular weight between crosslinks,  $\bar{M}_c$ , and with increasing solvent quality that changes the exponent,  $\nu$ , as follows<sup>15,16</sup>:

Equation (14), 
$$Q^{1/3} \propto (\bar{r}_o^2)^{1/2} \propto l(N)^\nu \propto l\left(\frac{2\bar{M}_c}{M_o}\right)^\nu$$

Where  $Q$  is the swelling ratio of the gel given by the  $\frac{\text{swollen volume or mass of the gel}}{\text{dry volume or mass of the gel}}$ .

For hydrogel thin films on a rigid substrate, swelling is confined by attachment to the substrate in the lateral direction and the swelling ratio  $\cong \frac{\text{wet(swollen) thickness}}{\text{dry thickness}}$ . The thin film hydrogels studied in this thesis fall in this category and experimentally measured changes in thickness reflect changes in  $Q$ .

### 1.2.2 Temperature responsive hydrogels.

In the class of temperature responsive hydrogels to be discussed in this thesis, changes in swelling degree are elicited through changes in solvent quality with temperature. Temperature responsive hydrogels include chemically crosslinked networks of thermo-responsive polymers or physically crosslinked gels held together by reversible, thermo-labile associations like hydrogen bonds<sup>17</sup>. Commonly used thermo-responsive polymers include ones with lower critical solution behavior in water. Examples are poly(*N*-substituted acrylamides), poly(*N*-vinyl alkylamides), and poly-(vinyl ethers) for which water is a good solvent and polymers are swollen below the lower critical solution temperature (LCST)<sup>17,18</sup>. Above the LCST, these polymers switch from their hydrogen-bonding hydrophilic configuration to a more hydrophobic state and collapse out of solution. These temperature driven changes in polymer-solvent interactions drive the swelling and de-swelling transitions of temperature responsive hydrogel networks<sup>18</sup>. The LCST behavior of poly(propylene oxide) used in this thesis will be discussed in more detail in Section 1.4.2a.

### 1.2.3 Relationship between gel swelling and functional gel properties.

It is useful to understand that while the physical gel size changes upon absorption of an equilibrium amount of solvent determined by the various factors discussed above, these changes are accompanied by changes in a host of other useful material properties, some of which are summarized in Figure 1-2.

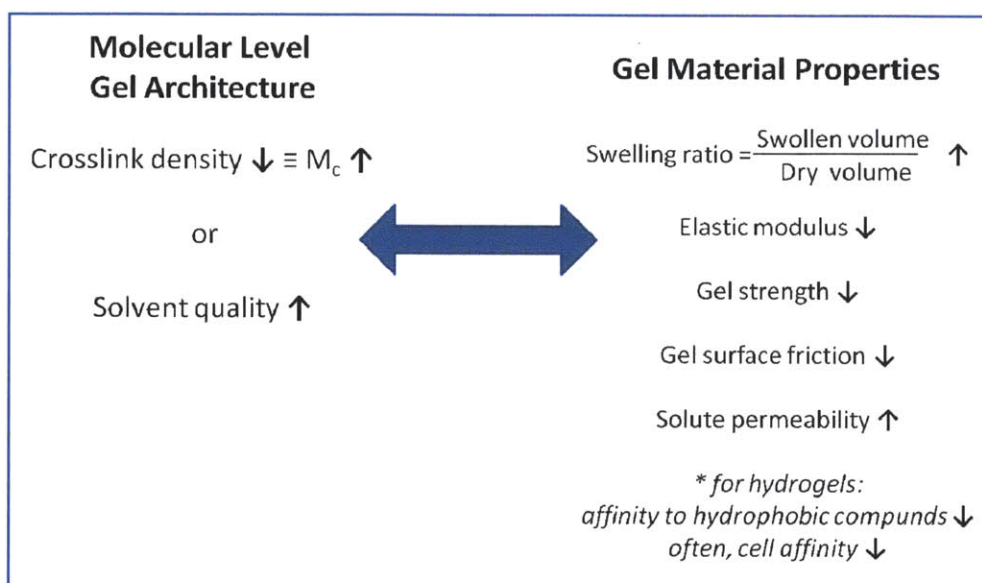


**Figure 1-2.** Scheme showing how molecular level architecture of gels on the left hand side affects gel properties, a list of which is found on the right hand side.

The impact of “mesh size” is of particular interest to the biomedical community in the application of hydrogels to therapeutic trapping and delivery or for (macro)molecular separations.<sup>15,16</sup> The mesh size,  $\xi$  is a measure of the size of openings between crosslinks in a hydrogel network, defined as illustrated in Figure 1-3. The mesh size dependence on experimentally tunable crosslinking density,  $\nu_e$ , and solvent condition dependent chain size is provided by<sup>15,16</sup>,

Equation (15) 
$$\xi \propto \bar{M}_c^{\nu} \propto \left( \sqrt[3]{\frac{1}{\nu_e}} \right)^{\nu}$$

In the case of temperature responsive gels, changes in temperature can elicit reversible association and dissociations between polymer chains. This effectively changes the crosslink density of the network and thus its average mesh size. As illustrated in Fig. 1-3, solutes that are larger than the mesh size ( $\xi$ ) cannot enter the gel matrix, allowing for temperature controlled size based exclusion.

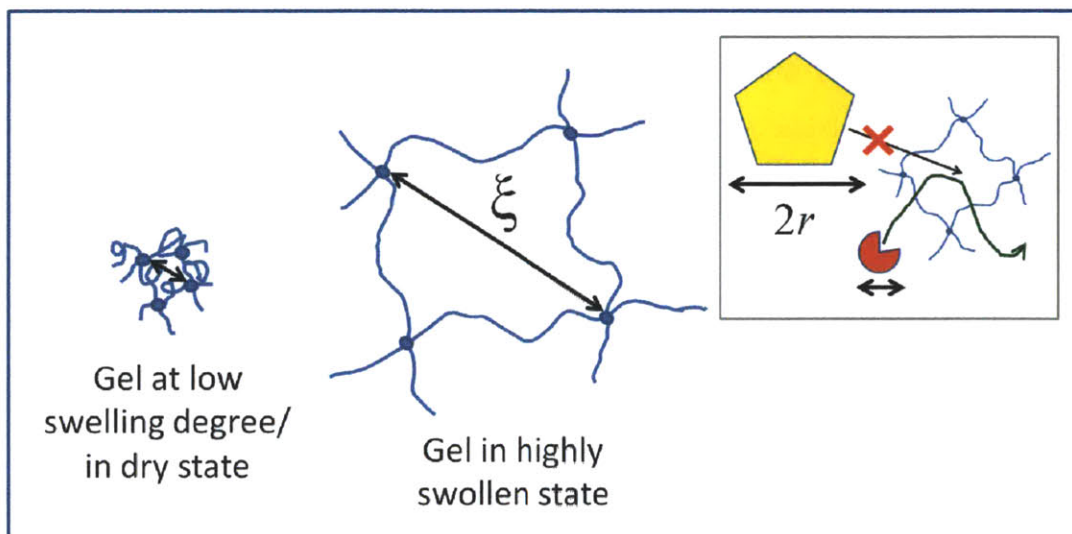


**Figure 1-3.** Schematic diagram illustrating the molecular level architecture of network chains within a hydrogel in a poorly hydrated state (on the leftmost) and in a highly swollen state (in the middle). The mesh size,  $\xi$  of the network is indicated. The inset in the top right corner illustrates how the mesh size of gels determines the size cut off for the passage of various species (e.g. drugs, proteins, or even cells) through gel networks.

For solutes small enough to enter the gel, changes in mesh size affect the rate of their diffusion within the gel<sup>16,19</sup>, as described by<sup>19</sup>

Equation (16) 
$$D_{gel} = D_o \left(1 - \frac{r}{\xi}\right) e^{-\frac{1}{(Q-1)}}$$

Where  $D_{gel}$  is the diffusion coefficient of the diffusing species in the gel;  $D_o$  is its diffusion coefficient in the surrounding medium;  $r$  is the size of the diffusing species (illustrated in Figure 1-3); and  $Q$  is the swelling ratio as defined before (ref. Section 1.2.1, Eqn. (14)).

As seen in Equation (16), the rate of diffusion of molecular species into and out of gels can be effectively controlled by changing the degree of swelling of gels. Responsive gels that respond to specific stimuli with changes in swelling degree are thus of particular interest in controlled drug/chemical release systems<sup>12,16,19</sup>. Diffusion of trapped species can be suppressed at low  $Q$  and their (rapid) release induced at high  $Q$ .

#### 1.2.4 Kinetic factors.

While key factors influencing equilibrium hydrogel swelling and properties have been discussed above, it is important to note that the swelling and shrinking of hydrogels require mass transport that takes time<sup>16,20,21</sup>. At least two transport mechanisms are involved in the volume phase transition of hydrogels. 1) The stimulus (such as temperature difference or pH change) that triggers the volume change needs to be transferred into the hydrogel and 2) solvent molecules or ions redistribution as a result of a chemical potential imbalances that develop within the hydrogel and in the surrounding solvent medium. *The redistribution of various species can in turn change the balance of the osmotic pressure and can cause further water redistribution.*<sup>20,21</sup> Concomitantly, polymer chains of the network need time to rearrange and achieve their expanded or collapsed configurations during hydrogel swelling or shrinking respectively<sup>20</sup>. Due to diffusion limited kinetics of hydrogel responses, where a macroscopically (mm-cm) dry gel might take hours to days to swell to its equilibrium state<sup>22</sup>, the equilibration time can be reduced by several orders of magnitude by shrinking at least one dimension ( $L$ ) of the hydrogel to the nanoscale, with the diffusion time,  $t \propto L^2$ . As a rapid response time is desired for several applications, the creation of thin film hydrogels or microgel particles is an active field of research. The work discussed in this thesis contributes to the former field in the development of temperature responsive thin film hydrogel coatings.

### 1.3 POLYELECTROLYTES

Polyelectrolytes are polymers that contain ionizable groups<sup>23</sup>. Common polyelectrolytes include ones that contain acidic or basic groups that can ionize or become protonated in aqueous solutions. Such polyelectrolytes are often divided into two groups, ‘strong’ polyelectrolytes and ‘weak’ polyelectrolytes. Examples of strong polyelectrolytes and weak polyelectrolytes used in this thesis are shown below.

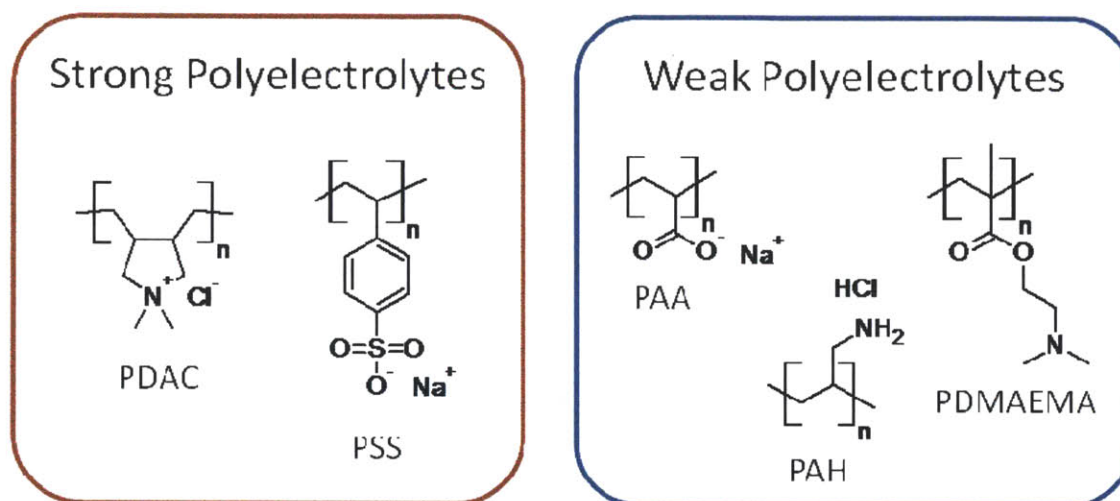


**Figure 1-4.** Chemical structures of various polyelectrolytes used in this thesis, grouped according to their classification as strong or weak polyelectrolytes: poly(dimethyldiallylammonium chloride) (PDAC), poly(sodium 4-styrenesulfonate) (PSS), poly(acrylic acid) (PAA), poly(allylamine hydrochloride) (PAH) and poly(dimethylamino ethylmethacrylate) (PDMAEMA). ‘n’ is the number of repeat units in the polymer chain (= degree of polymerization ‘N’) and varies linearly with molecular weight.

It is important to note that polyelectrolytes like those depicted in Figure 1-4, are different from low molecular weight electrolytes in many ways owing to the connectivity of polymer chains in which n commonly ranges from fifty to several hundred or even thousands of units<sup>23-25</sup>. In addition, charges are fixed at nanometer distances apart along the polymer backbone, often separated only by a handful of covalent bond lengths. As such, unlike typical electrolytes, polyelectrolytes, even in exceedingly dilute solution, have interacting charges along the polymer backbone and a concentrated electrostatic potential that extends further than low molecular weight electrolytes carrying only a few charges<sup>26</sup>. In dilute solution, individual polyelectrolyte molecules represent regions of higher charge density than the bulk solution<sup>26</sup>. Counterions are



attracted to the vicinity of charged groups on the polyelectrolyte and out in the bulk solvent, away from the polyelectrolyte chain, counterion concentration tends to be very low<sup>27</sup>.

In aqueous solutions, polyelectrolyte chain configurations are often related to their degree of ionization,  $\alpha$ , where  $\alpha = \frac{\text{number of charged ionized groups}}{\text{total number of ionizable groups}}$ . In general  $(R_g^2)^{1/2}$  increases as  $\alpha$  increases<sup>23,26,27</sup>. Strong polyelectrolytes are polymers carrying ionizable groups that are all dissociated in water, independent of pH (i. e.  $\alpha = 1$  regardless of solution pH). Often, groups that undergo pH independent ionization are either strongly acidic or strongly basic ones, thus the term ‘strong’ polyelectrolytes.

Weak polyelectrolytes, on the other hand, carry groups that undergo pH dependent ionization.

Ionization of weakly acid or weakly basic groups follow the Equations<sup>28,29</sup>:

$$(17) \quad \alpha = \frac{1}{(1 + 10^{(pk_a - pH)})} \quad \text{for weak acids}$$

$$\text{and (18),} \quad \alpha = 1 - \frac{1}{(1 + 10^{(pk_b - pH)})} \quad \text{for weak bases.}$$

As such, the fraction of charged, weakly acid or weakly basic, groups along a polyelectrolyte backbone correspondingly decrease or increase with increasing pH. The experimentally determined  $pK_a$  (or  $pK_b$ ) of a polyelectrolyte corresponds to the pH at which 50% of the ionizable groups on the polyacid (or polybase) are charged, as indicated by the dotted lines shown in Figure 1-5. It is important to note that  $pK_a$  or  $pK_b$  of polyelectrolytes differ from that of the small molecule acid or basic groups free in solution due to the proximity of the ionizable groups linked along the polyelectrolyte backbone.

To illustrate the effect of pH on polyelectrolyte ionization, Fig. 1-5 shows the idealized evolution of ionization degree with pH expected for a strong polyelectrolyte (PSS), a weak polyacid (PAA;  $pK_a = 6.5$ ) and a weak polybase (PDMAEMA;  $pK_b = 6.9$ ). Fig. 1-5 is illustrative in nature where the curves were drawn using the experimentally determined polyelectrolyte  $pK_a$  or  $pK_b$  and the trends in ionic equilibria expected from Equations 17 and 18. As seen in Fig. 1-5, a weak polybase like PDMAEMA carries basic tertiary amine groups that are fully protonated and positively charged at low pH and fully deprotonated (charge neutral) at high pH. Conversely, a

weak polyacid like PAA has carboxylic acid groups that are not dissociated and charge neutral at low pH, but fully ionized and negatively charged at high pH.

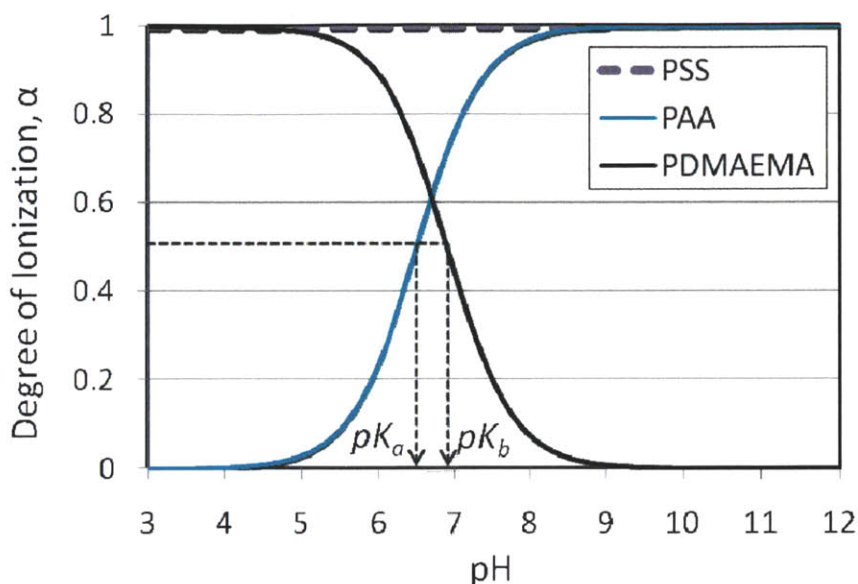


**Figure 1-5** Idealized evolution of ionization degree with pH expected for a strong polyelectrolyte (PSS), a weak polyacid (PAA) and a weak polybase (PDMAEMA).

As mentioned in Section 1.2, swelling of hydrogels containing weak polyelectrolyte components can be controlled by pH and the degree of ionization via electrostatic repulsive interactions and extra osmotic pressure accompanying counterions necessarily present to maintain overall electroneutrality of the gels. The degree of ionization of polyelectrolytes has several implications pertinent to this thesis. Namely, the charge density on the polyelectrolyte backbone affects the polymer chain configuration in solution<sup>23</sup> as illustrated in Figure 1-6 and also affects micellization to be discussed subsequently in Section 1.4.

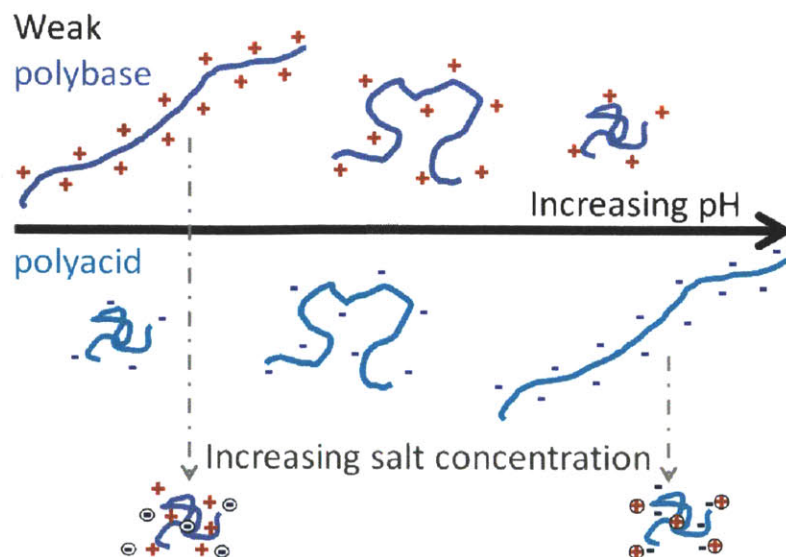


**Figure 1-6.** Schematic illustrating the effect of pH induced changes in  $\alpha$  on polymer chain configurations for weak polyelectrolytes. Grey dotted downward arrows illustrate the effect of added salt that can associate to the fixed charges on the polyelectrolyte backbone and through charge screening lead to more collapsed chain configurations.

Since like charges along the polymer backbone repel and would like to be spatially distanced as far apart from one another as possible, highly charged polyelectrolytes in low salt solutions are often highly outstretched linear chains<sup>23,26</sup> (as illustrated in Figure 1-6). Increasing the salt concentration in the solution screens the charges from one another by reducing the Debye length (the characteristic distance over which charges can feel one another) and allows the polymer chain to take on more compact, coiled conformation.<sup>23,27</sup> The same transition from a highly stretched chain to a more coiled configuration is seen in salt free solutions when the ionization degree,  $\alpha$ , of weak polyelectrolytes is reduced by changing the pH<sup>28,29</sup> as illustrated in Fig. 1-6. Keeping in mind the pH and salt concentration dependence of polyelectrolyte chain conformations in aqueous solution will be helpful in understanding how the deposition pH and salt concentration of polyelectrolyte solutions affect Layer-by-Layer assembly to be discussed in Section 1.5.

## 1.4 BLOCK COPOLYMERS & MICELLIZATION

### 1.4.1 Block copolymers.

Block copolymers are composed of 2 or more chemically distinct polymer chains covalently linked together<sup>30</sup>. They are useful in many applications as the different polymer chemistries when connected together can yield hybrid materials with new unique properties<sup>30-32</sup>. The simplest block copolymer is a diblock, typically denoted A-*b*-B (or simply A-B) to represent a block copolymer of polymer A and polymer B. Increasing in complexity, there are linear triblock copolymers, denoted A-B-A (for 2 polymer types) or A-B-C (for 3 different polymer chemistries) or linear multiblocks of any number of constituents connected in sequence, end to end. Further, 3 or more polymer chains could be connected at a single point as illustrated in Figure 1-7. These polymers are termed “star” polymers. While several other architectures exist, they are beyond the scope of discussion here.

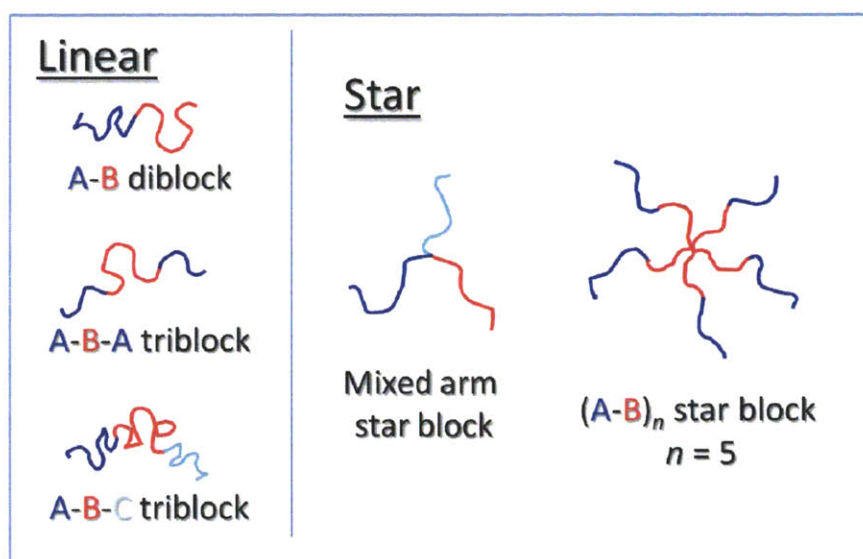


**Figure 1-7.** Drawings to illustrate some block copolymer architectures. A-B diblock, A-B-A triblock and  $(A-B)_n$  star block copolymers in particular are of interest in this thesis. To avoid confusion, only copolymers of 2 distinct chemistries will be discussed in this thesis henceforth.

The total degree of polymerization (in terms of a common reference segment),  $N$ , is proportional to the overall molecular weight, and the composition of the copolymer is typically expressed in terms of the volume fractions of the blocks,  $f_A \propto N_A/N$ , etc.. In this thesis, for convenience of block length identification, the degree of polymerization of each block is subscripted. For

example A<sub>50</sub>-B<sub>100</sub> refers to a block copolymer with 50 units of A connected to 100 units of B. The thermodynamic interactions between any two dissimilar monomers is given by the dimensionless interaction parameter  $\chi_{AB}$  (or simply  $\chi$ ), as described in Section 1.2.1. Here instead of a polymer-solvent interaction, the interaction between equivalent polymer segments of A and B are considered. Once again, the greater the value of  $\chi$  the less the polymer segments want to mix.

Without going too much into the details of block copolymer phase separation thermodynamics<sup>32</sup>, the important point to note is that while small molecules tend to mix due to the entropic gain from mixing, mixing of polymer chains (equivalent to 10s or hundreds of small molecule or typical solvent units covalently linked together) is generally energetically unfavorable unless specific attractive interactions exists between segments of the 2 dissimilar polymer chains. Mixing two non-interacting polymers thus almost always leads to macroscopic phase separation<sup>11</sup>. When 2 dissimilar polymer chains are forced to be connected on a single molecule level as in the case of block copolymers, macroscopic phase separation cannot occur and instead the tendency for A blocks to associate with A blocks and B blocks with B blocks leads to microphase separation<sup>30,32</sup>. As such, connectivity in block copolymers give rise to useful material properties by preserving important features of their constituent homopolymers whilst suppressing macroscopic phase separation<sup>30</sup>.

Further, equilibrium microstructures of block copolymers are composed of regular repeating domains of A and B where domain sizes can be continuously varied from  $\sim 5 - 50$  nm<sup>31</sup>. Even the simplest diblock copolymer exhibits various equilibrium symmetries that include lamellae (L), hexagonally arranged cylinders (C), bicontinuous gyroid (G), and body-centered cubic arrays of spherical micelles (S<sub>bcc</sub>)<sup>32</sup>. By varying the molecular weight of each block and the overall molecular weight of the block copolymer independently, independent control over the type of domains structure, as well as control over the nanoscaled dimension of each domain is possible<sup>32</sup>. Microphase separation of block copolymers makes them attractive self assembling systems for patterning and advanced nano-material applications<sup>31</sup>.

### 1.4.2 Micellization of block copolymers in solution.

In a solvent, block copolymer phase behavior is controlled by the interaction between various segments of the polymers, and, importantly the interactions between the polymer segments and solvent molecules<sup>33,34</sup>. A selective solvent is one that prefers one block over another. Below the crossover concentration at which polymers physically overlap, each block copolymer chain can be fully surrounded by solvent molecules. If the solvent is unfavorable for one block, this can lead to micelle formation<sup>33</sup> in dilute solution as illustrated in Figure 1-8.

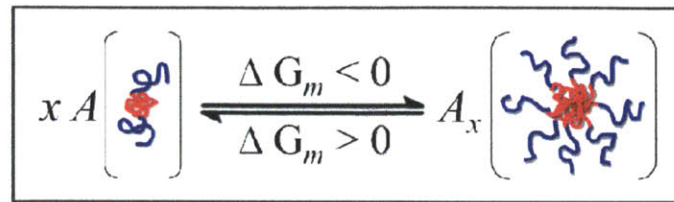


**Figure 1-8.** Schematic illustrating key features of block copolymer micellization.  $x$  is the aggregation number,  $A$  is the block copolymer in a single molecule (unimer) unaggregated state and  $A_x$  is a micelle composed of  $x$  unimers.  $\Delta G_m$  is the Gibbs free energy of micellization. Put simply, when  $\Delta G_m < 0$ , micellization is favored. On the other hand, dissociation of micelles into unimers is favored when  $\Delta G_m > 0$ .

Micellization can be thought of as a dynamic equilibrium between the block copolymers in a unimeric state and micelles of various aggregation numbers,  $x$ .<sup>33</sup> For ease of discussion, the solvophobic, micelle core forming block (drawn in Figure 1-8 in pink) is called P and the solvophilic, corona forming block (drawn in blue) is the B block. Through a balance of the various energetic contributions that drive micellization<sup>33</sup>, often, a dominant aggregation number is favored (to be discussed) and micelle size follows a Gaussian distribution around that value.

In general,  $\Delta G_m$  can be decomposed into three main components:

Equation (19), 
$$\Delta G_m = (\Delta G_m)_{transfer} + (\Delta G_m)_{interface} + (\Delta G_m)_{corona}$$

$(\Delta G_m)_{transfer}$  is related to the transfer of the P block from a unimeric state in contact with solvent molecules into the microphase separated environment within the micelle core where it is in contact with other P blocks. For solvophobic P blocks,  $\chi_{P-solvent}$  is generally large and the large and negative contribution of  $(\Delta G_m)_{transfer}$  is the main driving force for micellization.

$(\Delta G_m)_{interface}$  is the energetic cost of new interface formation between the P-rich micelle core and solvated corona of B. This factor represents the desire of the system to minimize interface per volume of B. This favors larger aggregation numbers and core size. Micelle core size however is physically limited by fact that B blocks have a fixed length and the micelle core size cannot exceed the length of a fully extended B block. Increasing core size is also opposed by the entropic cost of B block stretching required for B blocks to span the radius of the micelle core. A balance between the interface minimization and the entropic costs involved generally leads to a favored equilibrium micelle size<sup>33</sup>.

$(\Delta G_m)_{corona}$  involves the energetic cost of localizing the corona B chains to the corona region of micelles. The block copolymers discussed in this thesis have hydrophilic B blocks that are positively charged weak polyelectrolytes with pH dependent  $\alpha$  (as seen in Fig. 1-5). The positive charges on the B block experience electrostatic repulsion and thus add an additional (pH dependent) energetic cost to the localization of B blocks in the micelle corona. (The effects of pH on micellization are seen in Chapter 2.)

#### **1.4.2a Temperature dependent micellization.**

An important feature governing the micellization of block copolymers of poly(propylene oxide)<sup>35-37</sup> (PPO) (P blocks in Fig. 1-8 illustration) and poly(N,N dimethylamino ethylmethacrylate) (PDMAEMA) (B blocks in Fig. 1-8 illustration) is the fact that PPO exhibits lower critical solution behavior in water. Due to changes in the polymer backbone configuration of PPO with chain conformations able to hydrogen bond with water favored at low temperatures and hydrophobic conformations favored at higher temperature, PPO exhibits a temperature dependent solubility in water<sup>38-40</sup>. A typical phase diagram characteristic of polymers with a lower critical solution temperature (LCST) is shown in Figure 1-9.

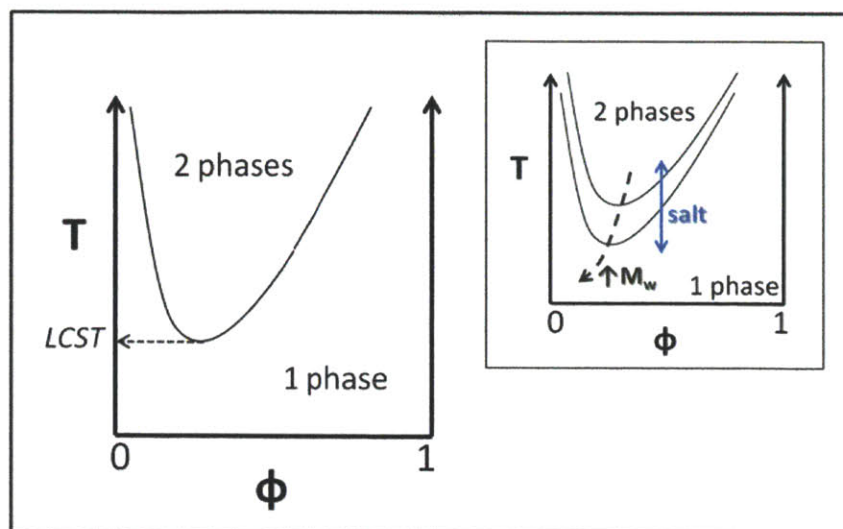


**Figure 1-9.** Typical phase diagram of LCST polymers. The inset shows how polymer molecular weight and other factors that can affect solvent quality like the addition of salt to water can shift the LCST.

As illustrated in Figure 1-9, LCST polymers like PPO phase separate in water at a temperature dependent on the concentration of PPO. PPO's LCST decreases with increasing molecular weight<sup>36</sup>. For reference, the LCST of PPO of molecular weight 3000 g/mol is  $\sim 15\text{ }^{\circ}\text{C}$ <sup>41</sup>. The addition of salt<sup>42</sup> or other additives (e.g. surfactants<sup>43</sup> or solvents<sup>44</sup>) can change the solvent quality of water and influence the phase transition temperature. In general, simple salts compete with PPO in associating with water molecules and lower the solubility of PPO, shifting the LCST down<sup>42,43</sup>. Chaotropic salts however, disrupt hydrogen bond formation in water and tend to have an opposite effect<sup>45</sup>.

When PPO is attached to a water soluble polymer, the resulting block copolymer exhibits temperature dependent micellization. At temperatures below the LCST of PPO, both blocks are soluble. With reference to Figure 1-8 and Equation (19),  $(\Delta G_m)_{transfer}$  is positive and so is the overall  $\Delta G_m$ . At these temperatures, block copolymers exist as single molecules (unimers) dissolved in a homogeneous single phase solution. When the temperature is increased, the interaction between the PPO block and water becomes increasingly disfavored and energetically costly;  $(\Delta G_m)_{transfer}$  decreases and becomes negative. At a critical temperature, termed the critical micellization temperature (CMT),  $(\Delta G_m)_{transfer}$  becomes sufficiently negative and  $\Delta G_m$



changes in sign. The overall negative  $\Delta G_m$  results in spontaneous micelle formation at temperatures above the CMT.

In summary, block copolymers of PPO and PDMAEMA studied in this thesis undergo temperature, pH and concentration dependent micellization that is also influenced by salt concentration via effects of salt on both the electrostatic interactions between charges on PDMAEMA and on the LCST behavior of the PPO block. Several of these factors interplay in this thesis.

## 1.5 LAYER-BY-LAYER ASSEMBLY & MULTILAYER FILMS

As mentioned in Section 1.2, shrinking one dimension of a responsive hydrogel can shorten response times by several orders of magnitude. Responsive hydrogel thin film coatings rather than bulk gels important for active control of surface properties within nano and colloidal science; at synthetic - biological interfaces:<sup>46</sup> of implants, tissue engineering scaffolds or cell culture substrates; and in microfluidic devices, separation columns or as pore linings for active membrane gating<sup>47-49</sup>. In general, there has been a growing focus on the creation of functional conformal thin film coatings for a broad range of advanced applications<sup>49</sup>. To this end, several surface functionalization techniques like surface initiated polymerization<sup>50</sup>, surface grafting<sup>51</sup>, chemical vapor<sup>52</sup> or plasma deposition<sup>53</sup>, spin and dip coating techniques have been utilized. Layer-by-Layer (LbL) assembly<sup>54</sup> has proven to be a facile conformal coating technique based on sequential adsorption of components that can associate via complimentary physical (electrostatic<sup>54</sup>, hydrophobic<sup>55</sup>, hydrogen-bonding<sup>56</sup>) interactions or chemical reactions forming covalent linkages<sup>57-59</sup>\_ENREF\_56. In this thesis, electrostatically driven LbL assembly is used to create functional thin film coatings.

As illustrated in Figure 1-10, panel (b), LbL assembly is done by the sequential dipping of substrates, first into a solution containing a positively charged species (+), rinsed three times (+R1, +R2, +R3), then dipped in a solution containing the negatively charged species (-) and then rinsed three times (-R1, -R2, -R3), after which this cycle is repeated.

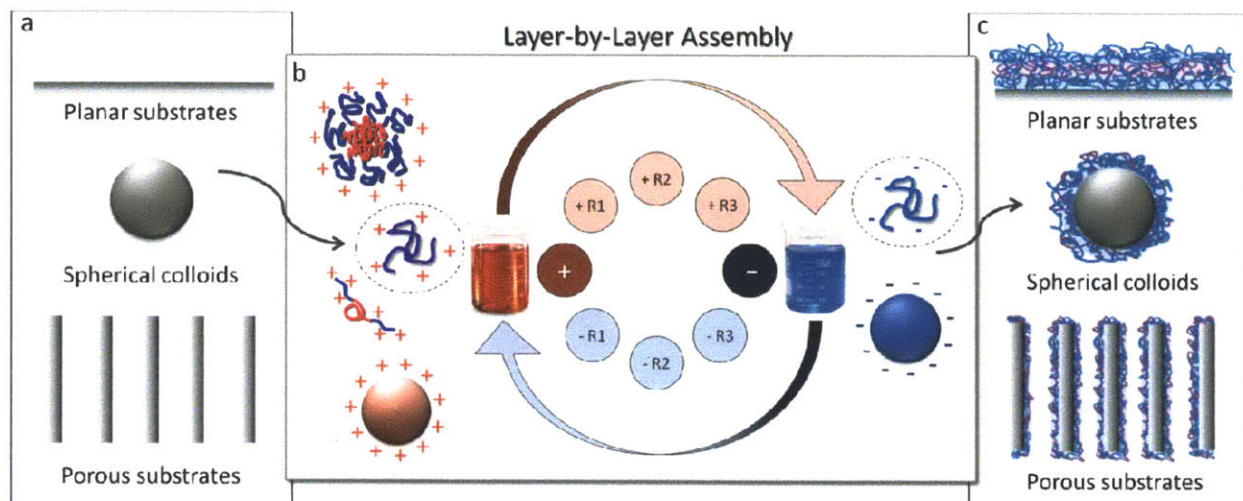


**Figure 1-10.** Schematic of Layer-by-Layer (LbL) assembly process.

The typical dipping sequence used for LbL assembly in this thesis consists of 10 min immersions in the (+) and (-) solutions followed by immersion in the respective rinse solutions, (R1) for 2 min, and (R2) and (R3) for 1 min each. Conventionally, LbL assembled coatings made after  $y$  deposition cycles are denoted as (Positive species  $Z_1$ / Negative species  $Z_2$ ) $_y$ , where  $Z_1$  is the pH of the (+) solutions and  $Z_2$  that of the (-) solutions unless mentioned otherwise.  $y$  is typically known as the bilayer number in the LbL community and stands for the number of positive and negative layers deposited in the sequence. Starting with a substrate with negative surface charge, the (+) species is deposited first and a whole number for  $y$  indicates that the deposition was ended with the negative species on top. A half bilayer, (e.g. 10.5 or 20.5 bilayers) indicates that the deposition cycle was ended with the deposition of the positive species on top. As depicted to the sides of the (+) and (-) solutions in panel (b), examples of Positive species used for LbL deposition in this thesis include positively charged micelles, polycations, unimers of positively charged block copolymers or positively charged inorganic nanoparticles. Negative species include polyanions and negatively charged inorganic nanoparticles. Further, as illustrated in panels (a) and (c), there is great flexibility in the choice of substrates used for LbL assembly<sup>58</sup>. The ability to create conformal coatings on substrates of unique geometries that range from macroscopic objects to free floating nano or micron sized colloids<sup>60,61</sup> and also within confined geometries of nano-channels<sup>62</sup> or membrane pores<sup>63-65</sup>, lends LbL assembly tremendous versatility<sup>66,67</sup>. The thickness of LbL assemblies can be controlled by the number of deposition cycles and fine tuned by adjusting key parameters like solution pH<sup>68,69</sup> and salt concentration<sup>70,71</sup>

which affect charge interactions and polyelectrolyte chain conformation<sup>23-26</sup> (described in Section 1.3) and surface deposition<sup>24,72</sup>. This thesis explores LbL assembly as a means to create responsive thin film hydrogel coatings (Chapters 2-5) and as a means to create tunable anti-reflective coatings (Chapters 6), demonstrating the broad capability of this technique in addressing a diverse set of technological problems.

## 1.6 THESIS OUTLINE

The main goal of this thesis is to develop Layer-by-Layer assembly of temperature responsive block copolymers as a facile method for creating conformal, thin film, responsive hydrogel coatings.

Chapter 2 explores the pH and temperature dependent micellization of temperature responsive triblock copolymers in solution and relates various LbL assembly parameters to the functionality of the final construct. Through the systematic study in Chapter 2, the LbL conditions necessary to allow for LbL assembly of thin films that exhibit temperature driven large scale, reversible swelling transitions are determined.

In Chapter 3, the synthesis of various block copolymers (BCPS), designed to complement the study in Chapter 2, is presented. There, the synthesis procedures for end functionalization of precursor poly(propylene oxide) molecules and atom transfer radical polymerization of poly(N,N dimethylamino ethylmethacrylate), in addition to the characterization of the synthesized BCP products are described.

In Chapter 4, the block copolymers synthesized in Chapter 2 are used to systematically study the effect of block copolymer architecture on the swelling transitions of temperature responsive multilayers assembled from the BCP micelles and poly(acrylic acid). Key influences of block copolymer connectivity and molecular weight are exposed.

Chapter 5 explores various functional aspects of conformal coatings composed of the temperature responsive hydrogels developed in earlier chapters. Their application to temperature based membrane gating; template based creation of functional nanostructures like nanotubes; temperature enabled loading and sustained release of proteins; and tunable disintegration useful for triggered release are demonstrated.

In Chapter 6 a different application of LbL assembly using inorganic nanoparticles is explored. LbL assembly proved to be a facile means to create porous low refractive index, high quality UV anti-reflective (AR) coatings for optical application to PMMA Fresnel lenses. Through this, the

versatility of LbL assembly as a conformal surface modification technique useful in addressing a diverse set of technological challenges is demonstrated. In addition, to achieving coatings of high AR quality, several strategies for stabilization of the inherently weak porous coatings are explored. The theme of block copolymer utility persists in the first strategy where diblock copolymers are applied to modify PMMA surfaces before LbL assembly. In particular, through the work in Chapter 6, a novel means to generate stable, inversely structured surface nanoporosity in thermoplastic materials is developed.

Chapter 7 closes this thesis with a summary of the key findings in each chapter and provides a broader perspective and recommendations for future work.

## 1.7 REFERENCES

- (1) Westman, L.; Lindström, T. *Journal of Applied Polymer Science* **1981**, *26*, 2533.
- (2) Skouri, R.; Schosseler, F.; Munch, J. P.; Candau, S. J. *Macromolecules* **1995**, *28*, 197.
- (3) Raj Singh, T. R.; Woolfson, A. D.; Donnelly, R. F. *Journal of Pharmacy and Pharmacology* **2010**, *62*, 829.
- (4) Kanazawa, H. *Journal of Separation Science* **2007**, *30*, 1646.
- (5) Peppas, N. A.; Khare, A. R. *Advanced Drug Delivery Reviews* **1993**, *11*, 1.
- (6) Dong, L.; Jiang, H. *Soft Matter* **2007**, *3*, 1223.
- (7) Gerlach, G.; Guenther, M.; Sorber, J.; Suchanek, G.; Arndt, K.-F.; Richter, A. *Sensors and Actuators B: Chemical* **2005**, *111-112*, 555.
- (8) Flory, P. J.; Rehner, J. *Statistical Mechanics of Cross-Linked Polymer Networks II. Swelling*; AIP, 1943; Vol. 11.
- (9) Ricka, J.; Tanaka, T. *Macromolecules* **1984**, *17*, 2916.
- (10) Vasheghani-Farahani, E.; Vera, J. H.; Cooper, D. G.; Weber, M. E. *Industrial & Engineering Chemistry Research* **1990**, *29*, 554.
- (11) Flory, P., J. *Principles of polymer chemistry*; Cornell University: Ithaca, N.Y., 1953.
- (12) Peppas, N. A.; Huang, Y.; Torres-Lugo, M.; Ward, J. H.; Zhang, J. *Annual Review of Biomedical Engineering* **2000**, *2*, 9.
- (13) Brannon-Peppas, L.; Peppas, N. A. *Journal of Controlled Release* **1991**, *16*, 319.
- (14) Doi, M. *Introduction to Polymer Physics*; Oxford University Press Inc.: New York, 1996.
- (15) Canal, T.; Peppas, N. A. *Journal of Biomedical Materials Research* **1989**, *23*, 1183.
- (16) Lin, C.-C.; Metters, A. T. *Advanced Drug Delivery Reviews* **2006**, *58*, 1379.
- (17) Huffman, A. S.; Afrassiabi, A.; Dong, L. C. *Journal of Controlled Release* **1986**, *4*, 213.
- (18) Hoare, T. R.; Kohane, D. S. *Polymer* **2008**, *49*, 1993.
- (19) Mason, M. N.; Metters, A. T.; Bowman, C. N.; Anseth, K. S. *Macromolecules* **2001**, *34*, 4630.
- (20) Tanaka, T.; Fillmore, D. J. *Kinetics of swelling of gels*; AIP, 1979; Vol. 70.

- (21) Li, Y.; Tanaka, T. *Kinetics of swelling and shrinking of gels*; AIP, 1990; Vol. 92.
- (22) Andersson, M.; Axelsson, A.; Zacchi, G. *Journal of Controlled Release* **1998**, *50*, 273.
- (23) Dobrynin, A. V.; Colby, R. H.; Rubinstein, M. *Macromolecules* **1995**, *28*, 1859.
- (24) Dobrynin, A. V.; Rubinstein, M. *Progress in Polymer Science* **2005**, *30*, 1049.
- (25) Holm, C.; Joanny, J. F.; Kremer, K.; Netz, R. R.; Reineker, P.; Seidel, C.; Vilgis, T. A.; Winkler, R. G. In *Polyelectrolytes with Defined Molecular Architecture II*; Schmidt, M., Ed.; Springer Berlin / Heidelberg: 2004; Vol. 166, p 3.
- (26) Dobrynin, A. V. *Current Opinion in Colloid & Interface Science* **2008**, *13*, 376.
- (27) Böhme, U.; Scheler, U. *Macromolecular Symposia* **2004**, *211*, 87.
- (28) Netz, R. R. *Journal of Physics: Condensed Matter* **2003**, *15*, S239.
- (29) Panagiotopoulos, A. Z. *Journal of Physics: Condensed Matter* **2009**, *21*, 424113.
- (30) Lodge, T. P. *Macromolecular Chemistry and Physics* **2003**, *204*, 265.
- (31) Hamley, I. W. *Nanotechnology* **2003**, *14*, R39.
- (32) Bates, F. S.; Fredrickson, G. H. *Annual Review of Physical Chemistry* **1990**, *41*, 525.
- (33) Nagarajan, R.; Ganesh, K. *Block copolymer self-assembly in selective solvents: Spherical micelles with segregated cores*; AIP, 1989; Vol. 90.
- (34) Svensson, M.; Alexandridis, P.; Linse, P. *Macromolecules* **1999**, *32*, 637.
- (35) Linse, P. *The Journal of Physical Chemistry* **1993**, *97*, 13896.
- (36) Alexandridis, P.; Holzwarth, J. F.; Hatton, T. A. *Macromolecules* **1994**, *27*, 2414.
- (37) Wanka, G.; Hoffmann, H.; Ulbricht, W. *Macromolecules* **1994**, *27*, 4145.
- (38) Alexandridis, P.; Nivaggioli, T.; Hatton, T. A. *Langmuir* **1995**, *11*, 1468.
- (39) Guo, C.; Liu, H. Z.; Chen, J. Y. *Colloid & Polymer Science* **1999**, *277*, 376.
- (40) Cau, F.; Lacelle, S. *Macromolecules* **1996**, *29*, 170.
- (41) Mortensen, K.; Pedersen, J. S. *Macromolecules* **1993**, *26*, 805.
- (42) Jain, N. J.; George, A.; Bahadur, P. *Colloids and Surfaces A: Physicochemical and Engineering Aspects* **1999**, *157*, 275.
- (43) Desai, P. R.; Jain, N. J.; Sharma, R. K.; Bahadur, P. *Colloids and Surfaces A: Physicochemical and Engineering Aspects* **2001**, *178*, 57.
- (44) Chaibundit, C.; Ricardo, N. g. M. P. S.; Ricardo, N. d. M. P. S.; Costa, F. v. d. M. L. L.; Wong, M. G. P.; Hermida-Merino, D.; Rodriguez-Perez, J.; Hamley, I. W.; Yeates, S. G.; Booth, C. *Langmuir* **2008**, *24*, 12260.
- (45) Alexandridis, P.; Athanassiou, V.; Hatton, T. A. *Langmuir* **1995**, *11*, 2442.
- (46) Costa, R. R.; Custódio, C. A.; Testera, A. M.; Arias, F. J.; Rodríguez-Cabello, J. C.; Alves, N. M.; Mano, J. F. *Advanced Functional Materials* **2009**, *19*, 3210.
- (47) Russell, T. P. *Science* **2002**, *297*, 964.
- (48) Stuart, M. A. C.; Huck, W. T. S.; Genzer, J.; Muller, M.; Ober, C.; Stamm, M.; Sukhorukov, G. B.; Szleifer, I.; Tsukruk, V. V.; Urban, M.; Winnik, F.; Zauscher, S.; Luzinov, I.; Minko, S. *Nat Mater* **2010**, *9*, 101.
- (49) Tokarev, I.; Minko, S. *Soft Matter* **2009**, *5*, 511.
- (50) Prucker, O.; Rühle, J. *Macromolecules* **1998**, *31*, 592.
- (51) Boven, G.; Oosterling, M. L. C. M.; Challa, G.; Jan Schouten, A. *Polymer* **1990**, *31*, 2377.
- (52) Chen, H.-Y.; Elkasabi, Y.; Lahann, J. *Journal of the American Chemical Society* **2005**, *128*, 374.

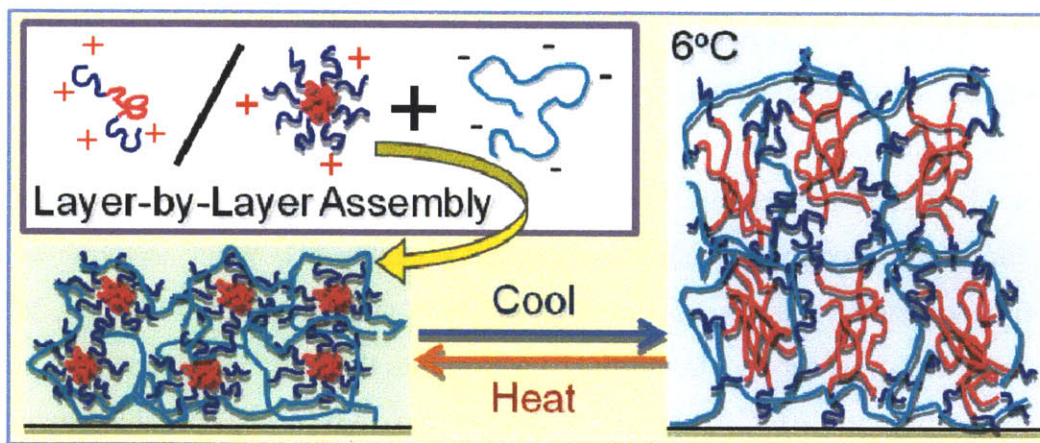
- (53) Coulson, S. R.; Woodward, I. S.; Badyal, J. P. S.; Brewer, S. A.; Willis, C. *Langmuir* **2000**, *16*, 6287.
- (54) Decher, G. *Science* **1997**, *277*, 1232.
- (55) Serizawa, T.; Hashiguchi, S.; Akashi, M. *Langmuir* **1999**, *15*, 5363.
- (56) Sukhishvili, S. A.; Granick, S. *Macromolecules* **2001**, *35*, 301.
- (57) Saurer, E. M.; Flessner, R. M.; Buck, M. E.; Lynn, D. M. *Journal of Materials Chemistry* **2011**, *21*, 1736.
- (58) Ariga, K.; Hill, J. P.; Ji, Q. *Physical Chemistry Chemical Physics* **2007**, *9*, 2319.
- (59) Bergbreiter, D. E.; Chance, B. S. *Macromolecules* **2007**, *40*, 5337.
- (60) Donath, E.; Sukhorukov, G. B.; Caruso, F.; Davis, S. A.; Möhwald, H. *Angewandte Chemie - International Edition* **1998**, *37*, 2202.
- (61) Johnston, A. P. R.; Cortez, C.; Angelatos, A. S.; Caruso, F. *Current Opinion in Colloid & Interface Science* **2006**, *11*, 203.
- (62) DeRocher, J. P.; Mao, P.; Han, J.; Rubner, M. F.; Cohen, R. E. *Macromolecules* **2010**, *43*, 2430.
- (63) Ai, S.; Lu, G.; He, Q.; Li, J. *Journal of the American Chemical Society* **2003**, *125*, 11140.
- (64) Hou, S.; Harrell, C. C.; Trofin, L.; Kohli, P.; Martin, C. R. *Journal of the American Chemical Society* **2004**, *126*, 5674.
- (65) Lee, D.; Nolte, A. J.; Kunz, A. L.; Rubner, M. F.; Cohen, R. E. *Journal of the American Chemical Society* **2006**, *128*, 8521.
- (66) Wang, Y.; Angelatos, A. S.; Caruso, F. *Chemistry of Materials* **2007**, *20*, 848.
- (67) Hammond, P. T. *Advanced Materials* **2004**, *16*, 1271.
- (68) Shiratori, S. S.; Rubner, M. F. *Macromolecules* **2000**, *33*, 4213.
- (69) Choi, J.; Rubner, M. F. *Macromolecules* **2004**, *38*, 116.
- (70) Dubas, S. T.; Schlenoff, J. B. *Macromolecules* **1999**, *32*, 8153.
- (71) Schlenoff, J. B.; Dubas, S. T. *Macromolecules* **2001**, *34*, 592.
- (72) Dobrynin, A. V.; Deshkovski, A.; Rubinstein, M. *Macromolecules* **2001**, *34*, 3421.





## CHAPTER 2: SWELLING TRANSITIONS IN MULTILAYERS OF A CATIONIC TRIBLOCK COPOLYMER AND A POLYACID

*This chapter is reproduced in part with permission from Wui Siew Tan, Robert E. Cohen, Michael F. Rubner, Svetlana A. Sukhishvili\*, Macromolecules, 2010, 43, 1950. Copyright 2010 American Chemical Society.*



\* Work described in this Chapter was initiated in collaboration with Prof. Svetlana A. Sukhishvili from Stevens Institute of Technology Department of Chemistry, Chemical Biology & Biomedical Engineering.

## 2.1 Abstract

In this chapter, layer-by-layer (LbL) assembly is explored as a means to create thin film hydrogels with the ability to undergo thermally-induced large-scale and fully-reversible volumetric changes. Poly(N,N-dimethylaminoethyl methacrylate)-*b*-poly(propylene oxide)-*b*-poly(N,N-dimethylaminoethyl methacrylate) (abbreviated “PD-PP-PD”) was used as a dual pH and temperature responsive component in the electrostatic self-assembly of multilayer thin films. In aqueous solution, the dehydration temperature of the central poly(propylene oxide)(PPO) block, attached to weak polyelectrolyte end blocks of poly(N,N-dimethylaminoethyl methacrylate) (PDMAEMA), was strongly dependent on solution pH, as shown by micro-differential scanning calorimetry (micro-DSC) and dye solubilization techniques. Multilayer films of this cationic triblock copolymer were assembled with poly(acrylic acid) (PAA) or poly(4-styrene sulfonate) (PSS) at various pH values, where the triblock copolymer was incorporated within the film either as unimers or micelles. Using *in situ* ellipsometry, we showed that the polyanion type and the self-assembly pH were both critical parameters in the construction of functional films that change their swelling degree in response to changes in temperature. In particular, strongly associated PD-PP-PD/PSS multilayers, regardless of assembly pH, lacked temperature sensitivity and maintained a constant swelling degree over a wide range of pH and temperature. On the other hand, the temperature response of PD-PP-PD/PAA films was strongly dependent on the self-assembly pH. While swelling of PD-PP-PD/PAA films constructed at  $\text{pH} \leq 5$  was independent of temperature, multilayers assembled at  $\text{pH} \geq 6$  showed fully reversible, 3 to 5-fold changes in film thickness in response to temperature cycling between 6 °C and 20 °C. This temperature responsive behavior is enabled by the ability of PPO domains to reversibly transit between swollen hydrated and collapsed poorly hydrated states. These nano-composite coatings show highly reproducible and reversible swelling transitions that can be useful for various biomedical and device applications.

## 2.2 Introduction

Materials that respond to environmental changes or enable triggered, on-demand responses when a suitable stimulus (such as light, temperature, pH, or salt concentration) is applied are promising for a range of biomedical and micro-mechanical device applications. In particular, for biological systems where pH is often limited to a narrow range of values, temperature, as opposed to pH control, provides a convenient means of externally triggered response. There has been considerable effort to develop responsive materials that change dimensions,<sup>1-3</sup> mechanical properties,<sup>4,5</sup> wettability,<sup>6-9</sup> and permeability<sup>10-12</sup> with temperature. To achieve the desired thermal responsiveness, polymers that undergo reversible temperature-dependent hydration in aqueous environments have been studied; examples include poly(*N*-substituted acrylamides), poly(*N*-vinyl alkyl amides), poly(vinyl ethers), and poly(ethylene oxide-*co*-propylene oxide)<sup>13-17</sup>. These polymers have traditionally been utilized as covalently cross-linked water-swelling bulk materials. However, the macroscopic dimensions of these polymerized gels result in slow response kinetics which may restrict their potential applications. To circumvent these limitations, several studies have focused on reducing the dimensions of these materials and creating thin film coatings of thermally responsive polymers.

Layer-by-layer (LbL) assembly by sequential adsorption of components that interact via electrostatics,<sup>18</sup> hydrogen bonding<sup>19</sup> or specific chemical reaction<sup>20</sup> has proven to be a facile method that can create conformal coatings, of several angstroms to microns thick, on a variety of substrates.<sup>18</sup> Major benefits of this technique are the ability to employ all-aqueous processing, to control nanometer-scale thicknesses, to customize the molecular composition, and to introduce porosity into thin film coatings. By applying the LbL technique to sacrificial template colloid materials, one can also easily create hollow capsules.<sup>21,22</sup> Temperature or pH responsive capsules have thus been created via LbL assembly.<sup>23-25</sup> In order to confer LbL multilayers with temperature sensitivity, a temperature responsive component is incorporated. One of the first approaches to create temperature responsive thin film hydrogels via the LbL method was demonstrated by Serizawa *et al.* and involved sequential reactions between poly(vinyl amine-*co*-*N*-vinylisobutyramide) and poly(acrylic acid) (PAA) on a gold surface.<sup>26</sup> Subsequently, electrostatically assembled multilayers were created by Steitz R *et al.* using a diblock of poly(4-styrene sulfonate)-*b*-poly(*N*-isopropylacrylamide) (PSS-*b*-PNIPAM) and polycations.<sup>27</sup> K. Glinel

*et. al.* reported the creation of hollow thermo-responsive multilayer capsules of similar diblock copolymers.<sup>28</sup> However, in these reports, the response of the LbL films to temperature was irreversible. While limited to micron scale dimensions and acidic media, reversible swelling of electrostatically assembled LbL films of PNIPAM-*co*-PAA microgels with poly(allylamine hydrochloride) (PAH) was reported by Serpe *et. al.*<sup>29</sup> These temperature-responsive microgel multilayers demonstrated thermally triggered release of insulin<sup>30</sup> and doxorubicin<sup>31</sup> at acidic pH values. Recently, Jaber and Schlenoff documented the molecular level reversible uptake and release of water from electrostatically self-assembled multilayers of random copolymers PNIPAM-*co*-PSS and PNIPAM-*co*-PAH with corresponding changes in multilayer permeability.<sup>32</sup> Hydrogen-bonded (H-bonded) LbL assembly of temperature responsive polymers is another viable route to create temperature responsive films. Several possible H-bonded systems are described by Kharlampieva, E. *et. al.*<sup>33</sup> Quinn and Caruso demonstrated the use of a PNIPAM and PAA H-bonded system to load and release a hydrophobic dye with temperature cycling,<sup>34</sup> while more recently, Z. Zhu *et. al.* demonstrated the temperature induced swelling and small molecule release from hydrogen bonded poly(*N*-vinylpyrrolidone)-*b*-PNIPAM micelles and poly(methacrylic acid) (PMAA).<sup>35</sup> Further, the stability of H-bonded multilayers containing temperature-responsive homopolymers (such a PNIPAM) has been found to be temperature dependent. The dissolution of these H-bonded multilayers below a critical temperature has been used to harvest micron sized patches of patterned polyelectrolyte multilayers,<sup>36</sup> and studied in detail for application as temperature-triggered release films.<sup>37</sup> One limitation of hydrogen-bonded films is their pH stability which is limited to pH values below the pK<sub>a</sub> of the H-bond donor.

In this Chapter, the creation of temperature-responsive LbL films that demonstrate temperature-triggered swelling transitions in a wide range of pH is described. This strategy offers a new avenue to confer novel and useful properties to LbL assemblies. We demonstrate that the use of an A-B-A triblock copolymer with charged end-blocks A and a thermo-responsive middle-block B provides large, well-defined and reversible dimensional changes of the film with temperature. Separation of binding and response functions between the end blocks and the central block of the A-B-A triblock copolymer is ideal for achieving two key functions of responsive multilayers. First, in such configuration, the temperature response properties, defined by the length and character of the central block, are conserved and not 'diluted' by a random distribution of

hydrophilic charged monomer units which would raise the lower critical solution temperature (LCST) of the copolymer<sup>38</sup> and form ionic crosslinks within electrostatically assembled films, both of which would compromise the temperature response of this unit. Second, the central B block of the A-B-A triblock copolymer, capable of collapsing in response to temperature variations, is able to effectively transmit this contraction throughout the electrostatically bound network because it is structurally fixed within the film by attachment through charged A blocks at both ends. We describe the use of a symmetric A-B-A triblock copolymer; PDMAEMA-*b*-PPO-*b*-PDMAEMA (abbreviated “PD-PP-PD”) to create reversibly temperature-responsive multilayers. PPO exhibits LCST behavior and its temperature dependent solubility in water as part of copolymers is best documented within the family of non-ionic di- and tri- block copolymers of poly(ethylene glycol) (PEO) and PPO commonly known as Pluronic® and commercialized under the trade name Pluronic®.<sup>39-44</sup> PD-PP-PD is an interesting polyelectrolyte analogue of the well-known PEO-*b*-PPO-*b*-PEO triblock copolymers which should have similar phase and temperature responsive properties based on the central PPO block of similar molecular weight. Armes and co-workers have done significant work on synthesis and solution characterization of various different PDMAEMA containing di-, tri- and ter-block copolymers,<sup>45-49</sup> while the solution pH and temperature sensitivity of PD-PP-PD in particular has been reported by Ni *et. al.*<sup>50</sup> Here we present the use of a triblock copolymer with charged anchoring end-blocks to create electrostatically assembled multilayers with broad pH stability and large amplitude, fully reversible swelling and de-swelling temperature responsive properties. We show that the multilayers’ temperature response is critically dependent on both the assembly conditions and the choice of anionic binding partner for electrostatic self-assembly. These findings demonstrate that the incorporation of triblock copolymers into multilayer films is an effective means to include nanoscopic domains with partitioning, reactive or stimuli responsive functions through selection of an appropriate central block.

### 2.3 Materials and methods

**Materials.** Poly(acrylic acid), PAA ( $M_w \geq 200000$  g/mol; 25% aqueous solution) from Polysciences, Inc., poly(4-styrene sulfonate), PSS ( $M_w \sim 70\ 000$ ) from Sigma-Aldrich, poly(N,N-dimethylaminoethyl methacrylate)-*b*-poly(propylene oxide)-*b*-poly(N,N-dimethylaminoethyl

methacrylate), PD-PP-PD ( $M_w \sim 1600-3000-1600$ ) triblock copolymers from Polymer Source, Inc., and 1,6-diphenyl-1,3,5-hexatriene (DPH) from Sigma Aldrich were used as received.

**Multilayer Construction.** For building of multilayers, we used  $10^{-2}$  M solutions (based on the repeat unit molecular weight) of PAA or PSS polyanions, and 0.1mg/ml solutions of PD-PP-PD polycation in de-ionized, ultrapure Millipore water with resistivity 18 M $\Omega$ ·cm (abbreviated as “DI” henceforth). The pH of all polymer solutions and the DI rinse solutions were adjusted to the desired dipping pH by the addition of 1M NaOH or 1M HCl. Substrates used were polished <100> silicon wafers purchased from Wafernet. Wafers were first UV irradiated for 2 hrs, rinsed in DI water, dried and further cleaned using 150 mTorr oxygen plasma (PDC-32G, Harrick Scientific Products, Inc.) for 30 min. All multilayer thin films were assembled at room temperature (RT) (of  $\sim 24$  °C) by an automated StratoSequence VI spin dipper (from nanoStrata Inc.), controlled by StratoSmart v6.2 software, with substrates spun at 130–160 rpm. The dipping time in each polymer solution was 10 min followed by three rinse steps (of 2, 1, and 1 min each) in DI water adjusted to the same pH as the polymer solutions used. The nomenclature for PEM films follows the convention (“polycation”/“polyanion” $Y$ ) $Z$ , where  $Y$  represents the pH of the polycation, polyanion and DI water rinse solutions used during assembly and  $Z$  is the total number of bilayers (polycation + polyanion) deposited. Since the substrates used have an originally negative surface potential, the first component deposited is the polycation and integral values of  $Z$  indicate that the PEM was finished with a polyanion deposition step.

**Spectroscopic Ellipsometry.** Thicknesses and refractive indices were measured using a Woollam Co. VASE spectroscopic ellipsometer. Data were collected between 300 and 1000 nm, at a 70° incidence angle, and analyzed with WVASE32 software package. Data were fitted with a Cauchy model, which assumes the real part of the refractive index,  $n_f$ , as a function of wavelength,  $\lambda$ , to be  $n_f(\lambda) = A_n + B_n/\lambda^2 + C_n/\lambda^4$ , where  $A_n$ ,  $B_n$ , and  $C_n$  are fitted constants. Film thicknesses were also independently confirmed (to be within 10%) using a P16 (KLA-Tencor Corporation) surface profiler. For *in situ* ellipsometry swelling measurements, a home-built quartz cell was used to measure film thickness when immersed in aqueous solution as described in a previous publication.<sup>51</sup> The refractive index of the pH-adjusted DI solutions was assumed to be that of water (1.33). Since the lateral dimensions of the substrate-bound thin films are

constrained, the swelling ratio of the PEMs in solution was defined as the ratio of the swollen film thickness to dry film thickness.

**Micro-Differential Scanning Calorimetry (micro-DSC).** Differential scanning calorimetry measurements were done using a Microcal MC-2 instrument (Microcal Inc., Amherst, MA). 0.7 ml of DI or sample was used in Hastelloy reference or sample cell, respectively. Both reference and sample cell were sealed during the measurements to prevent solvent evaporation at higher temperatures. Solutions of 3.3 mg/ml PD-PP-PD were adjusted to pH 4, 5, 6, 6.5, 7, 7.5, 8, or 11.4 prior measurements. Temperature scans were performed at a ramp rate of 1 K/min. Cycles between 5 and 65 °C were repeated at least three times for each sample to ensure reproducibility of the exothermic and endothermic temperature-induced transitions.

**Dye Solubilization.** A stock solution of 0.4 mM DPH in methanol and separately, PD-PP-PD solutions of 1 mg/ml and 0.1 mg/ml in DI were adjusted to pH 4, 7, and 8. 15 µL of the DPH/methanol solution was added to 1.5 ml of the PD-PP-PD solution to obtain a 0.004 mM solution of DPH in 1 v/v% methanol/water. Samples were poured in Teflon-stoppered disposable plastic UV-transparent cuvettes with a path length of 1cm, and left in the dark to equilibrate at 6 °C for 2 hrs before spectroscopic measurements. Using the method described by P. Alexandridis *et. al.*,<sup>52</sup> the absorption spectra of the copolymer/DPH/water samples were recorded in the 300 – 500 nm range using a Varian, Cary 500i UV-Vis-NIR dual-beam spectrophotometer, equipped with a temperature controller connected to an electro-thermal multi-cuvette holder. The temperature range of 6 – 40 °C was scanned with a heating rate of 0.06 K/min. The peak absorption at 356 nm, characteristic of DPH, was recorded as a function of temperature.

**Dynamic Light Scattering.** The number average hydrodynamic diameter of PD-PP-PD unimers and micelles in solution at various pH and temperature were determined using ZetaPals (Brookhaven Instrument Corp.) with temperature control and particle sizing functions.

## 2.4 Results and discussion

### 2.4.1 Temperature-triggered micellization of PD-PP-PD in solution.

#### 2.4.1a Effects of pH.

Prior to depositing PD-PP-PD within multilayer films, we studied the solution properties of PD-PP-PD to determine its temperature dependent hydration as a function of solution pH and ionic strength. We used two techniques: micro-DSC and a dye solubilization technique. Micro-DSC is a well documented method used to determine the LCST of polymer solutions,<sup>53</sup> study temperature dependent micellization,<sup>54</sup> or thermally induced collapse and aggregation of block copolymers.<sup>55,56</sup> For di- and tri-block copolymers containing 1.6 – 4 kDa PPO blocks, a range of micellization temperatures between 5 and 50 °C<sup>52,57</sup> have been reported. Since PDMAEMA has a LCST of ~75 °C for solutions at pH 7,<sup>58</sup> solutions were not heated above 65 °C to avoid precipitation of the polymers. In micro-DSC experiments, an endothermic event associated with PPO dehydration and aggregation is observed during heating, and a corresponding exothermic event associated with PPO hydration and dissolution occurs during cooling. Since the onset temperature of the thermal events were close to the lower temperature limit of the instrument in some cases, the micellization temperature (MT) was taken as the temperature at which peak heat flow was recorded during cooling. Although the cooling process corresponded to dissolution of micelles rather than micellization, this exothermic event was used to characterize the MT because it showed better reproducibility and more well-defined peaks. The aggregation and micellization process during heating gave broader and occasionally irregularly shaped peak regions that stretched across the same temperatures corresponding to the de-micellization event registered during cooling. Representative heating and cooling curves obtained from micro-calorimetric measurements of the triblock copolymer at 3.3 mg/ml in DI water adjusted to pH 7 are presented in Appendix A, Figure A-1.



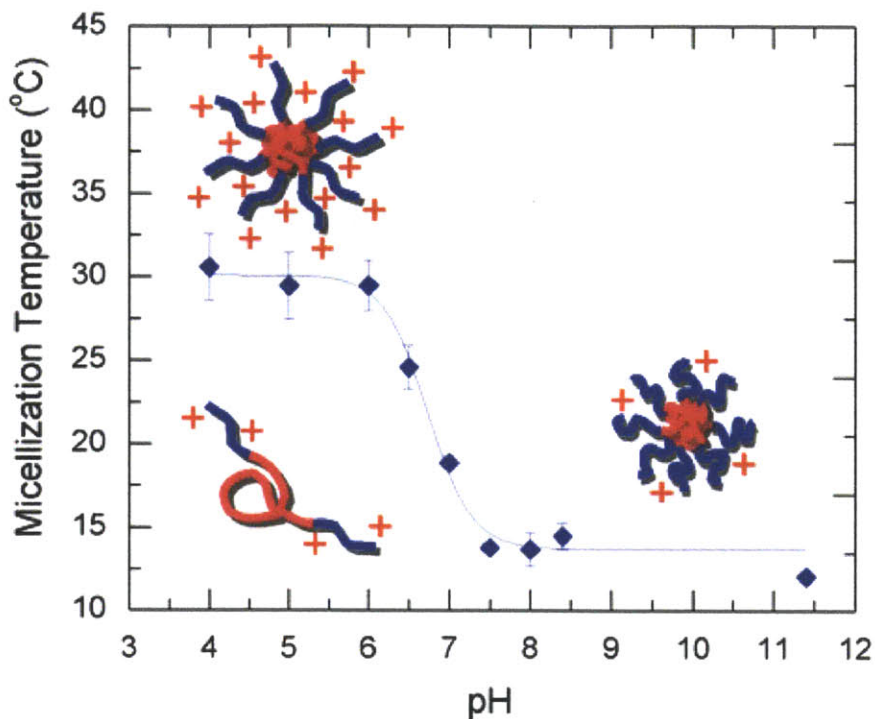


**Figure 2-1.** pH dependence of the micellization temperature in 3.3 mg/ml PD-PP-PD solutions with no added salt. The MT was determined from the peak exotherm observed during cooling from 65 to 6 °C in micro-DSC experiments. Cartoons show the state of the polymer chains above and below the MT at the pH extremes.

Figure 2-1 shows that the MT of PD-PP-PD was strongly dependent on solution pH. The MT decreased from 31 to 12 °C as the pH was increased from 4 to 11.4. As mentioned in the introduction, PPO has been extensively studied as part of di- and tri- block copolymers with hydrophilic polymer blocks, namely PEO. These amphiphilic block copolymers show rich composition, temperature and concentration dependent phase behavior<sup>40,57,59</sup> with micellization temperatures tunable between 5 – 50 °C.<sup>52,57</sup> Our data fall reasonably within this range of values. Unlike the end blocks of PEO-*b*-PPO-*b*-PEO, PDMAEMA is a weak polybase with a variable charge density. When a weak polyelectrolyte (wPE) acquires additional charge, its crowding in the micellar corona becomes increasingly energetically unfavorable, and the increased barrier towards micellization is revealed in an increase in MT. Indeed, in our case (Fig. 2-1), a sharp increase in MT from ~13 °C to ~30 °C occurred when pH was lowered from 7.5 to 6, i.e. in the region close to the pK<sub>a</sub> of PDMAEMA of ~6.7 as reported by others,<sup>60</sup> and confirmed for this

polymer by potentiometric titration. Our finding that the solution pH and ionization of the PDMAEMA end blocks strongly influence the ability of PD-PP-PD's to form micelles is consistent with the literature on other wPE block copolymers.<sup>48,61-63</sup> Above pH 7.5, the PDMAEMA blocks in PD-PP-PD were weakly ionized, and micellization occurred at around 13 °C. At pH 6 and below, the high positive charge density on PDMAEMA posed an energetic barrier to the formation of micelles increasing the MT to ~30 °C.<sup>†</sup>

The data on pH-dependent micellization of PD-PP-PD was also confirmed using a dye solubilization technique; another established method to determine critical micelle concentration (CMC) and critical micellization temperature (CMT).<sup>52</sup> Absorption and fluorescence of 1,6-diphenyl-1,3,5-hexatriene (DPH) is minimal in water, but increases significantly when DPH is incorporated into hydrophobic cores of micelles formed above the CMC (at a fixed temperature) or CMT (at a fixed concentration). Following the protocol used by P. Alexandridis *et. al.*,<sup>52</sup> the absorbance of PD-PP-PD and dye solutions was recorded at 356 nm as a function of solution temperature, and the CMTs were obtained from the first break in the sigmoid curves showing an increase in absorbance with increasing temperature (refer to Figure A-2 in Appendix A). Table 2-1 compares the CMT obtained from dye solubilization and the estimated MT from micro-DSC. The values for the MT obtained with the two different techniques agreed within 2 °C. From both the micro-DSC and dye solubilization data, we confirmed that, in the absence of added salt, in 0.1 mg/ml solutions of PD-PP-PD, at RT of ~24 °C, the triblock copolymer was molecularly dissolved at pH ≤ 6, while it formed PPO-core/PDMAEMA-corona micelles at pH ≥ 7.

**Table 2-1.** Micellization temperatures of PD-PP-PD solutions at different pH obtained using microDSC and DPH-solubilization techniques.

<b>Solution pH</b>	<b>MT<sub>micro-DSC</sub>, °C</b>	<b>CMT<sub>dye solubilization</sub>, °C</b>
4	30.5	30.0
7	18.0	16.5
8	13.5	12.0

<sup>†</sup> The thermodynamics of micellization is briefly described in Chapter 1, Section 1.4.2.

Micellization and micelle sizes were also studied using dynamic light scattering (DLS) (shown in Figure A-3, Appendix A). At temperatures below 10 °C, a number average hydrodynamic diameter of ~ 6 nm was detected in both PD-PP-PD solutions at pH 4 and pH 7, consistent with the presence of unimers. In contrast, as the temperature was increased, the hydrodynamic size evolution drastically differed between pH 4 and pH 7 solutions. While at pH 4, the small, unimer-like size of ~6 nm persisted up till 30 °C, a sharp increase in number average hydrodynamic diameter to ~19 nm occurred in PD-PP-PD solutions at pH 7 at ~20 °C. As a lower bound theoretical estimate of the block copolymer dimensions, we calculated the radius of gyration (assuming theta conditions),  $R_g = N^{0.5} b/6^{0.5}$ , where N is the number of polymer segments and b is the segmental length. The hydrodynamic radius,  $R_h = 0.66 R_g$  and for our triblock copolymer (N ~ 74, b ~ 0.33 nm), the resulting hydrodynamic diameter,  $D_h = 2 R_h \sim 1.53$  nm. The experimentally obtained  $D_h$  at low pH (pH 4) is ~ 4× higher because water is a good solvent for the PDMAEMA end blocks and electrostatic repulsions between DMA units cause further electrostatic chain extension. Above 20 °C at pH 7, the micellar diameter was ~ 19 nm – a reasonable size given PD-PP-PD has a contour length of 25 nm (assuming backbone C-C-O and C-O-C bond angles of 109.5° and 115° respectively, together with characteristic bond lengths of 1.54 Å for C-C bonds and 1.43 Å for C-O bonds). The DLS-inferred MT of PD-PP-PD indicated by the increase in hydrodynamic diameter agreed well with both the micro-DSC and dye solubilization data.

#### **2.4.1b Effects of salt on micellization.**

To confirm that the high degree of ionization and electrostatic repulsions between PDMAEMA end blocks was the key factor contributing to the increased CMT of PD-PP-PD at low pH values, we used salt to screen the charges on PD-PP-PD at pH 4 and investigated the effect this had on micellization. At pH 4, micellization of PD-PP-PD in 0.2 M NaCl solutions occurred at ~19 °C instead of ~31 °C in the absence of added salt (Figure A-4, Appendix A). This result shows that by screening the charges on the PE block, the decreased electrostatic repulsions between corona chains do indeed lead to more facile micellization.

## 2.4.2 Multilayers of PD-PP-PD with polyanions.

### 2.4.2a Layer-by-layer assembly of PD-PP-PD with PSS vs PAA.

With an understanding of the pH and temperature dependent solution behavior of PD-PP-PD, we set out to determine how the two possible molecular states (unimer versus micelle) could influence the multilayer assembly process. All multilayers discussed in this chapter were assembled from aqueous solutions with no added salt and at room temperature of  $\sim 24$  °C. Figure 2-2 shows the evolution of the dry ellipsometric film thickness from LbL assembly of PD-PP-PD with PAA or PSS at pH 4 or pH 7. The film growth was dramatically dependent on the polyanion type used in the multilayer assembly (Fig. 2-2). While the PD-PP-PD/PAA system exhibited exponential type growth and a large increase in thickness with layer number, growth of the PD-PP-PD/PSS multilayers was essentially linear with very small thickness increments per deposition cycle. Table 2-2 shows the average thickness increment per bilayer for each of the systems obtained from linear fits to regions of the growth curves shown in the inset of Figure 2-2.

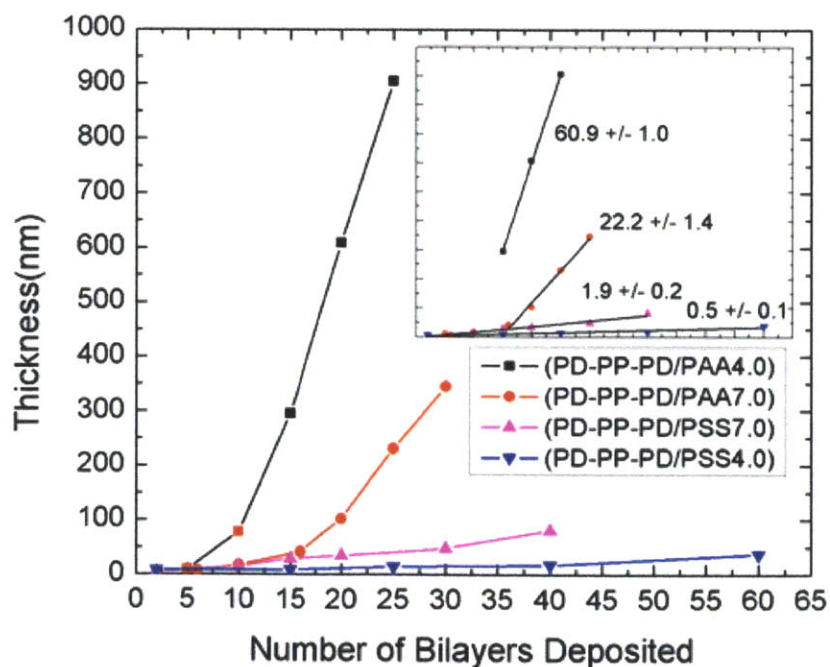


**Figure 2-2.** Thickness of multilayer assemblies as a function of the number of bilayers deposited from solutions without added salt at 24 °C. Inset shows the line fit to linear regions of each curve as well as the slope of the curve and standard error of the fit.

**Table 2-2.** Average thickness increment per bilayer for (PD-PP-PD/PAA4.0)<sub>15-25</sub>, (PD-PP-PD/PSS4.0)<sub>1-60</sub>, (PD-PP-PD/PAA7.0)<sub>16-30</sub>, and (PD-PP-PD/PSS7.0)<sub>1-40</sub>.\*

System	Thickness per bilayer (nm)
(PD-PP-PD/PAA4.0) <sub>15-25</sub>	60.9
(PD-PP-PD/PSS4.0) <sub>1-60</sub>	0.5
(PD-PP-PD/PAA7.0) <sub>16-30</sub>	22.2
(PD-PP-PD/PSS7.0) <sub>1-40</sub>	1.9

\* Subscripts indicate regions of linear film growth used to calculate the incremental bilayer thicknesses.

#### 2.4.2b Layer-by-layer assembly of PD-PP-PD with PSS.

In the case of the PD-PP-PD/PSS multilayer system assembled at pH 4.0, the very low thickness increments are similar to what has been observed when two fully charged polyelectrolytes were assembled in the absence of added salt.<sup>64</sup> AFM studies done by Tsukruk *et al.*,<sup>65</sup> for example, have also shown that PSS adsorbs to positively charged surfaces as a smooth thin layer composed of highly flattened macromolecular chains. Since PSS is a strong polyelectrolyte, the PSS chains are fully charged and present a high negative surface charge density to the adsorbing PD-PP-PD molecules that, in turn, adsorb in a flat outstretched manner. As such, the (PD-PP-PD/PSS4.0) multilayers consist of thin layers of PSS and PD-PP-PD. It is interesting to note that the neutral central PPO block does not seem to significantly influence the growth behavior under these conditions. Unlike the PD-PP-PD solution used at pH 4.0, at pH 7.0, the PD-PP-PD solutions at room temperature (~24 °C) contained both positively charged micelles and unimers (see Fig. 2-1). As a result of this difference, the (PD-PP-PD/PSS7.0) system had a larger thickness increment per bilayer than (PD-PP-PD/PSS4.0). Interestingly, compared to the thickness increment reported for LbL assembly of micelle-micelle multilayers, of 20 – 30 nm per layer of micelles deposited,<sup>66</sup> the bilayer thickness increment for the (PD-PP-PD/PSS7.0) film of 1.9 nm per bilayer is much lower and closer to that expected from LbL assemblies of non-micellar polyelectrolyte systems. It is possible that during LbL deposition, while micelles of ~19 nm in diameter attach to the substrate in the PD-PP-PD solution, in the PSS solution, the strong

complexation between PSS and the PD-PP-PD chains can result in partial dissolution of the micelles.

#### ***2.4.2c Layer-by-layer assembly of PD-PP-PD with PAA.***

In the case of the PD-PP-PD/PAA multilayer system, exponential growth with large bilayer thickness increments was observed. Exponential growth often results from the ability of at least one of the polyelectrolyte components deposited to diffuse into and out of the film during deposition.<sup>67-69</sup> Since AFM studies revealed insignificant changes in surface roughness of these films with bilayer deposition number, exponential growth of PD-PP-PD/PAA multilayers suggests that large-scale inter-diffusion is occurring during the assembly process. This diffusion enabled exponential growth has been observed in a variety of multilayer systems.<sup>67-70</sup> The weaker ionic bonding between the carboxylic groups on PAA and the charged amine groups on the PDMAEMA blocks allow inter-diffusion of components being deposited into the multilayer. Lynn and co-workers<sup>70</sup> observed exponential growth during the assembly of low molecular weight PAA chains with the weak polybase PAH. In our case, however, the molecular weight of the PAA chains is high enough to inhibit diffusion of PAA, suggesting that PD-PP-PD chains with a low molecular weight of 6200 Da are the diffusing entity. The average per bilayer thickness of 60 nm obtained for (PD-PP-PD/PAA4.0) is similar to the thickness increments of exponentially growing PAH/low molecular weight PAA multilayers previously reported,<sup>70</sup> while the thickness increment for the (PD-PP-PD/PAA7.0) system of ~ 20 nm per bilayer is of the order of the micelle size and similar to that seen in the all-micelle multilayers.<sup>66</sup>

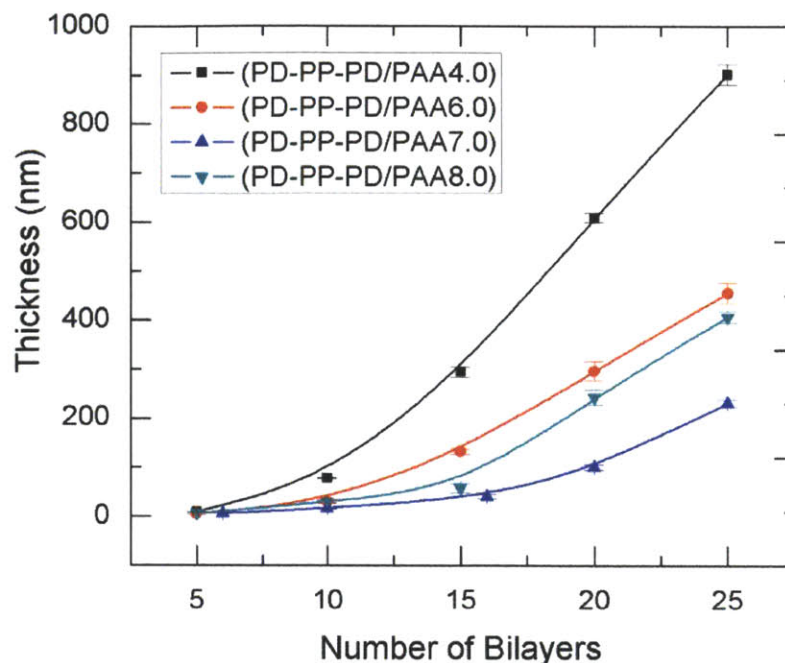


**Figure 2-3.** Growth curves obtained for (PD-PP-PD/PAA4.0), (PD-PP-PD/PAA6.0), (PD-PP-PD/PAA7.0), and (PD-PP-PD/PAA8.0) systems.

### 2.4.3 Effect of pH on the assembly of the PD-PP-PD/PAA system.

To further explore the effect of assembly pH on the growth behavior of the PD-PP-PD/PAA system, we studied LbL assembly at pH 4, 6, 7, and 8. Figure 2-3 shows the effect of pH on the assembly of PD-PP-PD with PAA. The largest overall thickness increments are observed at pH 4, well below the pH at which micelles are formed at RT ( $\sim 24$  °C) (see Fig. 2-1).

The pKa of PAA in the absence of added salt has been reported to be about 6.5.<sup>71</sup> Thus, in the pH range of 4 – 6, the PD-PP-PD triblock copolymers exist in solution as unimers and the PAA chains have a degree of ionization that ranges from about 10 to 40% (note: the degree of ionization of a weak polyelectrolyte can change significantly when chains are incorporated into a multilayer).<sup>64,71</sup> Below pH 7, the charge density on PAA increases with increasing solution pH, as such, from pH 4 to pH 6, the increasing charge density on the PAA chains inhibits this diffusive growth process to some extent and smaller thickness increments are observed with assembly at pH 6 compared to assembly at pH 4. At both pH 7 and pH 8, PAA chains are fully

charged. Instead PD-PP-PD micelles have PDMAEMA blocks with charge density that decreases with increasing pH. Larger bilayer thickness increments are thus observed at pH 8.

It is noteworthy that the behavior of a polymer chain free in solution often differs from its behavior when adsorbed at a surface. As seen in Fig. 2-1, at 24 °C, solutions of PD-PP-PD at pH 6 are close to the micellization temperature. Both theoretical<sup>72</sup> and experimental studies<sup>73</sup> indicate that charged amphiphilic block copolymers or surfactants in solutions below their CMC, can form micelles at oppositely charged surfaces as the local concentration of charged unimers in the vicinity of an oppositely charged surface exceeds their bulk solution concentration. Due to the similarities in the growth character, dry film morphology (shown in Appendix B, Fig. B-9) and swelling behavior (discussed in *section 2.4.4b.*) of the (PD-PP-PD/PAA6.0), (PD-PP-PD/PAA7.0) and (PD-PP-PD/PAA8.0), distinct from (PD-PP-PD/PAA4.0), we believe that micelles were incorporated into multilayers of PD-PP-PD and PAA assembled at pH 6.

#### **2.4.4 Temperature response of PD-PP-PD containing multilayers.**

##### ***2.4.4a Effect of PD-PP-PD morphology in solution and polyanionic binding partner on the swelling of PD-PP-PD/polyanion multilayers.***

The temperature dependent swelling of multilayers containing PD-PP-PD was monitored using *in situ* ellipsometry. For these experiments, all films were assembled from salt free solutions at ~ 24 °C. Comparing (PD-PP-PD/PSS7.0), (PD-PP-PD/PAA7.0), (PD-PP-PD/PSS4.0), and (PD-PP-PD/PAA4.0), it is evident from Figure 2-4 that only multilayers of (PD-PP-PD/PAA7.0) showed temperature dependent swelling in DI water adjusted to pH 7. The swelling ratio is defined as a ratio of the ellipsometric thickness of a multilayer in solution to that of a dry film. In the case of the (PD-PP-PD/PAA7.0), the thickness changes that occurred with changes in temperature were dramatic: the multilayer film thickness increased to 2146 nm (4.11× its dry thickness of 522 nm) at 6 °C and decreased to 941 nm (1.8× its dry thickness) at 20 °C.



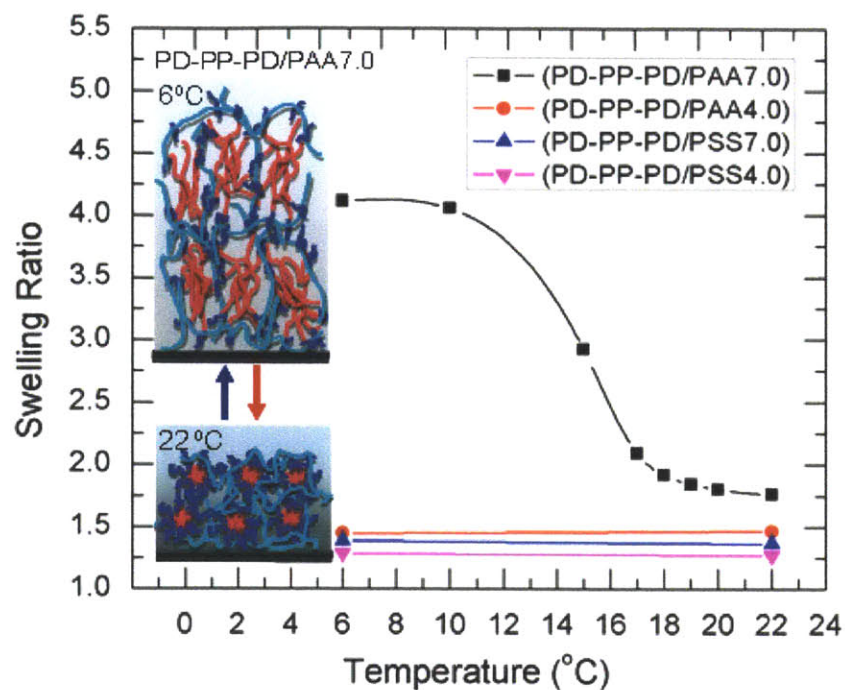


**Figure 2-4.** Temperature-dependent swelling of PD-PP-PD-containing multilayers deposited from solutions, with no added salt, at  $\sim 24$  °C and subsequently exposed to DI water adjusted to pH 7. Multilayers of PD-PP-PD were constructed at pH 4 or 7 using PAA or PSS as polyanions. The cartoon illustrates the temperature induced hydration of micelle cores and thus additional swelling of the (PD-PP-PD/PAA7.0) multilayer that occurs at low temperature.

This dramatic volumetric transition revealed by the sigmoid shape of the swelling ratio versus temperature plot is a direct consequence of temperature-induced conformational changes in the backbone of PPO that results in a transition from a hydrophilic to a more hydrophobic state as the temperature is raised.<sup>41,74</sup> At 6 °C, the PPO segments are able to form hydrogen bonds with water molecules and this association facilitates water uptake and the large degree of swelling at this temperature. Importantly, dissolution does not occur because ionic cross-links between PDMAEMA and PAA segments remain intact to sustain the network structure in the system. Between 10 and 16 °C, the PPO segments transition into a more hydrophobic form. At 20 °C, PPO is poorly hydrated and water is expelled from the PPO micelle cores resulting in the observed de-swelling.

In the (PD-PP-PD/PAA4.0) multilayers, PD-PP-PD chains were assembled as unimers and the exposed central PPO block can form hydrogen bonds with the –COOH groups on weakly ionized PAA at pH 4. Since the temperature-induced swelling response of PPO is dependent on hydrogen bond formation between PPO and water molecules at low temperatures, temperature-induced swelling would not be expected in systems where PPO is already H-bonded with PAA. At this point however, it is not conclusive whether the lack of temperature induced swelling in the (PD-PP-PD/PAA4.0) multilayers is caused by (1) the incorporation of the block copolymer as individual chains rather than phase separated micellar structures, (2) direct hydrogen bonding between the PPO blocks and the PAA, or (3) a higher ionic crosslink density resulting from the higher charge density of the PDMAEMA end blocks at pH 4 compared to pH 7, as each of these factors can contribute to the results observed.

While micelles are present in the PD-PP-PD solutions used in assembly of both (PD-PP-PD/PSS7.0) and (PD-PP-PD/PAA7.0) multilayers, a temperature dependent increase in swelling at low temperatures was not observed in the (PD-PP-PD/PSS7.0) multilayer. This is a result of the different types of polyanions used in multilayer assembly. PSS and PAA differ in their strength as polyacids and thus differ in the stability of the ionic bonds they form within the multilayer: sulfonate-ammonium versus carboxylate-ammonium interactions. Ionic cross-links between sulfonate groups on PSS and protonated amine groups on PDMAEMA, unlike the ionic cross-links between PAA and PDMAEMA are much stronger and not susceptible to exchange and rearrangement.<sup>75</sup> Consequently, (PD-PP-PD/PSS7.0) films are held together by a tighter network of stronger ionic crosslinks.

These results show that the morphology of the block copolymer, the type of bonding that operates within the multilayers, as well as the density and the nature of ionic bonds between different polyelectrolytes have a profound effect on the resulting molecular architecture of these multilayers, and their ability to respond to stimuli.

#### ***2.4.4b Effect of assembly pH on the swelling of PD-PP-PD/PAA multilayers.***

To examine more carefully the effect of assembly pH on the temperature-dependent swelling of PD-PP-PD/PAA films, we assembled multilayers at pH 5, 6 and 8 and compared them to the

films assembled at pH 4 and 7. Figure 2-5 shows the temperature-dependent swelling behavior of PD-PP-PD/PAA multilayers assembled at different pH when submerged in pH 7 DI water.

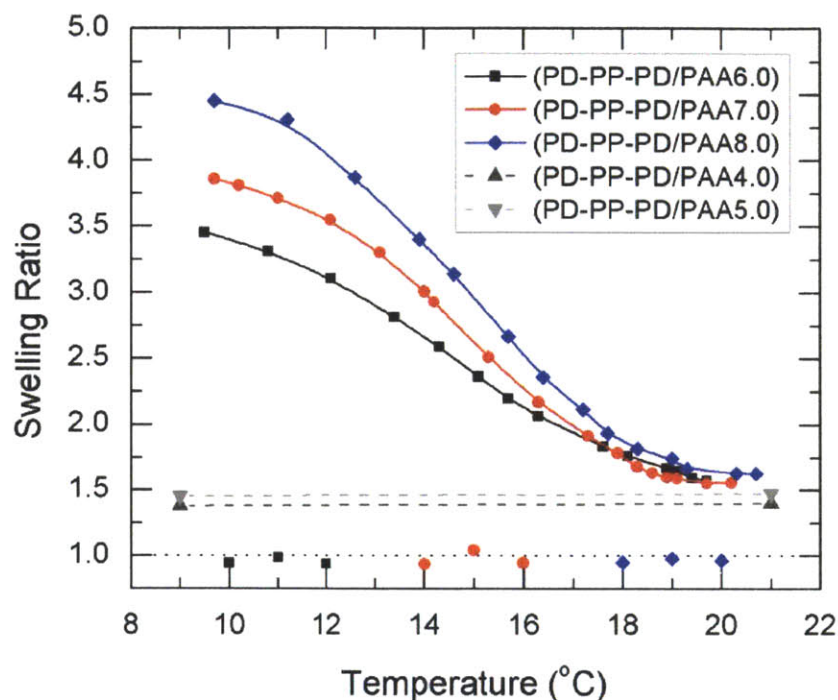


**Figure 2-5.** Temperature dependence of swelling of PD-PP-PD/PAA multilayers assembled from salt free solutions at pH 4, 5, 6, 7, or 8 submerged in DI adjusted to pH7. Color coded dots around swelling ratio  $\sim 1$  are the dry film thicknesses after each of 3 repeated swelling cycles. Swelling of PD-PP-PD/PAA multilayers assembled at pH 4 and 5 (dashed lines) reveal the lack of temperature dependent swelling in multilayers assembled at these pH values.

A temperature dependent increase in swelling ratio at low temperature was not observed in multilayers assembled at pH 4 or 5 where unimers were incorporated and PD end blocks are highly charged during deposition. The amplitude of the temperature-triggered swelling transition seen in micelle containing multilayers increased with increasing assembly pH (Fig. 2-5) for (PD-PP-PD/PAA6.0), (PD-PP-PD/PAA7.0), and (PD-PP-PD/PAA8.0) multilayers. ‡

‡ The differences in swelling degree resulting from different assembly pH is likely related to differences in ionic crosslinking density as the two are related by Eqn. (10) in Chapter 1, Section 1.2.1. Varying the assembly pH of weak polyelectrolytes (refer to Chapter 1, Section 1.3) can give rise to films with different ionic crosslinking degrees in turn would swell to different extents.

#### 2.4.4c. Reversibility of temperature-triggered swelling.

In order to harness the temperature induced volume dilation, the temperature induced swelling transition has to occur reversibly with high fidelity. Using *in situ* ellipsometry, the thickness of (PD-PP-PD/PAA7.0)<sub>40</sub> films were monitored over repeated cycles of immersion in DI water adjusted to pH 7, at 20°C, then at 6°C, and dried. Changes in the swelling ratio of a (PD-PP-PD/PAA7.0)<sub>40</sub> film during such cycling are shown in Fig. 2-6.

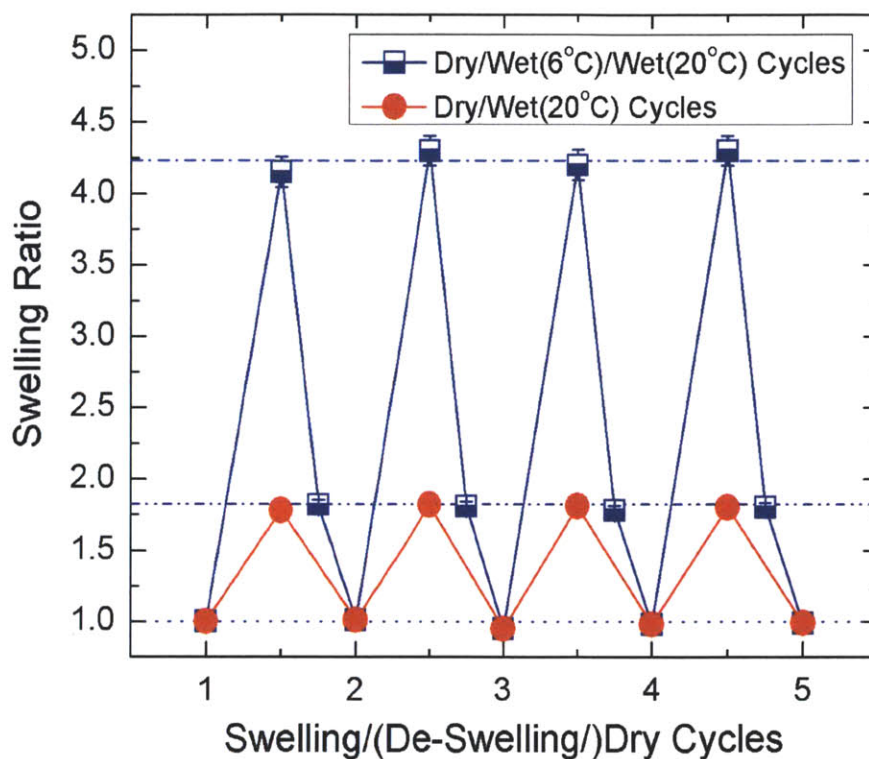


**Figure 2-6.** Plot of swelling ratio of (PD-PP-PD/PAA7.0)<sub>40</sub> multilayer as a function of immersion cycles in pH7 DI at 20°C, 6°C and dried in between.

Film swelling/de-swelling occurred in a highly reproducible manner, with negligible film loss over repeated wetting, temperature cycling and drying cycles. The thickness increases and decreases obtained from *in situ* ellipsometry were accompanied by corresponding decreases and increases in refractive index, indicating that negligible film loss occurred during these cycles.

**2.4.4d Effect of post-assembly salt concentration and pH on the swelling of PD-PP-PD/PAA multilayers.**

As discussed in Chapter 1, the salt concentration can have profound effects on polyelectrolyte multilayers immersed in aqueous solutions post-assembly. Since salt is known to destabilize ionic bonding in polyelectrolyte multilayers by competitively binding to charged ionic groups and the screening of charges,<sup>33,75-77</sup> multilayers were tested for stability in 0.15 M NaCl solutions. 0.15 M salt was chosen to replicate the ionic strength of physiologically relevant buffers. As demonstrated in Figure 2-7, the swelling amplitude at 6 °C was higher in 0.15 M NaCl solutions compared to that in salt-free solutions (compare Figs. 2-6 and 2-7).

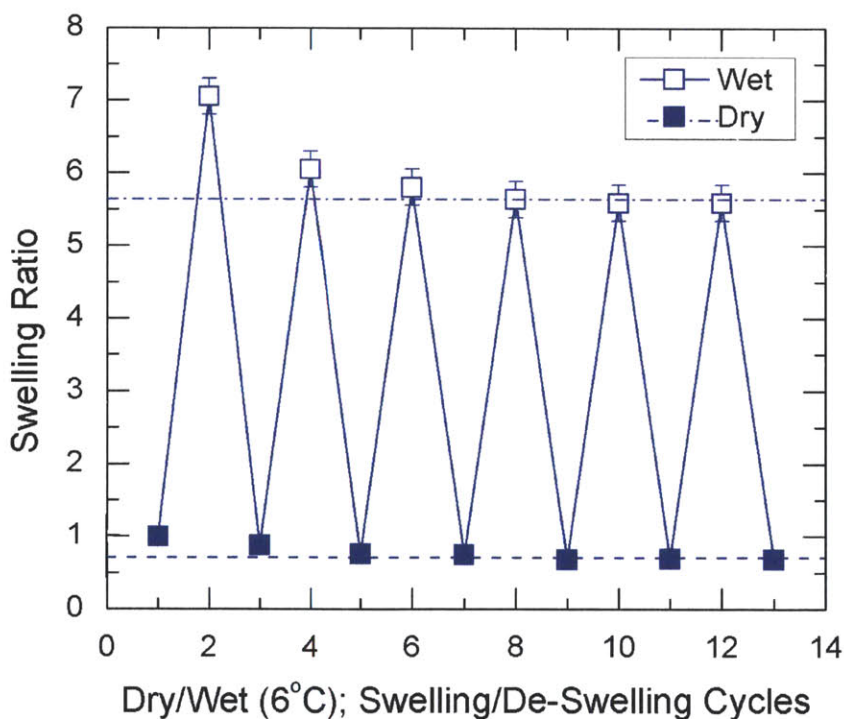


**Figure 2-7.** Reversible swelling of (PD-PP-PD/PAA7.0)<sub>24</sub> multilayers in 0.15 M NaCl solutions at pH 7 and temperatures, 6 °C (open squares) and 20 °C (filled squares).

This reflects the partial disruption of ionic cross-links within (PD-PP-PD/PAA7.0)<sub>24</sub> multilayers in salt solutions. Importantly, multilayers remained stable in 0.15 M NaCl solutions, exhibiting reproducible and reversible temperature dependent swelling responses after some initial

densification during the first two cycles. This opens up the possibility of applying these temperature responsive multilayers in biological systems<sup>§</sup>.

#### 2.4.4e Effect of post-assembly pH on film stability and swelling of PD-PP-PD/PAA multilayers.

pH is another important factor that influences the stability of polyelectrolyte multilayers by altering the ratio of positive to negative charges within the multilayer.<sup>33</sup> We studied the effect of immersion solution pH on the swelling of temperature responsive (PD-PP-PD/PAA7.0)<sub>24</sub> at both 20 °C and 6 °C.

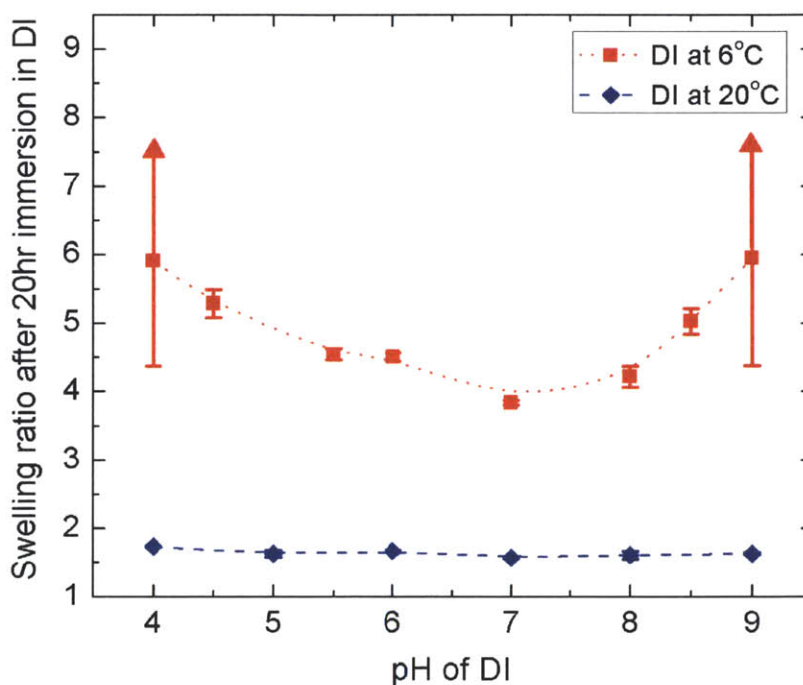


**Figure 2-8.** Effect of pH on the swelling of (PD-PP-PD/PAA7.0)<sub>24</sub> at 20 °C and 6 °C. At 20 °C (pH < 3 or > 10), as well as at 6 °C (pH < 4.5 or > 8.5), the multilayer films become highly swollen (by a factor of ~7× or more). For the extreme pH values shown at 6 °C, poor refractive index contrast between highly swollen films and the aqueous medium interfered with obtaining reliable *in situ* ellipsometric thickness measurements. In addition, multilayers begin to lose integrity at these extreme pH values.

<sup>§</sup> The effect of different salt concentrations on swelling as well as the stability of films in PBS solutions were subsequently explored (presented in more detail in Chapter 5, Section 5.4.4a).

Figure 2-8 shows that at 6 °C and 20 °C, (PD-PP-PD/PAA7.0) multilayers are stable and swell reversibly in solutions of pH between 4 and 9. At 20 °C, these films exhibit an approximately constant swelling ratio of ~ 1.7 independent of the solution pH. In these conditions, dehydrated hydrophobic PPO domains serve as physical cross-links that help hold the film together and could play a role in opposing the increased swelling (observed at 6 °C where the hydrophobic associations between PPO blocks are dissolved) induced by charge imbalances at pH values below or above the deposition pH of 7. At 6 °C, PPO cores in the self-assembled PD-PP-PD micelles dissolve, causing high, reversible, temperature-induced film swelling in a wide pH range of 4.5 to 8.5. Minimum swelling was observed in DI water at pH 7, the multilayer assembly pH, where the positive and negative charges within the film were balanced. As the immersion solution pH deviated from the assembly pH, additional protonation of the PDMAEMA and PAA (at lower pH), or de-protonation of PDMAEMA tertiary amino groups (at higher pH) resulted in excess positive and negative charge in the film, respectively. The (PD-PP-PD/PAA7.0) multilayers remained stable after 20 hours of immersion at 6 °C in solutions at  $3 < \text{pH} < 9$ , and their swelling was reversible. At 6 °C (pH 4 or pH 9), because of high (> 85%) water content in the film, the refractive index contrast between the film and water became too low to obtain reliable thickness measurements (as indicated by the arrows and large error bars for these points in Fig. 2-8). In addition, the films were highly unstable at these points and film disintegration occurred. The films were highly swollen and mechanically weak at extreme pH values. Films were not stable below pH 3 or above pH 10, at both 6 °C and room temperature of 24 °C, because the majority of ionic associations were disrupted. (Refer to Chapter 1, Sections 1.3 and 1.5 on pH dependence of weak polyelectrolyte multilayers)

## **2.5 Conclusions**

Triblock copolymers, like PD-PP-PD, with charged end blocks and a functionality-carrying central block are capable of incorporating novel functionality into electrostatically self assembled LbL multilayers. We have shown that PD-PP-PD, a polycationic A-B-A triblock copolymer, can be successfully assembled into multilayers that exhibit reversible temperature-induced swelling and de-swelling behavior over a wide range of pH and salt concentrations. As demonstrated here, an understanding of the morphology of the block copolymers being assembled from solution, the charge density of the assembled polyelectrolytes, the LbL assembly mechanism and the type of bonding involved in the self assembly process, allowed control over the film composition and architecture which ultimately enabled control over the extent of fully reversible temperature responses. By varying the deposition conditions, we exposed the important factors that enable the stimuli responsive properties in the multilayer films.

## **Acknowledgements**

Work in this chapter was supported in part by the MRSEC Program of the National Science Foundation under award number DMR – 0819762 and in part by NSF DMR-0710591 (S. Sukhishvili). We thank the Center for Materials Science and Engineering (CMSE), the Institute for Soldier Nanotechnologies (ISN) and Prof. T. Alan Hatton for use of their characterization facilities.



## References

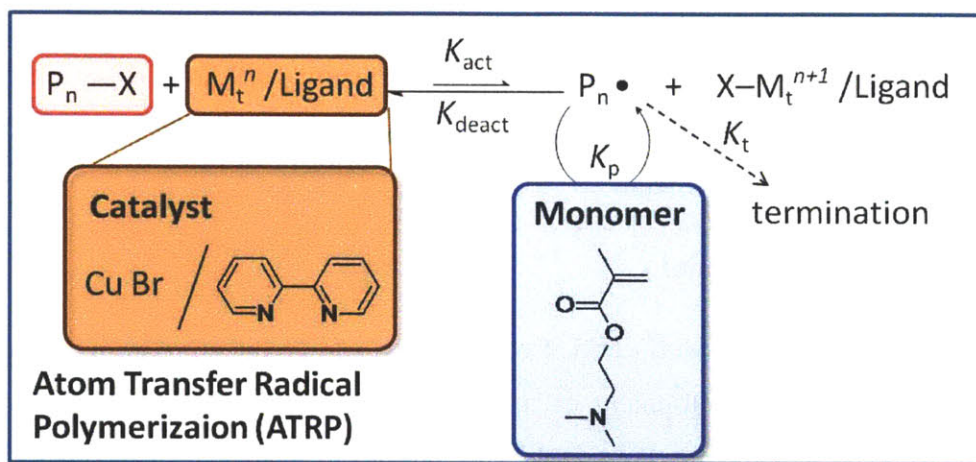
- (1) Gehrke, S. In *Responsive Gels: Volume Transitions II*; Springer Berlin: Heidelberg, 1993; Vol. 110, p 81.
- (2) Khurma, J. R.; Rohindra, D. R.; Nand, A. V. *Polym. Bull.* **2005**, *54*, 195.
- (3) Owens, D. E.; Jian, Y.; Fang, J. E.; Slaughter, B. V.; Chen, Y.-H.; Peppas, N. A. *Macromolecules* **2007**, *40*, 7306.
- (4) El-Din, H. M. N.; Alla, S. G. A.; El-Naggar, A. W. *J. Macromol. Sci., Part A: Pure Appl. Chem.* **2007**, *44*, 291.
- (5) Dang, J. M.; Sun, D. D. N.; Shin-Ya, Y.; Sieber, A. N.; Kostuik, J. P.; Leong, K. W. *Biomaterials* **2006**, *27*, 406.
- (6) Yokota, S.; Matsuyama, K.; Kitaoka, T.; Wariishi, H. *Appl. Surf. Sci.* **2007**, *253*, 5149.
- (7) Kwak, D.; Han, J. T.; Lee, J. H.; Lim, H. S.; Lee, D. H.; Cho, K. *Surf. Sci.* **2008**, *602*, 3100.
- (8) Nagase, K.; Kobayashi, J.; Okano, T. *J. R. Soc. Interface* **2009**, *6*, S293.
- (9) Nü, W.; Yong, Z.; Lei, J. *Macromol. Rapid Commun.* **2008**, *29*, 485.
- (10) Uto, K.; Yamamoto, K.; Hirase, S.; Aoyagi, T. *J. Controlled Release* **2006**, *110*, 408.
- (11) Nykanen, A.; Nuopponen, M.; Laukkanen, A.; Hirvonen, S.-P.; Rytela, M.; Turunen, O.; Tenhu, H.; Mezzenga, R.; Ikkala, O.; Ruokolainen, J. *Macromolecules* **2007**, *40*, 5827.
- (12) Violet, G.; Havazelet, B.-P. *Biotechnol. Prog.* **2003**, *19*, 1728.
- (13) Bromberg, L. E.; Ron, E. S. *Adv. Drug Delivery Rev.* **1998**, *31*, 197.
- (14) Kuckling, D.; Adler, H.-J. P.; Arndt, K.-F.; Long, L.; Habicher, W. D. *Macromol. Chem. Phys.* **2000**, *201*, 273.
- (15) Maeda, Y. *Langmuir* **2001**, *17*, 1737.
- (16) Lutz, J.-F.; Weichenhan, K.; Akdemir, O.; Hoth, A. *Macromolecules* **2007**, *40*, 2503.
- (17) Fournier, D.; Hoogenboom, R.; Thijs, H. M. L.; Paulus, R. M.; Schubert, U. S. *Macromolecules* **2007**, *40*, 915.
- (18) Decher, G. *Science* **1997**, *277*, 1232.
- (19) Stockton, W. B.; Rubner, M. F. *Macromolecules* **1997**, *30*, 2717.
- (20) Such, G. K.; Quinn, J. F.; Quinn, A.; Tjipto, E.; Caruso, F. *J. Am. Chem. Soc.* **2006**, *128*, 9318.
- (21) Donath, E.; Sukhorukov, G. B.; Caruso, F.; Davis, S. A.; Möhwald, H. *Angew. Chem., Int. Ed.* **1998**, *37*, 2201.
- (22) Peyratout, C. S.; Dähne, L. *Angew. Chem., Int. Ed.* **2004**, *43*, 3762.
- (23) Sukhorukov, G. B.; Antipov, A. A.; Voigt, A.; Donath, E.; Möhwald, H. *Macromol. Rapid Commun.* **2001**, *22*, 44.
- (24) Hiller, J. A.; Rubner, M. F. *Macromolecules* **2003**, *36*, 4078.
- (25) Sukhishvili, S. A. *Curr. Opin. Colloid Interface Sci.* **2005**, *10*, 37.
- (26) Serizawa, T.; Nanameki, K.; Yamamoto, K.; Akashi, M. *Macromolecules* **2002**, *35*, 2184.
- (27) Steitz, R.; Leiner, V.; Tauer, K.; Khrenov, V.; v. Klitzing, R. *Appl. Phys. A: Mater. Sci. Process.* **2002**, *74*, s519.
- (28) Glinel, K.; Sukhorukov, G. B.; Möhwald, H.; Khrenov, V.; Tauer, K. *Macromol. Chem. Phys.* **2003**, *204*, 1784.
- (29) Serpe, M. J.; Jones, C. D.; Lyon, L. A. *Langmuir* **2003**, *19*, 8759.
- (30) Nolan, C. M.; Serpe, M. J.; Lyon, L. A. *Biomacromolecules* **2004**, *5*, 1940.
- (31) Serpe, M. J.; Yarmey, K. A.; Nolan, C. M.; Lyon, L. A. *Biomacromolecules* **2005**, *6*, 408.
- (32) Jaber, J. A.; Schlenoff, J. B. *Macromolecules* **2005**, *38*, 1300.
- (33) Kharlampieva, E.; Sukhishvili, S. A. *Langmuir* **2003**, *19*, 1235.
- (34) Quinn, J. F.; Caruso, F. *Langmuir* **2004**, *20*, 20.
- (35) Zhu, Z.; Sukhishvili, S. A. *ACS Nano* **2009**.

- (36) Swiston, A. J.; Cheng, C.; Um, S. H.; Irvine, D. J.; Cohen, R. E.; Rubner, M. F. *Nano Letters* **2008**, *8*, 4446.
- (37) Zhuk, A.; Pavlukhina, S.; Sukhishvili, S. A. *Langmuir* **2009**.
- (38) Guohua, C.; Allan, S. H. *Macromol. Rapid Commun.* **1995**, *16*, 175.
- (39) Bromberg, L. J. *Phys. Chem. B* **1998**, *102*, 10736.
- (40) Kell, M. J. *Phys.: Condens. Matter* **1996**, A103.
- (41) Linse, P. J. *Phys. Chem.* **2002**, *97*, 13896.
- (42) Mortensen, K.; Pedersen, J. S. *Macromolecules* **1993**, *26*, 805.
- (43) Mortensen, K. J. *Phys.: Condens. Matter* **1996**, *8*, A103.
- (44) Su, Y.-I.; Wang, J.; Liu, H.-z. *Macromolecules* **2002**, *35*, 6426.
- (45) Lowe, A. B.; Billingham, N. C.; Armes, S. P. *Macromolecules* **1998**, *31*, 5991.
- (46) Lin, S.; Du, F.; Wang, Y.; Ji, S.; Liang, D.; Yu, L.; Li, Z. *Biomacromolecules* **2008**, *9*, 109.
- (47) Baines, F. L.; Armes, S. P.; Billingham, N. C.; Tuzar, Z. *Macromolecules* **1996**, *29*, 8151.
- (48) Lee, A. S.; Gast, A. P.; Butun, V.; Armes, S. P. *Macromolecules* **1999**, *32*, 4302.
- (49) Bütün, V.; Armes, S. P.; Billingham, N. C. *Polymer* **2001**, *42*, 5993.
- (50) Ni, P.-H.; Pan, Q.-S.; Zha, L.-S.; Wang, C.-C.; Elaïssari, A.; Fu, S.-K. *J. Polym. Sci., Part A: Polym. Chem.* **2002**, *40*, 624.
- (51) Lee, D.; Rubner, M. F.; Cohen, R. E. *Nano Lett.* **2006**, *6*, 2305.
- (52) Alexandridis, P.; Holzwarth, J. F.; Hatton, T. A. *Macromolecules* **1994**, *27*, 2414.
- (53) Schild, H. G.; Tirrell, D. A. *J. Phys. Chem.* **1990**, *94*, 4352.
- (54) Ballerat-Busserolles, K.; Rassinoux, S.; Roux-Desgranges, G.; Roux, A. J. *Therm. Anal. Calorim.* **1998**, *51*, 161.
- (55) Wang, Q.; Li, L.; Jiang, S. *Langmuir* **2005**, *21*, 9068.
- (56) Zhou, Y.; Jiang, K.; Song, Q.; Liu, S. *Langmuir* **2007**, *23*, 13076.
- (57) Wanka, G.; Hoffmann, H.; Ulbricht, W. *Macromolecules* **1994**, *27*, 4145.
- (58) Plamper, F. A.; Ruppel, M.; Schmalz, A.; Borisov, O.; Ballauff, M.; Müller, A. H. E. *Macromolecules* **2007**, *40*, 8361.
- (59) Gaisford, S.; Beezer, A. E.; Mitchell, J. C.; Bell, P. C.; Fakorede, F.; Finnie, J. K.; Williams, S. J. *Int. J. Pharm.* **1998**, *174*, 39.
- (60) An, S. W.; Thomas, R. K.; Baines, F. L.; Billingham, N. C.; Armes, S. P.; Penfold, J. *Macromolecules* **1998**, *31*, 7877.
- (61) Lee, A. S.; Butun, V.; Vamvakaki, M.; Armes, S. P.; Pople, J. A.; Gast, A. P. *Macromolecules* **2002**, *35*, 8540.
- (62) Martin, T. J.; Prochazka, K.; Munk, P.; Webber, S. E. *Macromolecules* **1996**, *29*, 6071.
- (63) Gohy, J.-F.; Antoun, S.; Jerome, R. *Macromolecules* **2001**, *34*, 7435.
- (64) Shiratori, S. S.; Rubner, M. F. *Macromolecules* **2000**, *33*, 4213.
- (65) Tsukruk, V. V.; Bliznyuk, V. N.; Visser, D.; Campbell, A. L.; Bunning, T. J.; Adams, W. W. *Macromolecules* **1997**, *30*, 6615.
- (66) Qi, B.; Tong, X.; Zhao, Y. *Macromolecules* **2006**, *39*, 5714.
- (67) Lavalley, P.; Gergely, C.; Cuisinier, F. J. G.; Decher, G.; Schaaf, P.; Voegel, J. C.; Picart, C. *Macromolecules* **2002**, *35*, 4458.
- (68) Picart, C.; Mutterer, J.; Richert, L.; Luo, Y.; Prestwich, G. D.; Schaaf, P.; Voegel, J. C.; Lavalley, P. *Proc. Natl. Acad. Sci. U. S. A.* **2002**, *99*, 12531.
- (69) Radeva, T.; Kamburova, K.; Petkanchin, I. J. *Colloid Interface Sci.* **2006**, *298*, 59.
- (70) Sun, B.; Jewell, C. M.; Fredin, N. J.; Lynn, D. M. *Langmuir* **2007**, *23*, 8452.
- (71) Choi, J.; Rubner, M. F. *Macromolecules* **2005**, *38*, 116.
- (72) Cheng, H.; Olvera de la Cruz, M. *Macromolecules* **2006**, *39*, 1961.
- (73) Liu, J.-F.; Ducker, W. A. *J. Phys. Chem. B* **1999**, *103*, 8558.

- (74) Hurter, P. N.; Scheutjens, J. M. H. M.; Hatton, T. A. *Macromolecules* **2002**, *26*, 5030.
- (75) Sukhishvili, S. A.; Kharlampieva, E.; Izumrudov, V. *Macromolecules* **2006**, *39*, 8873.
- (76) Nolte, A. J.; Takane, N.; Hindman, E.; Gaynor, W.; Rubner, M. F.; Cohen, R. E. *Macromolecules* **2007**, *40*, 5479.
- (77) Sukhishvili, S. A.; Granick, S. *Journal of the American Chemical Society* **2000**, *122*, 9550.



## CHAPTER 3: SYNTHESIS OF PDMAEMA CONTAINING BLOCK COPOLYMERS BY ATOM TRANSFER RADICAL POLYMERIZATION



The synthesis presented in this chapter was done in collaboration with Zhichen Zhu<sup>†</sup>, Swapnali Chaudhari<sup>‡</sup> and Svetlana A. Sukhishvili<sup>§</sup>

### SPECIAL REMARKS:

Before starting this chapter, I would like to thank Zhichen<sup>†</sup> for introducing me to the techniques in synthetic organic chemistry and teaching me how to do ATRP.

I would also like to thank Swapnali<sup>‡</sup> with whom I worked alongside for long hours in the Sukhishvili lab as we, together learned how to carry out ATRP. She was a step ahead of me in basic organic laboratory synthesis and knew where to find everything. I could not have imagined how it would have been without her.

Last but definitely not least, I need to thank Prof. Svetlana A. Sukhishvili<sup>§</sup> from Stevens Institute of Technology, Department of Chemistry, Chemical Biology & Biomedical Engineering who graciously allowed me to learn and carry out synthesis in her laboratory at Stevens. Both Zhichen and Swapnali are her students there. This work would not have been possible without her continuous enthusiastic support.

### **3.1 Abstract**

While Chapter 1 described the LbL deposition conditions required to enable the creation of thin film hydrogel coatings that swell with decreased temperature, this Chapter describes the synthesis of block copolymers containing the same chemical blocks of PD-PP-PD (used in the previous chapter) but of different block architecture. Block copolymers of poly(N,N dimethyl amino ethyl methacrylate) (D) and poly(propylene oxide) (P): a P-D diblock and a long D-P-D triblock copolymer, were synthesized in order to investigate the effect of block copolymer architecture on the temperature induced swelling of multilayers assembled from these molecules (to be discussed in Chapter 4). This Chapter provides some background and describes the synthesis used in detail, to serve as a guide to future students/researchers interested in synthesizing similar block copolymers.

### **3.2 Introduction and background**

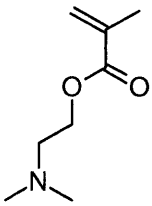
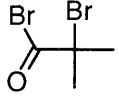
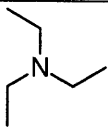
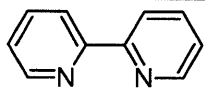
The synthesis of polymers with well defined composition and architecture is of great interest in polymer chemistry for the development of new functional polymeric materials as well as to provide fundamental insights into how molecular architecture affects final polymer material properties. Traditional anionic and cationic living polymerizations involve active species that tend to attack polar functional groups. This limited the types of polymers that could be synthesized, imposed stringent requirements on the purity of solvents, and required rigorous exclusion of oxygen and water from reactions. It was not until the late 1990s that direct synthesis of polymethacrylate and subsequently 2-(diethylamino) ethyl methacrylate (DEAEMA), and 2-(dimethylamino)ethyl methacrylate (DMAEMA) with terminal unsaturated groups was achieved by oxyanion-initiated polymerization. Unfortunately, the oxyanionic polymerizations suffered from poor initiator efficiencies and consequently poor molecular weight control. Free radical processes are more tolerant to impurities and thus have been the leading industrial method of polymer synthesis. Inevitable diffusion based bimolecular radical coupling and disproportionation reactions, however, mean that control over molecular weight in these free radical processes is limited. Controlled/living radical transfer (CRP) polymerization techniques have been developed over the last 15 years. Through rapid establishment of dynamic equilibrium between small numbers of growing free radical species and a large majority of dormant species, these techniques allow for robust living polymerization via radical pathways<sup>1</sup>. Common CRP

methods used today include atom transfer radical polymerization (ATRP) where free radicals are generated catalytically and alkyl halides are the dormant species; reversible addition fragmentation chain transfer polymerization (RAFT) involving degenerative transfer thioesters; nitroxide mediated polymerization (NMP) involving dormant alkocyanines; or stable free radical polymerization (SFRP)<sup>2</sup>. This chapter describes the use of ATRP as a means to create well defined block copolymers using commercially available polypropylene oxide (PPO) as a macroinitiator and DMAEMA as the monomer.

### 3.3 Materials

Poly(propylene glycol) methyl ether ( $M_n = 3800$  g/mol, PI=1.12) (methoxy-P<sub>65</sub>-OH) and  $\alpha,\omega$  - dihydroxy terminated-poly(propylene oxide) ( $M_n = 7400$  g/mol, PI = 1.07) (HO-P<sub>127</sub>- OH), poly(N,N-dimethyl amino ethyl methacrylate) ( $M_n = 1300$  g/mol, PI = 1.4) from Polymer Source; poly(acrylic acid) ( $M_w > 200\ 000$  g/mol; 25% aqueous solution) (PAA) from Polysciences; triethylamine (TEA), 2-bromoisobutyryl bromide (BiBB), 2-(dimethylamino)ethyl methacrylate (98%) (DMA), Copper (I) bromide (99.99%) (CuBr), 2,2'-Bipyridyl ( $\geq 99\%$ )(Bpy), and all solvents ( $\geq 99.9\%$ ): benzene, dichloromethane, methanol, hexane, and dimethylformamide purchased from Aldrich were used as received unless otherwise mentioned.

Chemical structures of key molecules:

Abbreviated name	Chemical Structure
DMAEMA	
BiBB	
TEA	
Bpy	

### 3.4 Synthesis Methods

#### 3.4.1 Synthesis of macroinitiators.

In order to initiate ATRP, poly(propylene oxide) (PPO) macro-initiators were activated by esterification of the hydroxyl end groups of precursor PPO molecules with 2-bromoisobutyryl bromide (BiBB). The esterification reaction (reaction schemes are shown in Figure 3-1) is sensitive to the presence of water. Since the propylene oxide monomer is hygroscopic, and BiBB reacts with water, it is important to remove any trace amounts of water from PPO before end functionalization. Azeotropic distillation with benzene<sup>\*\*</sup> as a solvent was used to remove trace amounts of water.

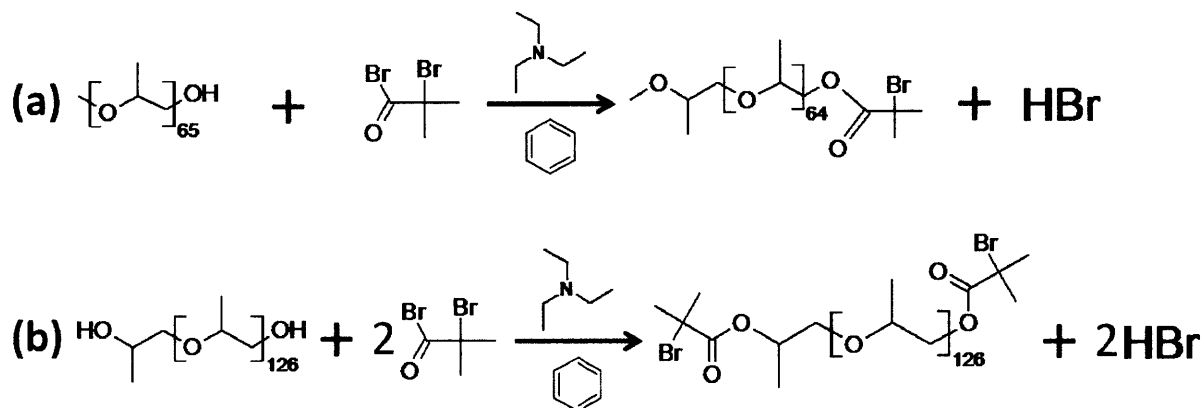


**Figure 3-1.** Chemical reaction schemes for end functionalization via esterification of hydroxyl groups on mono-hydroxy methoxy-P<sub>65</sub>-OH (a) and di-hydroxy HO-P<sub>127</sub>-OH (b).

Commercially purchased (a) methoxy-P<sub>65</sub>-OH (1.2 g, 29.3 mM) or (b) HO-P<sub>127</sub>-OH (2.5g, 27 mM) was dissolved in 100 ml of benzene in a round bottom flask (RBF). Water and benzene were co-distilled and the vapor condensate was allowed to collect and separate in a Dean-Stark trap as shown in Figure 3-2.

<sup>\*\*</sup> Benzene is highly toxic, carcinogenic and readily penetrates nitrile gloves. Use of rubber or latex gloves is preferable though not fool proof. While benzene was used here, azeotropic distillation with toluene is also a viable option. As a side note, most organic solvents are volatile, flammable and hazardous to health. They should be handled in the fume hood and with appropriate gloves. As most organic solvents are able to penetrate commonly used nitrile or latex lab gloves, gloves should be changed immediately should they come into contact with any organics.



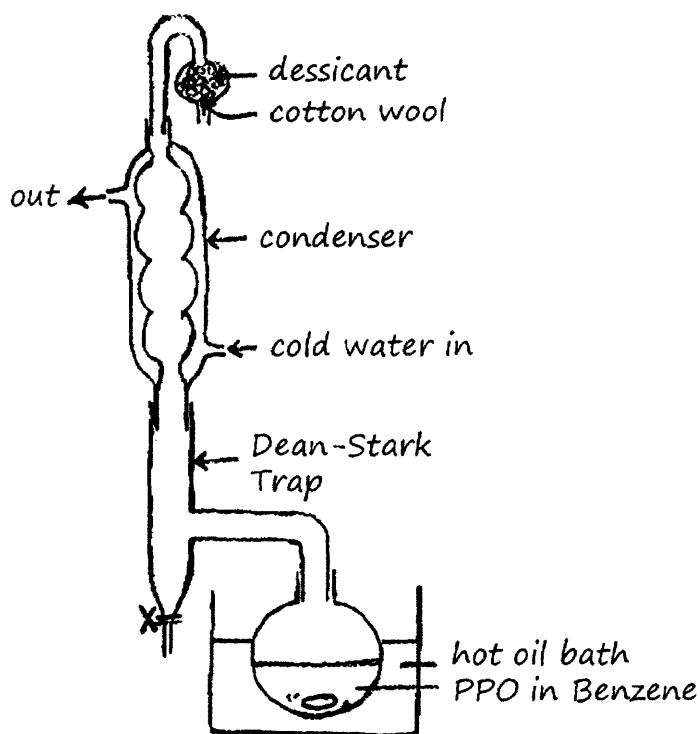


**Figure 3-2.** Drawing illustration of set-up used for azeotropic distillation drying of PPO before esterification.

Any water present in the distillate settles at the bottom of the trap while the organic solvent (benzene) runs back into the reaction mixture, through the side arm, and removes more water. The benzene-water minimum-boiling azeotropic mixture has a boiling temperature of  $\sim 69\text{ }^{\circ}\text{C}$  and water:benzene ratio of 9:91. Azeotropic distillation proceeded with stirring at 700 rpm, in an oil bath at  $120\text{ }^{\circ}\text{C}$ . 30 minutes after the Dean-Stark trap had filled with distillate, the bottom 5-10 ml containing water was run out of the trap. Distillation was then allowed to proceed for another hour. Without dismantling the apparatus, the solution was removed from the oil bath, wiped and cooled to  $0\text{ }^{\circ}\text{C}$  on ice. It is important that cooling is done with the condenser and its open end still connected to the desiccant to prevent water condensation from the atmosphere back into the mixture. After cooling for 5-10 min, still held on ice with stirring, 2.5 mol equivalents of TEA (73.3 mM for (a) or 135 mM for (b)) was quickly added. Fresh TEA (stored under vacuum when not in use) should be weighed out into a glass vial just before addition. To add TEA,  $\sim 5$  ml of

the PPO benzene mixture was added to dilute the TEA in the glass vial after which the diluted TEA was added to the reaction mixture. This process was repeated to rinse the glass vial. A pressure equalizing funnel was then connected to the top of the RBF for addition of BiBB (73.3 mM for (a) or 135 mM for (b)). BiBB was weighed out in a glass vial and ~ 15 ml of dry benzene from the Dean Stark trap (after removal of the bottom layer of water) was added to dilute the BiBB and rinse the glass vial after transferring the BiBB into the addition funnel. BiBB was allowed to drip into the RBF at a rate of ~ 1 drop per 2 seconds. The addition funnel was removed after BiBB addition and the RBF was capped and sealed with parrafilm. The temperature was allowed to rise to room temperature at which the reaction was left to proceed overnight. At the end of the reaction, 1 – 2 drops of TEA was added and allowed to react with any excess BiBB for 1 hr. The mixture was filtered to remove amine salts and the solvent was removed by vacuum distillation. The product was then dissolved in ~ 50–60 ml of dichloromethane (DCM) and extracted 3 times with about the same volume of 5 wt% sodium bicarbonate aqueous solution using a separating funnel. DCM ( $\rho = 1.33\text{g/cm}^3$ ) is denser than water and forms the bottom layer. The final DCM layer containing the brominated PPO was collected, dried over  $\text{MgSO}_4$ , and passed through a basic alumina column<sup>††</sup>. The final methoxy- $\text{P}_{65}\text{-Br}$  or difunctional  $\text{Br-P}_{127}\text{-Br}$ , macroinitiators were then obtained by removal of DCM by distillation.  $\text{H}^1$  NMR of the macroinitiators at 5 mg/ 0.1 ml of deuterated chloroform was done to confirm stoichiometric end functionalization of the PPO macroinitiators.

---

<sup>††</sup> Making a good alumina column takes some practice, to avoid trapped air pockets and formation of cracks that will allow mixtures to flow through quickly without separation. A well packed column should have a flow rate of less than ~1-2 drops per second (not a stream) when the burette valve is fully open. Dry Alumina powder is added to a column (stoppered at the base with a cotton or glass wool) that is already wet by solvent. The burette is left open and solvent flows out the bottom as alumina powder is added with constant swirling action. The solvent is added between addition of the alumina to keep the alumina powder wet with the level of solvent >1/2 cm above the alumina level at all times. With no prior experience, it would be helpful to watch a chemist do it once.

### 3.4.2 Synthesis of diblock and triblock copolymers.

Both the long triblock copolymer (LTB) and diblock copolymer (DB) were synthesized by atom transfer radical polymerization (ATRP).

#### 3.4.2a ATRP background information.

**Reaction mechanism.** The general mechanism for ATRP is shown in Figure 3-3.

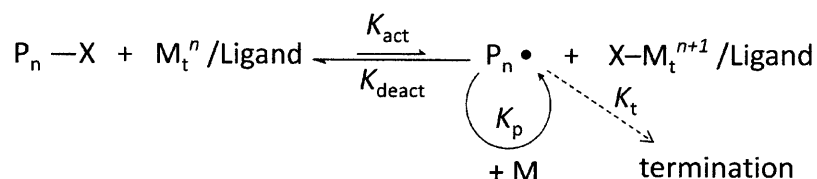


**Figure 3-3.** Schematic showing the general mechanism of atom transfer radical polymerization (ATRP).

In this work, X is Br and the transition metal catalyst ( $M_t$ ) used is Cu with 2,2'-Bipyridyl (Bpy) as the ligand. While the choice of catalyst and ligand used here was based on the unpublished experiences of my collaborators, a vast amount of published literature particularly by Krzysztof Matyjaszewski and his group is available and one can refer to a comprehensive review for more information on the polymerization technique and mechanism<sup>2</sup>. A good amount of detailed information on initiator, ligand and solvent selection for several monomers can also be found on the Matyjaszewski group webpage:

<http://www.cmu.edu/maty/atrp-how/starting%20points.html#starting%20points>

Alternative catalyst/ligand systems that would work well for controlled ATRP synthesis of DMAEMA include the CuCl/Bpy and CuBr/HMTETA systems amongst several others<sup>3</sup>. While an in depth study of the polymerization kinetics was not done here, it is useful to note that in the absence of side reactions other than termination by disproportionation and coupling, the rate of polymerization is determined largely by the magnitude of  $K_{\text{eq}} = K_{\text{act}}/K_{\text{deact}}$ , as opposed to  $K_p$ . If  $K_{\text{eq}}$  is too small, polymerization might not proceed. On the other hand, if  $K_{\text{eq}}$  is too large, a high concentration of active radical species will result in poorly controlled polymerization with a significant amount of termination<sup>2</sup>. Further, in the latter case, the overall speed of polymerization

might still be slow because the equilibrium position is such that there is a larger amount of deactivating oxidation state catalyst that can result in an apparently slow overall polymerization rate<sup>2</sup>. Since each rate constant involved in ATRP:  $K_{act}$ ,  $K_{deact}$ ,  $K_p$  and  $K_t$ , varies with the specific monomer, solvent, catalyst and ligand system chosen, as well as, the reaction temperature, for synthesis of a specific polymer or copolymer, these factors can be adjusted to allow for better control over polymerization.

Here, the main goal of synthesis was to obtain relatively well defined block copolymers of PPO and PDMAEMA in order to investigate the effect of block copolymer architecture on the temperature swelling responses of LbL assembled thin films. While successful synthesis was achieved here, there is room for additional optimization to achieve narrower polydispersities, for qualitative end functionalization, or for subsequent growth of another block. To avoid loss of chain end functionality, it is recommended that polymerization proceed only to about 75% conversion and strictly not more than 95% conversion. Since DMAEMA (D) end blocks were the only ones to be added, end group functionality was not a major issue here and the reactions were allowed to proceed to completion. The degree of polymerization (DP) varies with the ratio of initial monomer,  $[M]_0$ , to initiator concentration,  $[initiator]_0$ , and monomer conversion,  $p$ , as  $DP = [M]_0/[initiator]_0 \times p$ . For  $p = 1$  used in our polymerizations, the ratio of  $[M]_0/[initiator]_0$  added was approximately equal to the targeted DP. The molar ratios of macroinitiator, methoxy-P<sub>65</sub>-Br:CuBr:Bpy:DMA was 1:1:2.5:60 for synthesis of the diblock copolymer (DB) and that of Br-P<sub>127</sub>-Br:CuBr:Bpy:DMA was 1:1:2:5:100 for synthesis of the long triblock copolymer (LTB).

It is important to ensure all glassware are thoroughly cleaned just before use. Items cleaned include a 25 ml round bottom flask (RBF) and an appropriately sized magnetic stir bar to be used. Cleaning is done by soaking in a base bath overnight (or scrubbing with soap and water) followed by cleaning with cotton balls and tetrahydrofuran (THF), followed by rinsing with ethanol (2×) and finally rinsing with acetone and drying in an oven. It is generally good practice to have a clean dedicated hood containing the vacuum manifold. The joint on the Schlenk line to which the mouth of the RBF will be connected should be carefully cleaned with THF and acetone. The surface of the hood to be used was also wiped down well with THF before carrying out the polymerization procedures.

### 3.4.2b Atom transfer radical polymerization of DMAEMA.

Polymerization was carried out as follows: ~1 g of macroinitiator was added to the bottom of the clean RBF containing the stir bar, followed by the DMA monomer (distilled under reduced pressure before use) and dissolved in 6-8 ml of methanol. The reaction mixture was then deoxygenated by 3 freeze-pump-thaw cycles (see below). For deoxygenation, the RBF was connected to a Schlenk line with one manifold connected to an Ar source and the other to high vacuum. A double-oblique stopcock was used to switch between vacuum and Ar atmosphere.

A typical freeze-pump-thaw cycle was carried out as follows:

- 1) Open flask to vacuum. Allow bubbling to occur for 1 – 2 min until bubbling dies down. (*Note: low boiling point solvents will keep bubbling due to boiling under reduced pressure!*)
- 2) Close from vacuum, fill a styrofoam cup with liq N<sub>2</sub> and immerse the RBF in it to freeze the mixture. (*Freezing lowers solubility of air in the reaction mixture and forces air out.*)
- 3) Remove the liq N<sub>2</sub> and open the flask to Ar and wait until mixture melts (*this can be sped up using a container of RT water*). Allow Ar to dissolve into the liquid. (*After each thawing, wipe the exterior of the vessel dry to avoid forming an ice layer during the next freezing.*)
- 4) Close the RBF from Ar, freeze as in Step 2 and, open to vacuum for 30 sec then open to Argon to melt.
- 5) Repeat freeze-pump-thaw cycle 3 – 4 times.

On the side, a complexed Cu catalyst is prepared as follows:

- 1) Weigh out the required amount of Cu(I)Br onto a folded piece of Al foil.
- 2) Add Bpy in a molar ratio of 2 – 2.5 ×.
- 3) Fold over Al foil and crush them together with the spatula. Open mix and press to crush together. Repeat this to mix well and obtain a final uniformly grey complex.
- 4) Pour the mixture into a new folded Al foil trough and balance the complexed mixture on a bent spatula as shown in Figure 3-4.

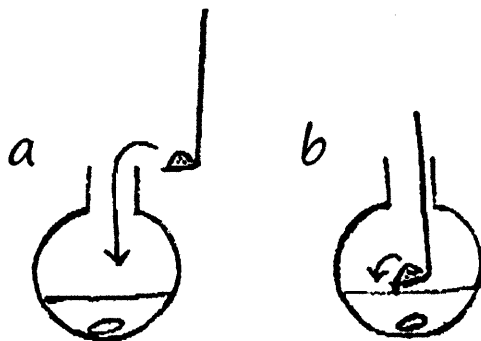


**Figure 3-4.** Illustration of how CuBr/Bpy complex was added to the deoxygenated reaction mixture. (a) shows the spatula bent into an “L” shape carrying a heap of the catalyst complex just before addition and (b) shows the spatula gently lowered to just above the liquid surface where the spatula is tilted and lightly tapped such that the catalyst powder is added with little disturbance to the Ar atmosphere in the RBF.

After the last freeze-pump-thaw cycle, backfill the RBF with Ar and open the vessel to air. Denser Ar stays inside the flask but move swiftly and carefully to minimize introduction of oxygen from the ambient air. Add the complexed initiator directly above the surface of the liquid (as illustrated in Figure 3-4) and immediately connect the flask back to Schlenk line and vacuum evacuate for 1 – 2 minutes with stirring. The mixture should turn into the color of rust. Open the vessel to Ar and repeat the vacuum cycle and then open the vessel to the Ar again. Increase the Ar flow briefly before closing off the reaction flask to maintain a higher than atmospheric pressure of Ar in the RBF. Maintain a high vacuum in the manifold and seal off the ends before switching off the vacuum pump. Control the Ar flow through the other manifold (at a flow rate of ~ 1 bubble per 2 seconds) to maintain the Ar pressure in the manifold throughout the polymerization. It is important that the reaction mixture stays brown. If it turns blue-green, a leak has occurred resulting in the oxidation of the Cu catalyst and the reaction is dead<sup>‡‡</sup>. Polymerization was allowed to proceed at room temperature in the dark for 6 – 12 hrs after which the reaction was stopped by exposure to air and addition of methanol. The products were

---

<sup>‡‡</sup>Several block polymers with shorter PDMAEMA end blocks were obtained as a result of reactions that prematurely terminated in this manner. Selected polymers proved useful in the further exploration of BCP architectural effects on multilayer stability as discussed in Chapter 5, Section 5.4.4c.

purified by passage through a basic alumina column to remove the catalyst, and the solvent was removed by vacuum assisted distillation. To purify, the dry product was dissolved in a small amount of THF and precipitated into a large excess of cold hexane (-30 °C).

### 3.4.3 Block copolymer characterization.

The purified polymer products were dissolved in CDCl<sub>3</sub> for <sup>1</sup>H NMR characterization using a Bruker 400 MHz spectrometer. Figure 3-5 shows the <sup>1</sup>H NMR spectra of the synthesized block copolymers LTB and DB along with the spectrum of a commercial D-P-D short triblock copolymer (STB) that will be used for comparisons subsequently in Chapter 4.

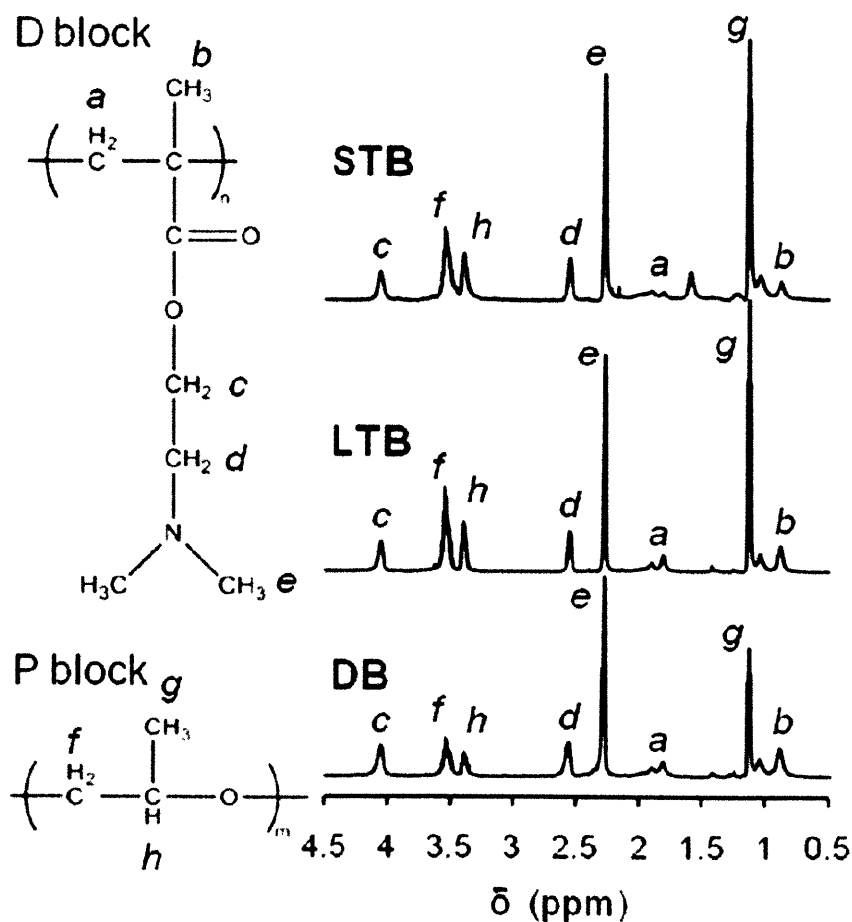


**Figure 3-5.** <sup>1</sup>H NMR spectra of the commercial short D-P-D triblock copolymer (STB) and synthesized block copolymers: long D-P-D triblock copolymer (LTB) and P-D diblock copolymer (DB) in CDCl<sub>3</sub>.

From integration of the non-overlapping peaks from the 2 ( $-\underline{\text{C}}\underline{\text{H}}_2\text{-N}$ ) protons of the D block at  $\delta = 4.06$  (denoted *c* in Fig. 3-5) and integration of the peaks at  $\delta = 3.54$  and  $3.40$  corresponding to 3 protons ( $-\text{O}-\underline{\text{C}}\underline{\text{H}}_2-\underline{\text{C}}\underline{\text{H}}-$ ) (*f* and *h*) along the polymer backbone of P, the compositions of the BCPs were determined as listed in Chapter 4, Table 4-1. The polymers were also dissolved in DMF (at 4 mg/ml) for molecular weight and polydispersity determination by gel permeation chromatography (GPC) using PMMA calibration standards. DMF GPC measurements were obtained using Water Breeze 1525 HPLC system equipped with two Polypore columns operated at 75 °C, series 2414 refractive index detector, series 1525 binary HPLC pump, and a 717plus autosampler. Waters' Breeze Chromatography Software Version 3.30 was used for data collection as well as data processing. The GPC traces obtained for the macroinitiators and synthesized block copolymers are shown in Figure 3-6.



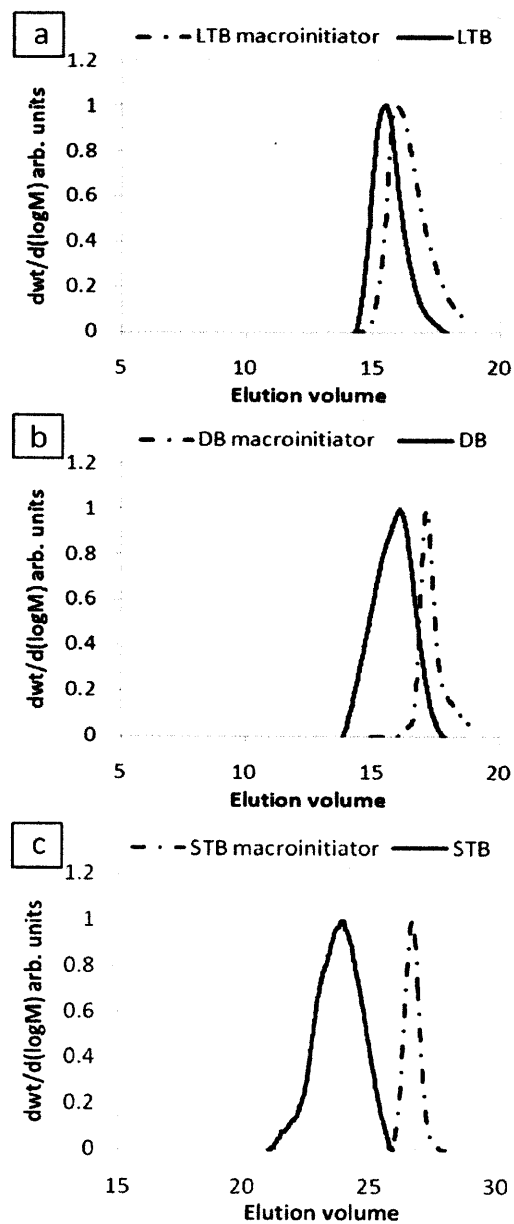


**Figure 3-6.** Gel Permeation Chromatography (GPC) curves of macroinitiators and synthesized block copolymers (a) LTB, (b) DB in dimethylformamide and (c) GPC curves of commercially obtained STB and its macroinitiator obtained from Polymer Source Inc<sup>§§</sup>.

<sup>§§</sup> While DMF GPC run as described above allowed for dissolution of the synthesized polymers and was able to distinguish mixtures of unreacted PPO homopolymer from the synthesized block copolymers, somehow attempts to obtain decent GPC curves from the commercial STB under these conditions failed; no trace was obtained despite trials using STB in DMF at various concentrations. The GPC curve shown was obtained from the information sheet that came with the polymer purchased from Polymer Source. It is likely that the GPC curve provided by Polymer Source Inc. was obtained using THF as solvent and different GPC running conditions. The synthesis route for STB might also be different from that described in this Chapter.

### 3.5 Conclusions

In this chapter, we discussed in detail the synthesis steps used for the creation of PPO and PDMAEMA block copolymers and show that ATRP is a facile means of creating block copolymers of well defined architecture. To achieve a narrower molecular weight distribution, use of a different solvent (anisole or IPA) and CuBr/HMTETA catalyst system might be recommended<sup>3</sup>.

### Acknowledgements

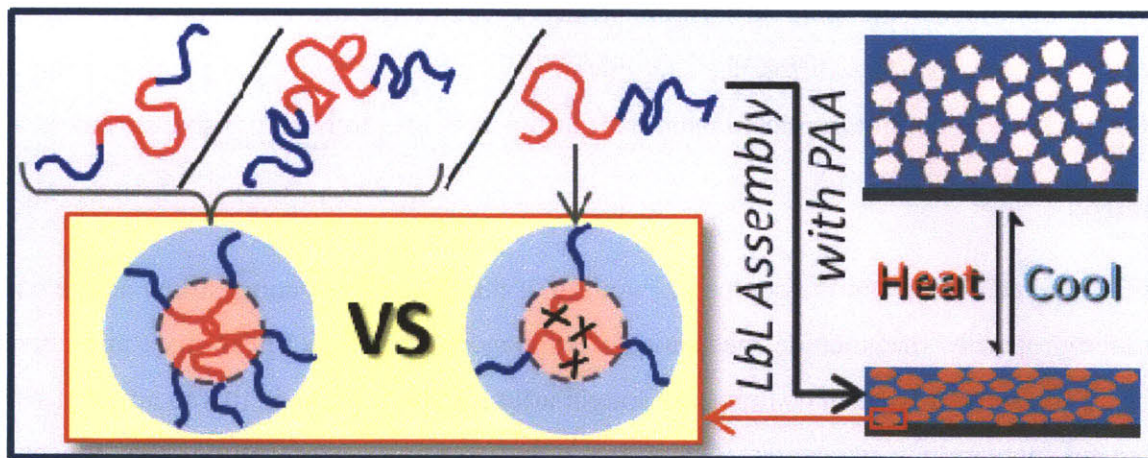
Work in this chapter was supported in part by the MRSEC Program of the National Science Foundation under award number DMR – 0819762 and in part by NSF DMR-0710591 (S. Sukhishvili). In addition to Stevens Institute of Technology, where the synthesis was done, we thank the Institute for Soldier Nanotechnologies (ISN) and the MIT Department of Chemistry Instrumentation Facility (DCIF) for use of their characterization facilities.

### References

- (1) Greszta, D.; Mardare, D.; Matyjaszewski, K. *Macromolecules* **1994**, *27*, 638.
- (2) Matyjaszewski, K.; Xia, J. *Chemical Reviews* **2001**, *101*, 2921.
- (3) Zhang, X.; Xia, J.; Matyjaszewski, K. *Macromolecules* **1998**, *31*, 5167.

# CHAPTER 4: EFFECTS OF BLOCK COPOLYMER ARCHITECTURE ON THE THERMALLY-INDUCED SWELLING OF MICELLE-CONTAINING MULTILAYER THIN FILMS

*This chapter is reproduced in part with permission from Wui Siew Tan, Zhichen Zhu, Svetlana A. Sukhishvili\*, Michael F. Rubner, and Robert E. Cohen, Macromolecules, accepted. Copyright 2011 American Chemical Society.*



\* Work described in this Chapter was done in collaboration with Prof. Svetlana A. Sukhishvili from Stevens Institute of Technology Department of Chemistry, Chemical Biology & Biomedical Engineering, via synthesis of block copolymers at Stevens Institute of Technology as described in Chapter 3.

## 4.1 Abstract

This chapter explores the effect of block copolymer (BCP) molecular weight and connectivity, on the morphology and time-temperature dependent swelling of thin film hydrogels created through Layer-by-Layer (LbL) assembly of BCP micelles with poly(acrylic acid). BCPs of poly(N,N dimethyl amino ethyl methacrylate) (D) and poly(propylene oxide) (P), a P-D diblock, a long D-P-D triblock and a short D-P-D triblock copolymer, were compared in terms of their temperature response in solution and within micelle-polyelectrolyte multilayers (mPEMs). The critical micellization concentration and micellization temperature of the BCPs in solution, as well as the swelling transition temperature,  $T_{stt}$ , of the mPEMs, decreased with increasing P block length. AFM imaging of dry mPEMs show regular dimpled surface structures that arise from surface relaxation of micelles. When the mPEMs are cooled below  $T_{stt}$  in water, the ~200 nm thick films can swell reversibly between 3 to 6 times their dry thicknesses within 2 min. The degree of swelling ( $\tau = \text{wet thickness/dry thickness}$ ) increases with undercooling ( $\Delta T = T_{stt} - T$ ) and shows time dependencies related to  $\Delta T$  and the constituent BCP connectivity. While the diblock films swell uncontrollably and lose integrity within 30 minutes at  $\Delta T \geq 6^\circ\text{C}$ , the triblock copolymer multilayers are able to sustain steady  $\tau$  values (in the range of 4 to 10) under equivalent conditions. The differences in dynamic swelling behavior originating from BCP architecture have important implications in their utility as temperature responsive surfaces.

## 4.2 Introduction

Stimuli triggered changes in the degree of swelling of thin hydrogel coatings allow active control of surface properties that include mechanical compliance<sup>1,2</sup>, solute permeability<sup>3</sup>, and chemical affinity<sup>4,5</sup>. Consequently, such coatings are sought after for applications in therapeutic delivery<sup>6,7</sup>, mechanical actuation<sup>8</sup>, molecular separations<sup>4</sup> and sensing<sup>9</sup>. Controlling the mechanical properties of surfaces is also critically importance at synthetic - biological interfaces because cell responses<sup>10,11</sup> and bacterial attachment<sup>12</sup> can be modulated by substrate compliance. Layer-by-Layer (LbL) assembly is a facile conformal coating technique well suited for the creation of responsive thin film hydrogels. pH responsive LbL assemblies that exhibit large changes in swelling with pH variation have been created in the form of flat films<sup>13,14</sup>, capsules<sup>15,16</sup> and within membrane pores<sup>17</sup>, with successful applications in controlled drug release<sup>18</sup> as well as membrane gating<sup>17</sup>. In contrast, there have been few reports of LbL assemblies able to exhibit

large swelling transitions in response to temperature. Over the past few years, several efforts have been made to create temperature responsive multilayer thin films through the incorporation of temperature responsive polymers utilizing either hydrogen bonding<sup>19</sup> or electrostatic<sup>20</sup> LbL assembly, as described in Chapter 2. There have been demonstrations of temperature responsive LbL systems able to reversibly load and release small molecules<sup>21-23</sup> or therapeutics<sup>24</sup>, as well as examples of systems that allow for temperature-triggered dissolution<sup>25,26</sup>. Attempts to create PEMs with large reversible swelling responses to temperature, however, have shown that polymers or copolymers that exhibit reversible temperature responses in solution, when incorporated into PEM films or capsules showed limited temperature driven swelling changes that were irreversible<sup>20,27,28</sup>. While Jaber and Schlenoff have reported reversible temperature dependent hydration of multilayers at the molecular level<sup>29</sup>, and swelling ratios reversible between 1.1 (at 45 °C) and 1.65 (at 20 or 25 °C) were reported in studies by Z. Zhu *et al.*<sup>22</sup> and L. Xu *et al.*<sup>23</sup>, these swelling degrees are small compared to typical hydrogels or the degree of swelling achievable in pH responsive LbL assemblies. In Chapter 2, we showed that LbL assembly of micelle forming block copolymers is a facile means to create temperature responsive thin films that exhibit reversible swelling transitions of large scale, involving hydrated states with more than 400 vol% of water. There we found that the assembly pH and the anionic binding partner used for LbL assembly of the micelle forming, temperature responsive, A-B-A triblock copolymer were critical factors that determined whether or not large temperature driven swelling could be observed<sup>30</sup>.

Micelle polyelectrolyte multilayers (mPEMs) were first reported in 2006 by groups interested in micelles as nano-particulate structures for porosity introduction in optical applications<sup>31,32</sup>. It was also recognized that the core-shell structure of micelles formed by block copolymers (hydrophobic core surrounded by a hydrophilic corona) allowed creation of local hydrophobic environments within multilayers created from all aqueous solutions<sup>33,34</sup>. This proved useful for loading of hydrophobic functional compounds<sup>18,33-38</sup>. In fact, owing to advances in BCP synthesis as discussed in Chapter 3, the chemical functionality carried within the micelle core forming block can be selected relatively independently of the hydrophilic corona forming block. As such, BCP micelles present opportunities for creating thin films of novel functionality, not limited by chemistries required for water solubility or the complementary bonding requirement

for LbL film assembly. In our work, we use this capability to create electrostatically assembled mPEMs that are responsive to temperature.

In this Chapter, we investigate the impact of BCP molecular weight and connectivity on the temperature-driven swelling behavior of LbL assembled thin film hydrogels. Three block copolymers of poly(N,N dimethyl amino ethyl methacrylate) (D) and poly(propylene oxide) (P): two D-P-D triblock copolymers, one having double the molecular weight of the other, and a D-P diblock copolymer, synthesized as described in Chapter 2, were assembled as micelles into thin 150 – 250 nm thick films by LbL assembly with poly(acrylic acid) (PAA). The BCP architectures strongly influenced the temperature-driven swelling of the mPEM thin films, with multilayers containing the triblock copolymers exhibiting better overall reversibility and stability than multilayers containing diblock copolymers.

### 4.3 Materials and methods

**Materials.** Poly(N,N-dimethyl amino ethyl methacrylate-*b*-propylene oxide-*b*-N,N-dimethyl amino ethyl methacrylate) ( $M_n$ : 1600-*b*-3000-*b*-1600, PI=1.5) (STB), from Polymer Source; poly(acrylic acid) ( $M_w > 200\,000$  g/mol; 25% aqueous solution) (PAA) from Polysciences; 1,2-bis-(2-iodoethoxy)ethane (BIEE), and 1,6-diphenyl-1,3,5-hexatriene (DPH) and solvents ( $\geq 99.9\%$ ): dichloromethane, and dimethylformamide purchased from Aldrich were used as received unless otherwise mentioned.

**BCP solution preparation and characterization.** To ensure solution equilibration, especially for the longest polymer LTB, all BCPs were dissolved at 1 – 2 mg/ml concentration in deionized, ultrapure Millipore water with resistivity  $18\text{ M}\Omega\text{ cm}^{-3}$  (abbreviated as “DI” henceforth), acidified with 0.1 M HCl (0.5 mol equivalent of the number of amine groups), by overnight refrigeration at 4 °C. The BCP solutions were then diluted to the desired concentration in room temperature DI water and adjusted to the desired pH by addition of 0.1 M NaOH or 0.1 M HCl. This solution was then refrigerated again for 5 hours to allow for re-dissolution of polymers at the desired concentration and pH. After the solution was retrieved from the refrigerator and allowed (3-5 hr) to equilibrate at room temperature, the pH was checked again and minor pH adjustments (if any) were made just prior to use of the solutions for micro differential scanning calorimetry (mDSC), Cryogenic scanning electron microscopy, shell crosslinking, dye solubilization or LbL assembly.

mDSC was done as described previously<sup>30</sup> to obtain the micellization temperature of 1 mg/ml BCP solutions at pH 8 and DPH dye solubilization, also described previously<sup>30</sup>, was carried out at room temperature on BCP solutions of concentrations between 0.0005 to 0.1 mg/ml for determination of BCP critical micelle concentration at pH 7. (Ref. to Methods Section, Chapter 2)

**Cryogenic scanning electron microscopy (Cryo-SEM).**<sup>†</sup> A FEI Helios 600 scanning electron microscope equipped with a Quorum Technologies PP2000 Cryo-SEM preparation system was used to obtain micelle images in the frozen state. BCP solutions of 0.1 mg/ml, pH 7, were injected into rivets, glued end to end and inserted standing into holes in an aluminum holder such that the bottom rivet is held fixed while the top rivet stuck out above the holder. The solutions, mounted on a transfer device, were flash frozen in freshly melted liquid nitrogen slush (-210 °C) and transferred immediately under vacuum into a preparation vacuum chamber held at -130 °C. The top rivets were then knocked off to expose freshly fractured surfaces within the interior region of the BCP solutions. Sublimation to expose BCP features was allowed to occur at -90 °C for 5 min, after which the temperature was reduced back to -130 °C and *in-situ* sputtering of 1–2 nm of Au/Pd was carried out before SEM imaging of the surfaces at 5 kV and -190 °C.

**Selective crosslinking of BCP micelles.** Crosslinking of DMA in the BCP micelle coronas was achieved at 25 °C and pH 7 by quaternization using BIEE, as described by Jiang *et al.*<sup>39</sup>. Briefly, BIEE (0.5 mol per mol of DMA residues) was added to 0.1 mg/ml BCP solutions adjusted to pH 7 and the reaction was allowed to proceed for 3 days.

**LbL assembly.** BCP solutions at 0.1 mg/ml, pH 7, freshly constituted as described above were used for LbL assembly on silicon substrates prepared as detailed in Chapter 2. 150 -250 nm thick films were assembled for temperature dependent swelling studies. The films in this chapter are simply denoted by their components as (polycation/polyanion)<sub>x</sub> because the same deposition pH of 7 was used to create all the multilayers studied here. The polycation is poly(N,N-dimethyl amino ethyl methacrylate) (D) or positively-charged BCP micelles of STB, LTB or DB and the polyanion is PAA. The subscript x denotes the number of polycation - polyanion deposition cycles. 150 nm to 250 nm thick films studied in this chapter correspond to (STB/PAA)<sub>30</sub>, (LTB/PAA)<sub>35</sub>, (DB/PAA)<sub>35</sub> and (D/PAA)<sub>40</sub>. The subscripts are dropped for simplicity in the

---

<sup>†</sup> I would like to thank Dr. Shiahn Chen from the Center of Materials Science Engineering for his invaluable assistance with Cryo-SEM imaging.

results section. All multilayers were deposited on 1 mm thick silicon wafers with both polymer solutions and rinse solutions adjusted to pH 7 with 1M HCl and 1M NaOH.

**Spectroscopic ellipsometry.** The dry film thicknesses and swelling behavior of the films in pH 7 DI was determined using a Woollam VASE spectroscopic ellipsometer, as described in Chapter 2. In order to hold the films at low temperature in pH 7 DI for time-dependent swelling studies, the fluid cell used for *in-situ* ellipsometry was housed in a custom made hollow stainless steel block through which cold water was circulated using a Julabo refrigerated circulator with PID1 temperature control, able to provide temperature stability of 0.03 °C, as illustrated in Fig. 4-M1 and Fig. 4-M2.

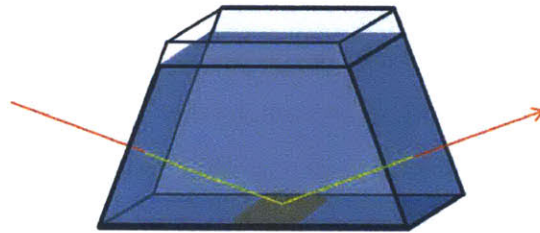


**Figure 4-M1.** Illustration of sample mounted in wet ellipsometric cell filled with pH adjusted DI water and showing the path of the light beam in the spectroscopic ellipsometry measurement, as used in Chapter 2.

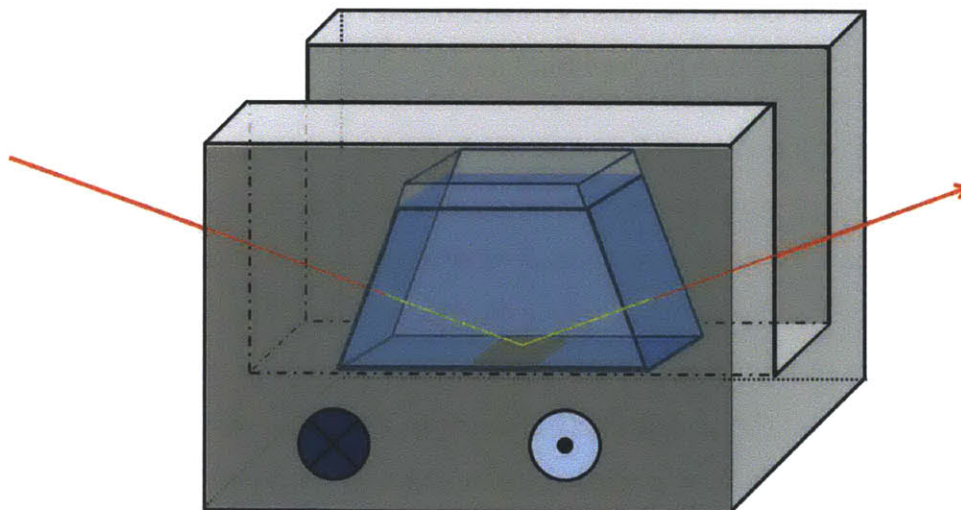


**Figure 4-M2.** Illustration of wet ellipsometric cell mounted within a custom made stainless steel heat sink through which cold water is circulated and used to maintain constant low temperatures for studying time dependent thickness evolution in this chapter.



**Atomic force microscopy (AFM).** All AFM images were obtained using a Digital Instruments Nanoscope IV, Dimension 3000 microscope operated in tapping mode. FM-20 AFM probes from NanoWorld, with force constant, 2.8 N/m, resonant frequency, 75 kHz and tip radius less than 8 nm were used for imaging.

## 4.4 Results and Discussion

### 4.4.1 BCP composition and polydispersity.

As described in the Chapter 3, ATRP was used to synthesize a P-D diblock copolymer (DB) and a D-P-D long triblock copolymer (LTB) for comparison to a commercially available D-P-D short triblock copolymer (STB) with compositions listed in Table 4-1.

**Table 4-1.** Composition and polydispersity of block copolymers.

Polymer	D:P <sup>a</sup>	$N_p^{b,*}$	$N_D^c$	Block architecture	$M_w/M_n$
STB	0.41	52	22	D <sub>11</sub> -P <sub>52</sub> -D <sub>11</sub>	1.5*
LTB	0.41	127	54	D <sub>27</sub> -P <sub>127</sub> -D <sub>27</sub>	1.38 <sup>d</sup>
DB	0.88	65	57	D <sub>57</sub> -P <sub>65</sub>	1.66 <sup>d</sup>

<sup>a</sup> Ratio of D to P units determined by <sup>1</sup>H NMR spectroscopy in CDCl<sub>3</sub> as described in Chapter 3.

<sup>b</sup> Degree of polymerization of P obtained from Polymer Source Inc.. <sup>c</sup> Degree of polymerization of D calculated from D:P. <sup>d</sup> Polydispersity of synthesized BCPs determined by GPC in DMF using poly(methyl methacrylate) calibration standards. \*Information provided by Polymer Source Inc. from which macroinitiators and STB were purchased.

### 4.4.2. BCP solution self assembly.

Dynamic light scattering (DLS) typically used to determine BCP micelle size in solution gave unreasonably large hydrodynamic radii of 100 – 200 nm for the LTB and DB solutions at 0.1 mg/ml concentration in DI water adjusted to pH 7, conditions used for LbL assembly (refer to Appendix A, Figure A-5). While such values of hydrodynamic radii have been reported for BCP polyelectrolyte micelles of similar molecular weight and corona chemistry<sup>40-42</sup>, it is useful to note

that such dimensions, several times the contour length of the BCPs cannot correspond to the size of individual spherical micelles. The DLS results either indicate the formation of larger aggregates (compound micelles or vesicles) or result from non-negligible inter-micellar correlations known to exist for charged polyelectrolyte micelles<sup>43,44</sup>. To determine the aggregate morphology of the BCPs present in the solutions used for LbL deposition, we used Cryogenic Scanning Electron Microscopy (Cryo-SEM). Solutions of each BCP were prepared at 0.1 mg/ml in DI water and adjusted to pH 7, identical to conditions used for LbL assembly. The solutions were vitrified in liquid nitrogen slush to avoid ice crystal formation and fractured at – 130 °C to expose the internal structure of the frozen solution. To enhance the topography, these exposed surfaces were held at low pressure ( $10^{-4}$  Pa) and – 90 °C to remove water by sublimation, leaving behind the BCP structures. Figure 4-1 shows that all three BCPs exist as relatively monodisperse spherical micelles in solution under the LbL assembly conditions. Analysis of several Cryo-SEM images allowed us to determine the average micelle diameters and histograms of the micelle size distribution are shown to the right of the representative SEM images in Fig 4-1. The average micelle diameters of the BCPs along with the standard deviation of the measurements are listed in Table 4-2. The sizes reported here are likely to be smaller than the hydrated micelle size due to removal of water by sublimation. Nonetheless, it is interesting to note that the differences in molecular weight and block architecture between the BCPs did not have a significant effect on the observed micelle sizes. This is possible because while the micelle core radius and aggregation number tend to increase with (the core forming) P block length<sup>45,46</sup>, increasing the corona D block length is expected to cause an opposite trend and decrease the aggregation number<sup>45-47</sup>. It is useful to note that in Cryo-SEM, optimizing the sublimation step (through time and temperature control) is important. While sufficient sublimation is needed to allow exposure of micelles at the surface, too much sublimation exposes several layers of micelles. In the latter case, large aggregates are seen, which upon close inspection, can be discerned to be clusters of smaller spherical micelles piled up on one another (shown in Appendix A, Figure A-6). Solutions of higher BCP concentrations 1 up to 5 mg/ml were prepared and imaged under the same conditions. Large hollow tubes, discs, reticulated networks and sheet-type BCP structures were readily observed at the higher concentrations (as shown in Appendix A, Figures A-7 to A-11 ), providing reassurance that the simple spherical micelle was the dominant BCP structure in the 0.1 mg/ml solutions used for LbL assembly.

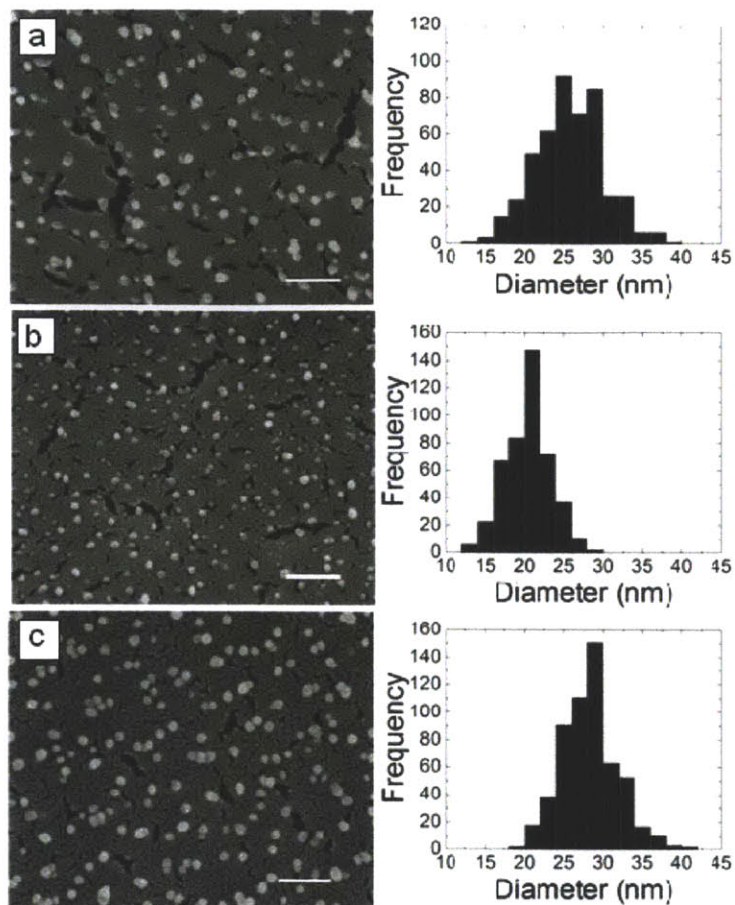


**Figure 4-1.** Cryo-SEM images of freeze fractured surfaces of flash frozen BCP solutions, taken after sublimation to expose micelles. STB (a), LTB (b), and DB (c) solutions were of 0.1 mg/ml concentration in DI water, adjusted to pH 7. The white scale bars at the bottom right of each image represents 150 nm. Size distributions of micelles obtained by measurements from at least 4 images are shown on the right hand side of each representative image.

The solution micellization temperatures (MTs) of 1 mg/ml BCP solutions were determined using micro differential scanning calorimetry (mDSC) as detailed in Chapter 2. Since MT is sensitive to the solution pH<sup>30</sup>, the micellization temperature was determined at pH 8 to avoid possible suppression of micellization by highly charged D blocks<sup>30,46,50-52</sup> as seen in Chapter 2. The MTs thus determined are listed in Table 4-2 and are in good agreement with the temperature at which aggregation was detected by DLS (Fig. A-5). The critical micellization concentration (CMC) of the BCPs at room temperature (22 °C) was determined using a well established DPH dye solubilization technique<sup>53</sup>. Here, BCP solutions of concentrations 0.0005, 0.001, 0.01, 0.02, 0.04,

0.06, 0.08 and 0.1 mg/ml were made, adjusted to pH 7, re-dissolved at low temperature and allowed to equilibrate at room temperature for 5 hours after which DPH was added and allowed to equilibrate in the BCP solution for another 5 hours. The fluorescence spectra of these solutions were then obtained and the fluorescence intensity at 457 nm plotted as a function of BCP concentration (Appendix A, Figure A-12). The CMC values listed in Table 4-2 were determined as the point at which a steep increase in fluorescence intensity with increasing polymer concentration was observed.

**Table 4-2.** BCP solution micellization characteristics.

Polymer	Micelle Diameter <sup>a</sup> (nm)	MT <sup>b</sup> (°C)	CMC <sup>c</sup> (mg/ml)
STB	26 ± 5	16	0.05
LTB	21 ± 3	10	0.02
DB	28 ± 3	15	0.04

<sup>a</sup> Average BCP micelle size and standard deviation of measurements obtained from Cryo-SEM images of 0.1 mg/ml BCP solutions at pH 7, 22 °C. <sup>b</sup> Micellization temperature (MT) of 1 mg/ml BCP solutions adjusted to pH 8, determined using micro differential scanning calorimetry. <sup>c</sup> Critical micelle concentration (CMC) at 22 °C, pH 7, determined by DPH dye solubilization.

As seen in Table 4-2, both the micellization temperature and critical micelle concentration of the BCPs decreased with the molecular weight of the poly(propylene oxide) (P) block. The decrease in micellization temperature at fixed concentration logically follows from the expected decrease in lower critical solution temperature (LCST) with molecular weight. The CMC at 22 °C also decreases in the order of P block length. While longer poly(N,N dimethyl amino ethyl methacrylate) (D) end blocks could be expected to contribute to an opposite trend, where longer D blocks would tend to lower the CMC and CMT, the effects of the P block length dominate in this case. Similar decreases in CMC and CMT with P block molecular weight have been reported for Pluronic; di- and tri-block copolymers of poly(propylene oxide) and poly(ethylene oxide) blocks instead of D blocks<sup>53</sup>.

As discussed in Chapter 2, the assembly pH and anionic binding partner used for LbL assembly of temperature responsive D-P-D triblock copolymers are key factors that determine whether the final films are able to respond to changes in temperature with large changes in swelling degree.

While using a strong polyacid (poly(4-styrene sulfonate)) as the anionic binding partner prohibited large swelling transitions, using a weak polyacid, poly(acrylic acid) (PAA), allows for large reversible swelling transitions when deposited at pH 7 but not at pH 4. Based on those findings, in this chapter, we assemble thin films from micelle containing BCP solutions of STB, LTB, or DB with PAA at pH 7, to expose the effects of block copolymer architecture on the temperature triggered swelling responses of mPEMs. It is important to note that the PD-PP-PD triblock copolymer used for studies in Chapter 2, though of the same average composition as STB used in this work, differs in terms of polydispersity. In the previous study, the PD-PP-PD block copolymer had end blocks of broad polydispersity, while here, STB has a polydispersity of 1.5 for meaningful comparison with the other two block copolymer architectures. Since all multilayers were assembled at pH 7, the nomenclature for the mPEMs in the following discussions is simplified just to contain the component polymer pairs. The temperature dependent swelling responses of (STB/PAA), (LTB/PAA), and (DB/PAA) mPEMs of comparable thicknesses between 150 and 250 nm were investigated.

#### **4.4.3 Surface morphology of BCP micelle LbL assemblies.**

As seen from AFM images of dried micelle polyelectrolyte multilayers (mPEMs) in Figure 4-2, the multilayers made with the shorter BCPs (STB and DB) are significantly rougher than the mPEM made from the higher molecular weight LTB. The RMS roughness values obtained from the images of the (STB/PAA), (DB/PAA), (LTB/PAA) and (D/PAA) multilayers are 10 nm, 4 nm, 1 nm, and 2 nm respectively. Unlike spherical structures expected for BCP micelle containing multilayers, as previously reported by several groups,<sup>22,23,31,34</sup> we observed surface depressions (described as ‘dimples’ henceforth), that are especially well ordered in the case of (LTB/PAA).

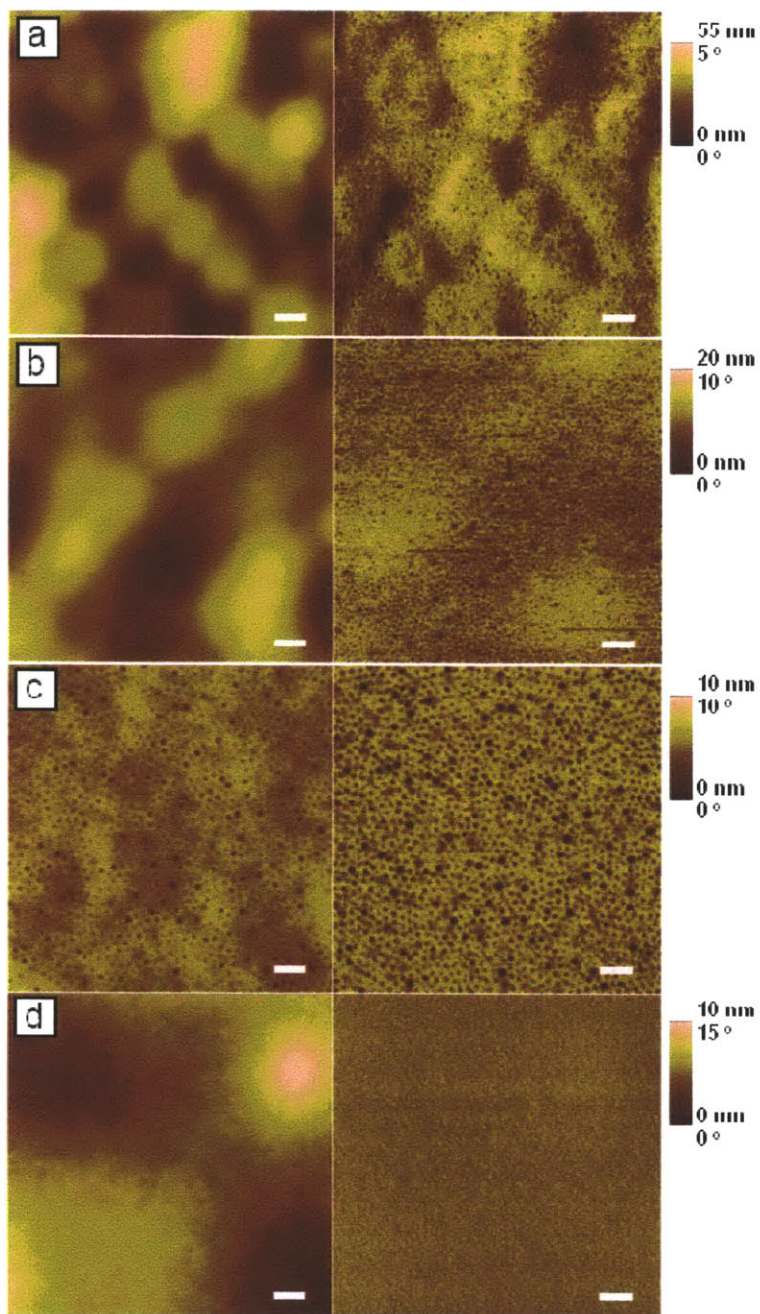


**Figure 4-2.**  $1\ \mu\text{m} \times 1\ \mu\text{m}$  atomic force microscope (AFM) images of BCP or homopolymer, poly (N,N dimethyl amino ethyl methacrylate) (D), multilayers assembled with PAA. The left column consists of height images while the right column consists of phase images. Rows a, b, c and d correspond to multilayers of  $(\text{STB}/\text{PAA})_{30}$ ,  $(\text{DB}/\text{PAA})_{35}$ ,  $(\text{LTB}/\text{PAA})_{35}$  and control  $(\text{D}/\text{PAA})_{40}$  respectively. White scale bars on images represent 100 nm, while height and phase scales are shown on the right.

The dimpled surface morphologies seen in the mPEMs are absent in the control assembly of D homopolymer with PAA assembled at the same pH of 7. Dimples seen in all mPEMs have regular lateral dimensions on the order of 10 – 30 nm and most have depths of less than 2 nm, with the exception of the more prominent dimples seen in (LTB/PAA) that have depths up to 6 nm. Since these types of surface morphologies had not been reported for BCP micelle multilayers before, we seek to clarify the origins of these surface structures, which, at a glance, resemble cavitated micelles<sup>54</sup> or toroid<sup>55,56</sup> type morphologies. To investigate this, we carried out solution crosslinking of micelles to determine what surface adsorbed BCPs would look like if surface rearrangement and micelle dissolution could be prevented through crosslinking. 1,2-bis-(2-iodoethoxy)ethane (BIEE), was used to crosslink D blocks in the micelle corona through quaternization of the tertiary amine groups. This crosslinking technique has frequently been applied to stabilize D block containing BCP micelles and several publications, particularly by the Armes group, describe this chemistry in detail<sup>40,57,58</sup>. In this work, we used the protocol of Jiang *et al.*<sup>39</sup> at room temperature to selectively crosslink the coronas of our BCPs at 0.1 mg/ml, pH 7. Crosslinking was allowed to proceed for 3 days after which the crosslinked BCP micelles were dip coated onto silicon wafers, allowed to dry and imaged with AFM in the dry state. By crosslinking the D end blocks in the corona of the micelles in solution, the spherical shape of micelles were better preserved and circular discs can be observed on the dip coated silicon wafer, as seen in Fig. 4a. Despite corona crosslinking, spreading and flattening of the crosslinked micelles on the silicon surface was observable, with the circular disc-like structures having diameters of 40 – 60 nm, several times greater than their corresponding heights of 3 – 6 nm (Fig. 4a, b and c). This indicated significant chain mobility, even within corona crosslinked micelles, that allowed for changes in micelle shape upon surface attachment. Several structures that resemble the dimpled surface structures on mPEMs were also observed, as pointed out by the arrow in Figure 4b. As shown in the line section height profile (inset of Fig. 4b), these features, unlike toroids, are not hollow in the central region, but rather, are discs with raised edges. While these structures could result from micelle cores that are not fully dehydrated, this is unlikely the case with several reports suggesting that micelle cores formed by P blocks are anhydrous and dense<sup>59-61</sup>. Without core plasticization by water molecules, significant surface rearrangement is still possible due to the low glass transition temperature ( $T_g \sim -75\text{ }^\circ\text{C}$ <sup>62,63</sup>) of the poly(propylene oxide) core. The depth profiles of dimple type structures observed in multiple images of corona

crosslinked micelles, like that in the inset of Fig. 4b, show that the central depression is typically 1 – 2 nm deep. This depth agrees well with the depths of dimples observed on the surface of the dry multilayers, showing that these structures in mPEMs originate directly from the BCP micellar self assembly in solution and not as a consequence of the LbL process with PAA. The well ordered surface patterns that can be achieved using LbL assembly of LTB micelles offers patterned surface heterogeneity on a 15 – 30 nm length scale. Ordering is less pronounced in the AFM images of the shorter (STB/PAA) and (DB/PAA) multilayers and could be related to AFM imaging resolution limitations.

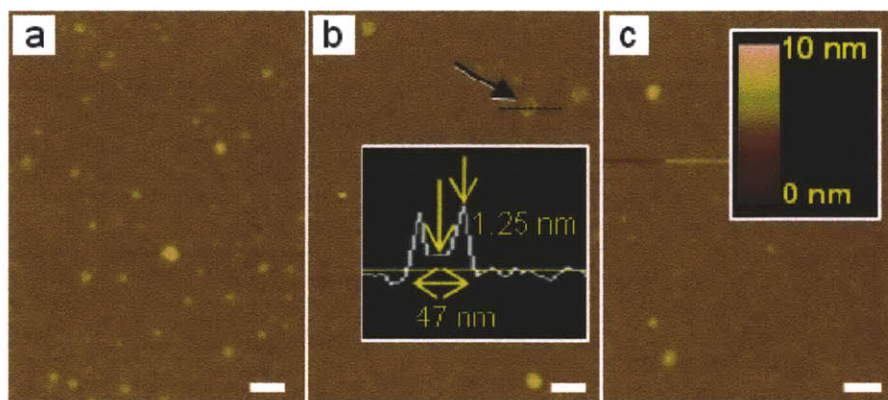


**Figure 4-3.** AFM images of BIEE shell cross-linked BCPs: STB (a), LTB (b) and DB (c), dip coated onto the surface of silicon wafers. The inset in (b) shows the height profile along the dotted line. All images have the same lateral and height scales. The height scale is shown as an inset in (c) and scale bars on the bottom right corners represent 100 nm.

#### 4.4.4 Thin film mPEM temperature swelling responses in aqueous media.

We next examined the temperature responsive swelling properties of the mPEM thin films in water. The three BCPs studied contain the same temperature responsive block, P, while differing in overall molecular weight and connectivity. At the supramolecular level (depicted in the leftmost column of Figure 4-4), the domain sizes and size distribution of the temperature responsive P micelle cores within all three BCP containing multilayers are expected to look relatively similar based on the solution, surface adsorption and dry state AFM studies described above. We expect the cross-section of the multilayer films to be comprised of P block domains of micelle cores (pink dots) surrounded (in blue) by micelle coronas of D blocks that are associated with PAA through ionic interactions between the protonated tertiary amine groups on



the D block and ionized carboxylic acid groups on PAA. In DI water at room temperature, the P blocks are poorly hydrated and preferentially self-aggregate in the micellar cores<sup>59-61</sup>. When the temperature is decreased to 6 °C, hydrogen bonding enhances water's interaction with the P blocks, causing the P block domains to swell. It is at these lower temperatures that differences in molecular connectivity between the triblock and diblock copolymers can become important, as shown schematically in the bottom row of Figure 4-4.

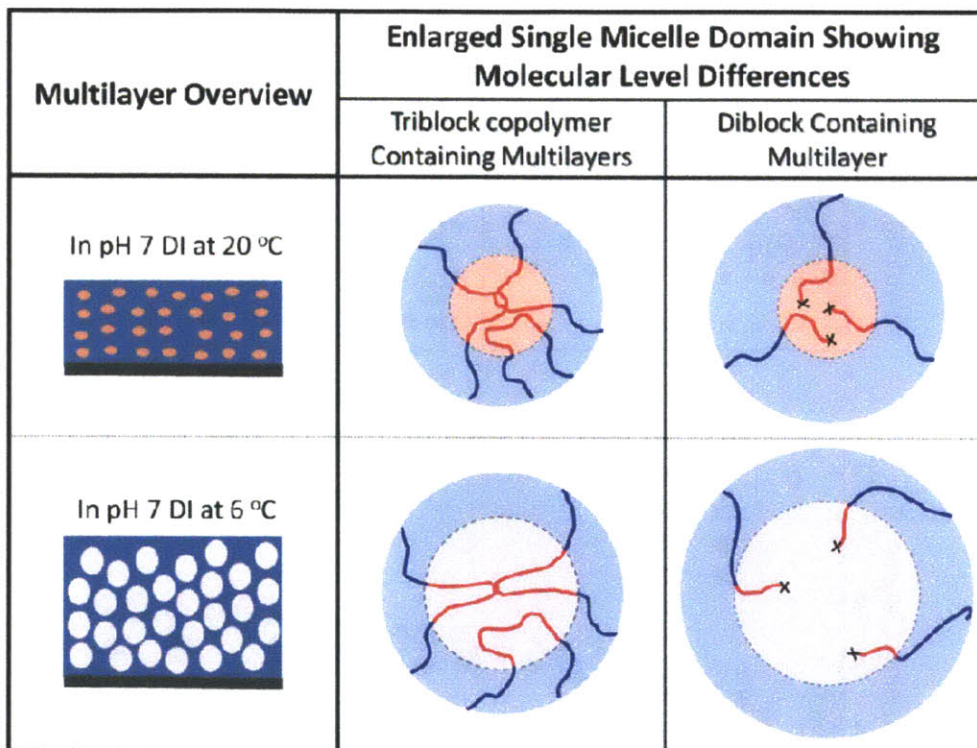


**Figure 4-4.** Drawings depicting the molecular configurations of BCPs within the mPEMs studied. The blue region surrounding the micelle cores are composed of D corona blocks ionically crosslinked to PAA chains (PAA not drawn for simplicity). The top row represents the multilayers in pH 7 DI water at 20 °C where the P domains are poorly hydrated while the bottom row represents the multilayers at 6 °C where micelle cores of all BCPs become highly swollen with water.

As seen in Chapter 2, D-P-D triblock copolymers assembled with PAA at pH 7 exhibit temperature-driven, reversible, swelling transitions<sup>30</sup>. In Chapter 2, only the instantaneous swelling response was accessible by *in situ* ellipsometric determination of wet film thickness upon addition of pre cooled aqueous solutions. With an improved set-up (details in Section 4.3),

in this chapter, we are able to investigate film swelling as a function of time while the mPEMs are immersed in pH 7 adjusted DI water at a controlled low temperature. As seen in Figure 4-5, the degree of swelling,  $\tau = \text{wet film thickness} / \text{dry film thickness}$ , shows both time and temperature dependences. Notably, the isochronous degree of swelling increases with decreasing temperature and the time dependence of swelling becomes more significant at lower temperatures.

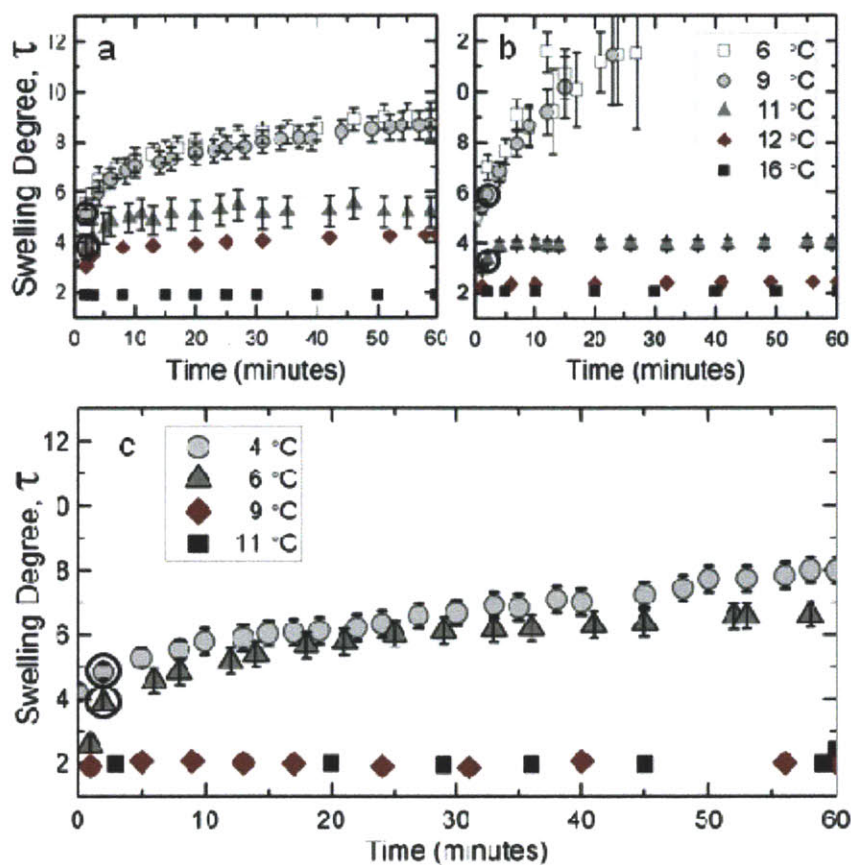


**Figure 4-5.** Graphs showing the time-dependent evolution of the swelling degree ( $\tau = \text{wet film thickness} / \text{dry film thickness}$ ) of mPEMs, (a) (STB/PAA), (b) (DB/PAA) and (c) (LTB/PAA) held at various temperatures. All films studied were of similar thicknesses between 150 and 250 nm. The swelling degrees at 2 minutes of low temperature exposure are circled as they correspond to points subsequently discussed in Figure 4-7.

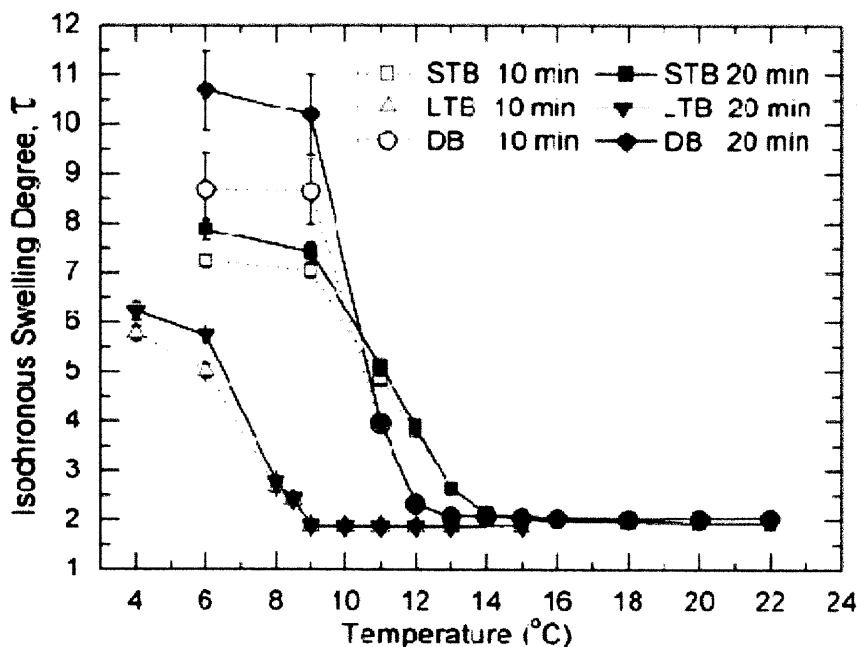


**Figure 4-6.** Isochronous swelling degree,  $\tau = \text{wet thickness} / \text{dry thickness}$ , of mPEM films held at various temperatures for 10 min (hollow symbols with dotted lines) or 20 min (solid symbols and lines). Legend indicates the BCP component of the mPEMs for convenient identification of curves.

As seen in Fig. 4-5, increased swelling with low temperature exposure, if any, is measurable within 2 min. To determine the mPEM film swelling transition temperature ( $T_{\text{stt}}$ ), below which increased film swelling occurs, isochronous values of  $\tau$  at 10 min and 20 min are plotted as a function of temperature in Figure 4-6. The curves show distinct swelling transitions near 13.5 °C, 12 °C and 8.5 °C for the STB, DB and LTB containing mPEMs respectively. At small degrees of undercooling, equilibrium can be established where the mixing and elastic contributions to free energy balance out and steady state swelling can be achieved (as seen in Fig. 4-5a at 11 and 12 °C, Fig. 4-5b at 11 °C, and Fig. 4-5c at 6 °C). With greater undercooling, the increasingly favored solvent-polymer interactions result in swelling forces strong enough to cause creep type behavior where the degree of swelling increases with time as seen at lower temperatures in Fig. 4-5. The transition between time-independent and time-dependent swelling is clear in Fig. 4-6 where the 10 min and 20 min curves deviate at a certain degree of cooling below  $T_{\text{stt}}$ . It is in this low temperature, time-dependent swelling regime that differences between the triblock and diblock

containing films become significant. Comparing the dynamic swelling curves in the low temperature range in Fig 4-5, we see that while (DB/PAA) quickly swells to failure at 9 °C, both (STB/PAA) and (LTB/PAA) are able to sustain stable  $\tau$  values in the range of 4 to 10. Deswelling and drying of the triblock based mPEMs from any of the points in Fig. 4-5 revealed no film loss, whereas diblock containing films swollen at 6 or 9 °C showed significant (60-80%) film loss when exposed to these temperatures for more than 30 min (AFM and optical images of disintegrating (DB/PAA 7.0) multilayers held at cold temperature for 30 min are shown in Appendix B, Fig. B-12). As illustrated in Figure 4-4, the mPEMs that contain triblock copolymers, (STB/PAA) and (LTB/PAA), have connectivity in the P domains, in turn covalently linked to D blocks in the ionically stabilized network. This topological connectivity in the triblocks leads to equilibrium load-bearing trapped entanglements that are not present in the diblock system. Consequently, the diblock-containing mPEMs show the largest propensity to disintegrate at low temperatures whereas the triblock-containing systems show greater ability to sustain controlled swelling and exhibit a greater range of reversible swelling phenomena.

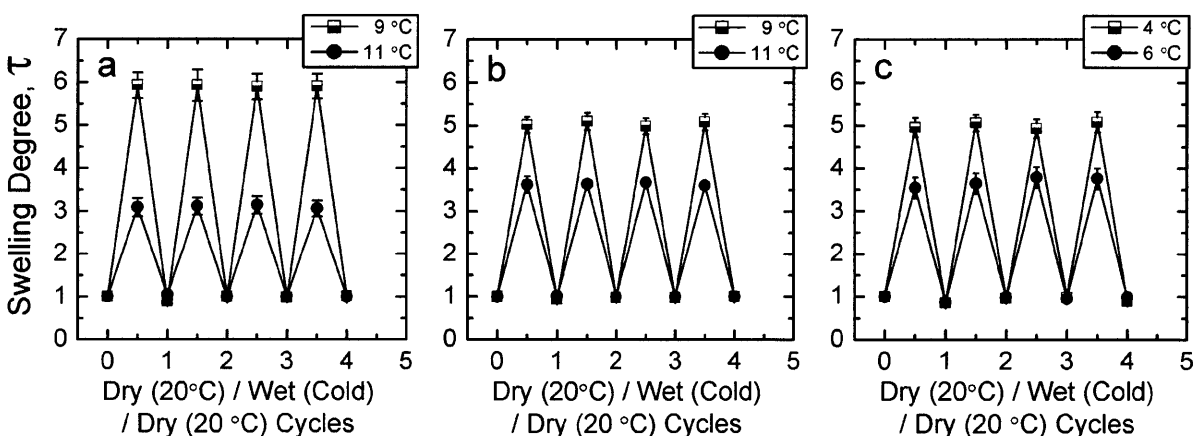


**Figure 4-7.** Changes in swelling degree,  $\tau$ , of mPEMs: (a) (DB/PAA), (b) (STB/PAA) and (c) (LTB/PAA), upon cycling between the dry state at room temperature (20 °C), wet state in cold DI water adjusted to pH 7 at 2 min immersion times, and de-swollen and dried at (20 °C).

Despite the time-dependent creep observed during extended low temperature exposure, Figure 4-7 shows that the short-time swelling response (points circled in Fig. 4-5) is reproducible and essentially fully reversible for all the BCP systems studied; no film lost or history dependence of this short time response was detected with repeated swelling and deswelling cycles. AFM images

of dry film morphology after 7 swelling and deswelling cycles are shown in Figure 4-8 and reveal negligible change in surface morphology compared to the pre swelling images in Fig. 4-2. The degree of swelling recorded at 2 minutes of low temperature exposure increased with the degree of undercooling,  $\Delta T = T - T_{\text{stt}}$ . Figure 4-7 shows the reversible short time swelling response at  $\Delta T = 4$  or  $6$  °C. These undercooling values correspond to temperatures of  $\sim 11$  and  $9$  °C for the STB and DB multilayers and  $6$  or  $4$  °C for the LTB multilayer. The degree of swelling,  $\tau$ , being a function of temperature and swelling time, is denoted as  $\tau_x(\Delta T, t)$ , where  $x$  is the BCP component present in the film under consideration,  $\Delta T$  is the undercooling, °C, and  $t$  is the swelling time, minutes. From Fig. 4-7, we see that the short time swelling response of the triblock copolymers with different molecular weights but the same P:D ratios is similar with  $\tau_{\text{STB}}(4, 2) \approx \tau_{\text{LTB}}(4, 2) \approx 3.6$  and  $\tau_{\text{STB}}(6, 2) \approx \tau_{\text{LTB}}(6, 2) \approx 5$ . In this respect, the overall triblock molecular weight did not affect the reversible behavior. On the other hand, short time response of the diblock-containing mPEM films (Fig. 8a) show marked differences from their triblock counterparts (Figs. 8b and 8c). The diblock films swell to lower extents than the triblock containing films at  $\Delta T = 4$  °C and to greater extents at  $\Delta T = 6$  °C. The lower degree of swelling at  $\Delta T = 4$  °C could reflect the lower P:D ratio of DB while the higher degree of swelling at  $\Delta T = 6$  °C is likely the effect of connectivity differences discussed above.

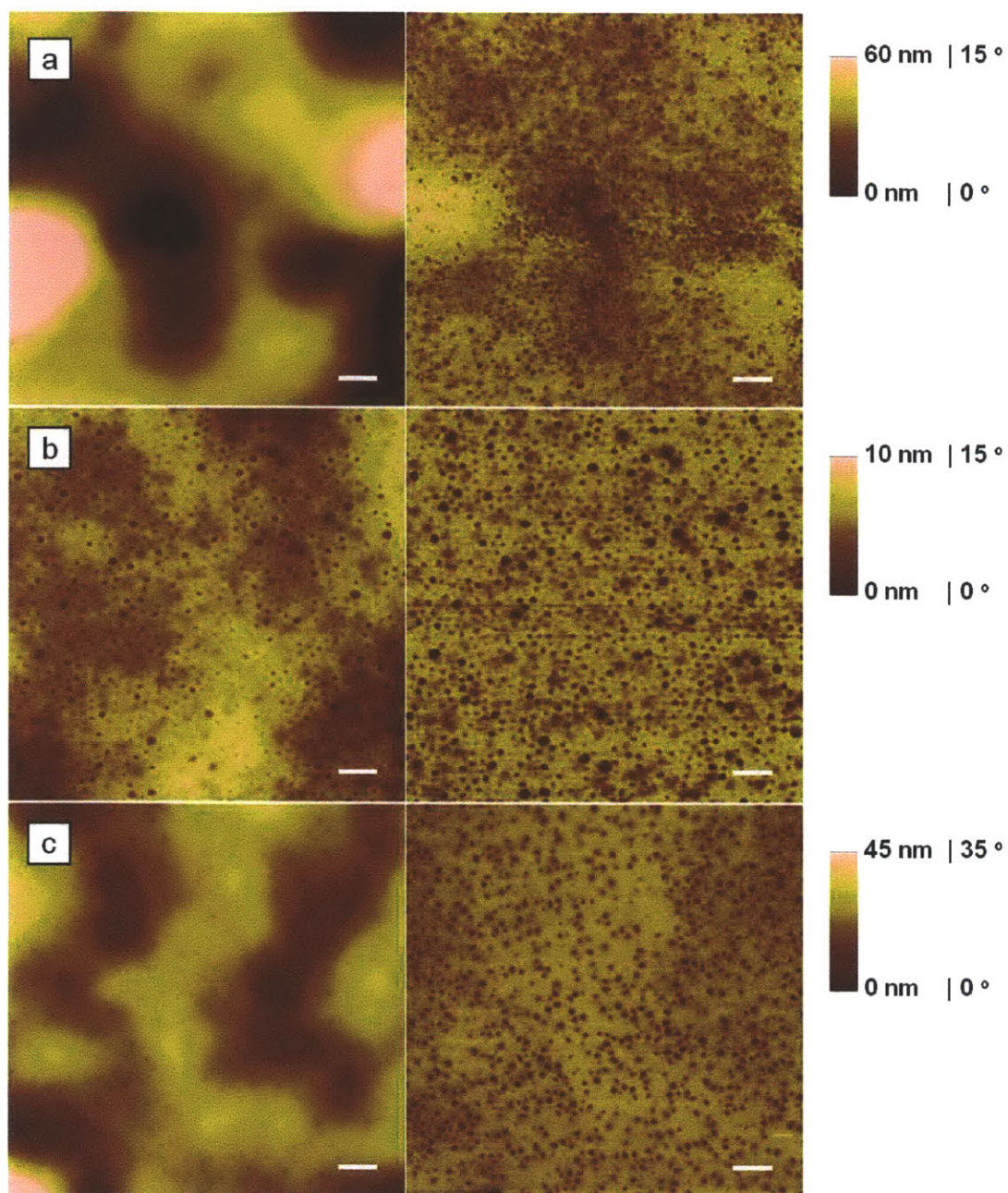


**Figure 4-8.**  $1\ \mu\text{m} \times 1\ \mu\text{m}$  atomic force microscope (AFM) images of dried mPEM multilayers after 7 cycles of swelling (at  $\Delta T = 6\ ^\circ\text{C}$ ) and deswelling (at  $20\ ^\circ\text{C}$ ) in pH 7 DI water. The left column consists of height images while the right column consists of phase images. Rows a, b, and c correspond to multilayers of  $(\text{STB}/\text{PAA})_{30}$  (swollen at  $9\ ^\circ\text{C}$ ),  $(\text{DB}/\text{PAA})_{35}$  (swollen at  $9\ ^\circ\text{C}$ ) and  $(\text{LTB}/\text{PAA})_{35}$  (swollen at  $4\ ^\circ\text{C}$ ) respectively. White scale bars on images represent 100 nm, while height and phase scales are shown on the right.

## 4.5 Conclusions

In this Chapter, we exposed the effects of BCP architecture on the properties of temperature responsive mPEM thin films created by LbL assembly. We found that both the solution micellization temperature (MT) and film swelling transition temperature ( $T_{st}$ ) depend on P block length. Importantly, our results reveal that while all three BCPs can be used to create temperature responsive films, the range of reversible swelling that is accessible depends critically on BCP connectivity. While the diblock containing films quickly swell to the point of failure at  $\Delta T = 6$  or more, the triblock copolymer containing multilayers, both (STB/PAA) and (LTB/PAA) are able to sustain significantly lower rates of creep and sustained swollen states with prolonged low temperature exposure. The differences in dynamic swelling responses uncovered in this study have significant implications in the application of these temperature-swellaible films. Where they might be suited for applications that require repeated rapid and transient low temperature exposure, the diblock copolymer containing films cannot be exposed to low temperature for long. That being said, the disintegration of the diblock copolymer containing film at low temperatures could make it useful as a low temperature release system. Extrapolating from the understanding gained in this chapter, star block copolymers with covalently connected temperature responsive core blocks and polyelectrolyte end blocks might represent the ideal architecture for creating of creep resistant temperature-swellaible multilayers.

## Acknowledgements

This work was supported by the MRSEC Program of the National Science Foundation under award number DMR – 0819762 and in part by NSF DMR-0906474 (S. Sukhishvili). We thank the Center for Materials Science and Engineering (CMSE), the Institute for Soldier Nanotechnologies (ISN) and Prof. T. Alan Hatton for use of their characterization facilities.

## References

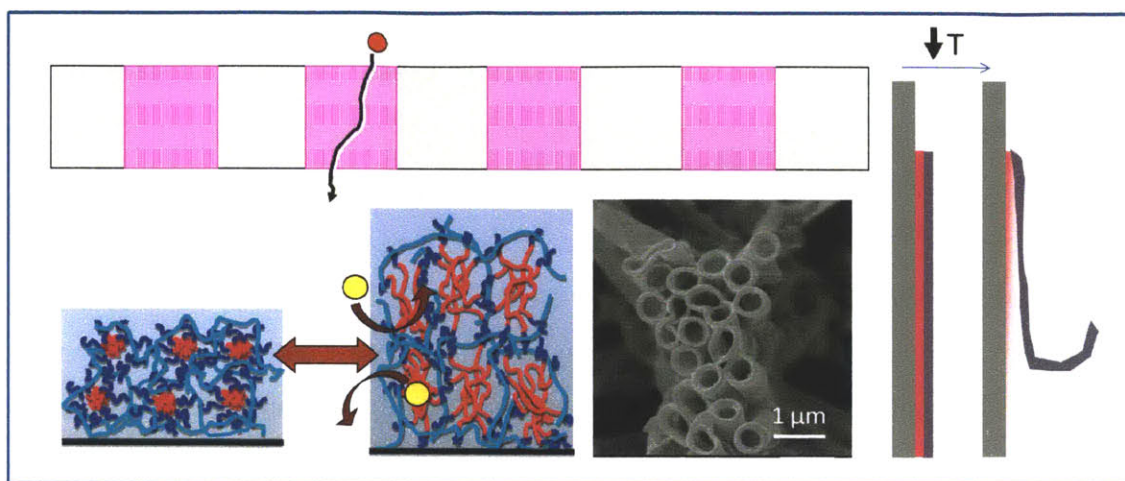
- (1) Westman, L.; Lindström, T. *Journal of Applied Polymer Science* **1981**, *26*, 2533.
- (2) Skouri, R.; Schosseler, F.; Munch, J. P.; Candau, S. J. *Macromolecules* **1995**, *28*, 197.
- (3) Raj Singh, T. R.; Woolfson, A. D.; Donnelly, R. F. *Journal of Pharmacy and Pharmacology* **2010**, *62*, 829.
- (4) Kanazawa, H. *Journal of Separation Science* **2007**, *30*, 1646.
- (5) Nagase, K.; Kobayashi, J.; Kikuchi, A.; Akiyama, Y.; Kanazawa, H.; Okano, T. *Biomaterials* **2011**, *32*, 619.
- (6) Peppas, N. A.; Khare, A. R. *Advanced Drug Delivery Reviews*, *11*, 1.
- (7) Dadsetan, M.; Liu, Z.; Pumberger, M.; Giraldo, C. V.; Ruesink, T.; Lu, L.; Yaszemski, M. J. *Biomaterials* **2010**, *31*, 8051.
- (8) Dong, L.; Jiang, H. *Soft Matter* **2007**, *3*, 1223.
- (9) Gerlach, G.; Guenther, M.; Sorber, J.; Suchanek, G.; Arndt, K.-F.; Richter, A. *Sensors and Actuators B: Chemical* **2005**, *111-112*, 555.
- (10) Discher, D. E.; Janmey, P.; Wang, Y.-I. *Science* **2005**, *310*, 1139.
- (11) Wong, J. Y.; Velasco, A.; Rajagopalan, P.; Pham, Q. *Langmuir* **2003**, *19*, 1908.
- (12) Lichter, J. A.; Thompson, M. T.; Delgadillo, M.; Nishikawa, T.; Rubner, M. F.; Van Vliet, K. J. *Biomacromolecules* **2008**, *9*, 1571.
- (13) Itano, K.; Choi, J.; Rubner, M. F. *Macromolecules* **2005**, *38*, 3450.
- (14) Hiller, J. A.; Rubner, M. F. *Macromolecules* **2003**, *36*, 4078.
- (15) Déjugnat, C.; Sukhorukov, G. B. *Langmuir* **2004**, *20*, 7265.
- (16) Kozlovskaya, V.; Kharlampieva, E.; Mansfield, M. L.; Sukhishvili, S. A. *Chemistry of Materials* **2005**, *18*, 328.
- (17) Lee, D.; Nolte, A. J.; Kunz, A. L.; Rubner, M. F.; Cohen, R. E. *Journal of the American Chemical Society* **2006**, *128*, 8521.
- (18) Kim, B.-S.; Lee, H.-i.; Min, Y.; Poon, Z.; Hammond, P. T. *Chemical Communications* **2009**, 4194.
- (19) Kharlampieva, E.; Kozlovskaya, V.; Tyutina, J.; Sukhishvili, S. A. *Macromolecules* **2005**, *38*, 10523.
- (20) Glinel, K.; Déjugnat, C.; Prevot, M.; Schöler, B.; Schönhoff, M.; Klitzing, R. v. *Colloids and Surfaces A: Physicochemical and Engineering Aspects* **2007**, *303*, 3.
- (21) Quinn, J. F.; Caruso, F. *Langmuir* **2003**, *20*, 20.
- (22) Zhu, Z.; Sukhishvili, S. A. *ACS Nano* **2009**, *3*, 3595.
- (23) Xu, L.; Zhu, Z.; Sukhishvili, S. A. *Langmuir* **2010**, *27*, 409.
- (24) Nolan, C. M.; Serpe, M. J.; Lyon, L. A. *Biomacromolecules* **2004**, *5*, 1940.
- (25) Zhuk, A.; Pavlkhina, S.; Sukhishvili, S. A. *Langmuir* **2009**, *25*, 14025.
- (26) Gui, Z.; Qian, J.; Zhao, Q.; Ji, Y.; Liu, Y.; Liu, T.; An, Q. *Colloids and Surfaces A: Physicochemical and Engineering Aspects* **2011**, *380*, 270.
- (27) Steitz, R.; Leiner, V.; Tauer, K.; Khrenov, V.; v. Klitzing, R. *Applied Physics A: Materials Science & Processing* **2002**, *74*, s519.



- (28) Glinel, K.; Sukhorukov, G. B.; Möhwald, H.; Khrenov, V.; Tauer, K. *Macromolecular Chemistry and Physics* **2003**, *204*, 1784.
- (29) Jaber, J. A.; Schlenoff, J. B. *Macromolecules* **2005**, *38*, 1300.
- (30) Tan, W. S.; Cohen, R. E.; Rubner, M. F.; Sukhishvili, S. A. *Macromolecules* **2010**, *43*, 1950.
- (31) Cho, J.; Hong, J.; Char, K.; Caruso, F. *Journal of the American Chemical Society* **2006**, *128*, 9935.
- (32) Hong, J.; Bae, W. K.; Lee, H.; Oh, S.; Char, K.; Caruso, F.; Cho, J. *Advanced Materials* **2007**, *19*, 4364.
- (33) Qi, B.; Tong, X.; Zhao, Y. *Macromolecules* **2006**, *39*, 5714.
- (34) Ma, N.; Wang, Y.; Wang, Z.; Zhang, X. *Langmuir* **2006**, *22*, 3906.
- (35) Addison, T.; Cayre, O. J.; Biggs, S.; Armes, S. P.; York, D. *Langmuir* **2008**, *24*, 13328.
- (36) Kim, B.-S.; Park, S. W.; Hammond, P. T. *ACS Nano* **2008**, *2*, 386.
- (37) Nguyen, P. M.; Zacharia, N. S.; Verploegen, E.; Hammond, P. T. *Chemistry of Materials* **2007**, *19*, 5524.
- (38) Lin, J.; Zhu, J.; Chen, T.; Lin, S.; Cai, C.; Zhang, L.; Zhuang, Y.; Wang, X.-S. *Biomaterials* **2009**, *30*, 108.
- (39) Jiang, X.; Ge, Z.; Xu, J.; Liu, H.; Liu, S. *Biomacromolecules* **2007**, *8*, 3184.
- (40) Li, Y.; Du, J.; Armes, S. P. *Macromolecular Rapid Communications* **2009**, *30*, 464.
- (41) Vamvakaki, M.; Palioura, D.; Spyros, A.; Armes, S. P.; Anastasiadis, S. H. *Macromolecules* **2006**, *39*, 5106.
- (42) Liu, S.; Billingham, N. C.; Armes, S. P. *Angewandte Chemie International Edition* **2001**, *40*, 2328.
- (43) Schurr, J. M.; Schmitz, K. S. *Annual Review of Physical Chemistry* **1986**, *37*, 271.
- (44) Fundin, J.; Brown, W.; Iliopoulos, I.; Claesson, P. M. *Colloid & Polymer Science* **1999**, *277*, 25.
- (45) Nagarajan, R.; Ganesh, K. *Macromolecules* **1989**, *22*, 4312.
- (46) Zhulina, E. B.; Borisov, O. V. *Macromolecules* **2002**, *35*, 9191.
- (47) Shusharina, N. P.; Linse, P.; Khokhlov, A. R. *Macromolecules* **2000**, *33*, 8488.
- (48) Butun, V.; C. Billingham, N.; P. Armes, S. *Chemical Communications* **1997**, 671.
- (49) Muller, F.; Guenoun, P.; Delsanti, M.; Demé, B.; Auvray, L.; Yang, J.; Mays, J. W. *The European Physical Journal E: Soft Matter and Biological Physics* **2004**, *15*, 465.
- (50) Lee, A. S.; Gast, A. P.; Bütün, V.; Armes, S. P. *Macromolecules* **1999**, *32*, 4302.
- (51) Lee, A. S.; Bütün, V.; Vamvakaki, M.; Armes, S. P.; Pople, J. A.; Gast, A. P. *Macromolecules* **2002**, *35*, 8540.
- (52) Xu, L.; Zhu, Z.; Borisov, O. V.; Zhulina, E. B.; Sukhishvili, S. A. *Physical Review Letters* **2009**, *103*, 118301.
- (53) Alexandridis, P.; Holzwarth, J. F.; Hatton, T. A. *Macromolecules* **1994**, *27*, 2414.
- (54) Boontongkong, Y.; Cohen, R. E. *Macromolecules* **2002**, *35*, 3647.
- (55) O'Driscoll, S. M.; O'Mahony, C. T.; Farrell, R. A.; Fitzgerald, T. G.; Holmes, J. D.; Morris, M. A. *Chemical Physics Letters* **2009**, *476*, 65.
- (56) Huang, H.; Chung, B.; Jung, J.; Park, H.-W.; Chang, T. *Angewandte Chemie International Edition* **2009**, *48*, 4594.

- (57) Bütün, V.; Lowe, A. B.; Billingham, N. C.; Armes, S. P. *Journal of the American Chemical Society* **1999**, *121*, 4288.
- (58) Liu, S.; Weaver, J. V. M.; Tang, Y.; Billingham, N. C.; Armes, S. P.; Tribe, K. *Macromolecules* **2002**, *35*, 6121.
- (59) Alexandridis, P.; Nivaggioli, T.; Hatton, T. A. *Langmuir* **1995**, *11*, 1468.
- (60) Guo, C.; Liu, H. Z.; Chen, J. Y. *Colloid & Polymer Science* **1999**, *277*, 376.
- (61) Cau, F.; Lacelle, S. *Macromolecules* **1996**, *29*, 170.
- (62) Johari, G. P. *Polymer* **1986**, *27*, 866.
- (63) Allen, G.; Booth, C.; Jones, M. N.; Marks, D. J.; Taylor, W. D. *Polymer* **1964**, *5*, 547.

# CHAPTER 5: APPLICATIONS AND FUTURE PERSPECTIVES FOR TEMPERATURE RESPONSIVE MICELLE MULTILAYER COATINGS



## 5.1 Abstract

This chapter explores some functional aspects of temperature responsive, micelle containing thin film hydrogel coatings created by LbL assembly. We first demonstrate that conformal coatings of the temperature responsive multilayers developed in this thesis can be used to gate membranes pores and allow temperature control of fluid flux through modified track etched polycarbonate membranes. Separately, we show that the LbL method of creating temperature responsive hydrogel coatings is amenable to sacrificial template-based creation of hollow nanotubes that present freestanding nano-structured elements. In addition, application of reversibly swellable hydrogel coatings for the entrapment and controlled release of proteins is investigated. Our results suggest that these temperature-responsive micelle multilayers, able to swell reversibly by large amounts, hold immense potential in the field of protein delivery. On a related note, the pH, salt concentration and temperature dependent stability of various temperature-responsive block copolymer multilayer systems is studied in detail. Through the choice of block copolymer architecture and anionic binding partner, these temperature responsive weak polyelectrolyte systems are shown to offer unique opportunities for customized dissolution. This makes them interesting as triggered surface release systems.

## 5.2 Introduction

As outlined in Chapter 1, Section 1.2.3, temperature responsive hydrogels are highly sought after because temperature can trigger and control their degree of swelling, along with other useful changes in material properties (ref. to Fig. 1-2). Chapter 2 demonstrated how Layer-by-Layer (LbL) assembly can be used as a facile means to create thin film temperature responsive coatings while Chapter 4, revealed how block copolymer architectural design influences the functionality of the responsive hydrogels. Armed with this knowledge, in this chapter, we seek to exploit the unique possibilities (summarized in Chapter 1, Section 1.5) offered by using LbL assembly to create thin film responsive hydrogels. Namely, the ability to create conformal coatings within confined geometries<sup>1-5</sup> is harnessed to modify the walls of membrane pores. In doing so, temperature induced swelling transitions of the pore coatings can be utilized to control the size of the membrane pore openings and function as a temperature controlled membrane gating mechanism<sup>4,6-8</sup>. In addition, the ability to create hydrogel coatings on uniquely shaped sacrificial templates<sup>9-11</sup> is used to create free standing entities composed of thin hydrogel walls left behind upon template removal. Where the creation of pH responsive freestanding nanotube forests<sup>12</sup> has been demonstrated, here, we attempt to create nanotube forests out of temperature responsive material. The unique structure of nanotube forests or capsule versions of temperature responsive hydrogel thin films can open up new possibilities for customized application of these materials<sup>9,13</sup>.

A significant market for responsive hydrogel materials is in the area of controlled delivery<sup>14</sup> (refer to Chapter 1, Section 1.2.3). The tunable porosity in hydrogels allows loading of drugs into the gel matrix and their subsequent release at rates dependent on the diffusion coefficient of the drug in the gel matrix<sup>15,16</sup>. Owing to the high water content of hydrogels, they have excellent biocompatibility<sup>17</sup> as reflected by their successful use in the peritoneum<sup>18</sup> and other *in vivo* sites. Furthermore, hydrogels are relatively compliant materials that can conform to the shape of sites to which they are applied<sup>17</sup>, allowing for good physical contact with the surrounding tissue. The benefits of hydrogels for drug delivery are largely pharmacokinetic<sup>16</sup>. Hydrogels loaded with drugs serve as a physically localized reservoir from which drugs slowly elute, allowing the maintenance of a high local concentration of drugs in the tissues surrounding the gel, over an extended period<sup>15,16</sup>. Specifically, changes in ‘mesh size’ of our temperature responsive

multilayers via the opening and closing of micelle core domains offer opportunities for rapid absorption (at low temperature), trapping of protein therapeutics (at room temperature) and subsequent slow release (at body temperature). Such a trapping mechanism<sup>14,19</sup> is particularly useful for protein therapeutics because proteins are very sensitive to changes in solvent polarity<sup>20</sup>, pH<sup>21</sup> and higher temperatures, above body temperature<sup>22,23</sup>. When exposed to the wrong solution conditions, proteins denature and can easily lose their bioactivity and therapeutic function. As a result, typical polymer drug delivery encapsulation methods that involve dispersion in organic solvents<sup>20</sup> and co-precipitation<sup>24</sup> applicable for small organic drug molecules often cannot be applied to protein therapeutics. Loading and encapsulation of proteins into hydrogel type matrices from all aqueous, buffered conditions is thus of great interest in the field<sup>25,26</sup>. The benign, all aqueous LbL assembly technique of hydrogel creation coupled with post-assembly protein loading also presents a great advantage over in-situ polymerization or cross-linking methods of hydrogel formation which require careful and thorough removal of toxic reagents. This is often difficult as leaching of loaded drugs out of the hydrogel needs to be prevented at the same time<sup>16</sup>. Further, while typical non-responsive hydrogels are highly hydrated in physiological environments and unable to offer slow and sustained rates of release<sup>27</sup>, our temperature responsive system offers opportunities for high loading capability and sustained release rates. This is likely a unique benefit of the nanocomposite chemical nature of the micelle multilayer system (as depicted in Section 5.4.3, Fig. 5-10).

Finally, as alluded to in Chapter 4, temperature triggered disintegration of block copolymer multilayers under certain conditions could make them useful as release layers for the creation of polyelectrolyte patches<sup>28</sup>, free standing films<sup>29-32</sup>, cell sheet engineering<sup>33,34</sup> as well as for triggered burst release<sup>35</sup>. Multilayer systems composed of various block copolymer architectures and assembled in a variety of conditions are studied to develop a deeper understanding of how these controllable parameters can tune final film stability. The temperature responsive thin films studied in Section 5.4.4 of this chapter exhibit a wide range of accessible disintegration behavior sensitive to the specific environmental combination of pH, salt and temperature conditions. The results reveal a high level of customizability and the possibility of tuning the dissolution to suit a wide range of specific release applications.

### 5.3 Materials and methods

**Materials.** Poly(acrylic acid) (PAA) (Mw 90 000, 25% aqueous solution) (Polysciences); Poly(N,N-dimethylaminoethyl methacrylate)-b-poly(propylene oxide)-b-poly(N,Ndimethylaminoethyl methacrylate) (STB) (Mw ca. 1600-3000-1600, PI=1.5) (Polymer Source), DB and LTB are used as synthesized in Chapter 3. All commercial polyelectrolytes were used as received without further purification. PAA was prepared as  $10^{-2}$  M solutions (based on the repeat-unit molecular weight), and PD-PP-PD was prepared as 0.1 mg/mL solution, all in ultrapure  $18\text{ M}\Omega\cdot\text{cm}$  deionized water (Millipore Milli-Q). The templates used during PEM assembly were track-etched polycarbonate (TEPC) membranes (Whatman) which have a thickness of ca.  $10\text{ }\mu\text{m}$  and a variety of pore sizes (membranes with cylindrical pores of diameter 200 nm, 800 nm, or  $3\text{ }\mu\text{m}$  were used). Dichloromethane used was from Sigma-Aldrich.

**Coating of TEPC membranes.** Membranes were modified by carrying out LbL assembly of PD-PP-PD or LTB with PAA on TEPC membranes as described in Chapters 2 and 4. The only difference being the use of membranes in place of silicon wafers as substrates.

**Water flux measurements.** The water flux through membranes (before and after coating) was studied using a Amicon stirred dead end filtration cell (Model 8010 Cat. No. 5121) sold by Millipore in a set-up illustrated in Figure 5-M1. For  $0\text{ }^{\circ}\text{C}$  measurements, the dead end filtration cell was immersed in an ice bath.

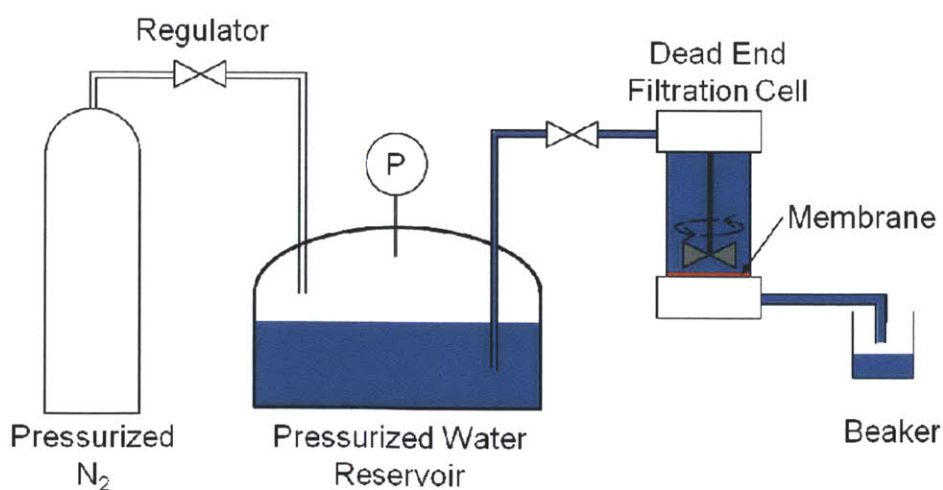


**Figure 5-M1.** Schematic of set-up used to measure water flux through membranes.

**Nanotube array synthesis and characterization\***. The overall nanotube synthesis scheme is summarized in Figure 5-M2: (i) use of track-etched polycarbonate (TEPC) membranes with commercially available variations in pore size and spacing and (ii) LbL assembly on the TEPC membrane. Conformal coatings are deposited both on outer flat surfaces and within the pores as illustrated in (iii). LbL assembly was done as described in Chapters 2 and 4. In step (iv), the coated membranes in (iii) are attached to a substrate (amine-treated glass slide or silicon wafer) by wetting the TEPC membrane with DI water, placing it on the substrate (which has positive residual surface charges), followed by heating in an oven at 60 °C for 15 min. In step (v), the unattached top surface of the coated membrane is plasma etched (Harrick Scientific Plasma Cleaner) to selectively remove the flat film deposited on the outer membrane surface. Optimal etching conditions for the plasma etching involved exposure to oxygen at 100 mTorr for 10 min. Finally the TEPC membrane template is removed by dissolution in dichloromethane (DCM) in step (vi). To do this, the entire sample is sequentially immersed into four fresh DCM solutions for 20, 2, 2, and 1 min.

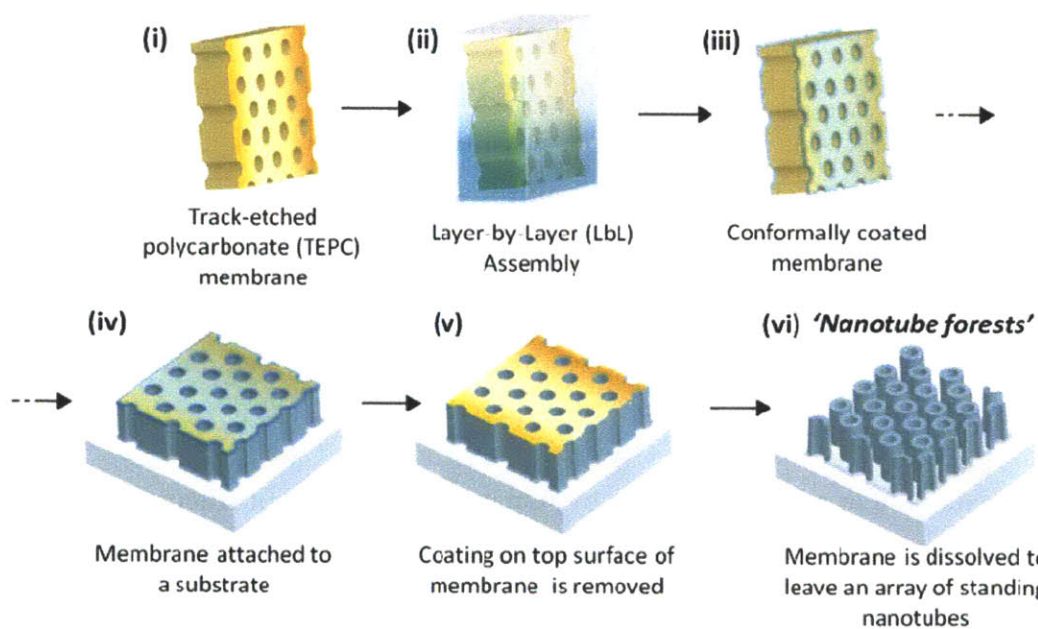


**Figure 5-M2.** Schematic of the steps used to create surface-bound nanotube arrays. An idealized, periodic spatial arrangement of pores and tubes are shown for illustration purposes. *Schematic is adapted with permission from the thesis of Gary Khek-Khiang Chia.*

\* Work on nanotubes arrays was done in collaboration with Gary Chia. Gary provided invaluable advice and support that enabled the creation of freestanding nanotubes seen in Section 5.4.2.

**Scanning electron microscope (SEM) imaging.** SEM images of samples sputter coated with ~1-2 nm of Au-Pd were taken using a JEOL JSM-6060 microscope operated at 5kV. The only exception is the high resolution SEM images of dry nanotube forests shown in Figure 5-9, that were imaged by Gary Chia using a JEOL 6320 HR-SEM.

**Protein loading.** To load protein into the (LTB/PAA 7.0) films<sup>†</sup>, 500  $\mu$ L of 2 mg/mL protein (FTIC-BSA) in 0.01 M, pH 7.4 phosphate buffer solution (PBS) was dispensed onto the surface of the (LTB/PAA 7.0) thin film such that the film is submerged. Since LbL assembly results in conformal coating of both the shiny and matte surfaces of the silicon wafer, the coating on the matte side of the silicon wafer was removed by wiping carefully with 1 M HCl using wet Kimwipes. This ensured that protein loading and release occurred only from one layer of the thin film coating. Protein loading described above was carried out on ~1 cm  $\times$  1 cm pieces of the top coated silicon wafers in the wells of a 12-well cell culture plate. The thin films covered by the protein solution were then enclosed in the 12-well plates and covered with parafilm (to prevent evaporation) and aluminium foil (to prevent photobleaching of fluorescein). The 12-well plates were then transferred to a fridge at 6  $^{\circ}$ C or left in the dark at room temperature (~24  $^{\circ}$ C) for 35 min to load the proteins. At the end of 35 min, the films were rinsed 5 times in 8 mL of 0.01 M PBS with drying in between the 3<sup>rd</sup>, 4<sup>th</sup> and 5<sup>th</sup> rinse. Each rinse was done quickly where the samples are dipped and shaken in 8 ml of fresh PBS solution for ~ 10 sec. The last rinse solution was checked for fluorescence. By the fifth rinse, the level of fluorescence was usually not detectable. Occasionally the rinse steps needed to be repeated such that no fluorescence was detectable in the rinse solution after the 30 sec rinse. These samples were then dried before use in the release studies.

**Protein release.** Protein release was done by immersing the pieces of silicon wafer carrying the protein loaded thin films into 8 mL of 0.01 M, pH 7.4 PBS solution in 50 mL centrifuge tubes, incubated at 37  $^{\circ}$ C. (Solutions were equilibrated at 37  $^{\circ}$ C before addition of the samples.) 3 aliquots of 100  $\mu$ L were removed (without replacement) at various time points for triplicate fluorescence determination of protein concentration. To ensure infinite sink conditions, the volume of solution was chosen such that at the end of experiments, the protein concentration was still less than 0.25 $\times$  the solubility limit of FITC-BSA. The total amount of protein released at

---

<sup>†</sup> (LTB/PAA 7.0)<sub>35</sub> multilayers of ~150 nm thick were used for these experiments.



each time point was calculated from the volume and concentration of the protein determined by fluorescence at that particular time point and addition of the summed amount of proteins removed (in the 300  $\mu\text{L}$  aliquots) at all prior time points. Control experiments were done with no sample, and a blank single side coated silicon wafer with no protein loaded. All samples were kept in the dark throughout the experiments.

**Fluorescence determination of protein concentration.** Protein concentrations of the solutions were determined using a Molecular Devices Spectramax M2<sup>e</sup> fluorescence plate reader with an excitation and emission wavelength of 485 and 535 nm, respectively. Fluorescence was converted to protein mass concentration using standard curves prepared from PBS solutions containing FITC- BSA in known serial dilutions; the fluorescence intensity was linear with respect to protein concentration from 0.05  $\mu\text{g}/\text{mL}$  to 10  $\mu\text{g}/\text{mL}$ .

## 5.4 Results and Discussion

### 5.4.1 Temperature Gating of TEPC Membranes.

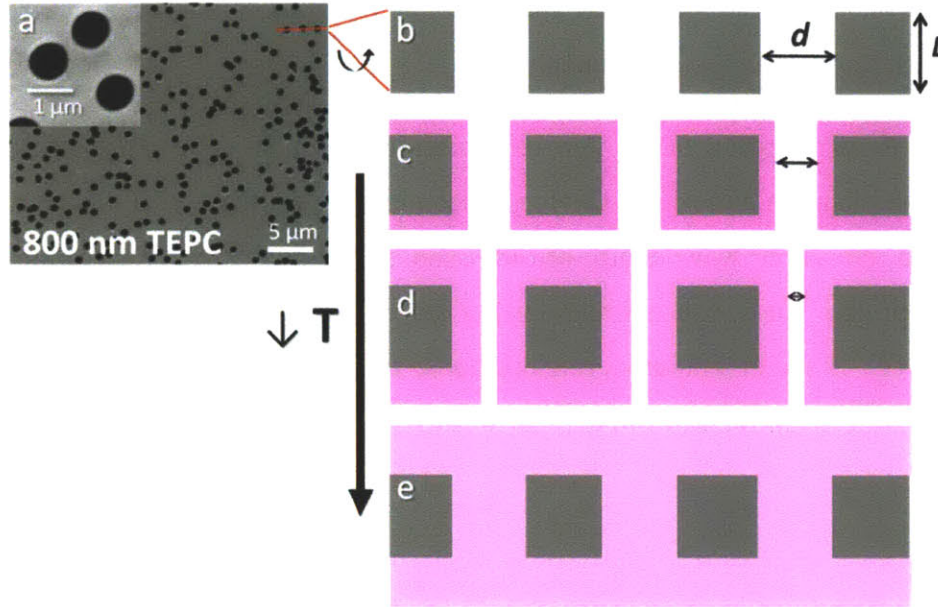


**Figure 5-1.** Scanning electron microscope (SEM) image of the top down overview of a typical track etched polycarbonate (TEPC) membrane (a). This membrane has 800 nm diameter pores and the inset in (a) shows a magnified view of three pores. (b) is a drawing that depicts the cross-sectional view through 3 pores (representing a cut through the red line drawn in (a)). The dimensional parameters that influence membrane flux  $d$  and  $L$  are indicated. (c) shows how a conformal LbL coating (in pink) can change the pore diameter and thus affect flux. It is important to note that the illustrations are distorted in terms of lateral and vertical scale. Where pore diameters of membranes available include  $d_o = 200$  nm, 800 nm or 3  $\mu\text{m}$ , the length of the pores,  $L$ , equal to the membrane thickness, is 10  $\mu\text{m}$ . (d) and (e) show how the pore diameter can be reduced by swelling of temperature responsive coatings induced by lowering the temperature.

The flux,  $J$ , across a porous membrane with cylindrical pores of average diameter  $d$  is given by the Hagen-Poiseuille (HP) equation, Equation 5-1.

Equation 5-1, 
$$J = \frac{Q}{A} = \frac{n\pi(d/2)^4\Delta P}{8\eta L}$$

Where  $Q$  is the volumetric flow rate,

$A$  is the cross-sectional membrane area,

$n$  is the number of pores per unit area of membrane,

$\eta$  is the fluid viscosity,

$\Delta P$  is the pressure difference across the membrane,

and  $L$  is the average length of the pores.

As shown in Figure 5-1, by conformally coating TEPC membranes using LbL assembly, the pore diameter,  $d$ , can be tuned easily as it decreases as the thickness of the coating,  $t$ , is increased. As noted in the caption of Fig. 5-1, the illustrations are not drawn to scale. It is important to note that  $L \gg d$  and thus  $\frac{L+2t}{L} \approx 1$ . Given that, the transmembrane flux is dominantly controlled by the pore diameter,  $d$ . At a constant  $\Delta P$ , the experimentally determined transmembrane flux,  $J_{exp}$ , depends on the pore diameter,  $d$ , according to the following relation:

Equation 5-2, 
$$\frac{d}{d_o} = \left(\frac{J_{exp}}{J_o}\right)^{1/4}$$

with reference states:

$d_o$  being the average pore diameter of the uncoated membrane

and  $J_o$  the flux through the uncoated membrane.

By conformally coating membrane pores with a responsive coating that swells in response to external stimuli, the stimuli can be used to elicit changes in pore diameter and membrane flux. Previous work from our group (by Lee *et al.*<sup>3</sup>) has nicely demonstrated the utility of controllable

membrane gating for separating macromolecules of different sizes using pH responsive multilayers.

Here, we show that the temperature responsive multilayers developed in this thesis can be used for temperature controlled membrane gating, where  $d$  and thus  $J_{exp}$  change as a function of temperature,  $T$ , and Equation 5-2 takes on a temperature dependence expressed in Equation 5-3.

Equation 5-3, 
$$\frac{d(T)}{d_o} = \left( \frac{J_{exp}(T)}{J_o(T)} \right)^{1/4}$$

*Note:  $J_o(T)$ , the transmembrane flux through the bare, uncoated TEPC membrane is also function of temperature because the viscosity of water changes with temperature<sup>‡</sup>.*

As illustrated in Fig. 5-1, by coating TEPC membranes ( $d_o = 200$  nm) with temperature responsive multilayers, the membrane flux can be controlled by temperature as shown in Figure 5-2. The flux through the coated membranes can be reduced (from the open state at 20 °C) by ~ 7× through swelling of the membrane coating induced at 0 °C. To give a physical sense of the flow rate, the flux at 20 °C was ~ 2.7 mL/ 2.5 cm<sup>2</sup>/10 min, equivalent to 18 mL/m<sup>2</sup>/s. The flux at 0 °C was ~2.6 mL/m<sup>2</sup>/s. The pressure applied across the membranes,  $\Delta P$ , was 8 psi and the membrane area,  $A$  was 2.5 cm<sup>2</sup>.

---

<sup>‡</sup>The transmembrane flux itself has a temperature dependence through temperature dependence of the viscosity of water,  $\eta(T)$ .

For example, all other factors held constant,  $\frac{J_o(20)}{J_o(0)} = \frac{\eta(0)}{\eta(20)} = \frac{1.75}{1} = 1.75$ .

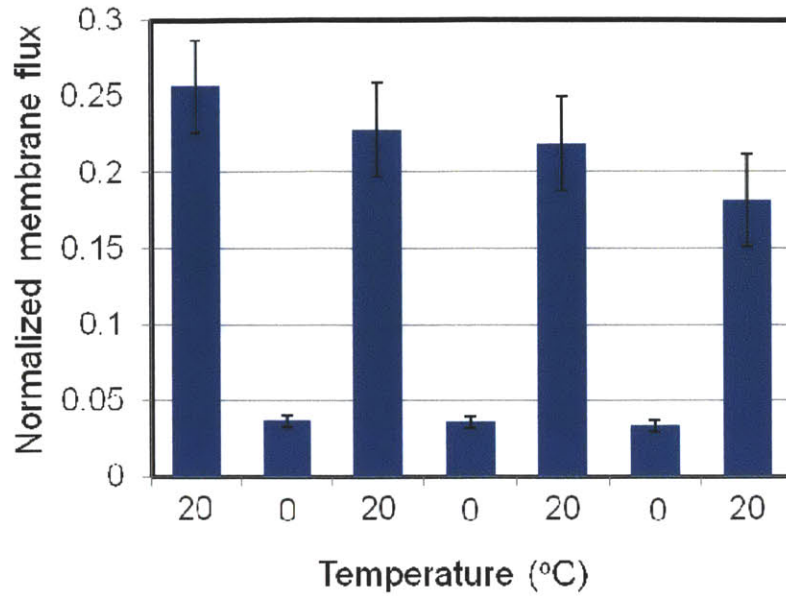


**Figure 5-2.** Plot showing the changes in normalized membrane flux,  $\frac{J_{exp}(T)}{J_o(T)}$ , through TEPC membranes with 200 nm pores coated with (PD-PP-PD/PAA 7.0)<sub>15</sub>, as the temperature, T, is cycled between 20 °C and 0 °C. §

By comparing the experimentally measured flux,  $J_{exp}(T)$ , of the coated TEPC membranes with the bare membranes (reference state), the pore diameters  $d(T)$  of the multilayer-modified membranes under different temperature conditions can be estimated using Equation (5-3). From  $d(T)$ , the pore wall coating thickness,  $t_p(T)$  can then be obtained from the relationship:  $d(T) = d_o - 2t_p(T)$ . Values for  $t_p(T)$  thus obtained are listed below in Table 5-1. While values of  $\frac{t_p(0)}{t_p(20)}$  obtained in this case, is the same as that obtained for changes in the thickness of flat films,  $t_{ff}(T)$ , with  $\frac{t_{ff}(0)}{t_{ff}(20)} = 2.5$ , this might not be expected, especially for thicker coatings where confinement effects within pores will become important. Here the pore wall swollen thickness at 0 °C of 70 nm is less than  $d_o/2$  and the pore walls did not physically impinge on each other in the swollen state.

§ There is a slight decrease in membrane flux with repeated cycling seen both in the uncoated membranes and coated ones likely due to membrane fouling by particles in the solution. Particles could have come from a rust spot found in the pressurized water reservoir system used.

**Table 5-1.** Pore wall coating thickness,  $t_p$ , at the different temperatures (T) as inferred from the transmembrane flux using Equation 5-3.

T, °C	$t_p(T)$ , nm	Standard Dev.
20	28	4.9
0	70	1.7

Figure 5-3 shows an SEM image of a TEPC membrane with  $d_o = 200$  nm pores. The average pore opening diameter of  $\sim 160$  nm agrees relatively well with a coating thickness of  $\sim 15.6$  nm deduced from flux measurements assuming film swelling at 20 °C (as seen in Chapter 2) is  $\sim 1.8\times$ .

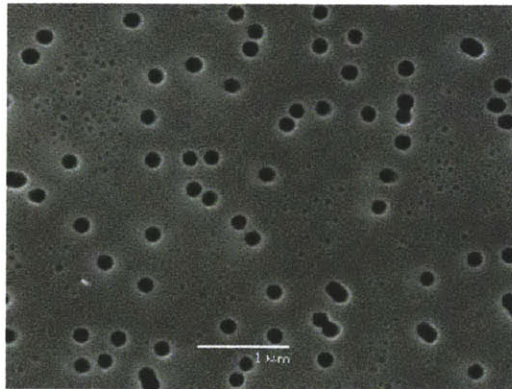


**Figure 5-3.** SEM image of a TEPC membrane ( $d_o = 200$  nm) coated with (PD-PP-PD/PAA 7.0)<sub>15</sub>.

#### 5.4.2 Freestanding Nanotubes made of Temperature Responsive Multilayers.

Apart from using LbL assembly to confer temperature responsive properties to membrane function, membranes are also interesting as sacrificial templates for creating freestanding 3-D nanostructured materials. As described in the work of my collaborator, Gary Chia, from our lab, a fabrication procedure to create surface-bound polymer nanotube arrays from pH responsive multilayers has been developed<sup>12</sup>. Nanotubes represent useful structures that offer high specific surface area (surface area per unit volume of material) and high aspect ratios<sup>9,10</sup>. Nanotube arrays with controllable intertube spacing as well as inner and outer tube diameter are interesting materials whose functionality can be tuned by control of these structural parameters. The multitude of structurally derived functions are well documented in nature, a prominent example being the attachment pads of gecko feet that are versatile and effective adhesives owing to nanoscaled fibrillar structures (setae) that allows for intimate high area contact with surfaces.

By creating nanotube arrays of stimuli responsive materials, new phenomena can result from collective behavior. As demonstrated by the work of L. Han *et al.*, *submitted*, percolative effects result in interesting mechanical behavior of pH responsive nanotube arrays. Here we investigate the possibility to create nanotube arrays out of the temperature responsive materials studied in the previous chapters. Multilayers of (PD-PP-PD/PAA 7.0) or (LTB/PAA 7.0) were built on TEPC membranes with different pore sizes,  $d_o = 800$  nm or  $3 \mu\text{m}$ . As seen in Figure 5-4 and Figure 5-5, the pores of 800 nm TEPC membranes and  $3 \mu\text{m}$  TEPC membranes respectively can be systematically closed by increasing the number of bilayers and thus the thickness of the LbL coating. (\* Figs 5-4 and 5-5 correspond to Step (iv) in the nanotube synthesis process illustrated in Figure 5-M2 in the Methods section.)

As seen in Figure 5-4, the original  $d_o = 800$  nm pore openings are significantly narrowed by coating (LTB/PAA 7.0)<sub>10</sub> (row (b)) and most of the pores are obscured by the (LTB/PAA 7.0)<sub>15</sub> coating (row (c)). For membranes of larger pores,  $d_o = 3 \mu\text{m}$  (shown in Figure 5-5), pore openings get incrementally smaller from row (a) (LTB/PAA 7.0)<sub>10</sub>, (b) (LTB/PAA 7.0)<sub>20</sub>, (c) (LTB/PAA 7.0)<sub>25</sub>, to (d) (LTB/PAA 7.0)<sub>30</sub>, with pores remaining open at (LTB/PAA 7.0)<sub>30</sub>.

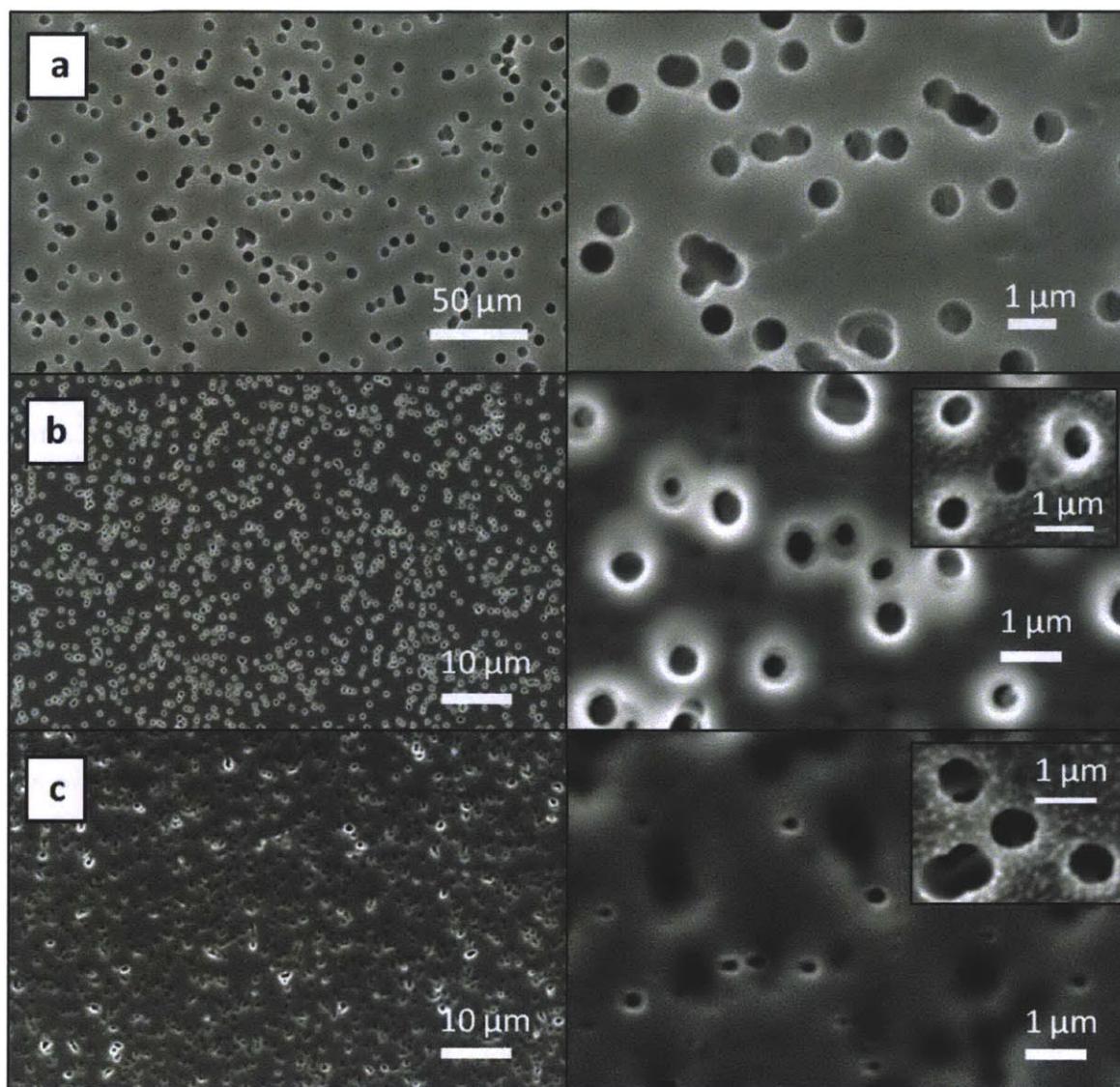


**Figure 5-4.** SEM images of TEPC membranes ( $d_o=800$  nm) coated with increasing numbers of bilayers of (LTB/PAA 7.0). Images of the same coated membrane at different magnifications are shown in each row; (a) (LTB/PAA 7.0)<sub>5</sub>, (b) (LTB/PAA 7.0)<sub>10</sub> and (c) (LTB/PAA 7.0)<sub>15</sub>. The insets in row (b) and (c) are of the membranes after plasma etching of the top surface.

The insets of Figure 5-4 in (b) and (c), have the top surface of the coated membranes plasma etched away to reveal the coated pores beneath as illustrated in step (v) of Fig. 5-M2. From the inset images, we see that while deposition of 5 more bilayers from (LTB/PAA 7.0)<sub>10</sub> to (LTB/PAA 7.0)<sub>15</sub> obscures the top surface of the  $d_o=800$  nm membranes, it did not seem to have narrowed the pores beneath further. This is likely a bridging effect where the deposited polymers bridged over the tops of the pores.



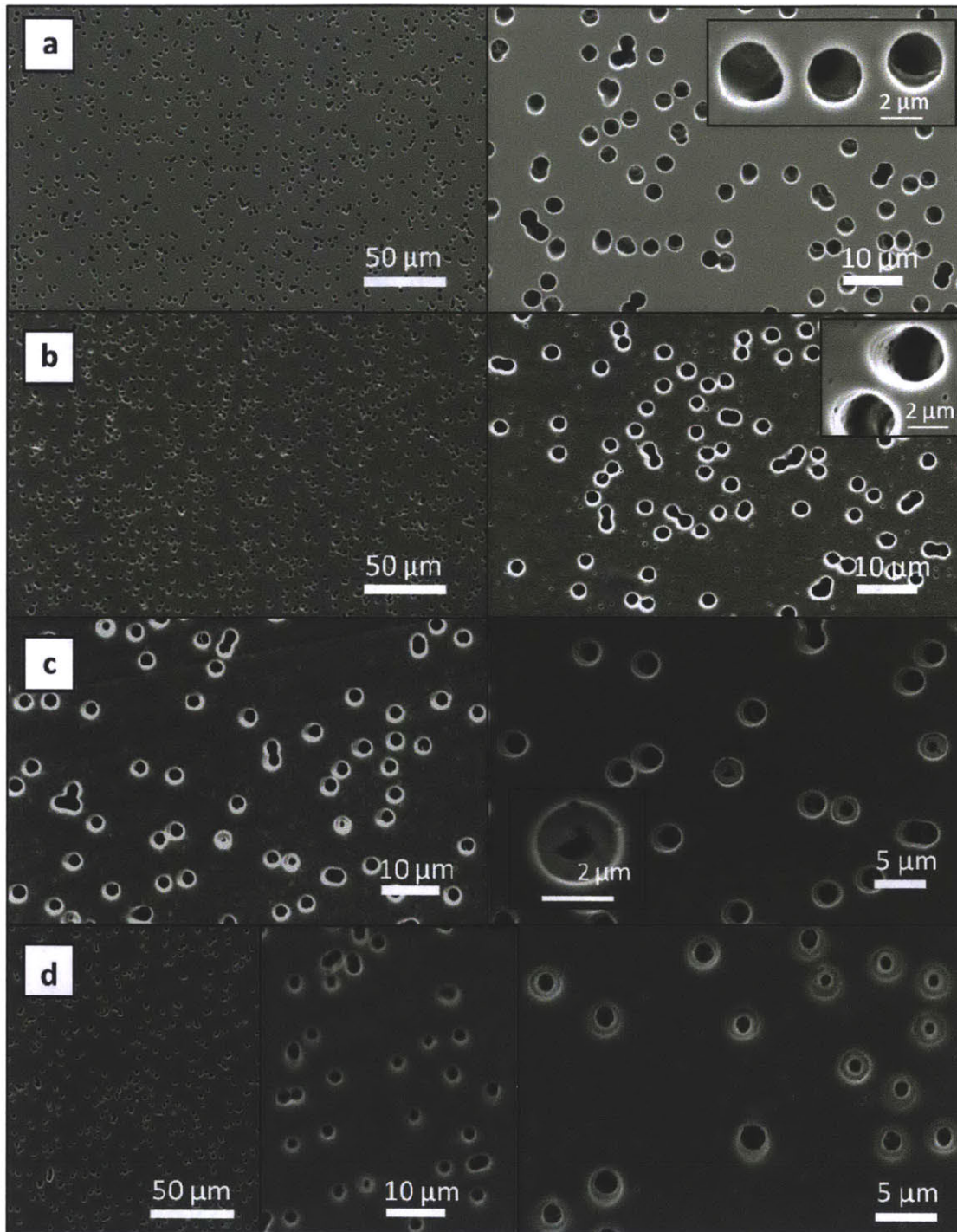


**Figure 5-5.** SEM image of TEPC membranes ( $d_o = 3 \mu\text{m}$ ) coated with increasing numbers of bilayers of (LTB/PAA 7.0). Images shown in each row are of the same coated membrane at different magnifications. Coatings are as follows, row (a) (LTB/PAA 7.0)<sub>10</sub>, (b) (LTB/PAA 7.0)<sub>20</sub>, (c) (LTB/PAA 7.0)<sub>25</sub>, and (d) (LTB/PAA 7.0)<sub>30</sub>.

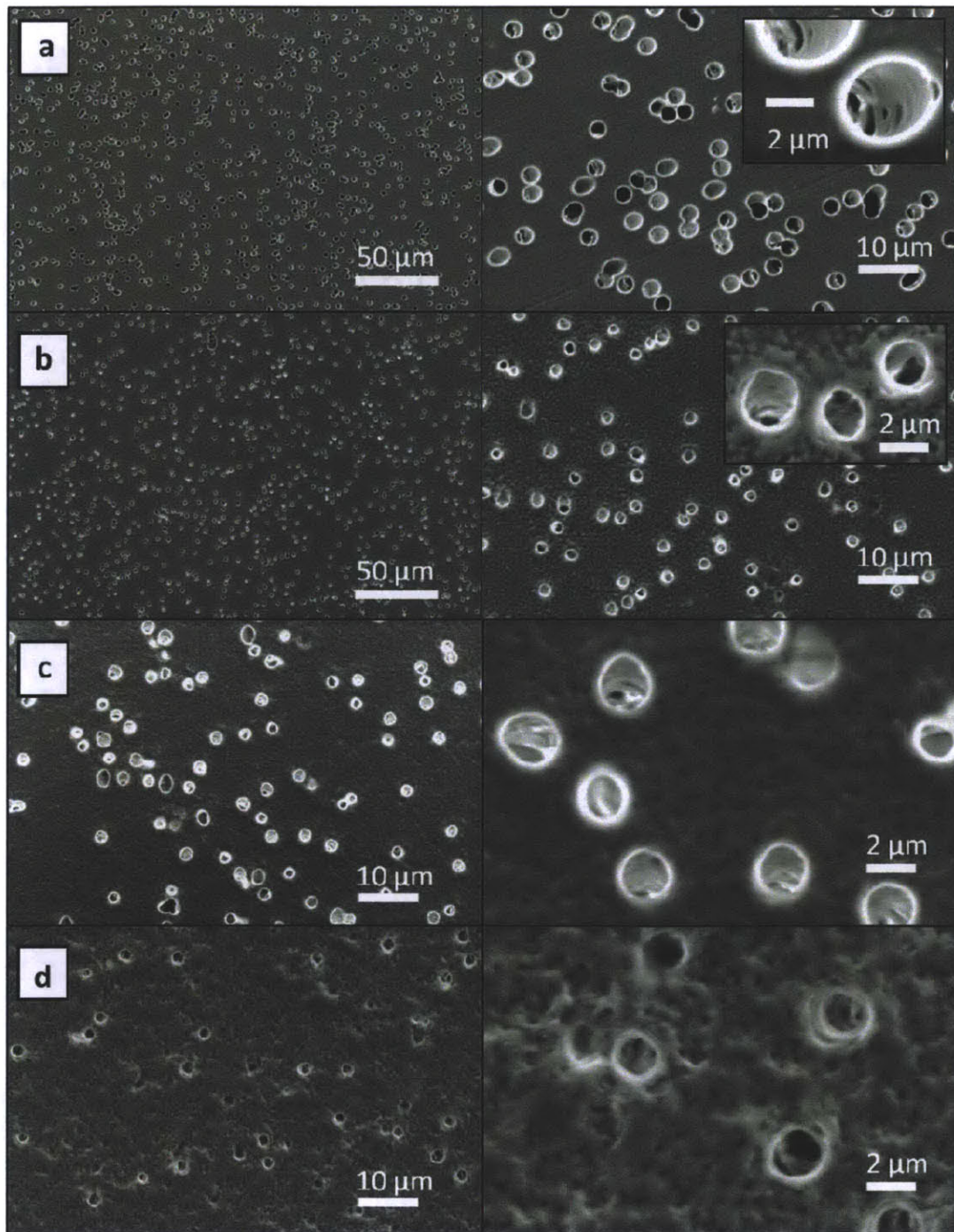
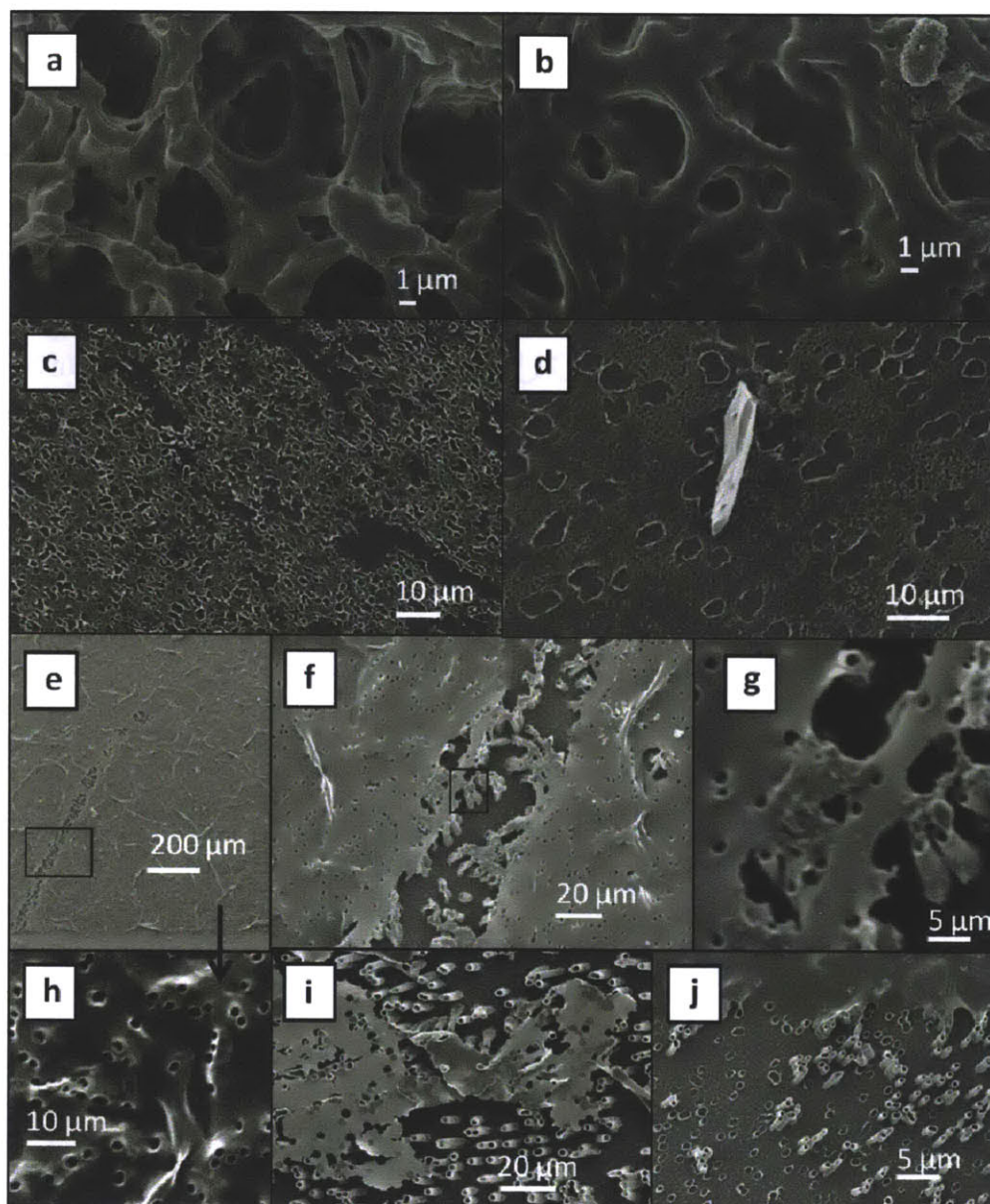


**Figure 5-6.** SEM image of TEPC membranes ( $d_o = 3 \mu\text{m}$ ) coated with increasing numbers of bilayers of (PD-PP-PD/PAA 7.0). Images shown in each row are of the same membrane at different magnifications. Coatings are as follows, row (a) (PD-PP-PD /PAA 7.0)<sub>10</sub>, (b) (PD-PP-PD /PAA 7.0)<sub>20</sub>, (c) (PD-PP-PD /PAA 7.0)<sub>25</sub>, and (d) (PD-PP-PD /PAA 7.0)<sub>30</sub>.

Notably, comparing the same  $d_o = 800$  nm TEPC membranes coated with different block copolymer (BCP) systems (shown in Figures 5-4 and 5-6) do result in some morphological differences. The membranes coated with lower molecular weight PD-PP-PD (that used in Chapter 2, of architecture  $D_{11}$ - $P_{58}$ - $D_{11}$ , and broad polydispersity), as shown in Figure 5-6, forms significantly rougher coating surfaces than the higher molecular weight LTB (of architecture  $D_{57}$ - $PP_{127}$ - $PD_{57}$  and polydispersity index 1.38). This agrees with the AFM studies (of Chapter 4) that showed films of higher molecular weight BCPs had lower roughness. In addition to differences in roughness on the flat regions, it also seems like the (LTB/PAA 7.0) system provides better coating uniformity within pores and allows for better control of pore diameter.

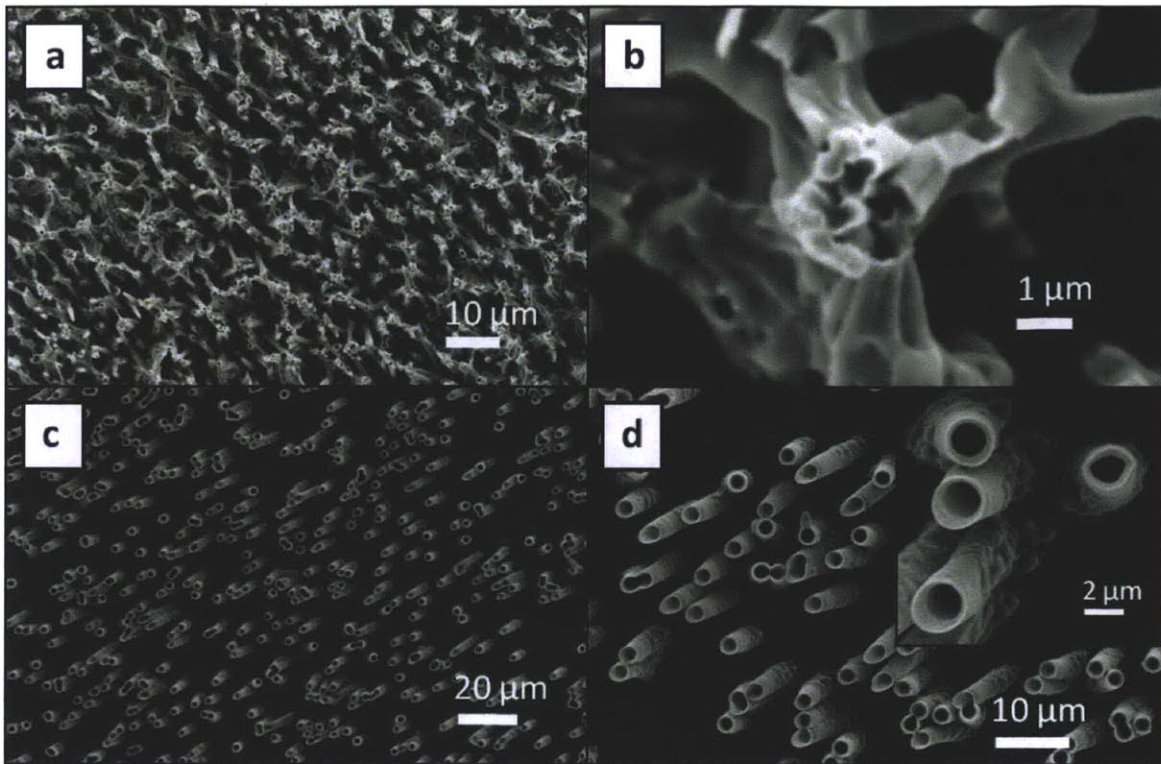
Next, we set out to create nanotubes, by following procedures developed by Chia *et al.*, from membranes with  $d_o = 800$  nm and  $d_o = 3$   $\mu$ m, coated with (LTB/PAA 7.0) as described in the Methods section.

Figure 5-7 is a collection of representative images showing some initial pitfalls that had to be overcome before we could create the free standing nanotube forests shown in Figure 5-8 and Figure 5-9.



**Figure 5-7.** SEM images illustrating possible pitfalls in nanotube creation. (a) and (b) are different magnifications of  $(\text{PD-PP-PD/PAA } 7.0)_{10}$  nanotubes (made from  $d_o = 800$  nm membranes) that were wet by water before drying. (c) and (d) show cases where nanotubes had torn off from the bottom surface; (c) is from TEPC membranes with  $d_o = 800$  nm and (d) from  $d_o = 3 \mu\text{m}$ . Images (e) through (h) show nanotubes of  $(\text{LTB/PAA } 7.0)_{10}$  where plasma etching failed and the top layer of the coating remained intact. The major flat region in (e) is shown at higher magnification in (h) and the crack, boxed in (f), is magnified in (e). (g) is further magnification of the boxed region in (f). (i)  $(\text{LTB/PAA } 7.0)_{10}$  nanotubes with incomplete etching of the top surface in some areas. (j) gives an overview of how the problems seen in (d) and (e) could be related.

From Fig. 5-7, we realized that wetting of formed nanotube arrays could result in the merging of nanotubes as seen in (a) and (b) while this is undesirable for the creation of discrete tubular entities, the tendency for the nanotubes to merge might reflect the potential for these multilayers to serve as self healing materials. The origin of most problems (seen in Fig. 5-7c-j) was found to be sub-optimal plasma etching conditions. Incomplete removal of the top surface of the coating could tear off the nanotubes during template removal in DCM (Fig. 5-M2, step (v)). The result of this is shown in Fig. 5-7(c) and (d). Alternatively, not removed, the top layer could also collapse onto the nanotubes as shown in Fig. 5-7 (e) and (h). In collaboration with Gary Chia in our lab, we found that the synthesis of (PD-PP-PD/PAA 7.0) and (LTB/PAA 7.0) nanotube arrays required a few modifications from the original nanotube fabrication procedure developed by Gary for creating (PAH7.5/PAA3.5) nanotubes. The key difference lay in step (v) (ref. to Fig. 5-M2), where plasma etching rate for the different polymer coatings was found to be different. While the (PAH7.5/PAA3.5) system etched well at 150 mTorr of Oxygen, for 15 min, the (PD-PP-PD/PAA 7.0) and (LTB/PAA 7.0) multilayers did not. The optimal etching conditions for these systems of interest here were found to be Oxygen at a lower pressure of 100 mTorr, and, surprisingly for a shorter amount of time (10 min). This indicated that the efficiency of PEM etching at this 100 mTorr Oxygen pressure was much higher. Using the optimized etching conditions, arrays of nanotubes were successfully created from (LTB/PAA 7.0) shown in Figure 5-8 as well as from (PD-PP-PD/PAA 7.0) (Fig. 5-9) built on both  $d_o = 800$  nm and  $d_o = 3$   $\mu$ m membranes. Particularly, in the smaller nanotube system shown in (a) and (b) of Figures 5-8 and 5-9, notable bunching together of nanotubes is observed. This arises from strong capillary forces that originate from the surface tension of the drying DCM film between the nanotubes. The liquid surface tension pulls the tubes together as DCM evaporates after the membrane removal step. This effect is less obvious in the case of the larger 3  $\mu$ m tubes that are further apart. (Capillary forces that draw tubes together scale inversely as the distance between tubes.) In addition, the larger tubes are likely to be more rigid structures. Comparing (c) and (d) of Figure 5-8 to those of 5-9, the (LTB/PAA 7.0)<sub>10</sub> system seems to form more rigid tubes with thicker walls than (PD-PP-PD/PAA7.0)<sub>10</sub>.



**Figure 5-8.** SEM images of nanotube forests made from TEPC membranes ( $d_o=800$  nm) coated with  $(\text{LTB/PAA } 7.0)_{10}$  at different magnifications are shown in (a) and (b), while nanotube forests made from TEPC membranes ( $d_o=3$  μm) coated with  $(\text{LTB/PAA } 7.0)_{10}$  at different magnifications are shown in (c) and (d).

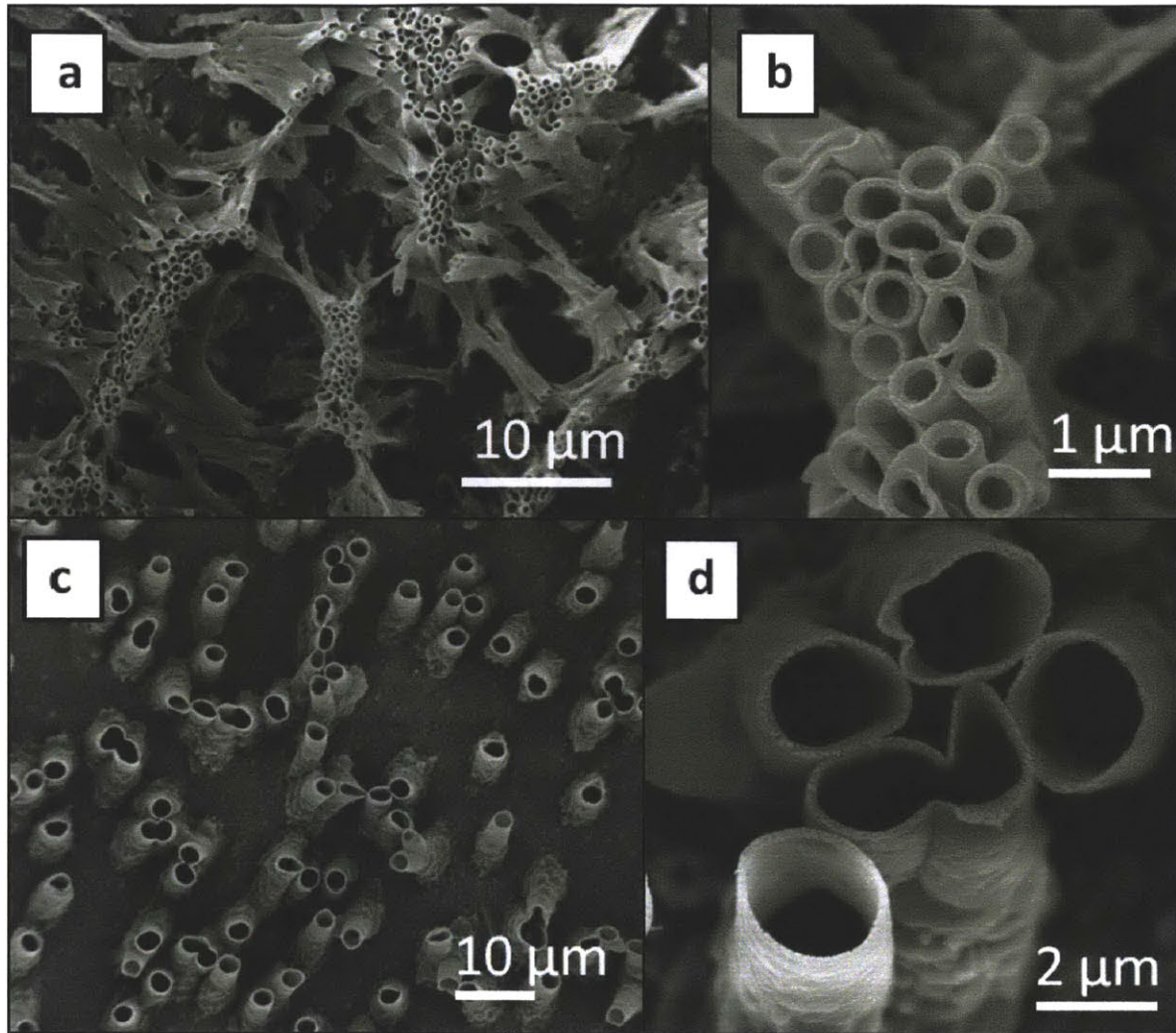


**Figure 5-9.** High resolution SEM images\*\* of nanotube forests made from TEPC membranes ( $d_o = 800$  nm) coated with  $(\text{PD-PP-PD/PAA } 7.0)_{10}$  at different magnifications are shown in (a) and (b), while nanotubes made from TEPC membranes ( $d_o = 3$  μm) coated with  $(\text{PD-PP-PD/PAA } 7.0)_{10}$  at different magnifications are shown in (c) and (d).

---

\*\* High resolution SEM images of nanotube forests shown in Fig. 5-9 were obtained by my collaborator Gary Khek Khiang Chia.

### 5.4.3 Protein Trapping and Release for Controlled Delivery.

In this section, the temperature controlled loading and release of bovine serum albumin (BSA) from (LTB/PAA 7.0) multilayers is studied. FTIC labeled BSA, a readily available 66 kDa protein of  $R_h \sim 4.5$  nm, negatively charged at neutral pH, was chosen as a model protein for studying the temperature dependent loading and subsequent release of protein therapeutics from temperature responsive (LTB/PAA 7.0) multilayers.

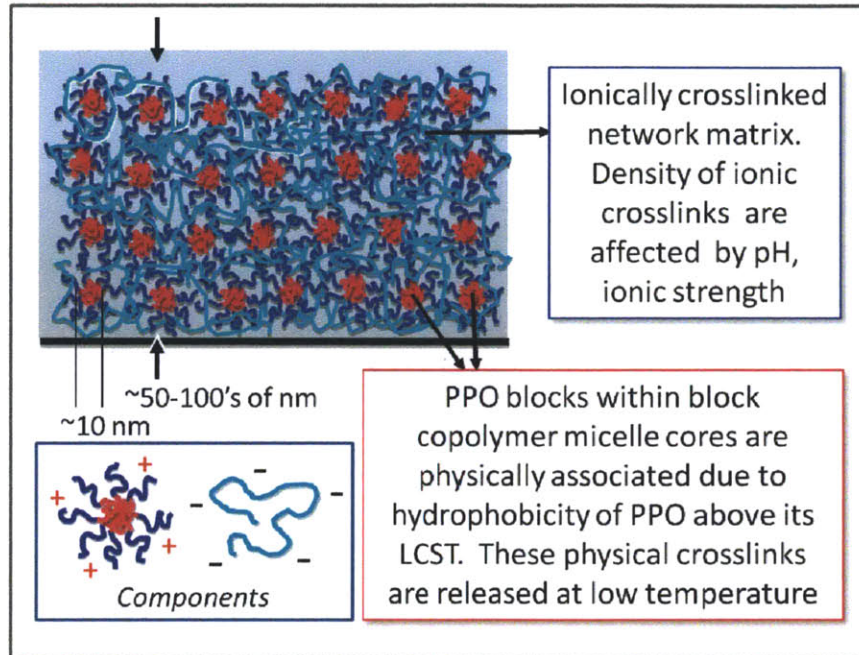


**Figure 5-10.** Schematic diagram illustrating the nanocomposite nature of block copolymer micelle/polyanion multilayers. Typical length scales of the nanostructure, as well as the two distinct types of crosslinks operative in holding the network together are depicted. In the case of micelles with temperature responsive poly(propylene oxide) (PPO) cores, crosslink density is affected by temperature, in addition to pH and salt concentration that affects the ionic bonds in weak polyelectrolyte multilayers.

As shown in Figure 5-10, the (LTB/PAA 7.0) polymeric networks are held together by crosslinks of two different types. Temperature affects the hydrophobic associations of the PPO component in the network. For LTB, at temperatures above 10 °C the PPO block associates with other PPO blocks to form hydrophobic domains in the film. These associated regions decrease the effective molecular weight between crosslinks,  $\bar{M}_c$ , resulting in mesh sizes,  $\xi$ , (described in Chapter 1,



Figure 1-3, Eqn. (12)), that are small and limited by the distance between ionic crosslinks in the ionic matrix. When the temperature is decreased below 10 °C, PPO blocks start interacting with water molecules by hydrogen bonding. PPO-water contacts are favored and the micelle cores open up as PPO chains dissociate from one another and become swollen with water. This creates open regions (from originally collapsed and dense micelle cores) with mesh sizes on the order of the root mean squared end to end distance,  $(\overline{r_o^2})^{1/2}$ , of the swollen central PPO block of LTB. The average mesh size offered between LTB PPO blocks are expected to range from zero in the collapsed dehydrated state, to something between that of a theta solvent condition,  $(\overline{r_o^2})^{1/2} \sim 4$  nm and less than the core block contour length of  $\sim 40$  nm.

As seen in Chapter 4, the  $Q$  values for various block copolymer multilayers here can take on time and temperature dependences. The value of  $Q$  for (LTB/PAA 7.0) at 6 °C, 30 min is 6 and that at room temperature is 2. Following from the effects of mesh size ( $\xi$ ) and swelling ratio ( $Q$ ) on the diffusion of molecules in gels as described by Eqn. (12) in Chapter 1, Section 1.2.3, we harness the temperature induced changes in  $Q$ , to allow for quick loading of protein molecules into the gel matrix at low temperature (6 °C; high  $Q$ ), trapping of the proteins (at room temperature; low  $Q$ ) and sustained slow release of the proteins out of the gel at body temperature (37 °C; low  $Q$ ).

As seen in Figure 5-11, the total amount of protein released from the same (LTB/PAA 7.0)<sub>35</sub> film is different depending on the protein loading temperature. The films loaded by immersing in protein solution at 6 °C released a total of 3.3 µg of FTIC-BSA after 430 hours while films loaded for the same duration at 22 °C released a total of 0.81 µg of protein after 430 hours<sup>††</sup>. This amount of protein represents the respective maximum amount of protein ( $M_f$ ; plateau value) that can be released from the films loaded with the specified conditions. Given the dry film dimensions of  $\sim 150$  nm  $\times$  1 cm  $\times$  1 cm, and taking the dry film density to be  $\sim 1$  g/cm<sup>3</sup> the loading capacity of the gel given by  $\frac{\text{mass of protein loaded (taken as total protein released)}}{\text{dry mass of gel}} \sim 22\%$  for loading at 6 °C for 35 min.

---

<sup>††</sup> Side note: (LTB/PAA 7.0)<sub>35</sub> films remained intact at the end of the loading and release process.

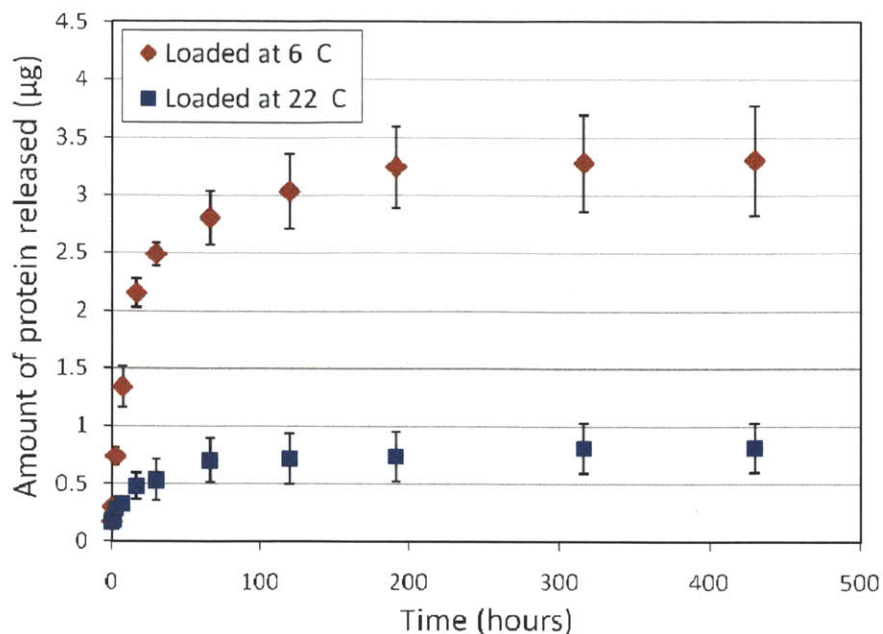


**Figure 5-11.** Cumulative FTIC-BSA released into 0.01 M PBS buffered solution (at 37 °C) as a function of time.

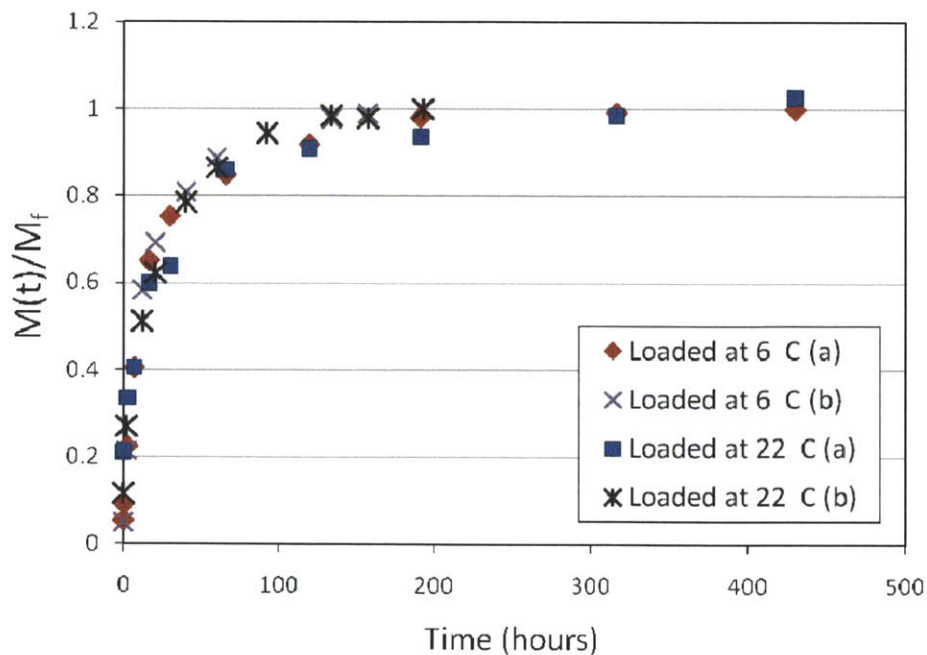


**Figure 5-12.** Relative amount of FTIC-BSA released,  $M(t)/M_f$ , as a function of time. Curves labeled (a) correspond to the data in Figure 5-11, while curves labeled (b) are data from a separate set of samples and separate release trial.

Since the release conditions are identical, wherein loaded films release proteins into the same volume of solution at the same temperature of 37 °C, the state of the hydrogel network ( $\xi$  and  $Q$ ) should be the same despite the different protein loading. This is reflected by the same kinetics of protein release described by the mass of protein released at time,  $t$ ,  $M(t)$ , normalized by  $M_f$ , i.e.  $M(t)/M_f$ , as shown in Figure 5-12. The kinetics of release from the 3 samples per loading condition studied in Figure 5-11, curves labeled (a) in Fig. 5-12 as well as results from different samples in a separate trial, curves labeled (b) in Fig. 5-12 fall on top of one another reflecting the same release kinetics. Protein release from these nanocomposite films (as depicted in Fig. 5-10) does not follow first order release kinetics.

While several more experiments should be done to confirm the reproducibility of these results as and to further understand the loading dependence on time and film thickness, the preliminary data shown here is telling. By using a low loading temperature, we can quickly load a large amount of protein into the swollen polymer matrix and trap these proteins by increasing the temperature to elicit gel collapse through the hydrophobic associations induced. The relatively high loading capacity and reasonably sustained rates of protein release from these films make them promising materials for protein therapeutic delivery.

#### **5.4.4 Tunable Disintegration of Multilayers for Triggered Release.**

Environmentally triggered disintegration of thin film coatings can be useful for a variety of applications including triggered ‘burst’ release with dispersion of materials carried within the gel matrix or triggered release of material layers or cell sheets held on the top surface of these films. The nanostructure of our temperature responsive micelle multilayers, held together by two different types of associations (illustrated in Figure 5-10), offers the unique ability to affect film stability by changes in temperature, pH and salt concentration. In short, the ionic crosslinks in the matrix of micelle corona chains associated with PAA are destabilized (1) at pH values removed from the film assembly pH and (2) at high salt concentrations. While the impact of pH is operative specifically in the case of weak polyelectrolytes with pH dependent ionization described in Chapter 1, Section 1.3, the effect of salt on polyelectrolyte multilayer stability is operative for both strong and weak polyelectrolyte combinations<sup>36</sup>.

##### ***5.4.4a Salt induced film instability.***

When salt is added to the aqueous medium bathing the polyelectrolyte multilayer, a dynamic equilibrium between all the charged species is reached<sup>36</sup>. The charged groups on each polyelectrolyte can bind to either the oppositely charged groups on the other polyelectrolyte or oppositely charged free ions. By increasing the salt concentration, the equilibrium is shifted to favor polyelectrolyte associations with free salt ions, effectively decreasing the ionic crosslink density operative in the polyelectrolyte multilayer. This increases the effective molecular weight between crosslinks and the swelling ratio as seen in Figure 5-13. Figure 5-13 shows the effect of salt (NaCl) concentration on the swelling and stability of homopolymer containing (D/PAA 7.0) and block copolymer (PD-PP-PD/PAA 7.0) multilayers; swelling ratio =  $\frac{\text{wet (swollen) film thickness}}{\text{dry film thickness}}$ .

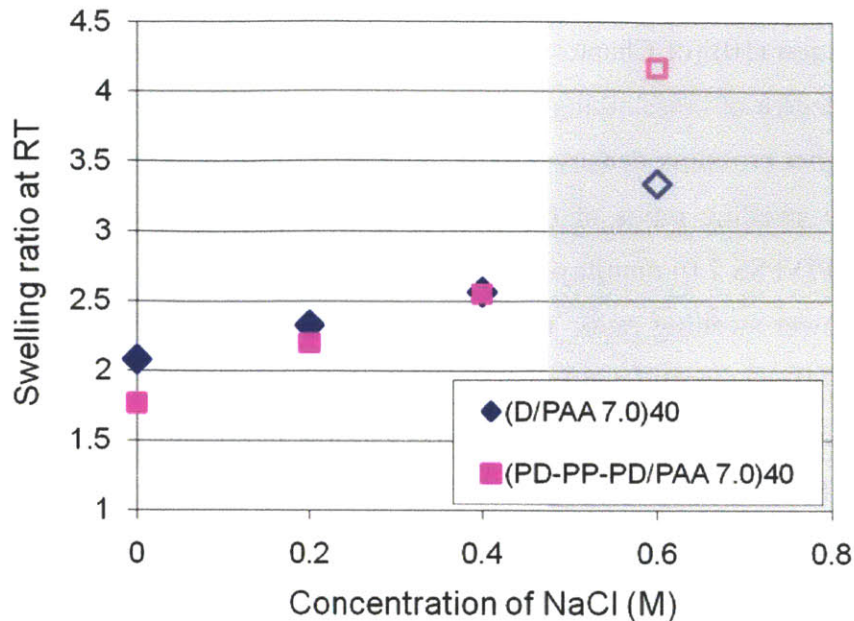


**Figure 5-13.** The swelling of (D/PAA 7.0)<sub>40</sub> and (PD-PP-PD/PAA 7.0)<sub>40</sub> multilayers at room temperature, RT, of 22 °C is plotted as a function of NaCl salt concentration. The swelling ratio is defined as the  $\frac{\text{wet (swollen) film thickness}}{\text{dry film thickness}}$ . Solid points are stable to the salt solution in which swelling is reversible. The shaded region (and hollow points at 0.6 M salt concentration) indicates the region of film instability where film loss starts to occur.

As mentioned in Chapter 2, when assembled with poly(styrene-4-sulfonate) (PSS), PD-PP-PD containing multilayers (PD-PP-PD/PSS 7.0) fail to exhibit temperature dependent swelling. This is likely the result of tight and dense ionic crosslinking in ionic matrix that prohibits the expansion of the PPO micelle cores at low temperature. Given the ability of salt to destabilize ionic associations through charge screening and competitive binding, we tested to see if loosening of the ionic linkages in (PD-PP-PD/PSS 7.0) multilayers could allow for temperature responsive swelling. Figure 5-14 shows the swelling of (PD-PP-PD/PSS 7.0)<sub>50</sub> in DI water solutions with different concentrations of salt (NaCl) added. All solutions were adjusted to pH 7 and the swelling ratio in each salt solution was determined at both room temperature (~22 °C) and in cold conditions (6 °C). As seen in Figure 5-14, the swelling at both 22 and 6 °C increases with increasing salt concentration. Notably, there is no significant difference in swelling ratio resulting from temperature at NaCl concentrations of 0.6 M and below. This is the same case for

swelling in 1× PBS buffer. At these salt concentrations, the swelling ratio is  $\leq 1.4$ . With reference to Equation (10) (of Chapter 1, Section 1.2.1), we know that the swelling ratio ( $Q$ ) is reflective of the degree of crosslinking within polymer network, where more tightly crosslinked networks with higher crosslink density will exhibit lower swelling ratios. When we compare the room temperature swelling ratios of (PD-PP-PD/PAA 7.0) to the room temperature swelling ratios of (PD-PP-PD/PSS 7.0) multilayers in low salt conditions we see that in the same solution, the latter has a lower swelling ratio. This indeed supports the case made in Chapter 2, where (PD-PP-PD/PSS 7.0) was postulated to have a more tightly crosslinked polyelectrolyte network that prohibited water imbibition into micelle cores at low temperature. Further confirming our hypothesis is the fact that addition of 0.8 M of salt loosens the polyelectrolyte network in (PD-PP-PD/PSS 7.0) sufficiently to allow for increased swelling at 6 °C. Owing to the greater stability of sulfonate – tertiary amine electrostatic interactions in (PD-PP-PD/PSS 7.0) compared to those of carboxylic acid – tertiary amine interactions in (PD-PP-PD/PAA 7.0), while film instability starts at 0.6M NaCl for the latter, instability and dissolution in of (PD-PP-PD/PSS 7.0) starts at a slightly higher salt concentration of 1 M.

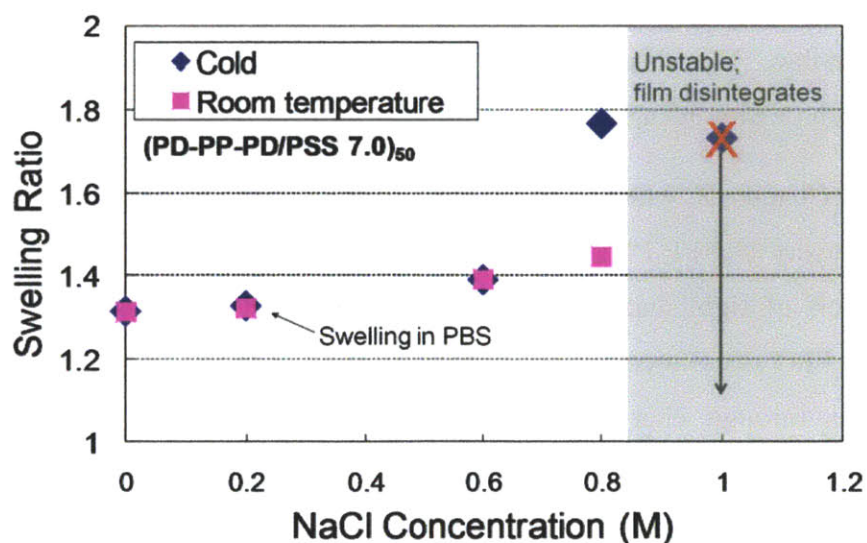


**Figure 5-14.** The swelling of (PD-PP-PD/PSS 7.0) multilayers at room temperature ( $\sim 22$  °C) and cold temperature (6 °C) is plotted as a function of NaCl concentration. The swelling ratio in PBS is the same as the swelling in solutions with 0.2 M NaCl, as indicated by the labeled arrow. The shaded region indicates the region of film instability where the multilayer starts to disintegrate.

#### 5.4.4b pH induced film instability.

As mentioned before, another factor that affects polyelectrolyte multilayer (PEM) stability is solution pH. The effect of pH operates via the dynamic equilibrium between the weakly acid and weakly basic groups on weak polyelectrolytes and  $H^+$  ions. As described in Chapter 1, Section 1-3, the degree of ionization of both the PDMAEMA block and the PAA homopolymer depend on the solution pH. At the LbL assembly pH, the free positive charges on the PDMAEMA are fully compensated for by association with the negatively charged ionized groups on PAA; the PEM is charge neutral. As seen in Figure 1-5 of Chapter 1, the number of positive charges on PDMAEMA tends to decrease with increasing pH, while the number of negative charges on PAA tends to increase with solution pH. In this manner, immersing the PEM in a solution of pH greater than the assembly pH of 7 creates an excess of negative charge in the film. The contrary is also true, where immersion in solutions of pH less than 7 can result in an excess of positive charge in the film. The greater the difference between the immersion solution pH and the assembly pH, the greater the disruption of the balance of ionic bonds and the greater the number of excess charges generated. The disruption of ionic bonds weakens the multilayer while the generation of excess charge results in additional swelling of the hydrogel, through electrostatic repulsion and the generation of increased osmotic pressure within the gel (as described in Chapter 1, Section 1.2). Both these effects cause destabilization of PEMs. The destabilization of PEMs can be qualitatively quantified by immersing PEMs in solutions of various pH for a fixed amount of time, drying the films and then measuring the thickness of films remaining on the substrate post pH annealing. The fraction of film thickness remaining after annealing is defined as the  $\frac{\text{Final dry film thickness post annealing}}{\text{Initial dry film thickness}} \equiv \frac{T_f}{T_i}$ . Figure 5-15 shows the fraction of film thickness of PEMs remaining after 18 hours of immersion in solutions of different pH done at either 20 °C or 6 °C. Both PEMs of pure homopolymer films, (D/PAA) assembled at pH 4 and at pH 7, as well as micelle containing (PD-PP-PD/PAA 7.0) multilayers were studied to illustrate the effects of assembly pH and the effect of additional hydrophobic associations operative in the micelle containing multilayers.

Looking at the (D/PAA 4.0) system annealed at 20 °C, we see that films are stable at the assembly pH 4, as well as at pH 3. Film loss starts to occur within 18 hours in solutions of pH > 4.5. The higher the pH of the solution the film was immersed in, the greater the amount of film

loss. For the (D/PAA 7.0) system, films are stable at the assembly pH of 7 while film loss increases as the immersion solution pH departs from pH 7 in either direction. The effect of acidic solutions seems to be more severe in this case. At pH 4 and below, the films completely dissolve away. Comparing the results from annealing the homopolymer films at room temperature (20 °C) versus annealing at a colder temperature of 5 °C, we see that film retention was slightly higher at the lower temperature. This is likely the result of faster film dissolution kinetics at the higher temperature as expected from the Arrhenius Equation, where the reaction rate,  $k$ , varies with temperature,  $T$ , as:  $k \propto e^{-\frac{E_a}{RT}}$ ,  $E_a$  being the activation energy of the reaction (positive in the case of bond breakage and film dissolution) and  $R$  the universal gas constant, 8.314 J/mol/K.

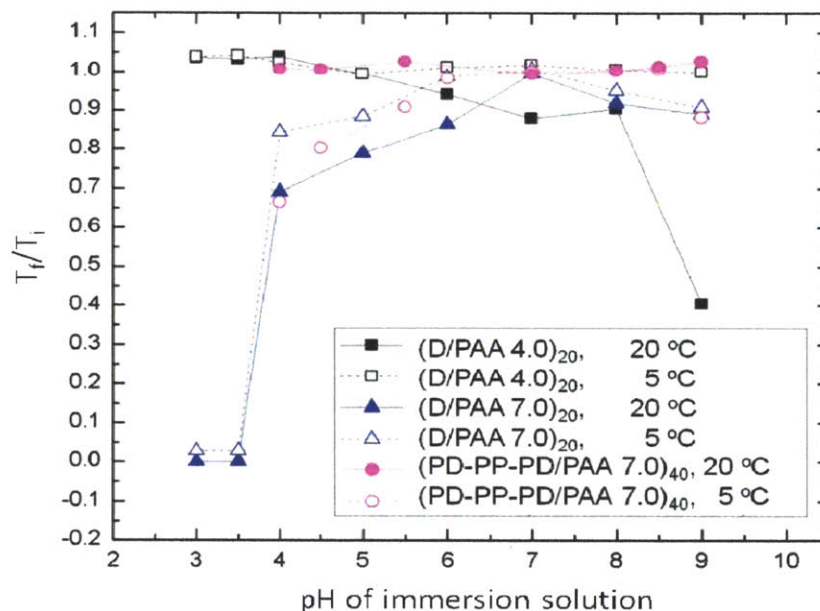


**Figure 5-15.** Fraction of multilayer films remaining ( $\frac{T_f}{T_i}$ ) for (D/PAA 4.0)<sub>20</sub> (squares), (D/PAA 7.0)<sub>20</sub> (triangles), (PD-PP-PD/PAA 7.0)<sub>40</sub> (circles) post annealing for 20 hours in DI water, adjusted to various pH values, at either 20 °C (solid symbols and lines) or 5 °C (hollow symbols and dotted lines).

Examining the results from annealing (PD-PP-PD/PAA 7.0) films, pink circles in Fig. 5-15, we see the interesting effect of the temperature responsive PPO micelle cores. At the low temperature of 5 °C, PPO is hydrated and do not contribute to additional bonding within the multilayer. The behavior of (PD-PP-PD/PAA 7.0) (hollow circles) is thus similar to that of



(D/PAA 7.0) (hollow triangles). At 20 °C, the PPO midblocks of PD-PP-PD are hydrophobically associated in micelle cores that serve as additional crosslinks in the multilayer network. These associations are relatively insensitive to pH variation and help stabilize the film. (PD-PP-PD/PAA 7.0) annealed at 20 °C (solid circles), thus exhibits better film stability than the homopolymer (D/PAA 7.0) films annealed at the same conditions (solid triangles). In summary, the stability of weak polyelectrolyte multilayers can be tailored through selection of the film assembly pH relative to the pH at which film stability or dissolution is desired. In addition, use of temperature responsive triblock copolymers like PD-PP-PD adds an additional temperature control over film stability, making these multilayers highly customizable for release under specific temperature and pH combinations.

#### ***5.4.4c Effect of block copolymer architecture on film stability.***

While the presence of aggregated PPO segments in (PD-PP-PD/PAA 7.0) can help stabilize the film at room temperature as seen in the previous section, the additional swelling of films induced by dissolution of the PPO micelle cores at low temperatures can increase the film sensitivity to pH at low temperature. As seen in Chapter 4, as the temperature is decreased below the LCST of PPO, the osmotic pressure developed within micelle containing polyelectrolyte multilayers (mPEMs), assembled with PPO in the dehydrated state at room temperature, can be so strong that they tear the mPEM apart. As follows from the findings in Chapter 4, the temperature responsive mPEM film stability at low temperatures is critically dependent on  $\Delta T$  and the block copolymer (BCP) architecture. Key features of BCP architecture that affect film stability include BCP connectivity and the ratio of PDMAEMA (abbreviated PD) to PPO (abbreviated PP) units. At low temperatures in pH 7 DI, the PD units hold the mPEM together through ionic associations with PAA while the PP units contribute to generation of swelling forces and tend to drive film dissolution. As such, films with higher PD:PP ratios are expected to be more stable at low temperatures. This is indeed the case, as demonstrated in Figure 5-16. As expected, at the low temperatures where PPO blocks become swollen with water, the stability of the multilayers (held together solely by ionic bonding between the weak polyelectrolytes PDMAEMA and PAA), decreases with departure of the immersion solution pH away from the assembly pH of 7. Notably, for the films containing triblock copolymers PD7-PP127-PD7, PD20-PP127-PD20, PD27-PP127-PD27, film stability decreases with increasing PP:PD ratio. Thus PD27-PP127-PD27

films are the most stable. The films of PD7-PP127-PD7 are not stable at the low temperatures regardless of solution pH as the mere 7 units of PD are unable to sustain the network with the majority PPO component going into solution at 5 °C. Similarly, the low temperature stability of (PP65-PD65/PAA 7.0) is slightly higher than that of (PP65-PD58/PAA 7.0)<sup>‡‡</sup>. In agreement with results in Chapter 4, the triblock copolymer connectivity results in higher stability of the triblock containing (PD27-PP127-PD27/PAA 7.0) compared to that of either of the diblock copolymer films, (PP65-PD58/PAA 7.0) or (PP65-PD65/PAA 7.0), despite the higher PD:PP ratios of the diblock containing films. In summary molecular design of block copolymer architecture can be used to tune the stability of these temperature responsive coatings.

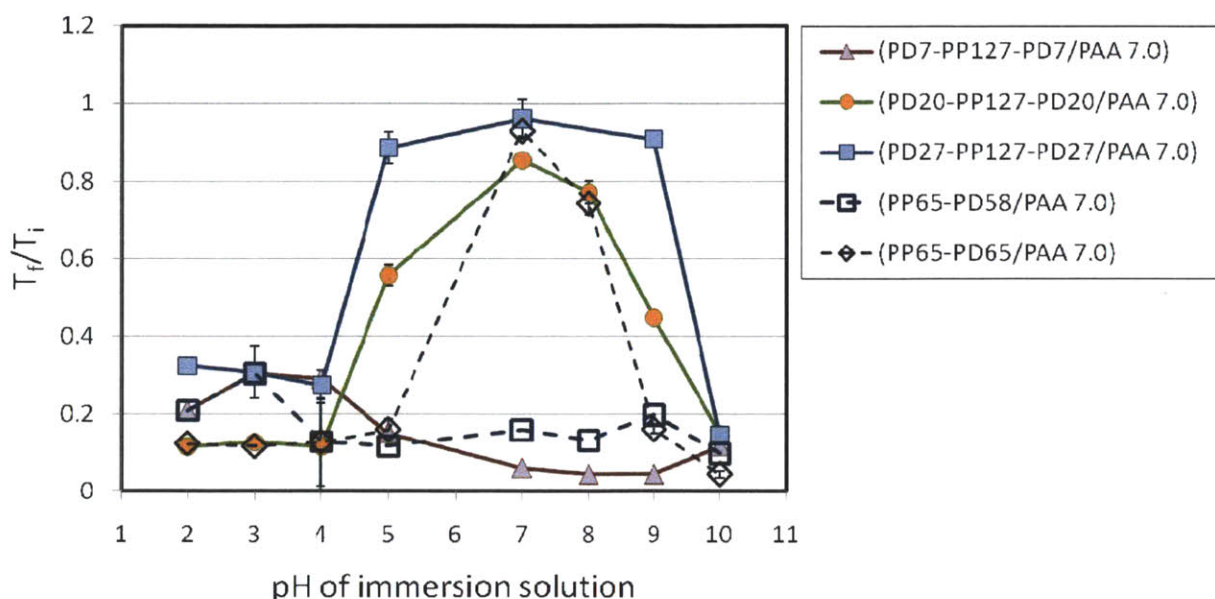
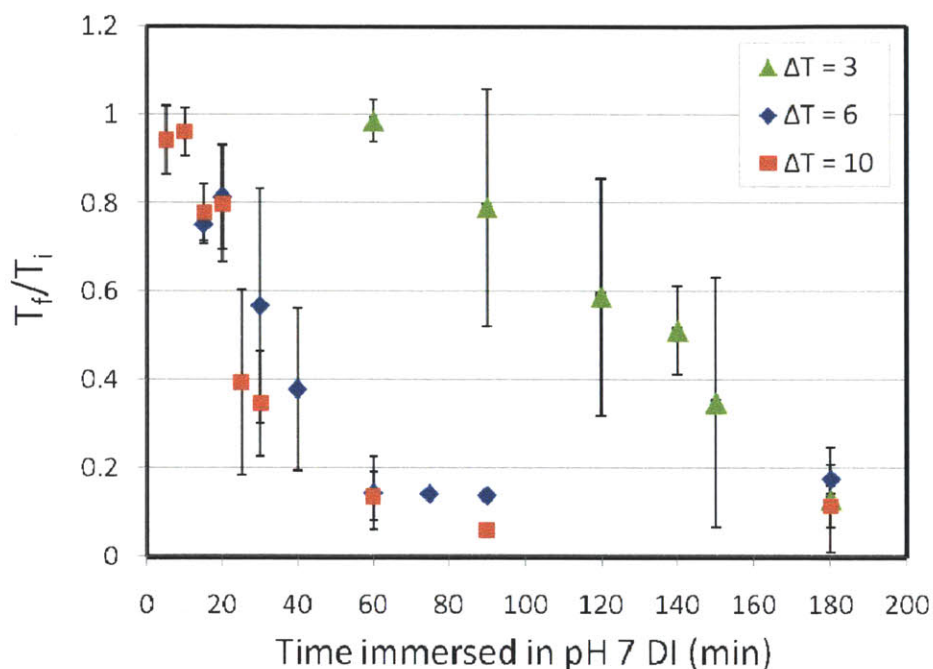


**Figure 5-16.** Fraction of multilayer film thickness remaining,  $\frac{T_f}{T_i}$ , after 20 hours of immersion in DI water adjusted to various pH at 5 °C. All multilayers studied were assembled at pH 7 but contain block copolymers of different architecture, where PD is the PDMAEMA block, PP the PPO block and the numbers following each abbreviation being the degree of polymerization of the block. Block copolymer components used include triblocks (solid symbols and lines): PD7-PP127-PD7, PD20-PP127-PD20 and D20-PP127-PD20 as well as diblocks (hollow symbols; dotted lines): PP65-PD58 and PP65-PD65.

<sup>‡‡</sup> PP65-PD58 is the same block copolymer abbreviated as DB in Chapters 3 and 4 while PD27-PP127-PD27 is the same as LTB. Abbreviations that express the block copolymer architecture are adopted in this section for ease of comparison and discussion.

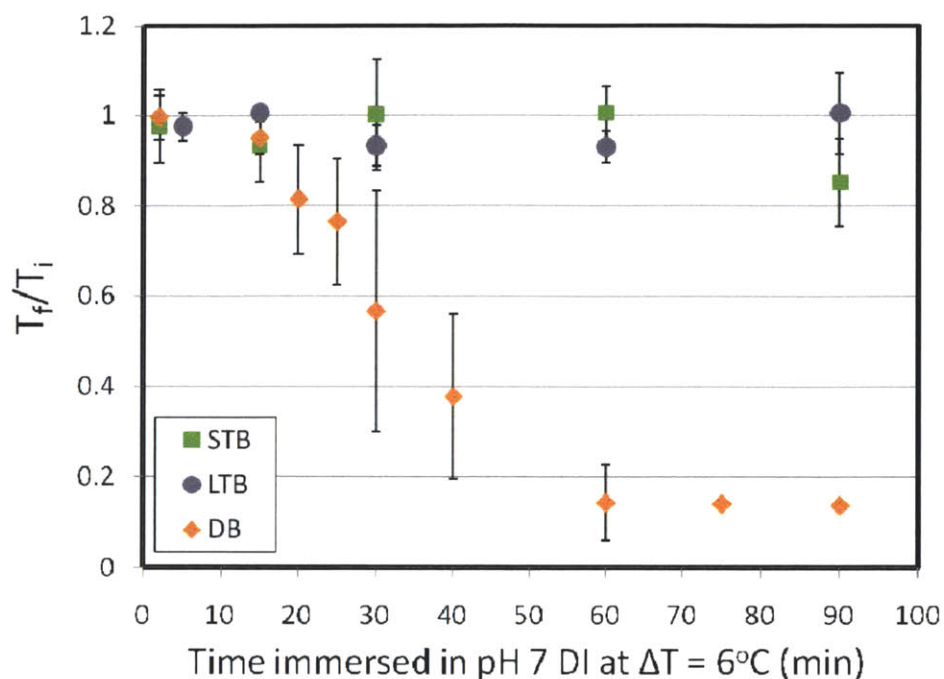
#### 5.4.4b. Time and temperature dependence of film disintegration.

While it was easiest to study the pH, salt and temperature impact on the stability of various multilayers by annealing in different solutions for a fixed, long time, as seen in above, the degree of film swelling and film disintegration, as described in Chapter 4, is time and temperature dependent. As demonstrated in Figure 5-17, the rate of film loss for (DB/PAA 7.0) multilayers increases over time and with increasing degree of undercooling,  $\Delta T = T - T_{\text{stt}}$  (ref. to Chapter 4).



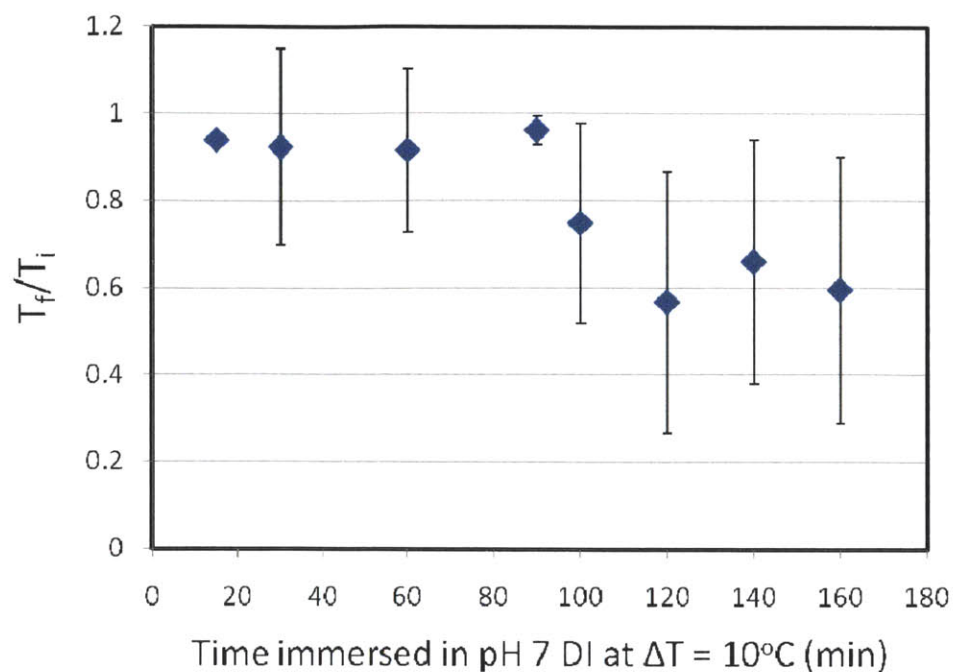
**Figure 5-17.** Variation in the fraction of (DB/PAA 7.0) film thickness remaining,  $\frac{T_f}{T_i}$ , with time of annealing in pH 7 adjusted DI water at different degrees of undercooling,  $\Delta T = 3, 6$  or  $10$  °C.

Figure 5-18 contrasts the film stability of multilayers studied in Chapter 4 and demonstrates clearly the fact that the triblock containing multilayers are more stable than the diblock containing multilayer. While the diblock film (DB/PAA 7.0) almost completely disintegrates in an hour, no film loss is detected after holding the triblock containing multilayers (STB/PAA 7.0) and (LTB/PAA 7.0) at  $\Delta T = 6$  °C.



**Figure 5-18.** Variation of the fraction of multilayer film thickness remaining,  $\frac{T_f}{T_i}$ , with time of annealing in pH 7 adjusted DI water at  $\Delta T = 6^\circ\text{C}$  for different multilayer systems: (STB/PAA 7.0) (squares), (LTB/PAA 7.0) (circles) and (DB/PAA 7.0) (diamonds).

While no film disintegration for (LTB/PAA 7.0) multilayers is detectable after 20 hours of annealing at  $\Delta T = 5^\circ\text{C}$  (seen in Fig. 5-16, labeled there as (PD27-PP127-PD27/PAA 7.0)), further undercooling of (LTB/PAA 7.0) to  $\Delta T = 10^\circ\text{C}$  causes measureable film loss within 180 mins, as shown in Figure 5-19.



**Figure 5-19.** Variation of the fraction of (LTB/PAA 7.0) film remaining,  $\frac{T_f}{T_i}$ , with time of annealing in pH 7 adjusted DI water at  $\Delta T = 10^\circ\text{C}$ .

In summary of results presented this section, the time dependent film disintegration of temperature responsive block copolymer containing thin film multilayers can be controlled by the block copolymer architecture, solution pH, salt concentration and degree of undercooling,  $\Delta T$ .

As a whole, the temperature responsive block copolymer containing thin film multilayers demonstrate a wide range of tunable disintegration behavior that give them useful potential as customizable controlled release systems.

## **5.5 Conclusions**

In this Chapter, several applications of temperature responsive micelle multilayers were investigated. The key experimental data presented in this Chapter serves as a proof of principle for further pursuit of potential applications possible. In Section 5.4.1, the opportunity to apply these multilayers to temperature controlled membrane gating was demonstrated. In Section 5.4.2, using a sacrificial template based method, the ability to create unique freestanding nanostructures out of temperature responsive materials was developed. In Section 5.4.3, the utility of temperature swellable multilayers for protein entrapment and sustained release was explored. Finally in 5.4.4, the ability to control film stability by a variety of environmental factors including pH, salt concentration, temperature and component block copolymer architecture was demonstrated, showing the potential of such systems to serve as highly customizable release materials.

## **Acknowledgements**

This work was supported by the MRSEC Program of the National Science Foundation under award number DMR – 0819762. We thank the Center for Materials Science and Engineering (CMSE), the Institute for Soldier Nanotechnologies (ISN) and the MIT Biotechnology Processing Center (BPEC), for use of their characterization facilities.

## References

- (1) Yu, A.; Liang, Z.; Caruso, F. *Chemistry of Materials* **2004**, *17*, 171.
- (2) Dai, J.; Baker, G. L.; Bruening, M. L. *Analytical Chemistry* **2005**, *78*, 135.
- (3) Lee, D.; Nolte, A. J.; Kunz, A. L.; Rubner, M. F.; Cohen, R. E. *Journal of the American Chemical Society* **2006**, *128*, 8521.
- (4) Alem, H.; Blondeau, F.; Glinel, K.; Demoustier-Champagne, S.; Jonas, A. M. *Macromolecules* **2007**, *40*, 3366.
- (5) DeRocher, J. P.; Mao, P.; Han, J.; Rubner, M. F.; Cohen, R. E. *Macromolecules* **2010**, *43*, 2430.
- (6) Xie, R.; Li, Y.; Chu, L.-Y. *Journal of Membrane Science* **2007**, *289*, 76.
- (7) Wandera, D.; Wickramasinghe, S. R.; Husson, S. M. *Journal of Membrane Science* **2010**, *357*, 6.
- (8) Ye, Y.; Mao, Y. *Journal of Materials Chemistry* **2011**, *21*, 7946.
- (9) Martin, C. R. *Science* **1994**, *266*, 1961.
- (10) Hou, S.; Harrell, C. C.; Trofin, L.; Kohli, P.; Martin, C. R. *Journal of the American Chemical Society* **2004**, *126*, 5674.
- (11) Möhwald, H.; Lichtenfeld, H.; Moya, S.; Voigt, A.; Sukhorukov, G.; Leporatti, S.; Dähne, L.; Antipov, A.; Gao, C. Y.; Donath, E. In *Studies in Surface Science and Catalysis*; Yasuhiro Iwasawa, N. O., Hironobu, K., Eds.; Elsevier: 2001; Vol. Volume 132, p 485.
- (12) Chia, K.-K.; Rubner, M. F.; Cohen, R. E. *Langmuir* **2009**, *25*, 14044.
- (13) Goldberg, M.; Langer, R.; Jia, X. *Journal of Biomaterials Science, Polymer Edition* **2007**, *18*, 241.
- (14) Klouda, L.; Mikos, A. G. *European Journal of Pharmaceutics and Biopharmaceutics* **2008**, *68*, 34.
- (15) Lin, C.-C.; Metters, A. T. *Advanced Drug Delivery Reviews* **2006**, *58*, 1379.
- (16) Hoare, T. R.; Kohane, D. S. *Polymer* **2008**, *49*, 1993.
- (17) Bhattarai, N.; Gunn, J.; Zhang, M. *Advanced Drug Delivery Reviews* **2010**, *62*, 83.
- (18) Sutton, C. *The Obstetrician & Gynaecologist* **2005**, *7*, 168.
- (19) Ninawe, P. R.; Parulekar, S. J. *Industrial & Engineering Chemistry Research* **2011**, null.
- (20) Raghuvanshi, R. S.; Goyal, S.; Singh, O.; Panda, A. K. *Pharmaceutical Development and Technology* **1998**, *3*, 269.
- (21) Anderson, D. E.; Becktel, W. J.; Dahlquist, F. W. *Biochemistry* **1990**, *29*, 2403.
- (22) Lepock, J.; Frey, H.; Ritchie, K. *The Journal of Cell Biology* **1993**, *122*, 1267.
- (23) Chi, E. Y.; Krishnan, S.; Randolph, T. W.; Carpenter, J. F. *Pharmaceutical Research* **2003**, *20*, 1325.
- (24) Takeuchi, H.; Yamamoto, H.; Kawashima, Y. *Advanced Drug Delivery Reviews* **2001**, *47*, 39.
- (25) Cleland, J. L.; Daugherty, A.; Mrsny, R. *Current Opinion in Biotechnology* **2001**, *12*, 212.
- (26) Torchilin, V. P.; Lukyanov, A. N. *Drug Discovery Today* **2003**, *8*, 259.
- (27) Lin, C.-C.; Anseth, K. *Pharmaceutical Research* **2009**, *26*, 631.
- (28) Swiston, A. J.; Cheng, C.; Um, S. H.; Irvine, D. J.; Cohen, R. E.; Rubner, M. F. *Nano Letters* **2008**, *8*, 4446.
- (29) Sukhishvili, S. A.; Granick, S. *Journal of the American Chemical Society* **2000**, *122*, 9550.
- (30) Zhuk, A.; Pavlukhina, S.; Sukhishvili, S. A. *Langmuir* **2009**, *25*, 14025.
- (31) Larkin, A. L.; Davis, R. M.; Rajagopalan, P. *Biomacromolecules* **2010**, *11*, 2788.

- (32) Gui, Z.; Qian, J.; An, Q.; Zhao, Q.; Jin, H.; Du, B. *Journal of Materials Chemistry* **2010**, *20*, 1467.
- (33) Yamato, M.; Okano, T. *Materials Today* **2004**, *7*, 42.
- (34) Yamato, M.; Akiyama, Y.; Kobayashi, J.; Yang, J.; Kikuchi, A.; Okano, T. *Progress in Polymer Science* **2007**, *32*, 1123.
- (35) Vreugdenhil, A. J.; Woods, M. E. *Progress in Organic Coatings* **2005**, *53*, 119.
- (36) Dubas, S. T.; Schlenoff, J. B. *Macromolecules* **2001**, *34*, 3736.



# CHAPTER 6: LAYER BY LAYER ASSEMBLY FOR ANTI-REFLECTION ON THERMOPLASTIC SUBSTRATES

## 6.1 Abstract

Reflections occur when light passes through interfaces separating media of different optical density. Coatings able to suppress reflection from lens surfaces are thus needed for proper function of advanced optical systems. In order to study cosmic rays in outer space, NASA requires anti-reflection coatings on large poly(methyl methacrylate) (PMMA) Fresnel lenses. Due to the large size of these lenses and the glass transition of PMMA of  $\sim 105^{\circ}\text{C}$ , many conventional vacuum-based/ high-temperature methods used to create AR coatings cannot be applied. Here we demonstrate LbL assembly of silica nanoparticles and poly(allyamine hydrochloride) as an elegant means to create conformal low reflective index coatings for UV AR on PMMA. We reveal several salient features of LbL nanoparticle assembly in creating thin sub-90 nm thick coatings. Further, we propose several strategies to increase the robustness of these highly porous coatings. Interfacial stabilization was pursued using diblock copolymers of PMMA-PAA, while stabilization within the nanoparticle layer was achieved by chemical crosslinking. In addition, a novel thermoplasticity based (“sink and etch”) technique to create inverse surface porosity was proposed and demonstrated. Enhanced mechanical stability of functional surface features, which allowed them to withstand typical lens cleaning procedures, was achieved using dehydration crosslinking or the “sink and etch” approach. The mechanical stability conferred by post LbL treatments made them amenable to industrial applications, not possible for as assembled (aa) coatings due to the inherent weakness of highly porous aa nanoparticle layers. In addition, using cross-sectional SEM imaging, we show that the LbL assembled AR coatings can be applied conformally to Fresnel lenses with  $150\ \mu\text{m}$  saw-toothed edges.

## 6.2 Introduction

While Chapters 2 – 4 have focused on the use of LbL assembly to create temperature responsive thin film hydrogel coatings, LbL assembly is a highly versatile surface modification technique that can be applied to a wide variety of technological challenges, as described in Chapter 1 (Section 1.6). This Chapter demonstrates how the use of a different assembly component, inorganic nanoparticles, as opposed to responsive block copolymer micelles, can create conformal coatings of uniquely different functionality.

Anti reflection (AR) coatings that prevent reflection of specific wavelengths are needed for a wide range of applications<sup>1</sup>. For light collection and imaging, light needs to be passed through a series of lenses, that present multiple interfaces at which light is lost from reflections. For uncoated optics made of glass or plastics, 4-5% of light is lost by reflection at each interface. In addition to light loss, reflected light within optical setups can result in optical artifacts such as halos or ghost images. As such, AR coatings are essential to advanced optical systems like microscopes, cameras and telescopes, and various theoretical approaches to the optical design of AR coatings have been developed and refined since 1936<sup>1-4</sup>. One of the aims in a NASA international space station initiative was to have a large cosmic camera collect and study cosmic ray showers of UV wavelengths between 300-400 nm. To effectively gather this range of UV light, an AR coating suitable for large plastic optics is required. The targeted optics are Fresnel lenses (2.5 m in diameter) and made polymethyl methacrylate (PMMA) material that has a relatively low glass transition temperature ( $T_g$ ) of 105 °C. A facile, low temperature (< 105 °C), low-cost process to enable the creation of large-scaled, conformal AR coatings on the Fresnel lenses with preformed saw-tooth type surface structures thus needed to be developed.

Based on the principles of destructive interference, several theoretical algorithms able to reduce reflections from interfaces have been described<sup>1-6</sup>. Broadly, AR designs commonly used include: single refractive index coatings with tailored quarter wavelength optical thickness for narrow bandwidth AR<sup>4,6</sup>, multi-stack designs with alternating high and low refractive index layers<sup>5,7</sup> or graded index designs<sup>8</sup> for broad-band anti reflection<sup>4,5</sup>. In this Chapter we will make use of the single layer design. To suppress reflection at a single wavelength ( $\lambda_0$ ), the ideal single layer AR coating is one with homogeneous refractive index:  $n_c = (n_1 n_2)^{1/2}$  (where  $n_c$ ,  $n_1$ , and  $n_2$  are the refractive indices of the coating, the substrate, and its surrounding media

respectively), and of quarter-wavelength optical thickness:  $d_c$ , where  $n_c d_c = \lambda_0/4$ .<sup>4,6</sup> If AR is desired over a spectral region between wavelengths  $\lambda_1$  and  $\lambda_2$ , the reference wavelength  $\lambda_0$  is given by  $\lambda_0 = 2\lambda_1\lambda_2/(\lambda_1 + \lambda_2)$ .<sup>3,4,6</sup> Following from this relation, to create an AR coating for 300 nm to 400 nm on PMMA ( $n=1.49$ ) substrates, a coating of index 1.22 and thickness 70.3nm is required.

To date, low refractive index (RI) materials  $MgF_2$  ( $n = 1.40$  at 248nm)<sup>9,10</sup>,  $CaF_2$  ( $n = 1.47$  at 248nm)<sup>10</sup> and fused silica have been used to coat KrF laser windows as well as photolithographic elements for AR in the deep UV wavelengths of 193 to 248 nm<sup>10-12</sup>. Unfortunately these materials can often only be deposited as molecularly thin and smooth layers by high vacuum methods like electron beam evaporation<sup>10,13</sup>, molecular beam deposition<sup>11</sup> or chemical vapor deposition<sup>14</sup>. Due to the lower substrate RI of PMMA as compared to KrF laser windows, the RI of available bulk materials are higher than our desired optimal index of 1.22<sup>12</sup>. In order to achieve an effective single layer AR coating with a lower RI than component materials of a higher bulk RI, one can use equivalent quarter wavelength stacks as described in literature<sup>4</sup>, or introduce porosity that will lower the effective index of the single layer<sup>15</sup>.

Porous AR layers have been successfully created by sol-gel methods<sup>16</sup>, layer-by-layer assembly<sup>17</sup> and selective etching<sup>18</sup>. Since the lenses of interest are made of polymeric PMMA, organic solvents that can dissolve or plasticize PMMA need to be avoided. In addition, techniques such as colloidal sols<sup>19</sup> and sol-gel processes<sup>16</sup> that involve heat treatment cannot be applied to PMMA due to its  $T_g$  of 105 °C. The large size of the targeted optic poses an additional challenge to the AR coating deposition. For example, while the Masuda group has reported a conformal AR coating on Fresnel lenses using ordered anodic porous alumina<sup>20</sup>, their method involved multistep preparation under high vacuum and is cost limiting for large substrates.

Given the unique constraints of this project posed by the short wavelength AR desired; low index coating needed; heat and solvent sensitive substrate; micro-structured surfaces to be coated; and large overall size (2.5m across) of the optic to be coated, electrostatic layer-by-layer (LbL) deposition surfaced as the most suitable coating approach for this challenge.

Electrostatic LbL deposition of charged nanoparticles in conjunction with an oppositely charged polyelectrolyte has proven to be a feasible means to create porous conformal coatings with nanometer scaled thickness control on a wide variety of substrates<sup>17,21</sup>. This method involves deposition from aqueous solution and can be carried out in at room temperature under environmental conditions. It is thus cheap, environmentally friendly, easy to upscale, and amenable to PMMA substrates. By creating a layer of loosely packed silica nanoparticles on the surface of PMMA, LbL assembly can be used to form a layer of suitable optical thickness or provide a graduated change in refractive index between the PMMA substrate and air. Either approach can be tuned to provide the desired AR properties. In this chapter the LbL deposition conditions are explored and optimized to provide high quality AR in the desired UV spectrum.

In addition to optical performance, coatings need to be sufficiently robust to withstand typical handling and lens cleaning procedures. The high porosity and limited contact points between nanoparticles of low index coatings make them mechanically weak structures. As such, improving the mechanical robustness of porous nanoparticle coatings has been a longstanding challenge that also needs to be addressed. While Gemici *et. al.*<sup>22</sup> has presented hydrothermal treatment as a means to achieve highly robust nanoparticle coatings, such a technique cannot be applied to PMMA lenses since the hydrothermal treatment temperature is greater than its  $T_g$ . In this chapter, approaches to mechanically stabilize the porous nanoparticle/polymer AR coating both at the interface between the substrate and the coating, as well as within the coating itself are discussed. Notably a diblock copolymer of PMMA and PAA is employed to enhance adhesion at the coating-substrate interface while dehydration crosslinking between carboxylated silica nanoparticles and PAA was applied to improve film stability.

In attempts to find hydrothermal annealing conditions possibly amenable to PMMA substrates, we found that the surface mobility of PMMA was sufficiently high, even at temperatures below its  $T_g$ ; heating at 90 °C was sufficient to result in significant surface rearrangement that caused substrates to turn cloudy. This is not surprising because thermoplastics often exhibit free-surface suppression of  $T_g$  where polymer chains at the free surface have a lower  $T_g$  than the bulk value<sup>23,24</sup>. This phenomenon was investigated in more detail and utilized in the creation of robust inversely structured surface nanoporosity.

### 6.3 Materials and methods

**Materials.** Silica nanoparticles Ludox SM-30 (30 wt % SiO<sub>2</sub> suspension in water), Ludox HS-40 (40 wt % SiO<sub>2</sub> suspension in water), and Ludox TM-40 (40 wt% SiO<sub>2</sub> suspension in water, average particle size 24 nm), were purchased from Sigma-Aldrich (St. Louis, MO). Zirconium (IV) oxide (20 wt% ZrO<sub>2</sub> suspension in water, average particle size 5 nm) was purchased from Alfa Aesar. The average size of the nanoparticles was made known by the suppliers. Silica nanoparticles 50 nm in diameter (denoted simply as “SiO<sub>2</sub>”), product #24040, was purchased from Polysciences Inc.. and carboxylated 50 nm diameter Silica nanoparticles (denoted “SiO<sub>2</sub>-COOH”) were purchased from Kisker Biotech GmbH & Co.. Poly(allylamine hydrochloride) (PAH, M<sub>w</sub> ~ 56,000) and Ethyl alcohol (> 99.9% pure) were purchased from Sigma-Aldrich and UV transparent 1.5 mm thick PMMA, in sheets, (product # 530090) was purchased from ThyssenKrupp Materials North America and cut into 3” × 1” pieces.

**Layer-by-Layer (LbL) assembly of nanoparticle containing coatings.** LbL assembly of all nanoparticle and nanoparticle/polymer coatings onto PMMA substrates was performed using an automated StratoSequence VI spin dipper (from nanoStrata), controlled by StratoSmart v6.2 software, with substrates spun at 130–160 rpm as described in detail elsewhere<sup>25-27</sup> and in Chapters 1, 2 and 4. Here, 0.03 wt% nanoparticle solutions were made in DI water and adjusted to the desired pH with 1M NaOH or 1M HCl. pH 9 buffer was used for SiO<sub>2</sub> (50 nm diameter silica nanoparticles and multilayers deposited from SiO<sub>2</sub> in pH 9 buffer are denoted (positive component/SiO<sub>2</sub>(9b)) or (positive component/SiO<sub>2</sub>-COOH(9b)). 10 mM PAH solution (concentration based on the repeat unit) in DI water was used for LbL deposition. PMMA substrates were sonicated in 2 vol % Alconox detergent solution for at least 1 hr, rinsed 3 times with excess DI water and then sonicated in DI water for an additional hour and rinsed another 2 times before use. As opposed to all the previous multilayers discussed in this thesis, that involve one assembly pH, i.e. the pH of the positive solution, the negative solution and all rinse solutions were the same, several multilayers made in this chapter involve deposition from positive and negative solutions of different pH. For these cases, the rinse solutions of DI water were pH adjusted either to the pH of the positive solution or that of the negative solution, and arranged as illustrated in Figure 6-M1.

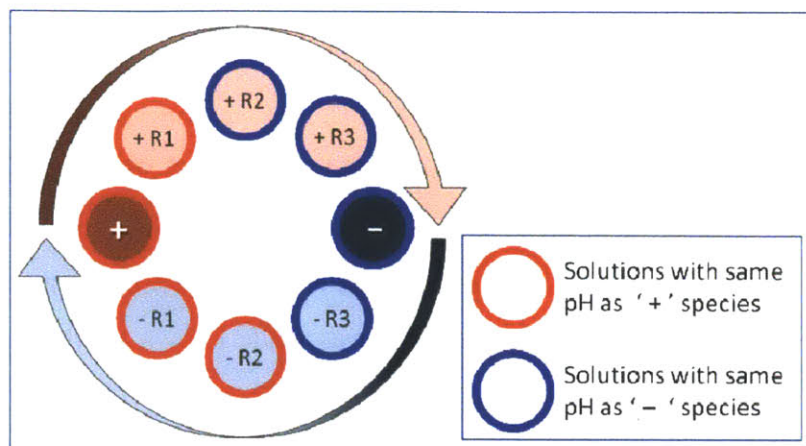


**Figure 6-M1.** LbL assembly arrangement of rinse solutions (adjusted to either the pH of the positive solution or the pH of the negative solution) adopted to minimize pH drift over the course of LbL assembly when positive species and negative species were deposited from solutions of different pH.

When pH 9 buffer was used in the case of SiO<sub>2</sub> and SiO<sub>2</sub>-COOH, rinse solutions used were just unadjusted DI water.

**Coating characterization.** Reflectivity measurements were performed between 200 and 800 nm using a Varian Cary 500i spectrophotometer. Spectroscopic ellipsometry (M2000-D, J. A. Woollam Co.) was used to determine the refractive index and thickness of the coatings. Results were collected from 300 to 900 nm at a 70° angle of incidence. The morphology coating surfaces was investigated with atomic force microscopy (AFM) by using a Nanoscope IV, Dimension 3000 AFM microscope (Digital Instruments, Santa Barbara) in tapping mode in air.

**Mechanical testing: ethanol wipe cleaning procedure.** This wiping method used is a typical PMMA optic lens cleaning procedure: a folded lint free cleaning tissue (Kimwipe) is saturated with ethyl alcohol and gently swiped across the optic/substrate in one direction with the optic/substrate held stationary. Tissues are never reused and a new piece is used for cleaning of larger areas and for repeating cleaning of the same spot.

## 6.4 Results and Discussion

### 6.4.1 Theoretical design of AR coatings on PMMA for 300-400nm UV wavelengths.

From Fresnel's equations<sup>3</sup>, optimal reflection suppression over the wavelengths of 300 – 400 nm is expected from a coating of refractive index,  $n_c=1.22$  and coating thickness,  $d_c=70.3$  nm. Matlab simulations\* were done to determine the AR sensitivity to variations in refractive index around this value. As seen in Figure 6-1, while a coating of  $n_c=1.22$  gives the best AR performance, coatings with  $n_c$  between 1.21 and 1.24 (of quarter wavelength optical thickness) work almost equally well. Coatings of lower or higher indices like 1.19, 1.2 or 1.25 cannot provide the same level of AR quality, despite having optimized thicknesses. The integrated area under each curve in Fig. 6-1a measures the total percentage of light intensity lost as a result of reflections in the 300 – 400 nm wavelength regime of interest. As seen in Fig. 6-1b the percentage of light lost steeply increases when the refractive index of the coating departs from the optimal value of 1.22. The objective of this work was to achieve less than 0.5% reflection for UV wavelengths between 300 – 400 nm. From the simulations, we found that coatings of refractive index between 1.21 and 1.23 were needed to satisfy this requirement.

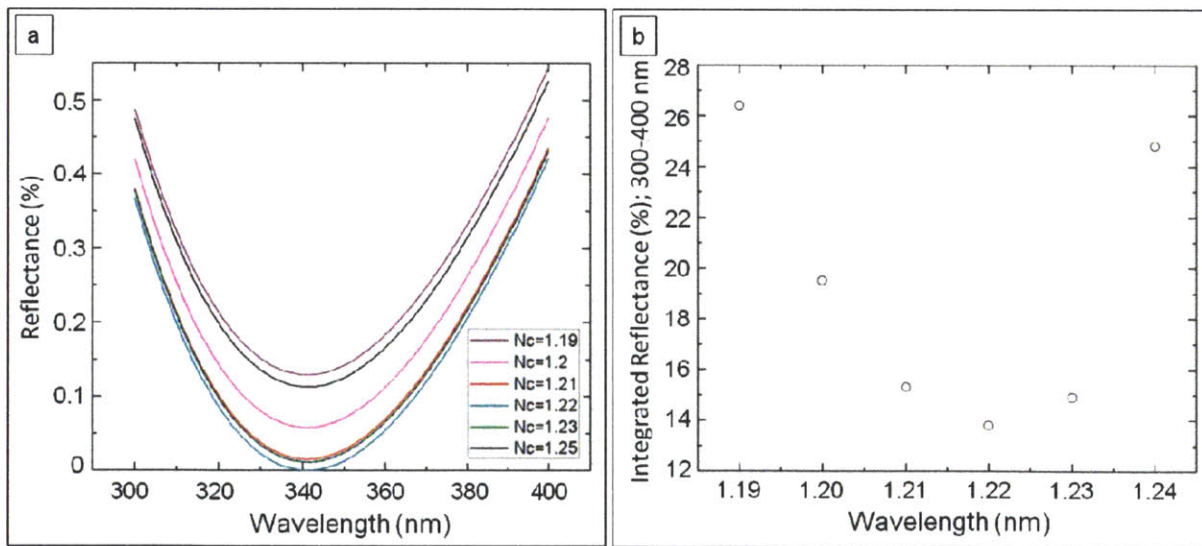


**Figure 6-1.** Sensitivity of single index coatings to changes in refractive index: (a) reflectance from single index coatings of various refractive indices; (b) integrated total reflectance (area under curve) between 300-400nm for coatings of the different refractive indices.

\*Computer simulations were done using Matlab® programs composed by previous lab members and details of the program can be found in the theses of A. J. Nolte and Z. Gemici.

## 6.4.2 Creating single layer AR coatings using Layer-by-Layer assembly.

Since most bulk materials have an RI greater than 1.23,<sup>10,12</sup> the need of a coating with such low RI is satisfied by the incorporation of porosity. The RI of a porous nanoparticle coating  $n_c$  can be estimated by a simple mixing rule<sup>17</sup>

$$n_c = f_{air} \cdot n_{air} + f_{nanoparticle} \cdot n_{nanoparticle}$$

$f_x$  and  $n_x$  are the volume fraction and refractive index of component  $x$  respectively. The index of the resultant coating is thus determined by the refractive index of the components used in the assembly, as well as the level of porosity ( $f_{air}$ ) incorporated. Varying the deposition pH of all nanoparticle and polymer/nanoparticle multilayers has been shown to affect the level of porosity incorporated within these LbL assemblies<sup>28,29</sup>.

To obtain a single index coating of appropriate refractive index using LbL assembly, a variety of UV transparent deposition materials and LbL deposition conditions were explored. A comprehensive list of coating refractive index and the thickness increment per bilayer of multilayers deposited from varied combinations of substrate modification, LbL components, LbL conditions and post assembly treatments can be found in Table C-1 in Appendix C. A shorter list of  $N_c$  and film thickness data<sup>†</sup> is shown in Table 6-1 to highlight key features of the nanoparticle multilayers studied for their optical properties.

By studying the assembly of negatively charged silica nanoparticles of different sizes with either small positively charged nanoparticles of ZrO (~5 nm diameter) or polycationic poly(allylamine hydrochloride) (PAH), we found the following trends. As shown in Table 6-1, the RI of nanoparticle coatings decreased with increasing size of the silica nanoparticle component assembled with the same, small, ZrO component.  $N_c$  of the all nanoparticle coatings decreased from 1.35 to 1.27 when the size of the silica nanoparticles used was increased from 9 nm (SM30) to 24 nm (TM40).

---

<sup>†</sup> A useful feature to note in the translation of theory to experiment is that while simulations search for optimized conditions based on continuous variables, thickness increments in the case of experimentally accessible nanoparticle multilayer coatings occur in discrete steps as each nanoparticle has a finite size and per bilayer thickness associated to it.



**Table 6-1.** Refractive index and thicknesses of various nanoparticle/nanoparticle and nanoparticle/polymer components used in LbL assembly of coatings on PMMA.

Multilayer components <sup>a</sup>	$N_c$	Thickness of 20bL film (nm)	Thickness per bL <sup>†</sup> (nm)
SM30(5) & ZrO <sub>2</sub> (3)	1.35	32	1.6
HS40(4.5) & ZrO <sub>2</sub> (3)	1.31	120	6.0
TM40(3) & ZrO <sub>2</sub> (3)	1.27	360	18
SM30(5) & PAH(5)	1.26	200	17
TM40(3) & PAH(4.5)	1.25	207	14

<sup>a</sup>Multilayer components used, include negative nanoparticles of silica: SM30(5) with average diameter 9 nm at pH 5; HS40(4.5) with average diameter 15 nm at pH 4.5; and TM40(3) with average diameter of 24 nm at pH 3. The deposition pH for each nanoparticle was selected to give them ~ the same zeta potential of -15 mV found to be optimal for LbL assembly.<sup>28</sup> Positively charged species used include ZrO(3): Zirconia nanoparticles of ~ 5 nm in diameter at pH 3, and poly(allylamine hydrochloride) (PAH) at pH 5 or pH 4.5.

Alongside the changes in refractive index, the mechanical stability of films was found to decrease with increasing porosity and decreasing refractive index of these systems. Mechanical stability is addressed in more detail in Section 6.4.3. A notable observation here is that assembly with PAH rather than ZrO resulted in coatings with lower RI. Following these findings, larger 50 nm diameter Silica nanoparticles (henceforth referred to as ‘SiO<sub>2</sub>’) are subsequently used in LbL assemblies with PAH to achieve coatings with the desired (lower) RI of ~1.22. Before moving on the studies done with the larger nanoparticles, it is important to note that most of the data in both Table 6-1 and Table C-1 were obtained from multilayers of thicknesses several times the diameter of the component nanoparticles. This was also the case for prior studies on LbL assembled AR coatings designed to suppress reflection in the visible spectrum. Here, the shorter UV wavelengths of interest necessitate thinner coatings, the ideal coating being ~70 nm thick. This thin film thickness is of the order of the individual SiO<sub>2</sub> nanoparticle size of 50 nm. While a 70 nm thick film would correspond to roughly 9 layers of

SM30 (8 nm particles) stacked on top of one another, a 70 nm thick film would be composed of less than 2 stacks of 50 nm SiO<sub>2</sub> particles. This brings us into a region of nanoparticle LbL assembly space that has been less explored.

It is important to distinguish the number of bilayers, which refers to the number of deposition cycles involved in LbL assembly, from the actual number of nanoparticle layers that exist in the coating. These two often will not correspond to one another. In the first deposition cycle the number of nanoparticles attached to the substrate surface can be less than that of a close packed layer of particles. Particles are randomly distributed and often do not completely fill the substrate surface, as demonstrated in Figure 6-2 and described in more detail by Olander *et al.*<sup>30</sup>.

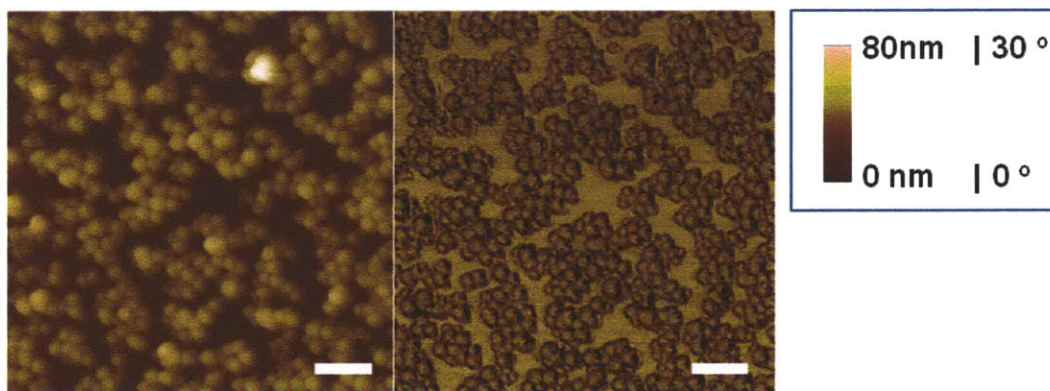


**Figure 6-2.** AFM images of (PAH(3)/SiO<sub>2</sub>(9b))<sub>1</sub>. The height image is shown on the left and the corresponding phase image, followed by the vertical scale bar is shown on the right. White scale bars in the images represent 300 nm.

The density of particles deposited at this stage depends strongly on the balance of electrostatic charge interactions. A more highly charged surface would attract a denser packing of nanoparticles, while highly charged nanoparticles tend to repel one another and be more sparsely dispersed on a substrate surface. In this manner the density of nanoparticle packing in the first few cycles of LbL deposition are highly sensitive to solution pH<sup>28</sup> and salt concentration<sup>29</sup> that influences the range of over which electrostatic interactions act. Addition of salt for example screens charges and can result in clustering of charge stabilized nanoparticles<sup>31</sup> in solution. Nanoparticles from solutions with added salt can then deposit as clusters rather than individual particles. Tuning pH and salt concentration in the first few

bilayers of nanoparticle deposition can thus effectively tune the particle packing density and hence the effective refractive index of the layer.

As seen in Figure 6-3, upon charge compensation by the layer of PAH deposited onto the nanoparticles deposited in the first cycle, more nanoparticles are able to fill the spaces between them during the second deposition cycle.

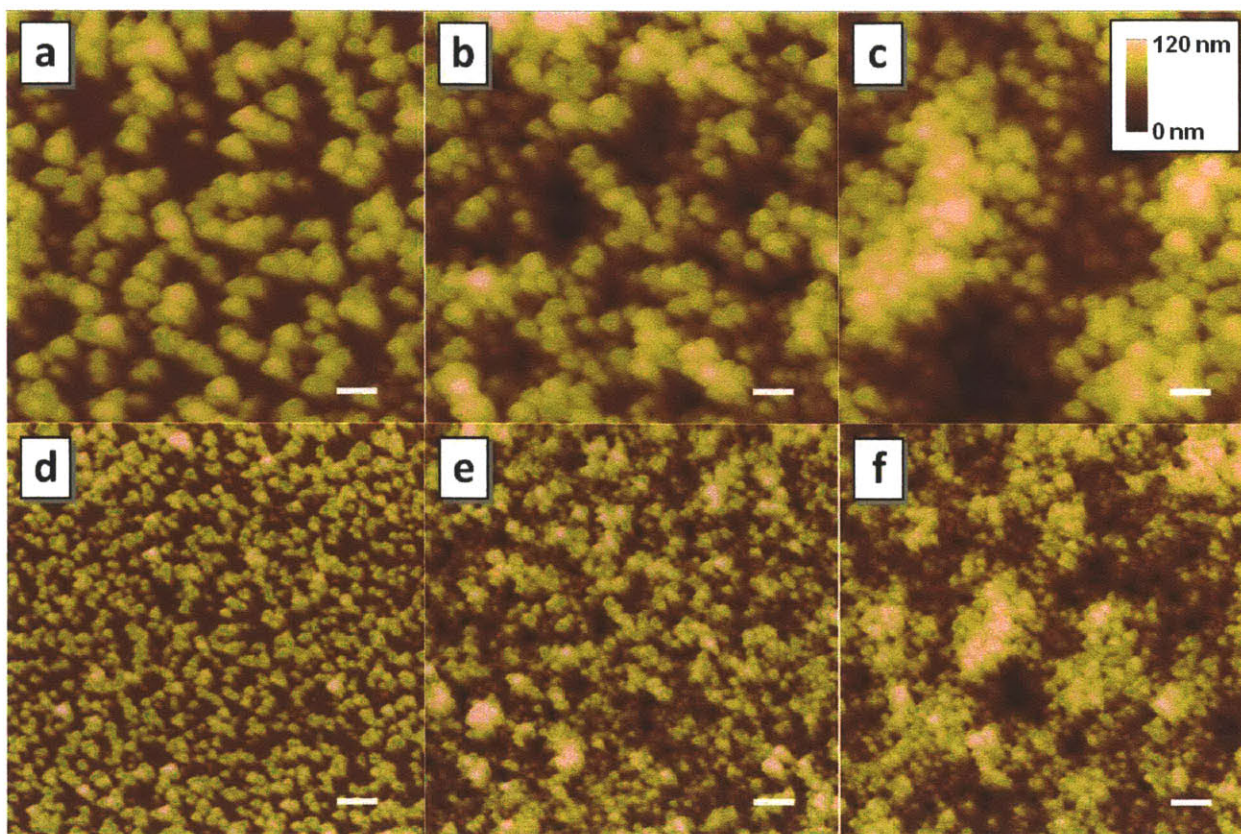


**Figure 6-3<sup>‡</sup>.** AFM height images of  $(\text{PAH}(6)/\text{SiO}_2(9b))_1$  ((a) and (d)),  $(\text{PAH}(6)/\text{SiO}_2(9b))_2$  ((b) and (e)) and  $(\text{PAH}(6)/\text{SiO}_2(9b))_3$  ((c) and (f)). The top row consist of  $2 \mu\text{m} \times 2 \mu\text{m}$  images while the bottom row consists of  $5 \mu\text{m} \times 5 \mu\text{m}$  images. Lateral scale bars shown in the bottom right represent 200 nm in the top row and 500 nm in the bottom row. The height scales for all images are the same and shown on the top right corner of (c).

Filling of the space between nanoparticles over multiple deposition cycles is reflected by the increasing RI seen in Fig. 6-4. From Fig. 6-4, we observe that the effective RI of

<sup>‡</sup> AFM images shown in Figure 6-3 were obtained by summer student Yassine Khitass. I thank him for his hard work and enthusiasm.

(PAH(6)/SiO<sub>2</sub>(9b)) coatings increase with bilayer number over the first 3 deposition cycles. The inset of Fig. 6-4 demonstrates how the refractive index of a 2 bilayer coating of PAH/SiO<sub>2</sub> can be tuned by varying the pH of the PAH deposition solution used for LbL assembly.

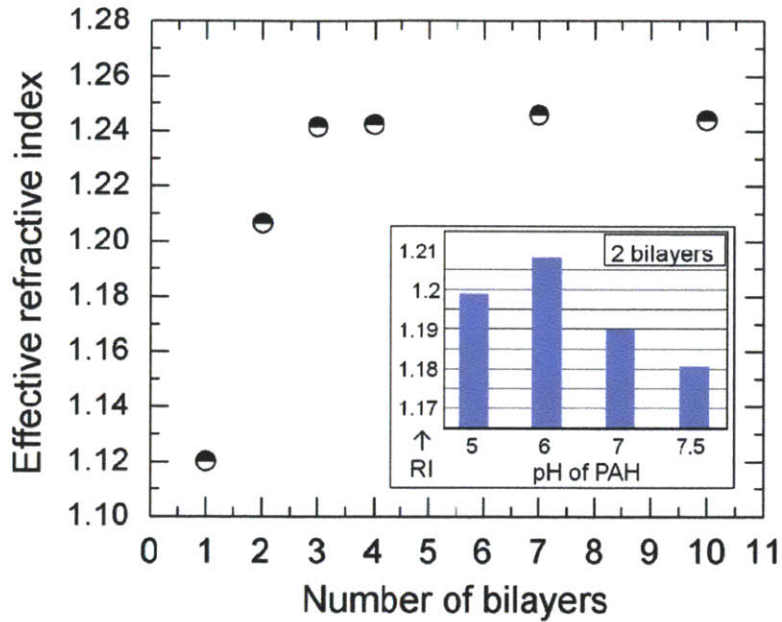


**Figure 6-4.** Effective refractive index (RI) of porous silica nanoparticle layers, (PAH(6)/SiO<sub>2</sub>(9b)), on PMMA, determined by spectroscopic ellipsometry, as a function of the number of bilayers (i.e. number of LbL deposition cycles). Inset shows the RI variation for 2 bilayers of SiO<sub>2</sub>(9b) assembled with PAH at different pH.

As predicted from the simulations in Section 6.4.1, the experimentally optimized coating (PAH(6)/SiO<sub>2</sub>(9b))<sub>2</sub> of RI 1.21 and thickness 80 nm proved to provide the desired high quality reflection suppression between 300 – 400 nm as shown in Figure 6-5. Figure 6-5 shows that native uncoated PMMA substrates reflect 7 – 8 % of the incident light of wavelengths between 300 – 400 nm. By coating PMMA substrates with 2 bilayers of (PAH(6)/SiO<sub>2</sub>(9b)), reflection can be reduced to less than 0.5 % in the 300 – 400 nm region of interest. This coating thus satisfies the AR quality desired by NASA for its space telescope lens. Since light collection is was the ultimate goal of reducing reflection, we also examined the transmittance of the native and coated PMMA substrates.

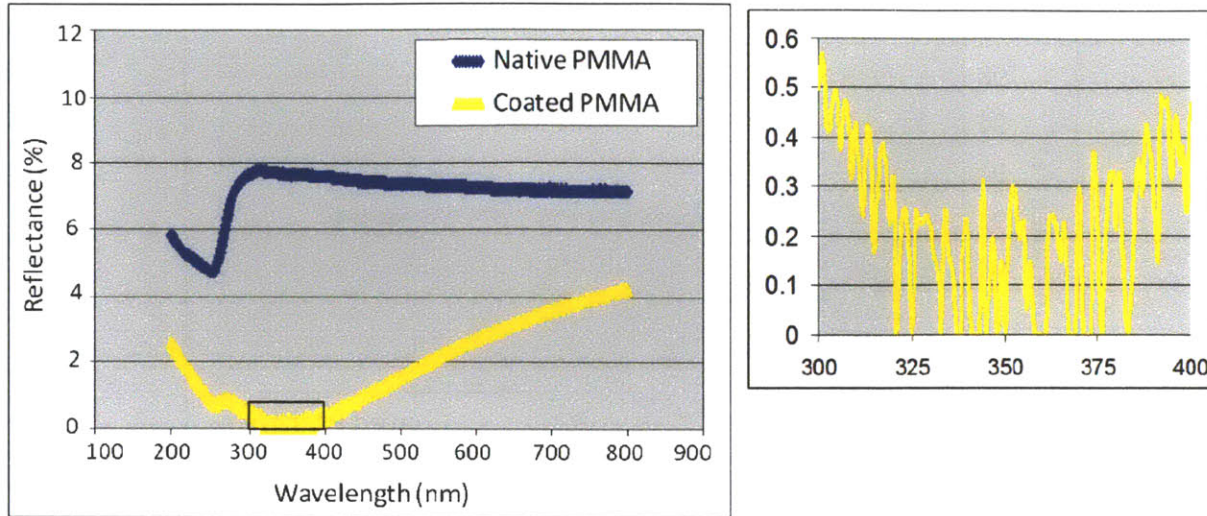


**Figure 6-5.** Reflectance from 1.5 mm thick PMMA samples coated on both sides with  $(\text{PAH}(6)/\text{SiO}_2(9b))_2$  (yellow) contrasted with the bare uncoated native PMMA substrate (blue) over wavelengths of 200 – 800 nm. Reflectance was determined by UV-Vis spectroscopy in reflectance mode. On the right is a zoom into the reflectance from the coated sample over the 300 – 400 nm wavelength region of interest.

As seen in Figure 6-6, application of our AR coating can significantly increase the amount of transmitted light from 92% to 98% in the region of interest.

It is important to note that the substrates used in our studies are not of high optical quality. As a result, incident light is lost through reflection as well as through scattering and absorption during the passage of light through the PMMA substrate. The percentage of light lost from the latter processes can be quantified by  $(100 - A - B) \%$ , where A is the percentage of incident light transmitted and B is the percentage of incident light reflected. The losses obtained in this manner are plotted as a function of wavelength in Figure 6-7.

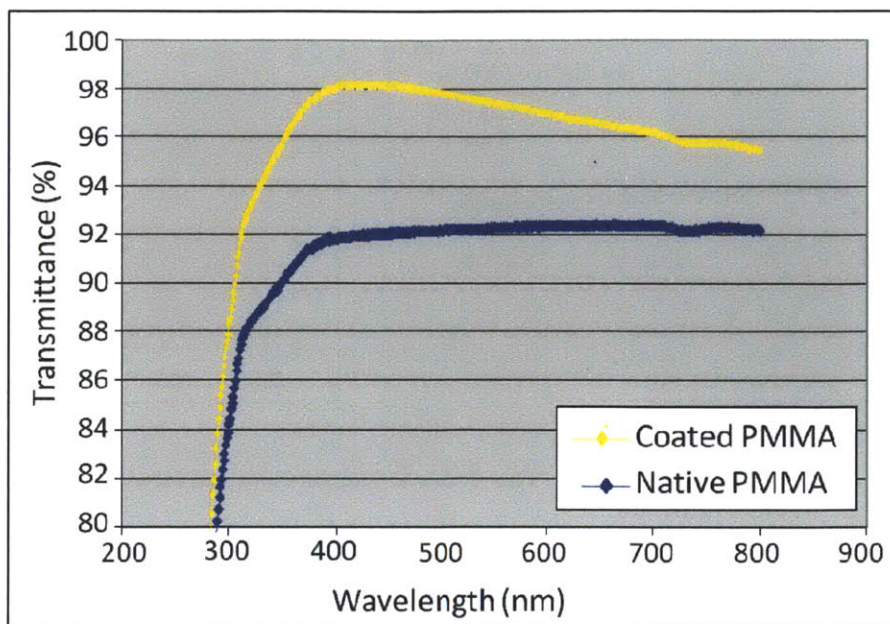


**Figure 6-6.** Transmittance of native uncoated PMMA (blue) and PMMA coated with  $(\text{PAH}(6)/\text{SiO}_2(9b))_2$  (yellow) determined by UV-Vis spectroscopy in transmission mode.

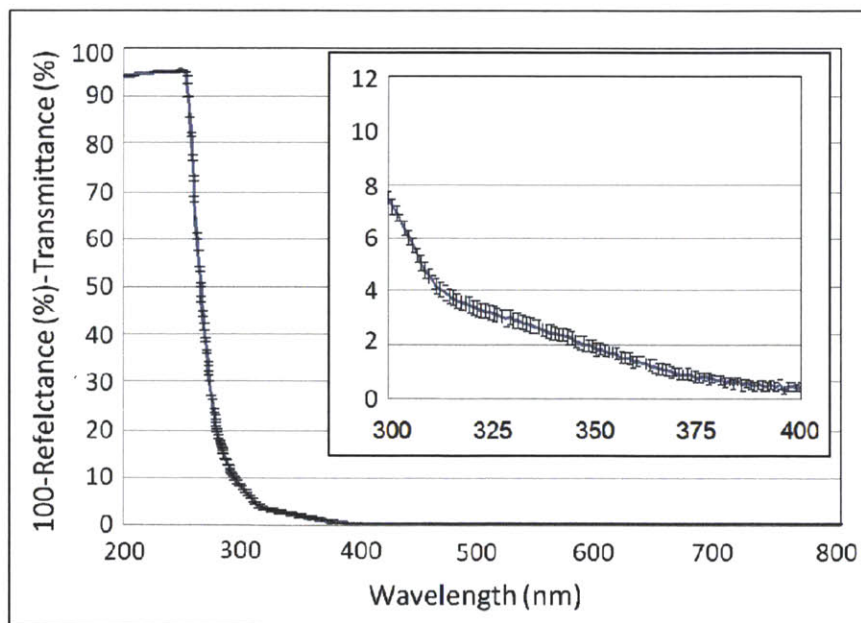


**Figure 6-7.** The wavelength dependent scattering and absorptive losses ( $100 - \text{Reflectance} (\%) - \text{Transmittance} (\%)$ ) of native (uncoated) PMMA substrates used in our studies.

Figure 6-7 shows that as much as 8 % of incident light with wavelengths between 300 – 400 nm is lost through scattering and absorption. Scattering losses were likely related to surface defects that we found present on the substrate surfaces (refer to Appendix D, Figure D-1). As seen in Fig. 6-7, losses increase drastically at short wavelength ( $\lambda$ ). This is because losses via Rayleigh scattering scale as  $\lambda^{-4}$ . While little loss occurs for light of longer wavelength (above 400 nm), Rayleigh scattering creates significant loss of transmitted light at shorter wavelengths between 300 – 400 nm, in the UV region of interest. Losses from molecular absorption become significant and result in a sharp increase in light loss below 300 nm. Normalizing for the inherent scattering of the substrates, the passage of 300 – 400 nm light through AR coating itself can be deduced to cause ~2 – 4 % loss in light intensity. This is because the nanoparticles in the coating (diameter ~ 50 nm) are, themselves, scattering bodies. Since scattering from particles scale as  $d^6$ , with  $d$  being the diameter of the particle, smaller nanoparticles might be preferred over larger ones to reduce scattering. New methods to create AR coatings of suitably high porosity with smaller nanoparticles may help reduce these losses. Unfortunately, the creation of sufficiently porous multilayers using small nanoparticles is a challenge as seen in Section 6.4.2. For these reasons, thin walled hollow silica nanoparticles were pursued as an alternative means to achieve tunable low refractive index coatings in collaboration<sup>32</sup>. This was an attempt to create lower index coatings with smaller nanoparticles. While smaller particles pack more densely, and have lower inter-particle porosity, introduction of porosity within the nanoparticles can possibly compensate for this and maintain the high porosity at higher particle packing density. Hollow nanoparticles were shown to provide additional tunable parameters, expanding the toolset we have available for creating AR coatings with LbL assembly<sup>32</sup>.

As mentioned previously, a large part of the motivation for using LbL assembly to create UV AR coatings intended for NASA space lenses was the fact that LbL assembly is known to create conformal coatings that would be applicable to the grooved surfaces of Fresnel lenses. Figure 6-8 shows that (PAH(6)/SiO<sub>2</sub>(9b))<sub>2</sub> coatings optimized for the desired AR properties on flat substrates can indeed be conformally applied to the saw-toothed (~ 150  $\mu$ m) surface features of a Fresnel lens. Regions of abrasion damage resulting from the freeze fracture process reveal parts of the bare substrate surface. High magnification images of the fractured edge seen in Fig. 6-8d demonstrate conformality of the coating.

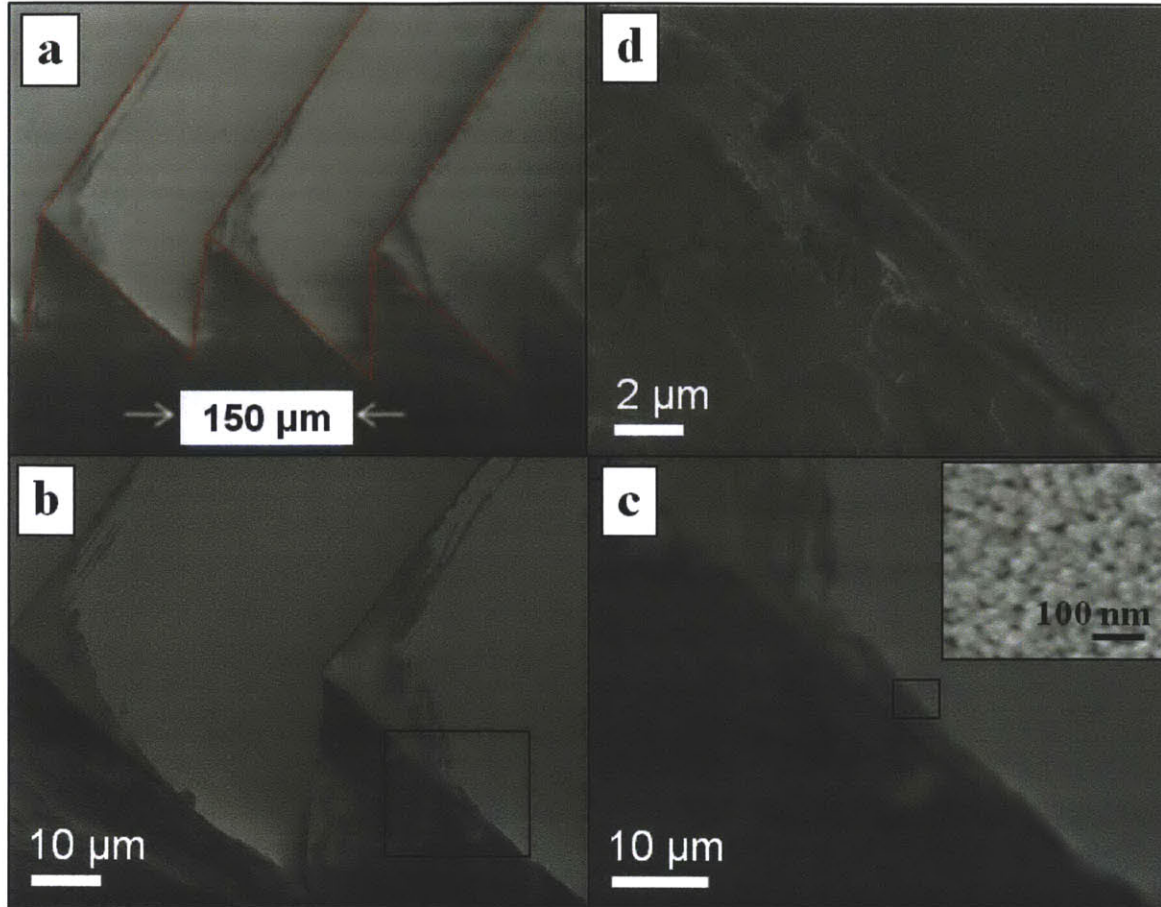


**Figure 6-8<sup>§</sup>.** SEM images of a PMMA Fresnel lens coated with  $(\text{PAH}(6)/\text{SiO}_2(9b))_3$  show conformal coating by the LbL assembly method. (a) is an overview of the grooved saw-toothed edged surface of the coated, freeze fractured PMMA Fresnel lens; (b) is an enlarged image of one of the grooves and (c) is a higher magnification of the boxed region in (b). (d) is a higher resolution magnified image of the boxed region in (c). The inset in (c) shows a magnified view of the flat, sloping coated surface of the nanoparticle coated groove.

<sup>§</sup> SEM image obtained by collaborator, post doc, Yi Du, in Prof Cohen's Lab, who subsequently took over the anti-reflection project.



### **6.4.3. Improving the mechanical stability of nanoparticle multilayers.**

Highly porous nanoparticle coatings suffer from poor mechanical stability. While the low-index coatings developed in the previous section have excellent AR functionality, they are not mechanically durable as assembled. Unacceptable loss of AR properties were found to result when as assembled nanoparticle coatings are gently wiped in typical lens cleaning procedures (refer to Methods). Although mechanical durability can be imparted to all-silica coatings by hydrothermal treatment<sup>22</sup> at 124 – 134 °C, due the 105 °C glass transition temperature of PMMA, this procedure cannot be applied here. While hydrothermal treatment at lower temperatures tolerated by PMMA was investigated, this treatment resulted in densification of the LbL film and loss of AR properties (refer to Appendix D, Table D-2 for data on changes in RI and thickness of coatings resulting from hydrothermal treatment). Additionally hydrothermal treatment, when done at lower temperatures, did not afford observable improvements in coating robustness.

In order to improve the mechanical robustness of these UV AR coatings, we tried a few different approaches. The first approach sought to improve interfacial adhesion through surface functionalization of the PMMA substrates with diblock copolymers of PMMA and PAA. Next we explored chemical crosslinking as a means to enhance robustness within the coating layer itself, and finally, we proposed a method that utilizes the thermoplasticity of PMMA to our advantage in the creation of inverse surface nanoporosity.

#### ***6.4.3a Improving interfacial adhesion through surface functionalization with PMMA-PAA.***

As described in Chapter 1, Section 1.4 block copolymers exhibit interesting self assembly behavior driven by differences in chemical affinity of the connected blocks. Here, we utilize solvent selectivity to drive the adsorption of PMMA-PAA diblock copolymers onto the surface of PMMA as illustrated in Figure 6-9 (a) and (b). Subsequently, thermal annealing was employed to allow the surface adsorbed PMMA block to mix and form entanglements with the PMMA chains of the substrate surface (Fig. 6-9c). In doing so, we hoped to achieve a surface anchoring layer of block copolymer molecules that would be part entangled in the substrate and part actively bonded to the nanoparticle coating as shown in Fig. 6-9d.

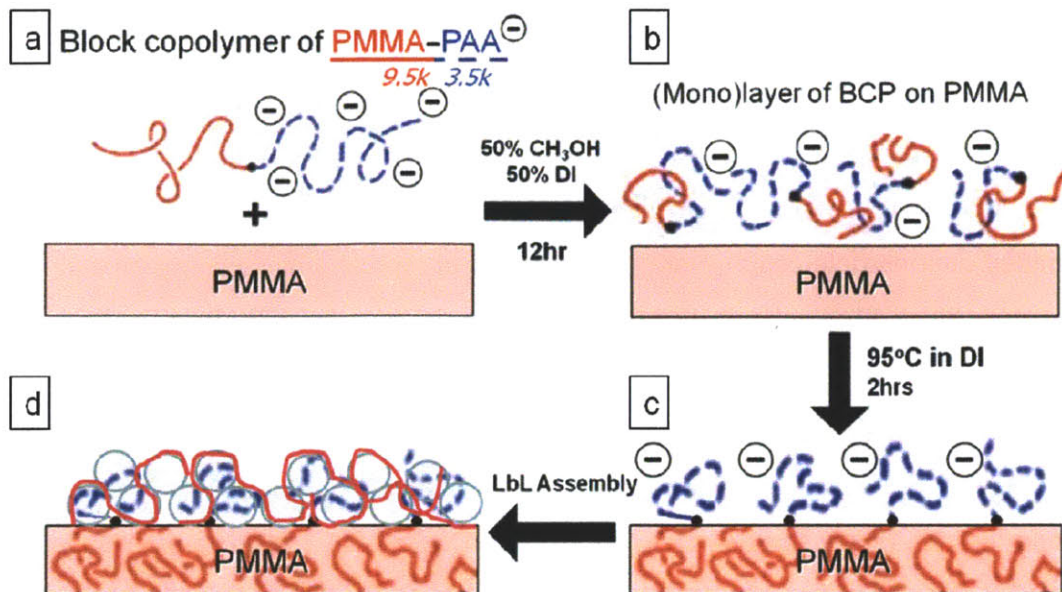


**Figure 6-9.** Schematic illustration of the method developed to modify the PMMA substrate with an anchoring layer of PMMA-PAA.

Careful attention should be paid to the choice of the solvent used in the deposition step of Fig. 6-9(a-b). While methanol is a good solvent for PMMA and the PMMA-PAA diblock copolymers, using pure methanol resulted in etching of the PMMA substrate surface and loss of optical clarity. On the other hand, using a non-solvent for PMMA made dispersion of the PMMA-PAA block difficult. As such, a mixed solvent system, of 50 % Methanol and 50 % DI water by volume, was used to allow for dissolution of the PMMA-PAA diblock but not the PMMA substrate.

Upon surface adsorption, annealing was done in water at 95 °C to provide thermal mobility to the PMMA chains and allow for integration of the surface adsorbed PMMA block into the PMMA substrate surface. The annealing was done in water to encourage extension of the water soluble PAA block out of the PMMA surface while surface mixing of PMMA proceeded. As shown in Figure 6-10, surface modification with PMMA-PAA results in a surface layer of hydrophilic PAA that lowers the contact angle of PMMA. Uncoated PMMA has a static contact angle similar to the advancing contact angle of 73° and a receding contact angle of 48°. As shown in Figure 6-10, while a 12 hr deposition time was used here, the equilibrium coating

of PMMA-PAA was likely achieved within 2 hrs and a shorter time can be used in the future. Also the annealing step at 95 °C in water was effective in further reducing both the static and advancing contact angles of the PMMA coated with PMMA-PAA.

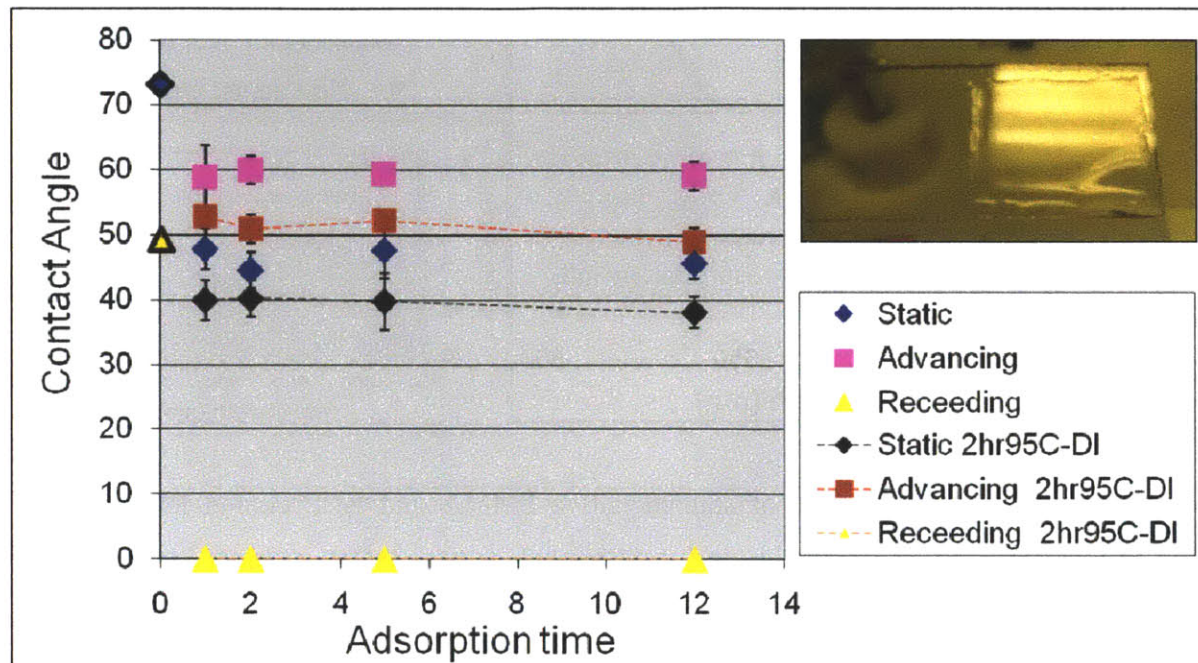


**Figure 6-10.** Static (diamonds), advancing (squares) and receding (triangles) contact angles of water: on uncoated PMMA substrates (points on the y-axis); on PMMA substrates with PMMA-PAA adsorbed from solutions of 1 mg/ml 50% methanol 50% DI water. Adsorption was done over 1, 2, 5, and 12 hrs. Contact angles measured before (symbols not connected) and after 2 hrs annealing in aqueous solution at 95 °C (symbols connected by dotted lines) are presented. The photograph on the top right shows the BCP modified region of PMMA holding onto a film of water.

Methylene blue (MB) staining was used to confirm the presence of carboxylic acid groups on the BCP surface modified PMMA substrates. As shown in Figure 6-11, the surface modification of PMMA with PMMA-PAA diblocks present carboxylic acid groups on the PMMA substrate surface. While MB staining of native PMMA was negligible, MB binds to the carboxylic acid groups of PAA on the BCP coated PMMA. MB staining of the BCP coated PMMA is reflected by the dip in transmission over the 550 nm region where MB absorbs light.

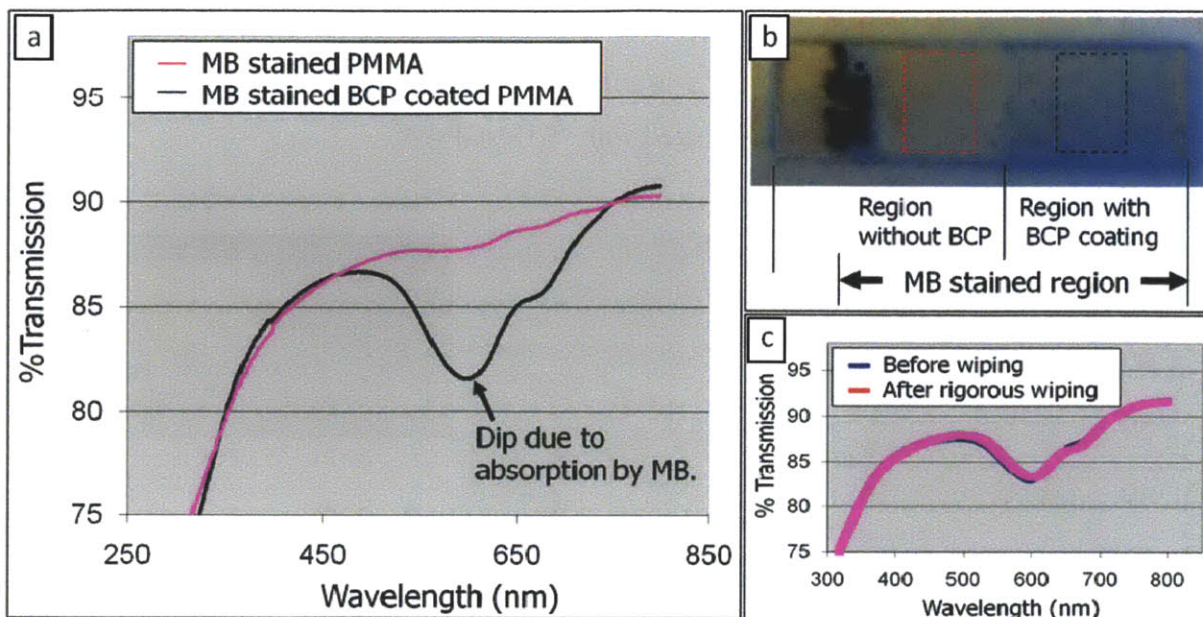


**Figure 6-11.** Transmission spectra of stained native PMMA and BCP coated PMMA (a). Staining was done by 1.5 hr immersion in 0.1 M methylene blue (MB) solution. Staining and absorption at 550 nm indicates presence of acid groups. (b) shows a photograph of the uniformly coated and MB stained vs uncoated, MB stained regions of a PMMA sample. (c) shows the transmission spectrum before and after vigorous wiping with kimwipes.

Rigorous (not gentle lens cleaning) wiping of the surface with kimwipes did not change the absorption spectra of the BCP coated regions as seen in Fig. 6-11c. This indicated that the diblock copolymer was strongly anchored into the PMMA substrate.

Despite the successful and robust surface modification with the diblock copolymers, the BCP coating did not noticeably enhance the mechanical robustness of the nanoparticle layers subsequently built on the modified interface. This could mean that coating failure was not dominated by poor interfacial adhesion but occurred through failure within the coating itself. Further it is possible that using block copolymers with a longer polyelectrolyte block, and in particular, a PMMA-polycation (rather than polyanionic PAA) could be more effective in coating stabilization.

### 6.4.3b Use of carboxylated Silica nanoparticles and dehydration crosslinking of AR coatings for mechanical stabilization within the multilayer coating.

A simple crosslinking approach was employed to stabilize the LbL assembly. In order to do this, carboxylated 50 nm Silica nanoparticles were used. The carboxylic acid groups on the silica nanoparticles can be covalently linked to the amine groups on PAH through the formation of amide linkages via thermal dehydration at 70 °C in a dry environment for 72 hrs. As shown in Figure 6-12, due to the different surface chemistry of carboxylated Silica nanoparticles (SiO<sub>2</sub>-COOH) as compared to SiO<sub>2</sub> studied in Section 6.4.2, (PAH(6)/SiO<sub>2</sub>-COOH(9b))<sub>2</sub> does not have the exact same AR properties as (PAH(6)/SiO<sub>2</sub>(9b))<sub>2</sub>. In addition to that, dehydration crosslinking of the as assembled (PAH(6)/SiO<sub>2</sub>-COOH(9b))<sub>2</sub> coating at 70 °C for 72 hrs, results in a dramatic shift in the AR peak from ~ 410 nm to less than 200 nm as seen in Figure 6-12. This is likely to result from film densification during the thermal dehydration crosslinking process and partial sinking of nanoparticles into the PMMA substrate surface. The latter phenomena will be discussed further in Section 6.4.3c.

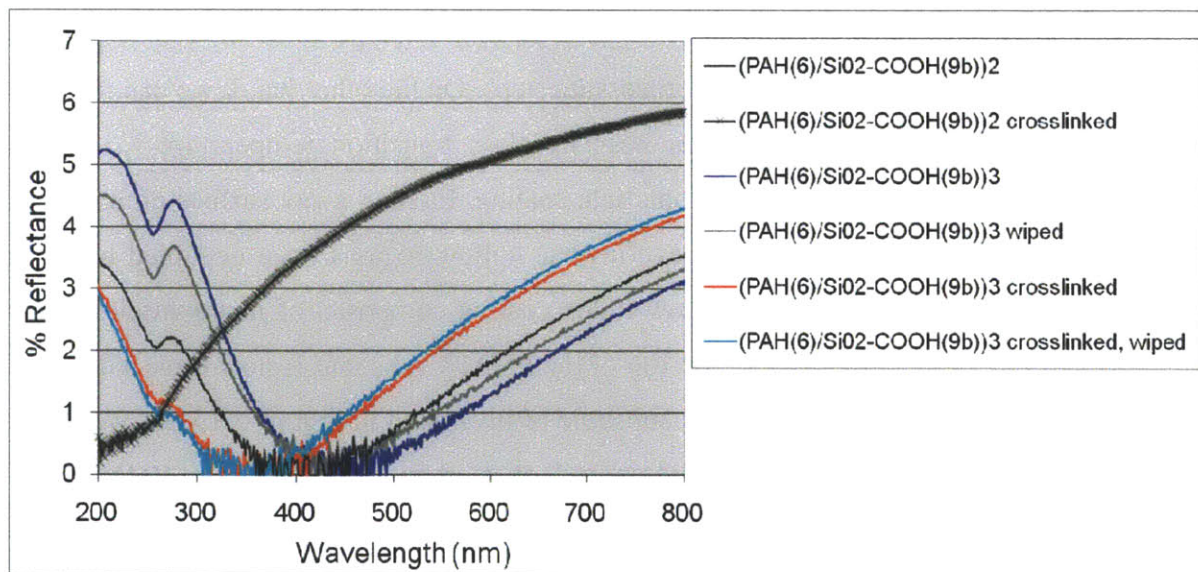


**Figure 6-12.** Reflectance from PMMA coated with (PAH(6)/SiO<sub>2</sub>-COOH(9b)) multilayers showing the effects of thermal dehydration crosslinking at 70 °C for 72 hrs and the stability of the films to typical lens cleaning procedures (labeled wiped in the legend).

As seen in Fig. 6-12, using a thicker (PAH(6)/SiO<sub>2</sub>-COOH (9b))<sub>3</sub> rather than (PAH(6)/SiO<sub>2</sub>-COOH (9b))<sub>2</sub> coating, the post crosslinking film affords the desired AR properties in the 300 –

400 nm regime as shown by the red curve. The resistance of various as assembled and crosslinked coatings to standard lens cleaning procedures (described in the methods section) was studied by measuring AR performance before and after the cleaning procedure, with results included in Fig. 6-12. While the AR performance of as assembled films significantly changed upon simple cleaning, the dehydration crosslinking helped to stabilize the LbL assembly and allowed coatings to resist changes in AR properties upon cleaning. Although the AR properties are not perfectly conserved, the shape, width and position of the AR minima is mostly conserved and satisfies our requirements of  $< 0.5\%$  reflection within the 300 – 400 nm range.

#### ***6.4.3c “Sink and Etch”: Creating an inverse nanoporous surface layer in PMMA substrates for robust AR properties.\*\****

In addition to the use of dehydration crosslinking to create robust thin AR coatings for the 300 – 400 nm UV regime on PMMA, a novel method was conceived to create an inverse surface porous layer. As mentioned above, PMMA’s glass transition temperature of 105°C poses limitations by prohibiting high temperature processing steps. On the other hand, we can utilize thermoplasticity of PMMA at temperatures near its glass transition temperature to drive PMMA surface engulfment of the SiO<sub>2</sub> nanoparticle coating. Etching away surface embedded Silica nanoparticles with NaOH can then leave inverse hollow regions once occupied by the nanoparticles. In this manner, the original low index coating composed of nanoparticles and porosity between individual nanoparticles on top of the PMMA substrate is now replaced by a series of holes in the top layer of the PMMA substrate as illustrated in Figure 6-13. As we will show, such inversely structured porosity composed of a continuous piece of PMMA is mechanically more stable than as assembled nanoparticle coatings.

---

\*\* The work presented this section was done in collaboration with Yi Du (Post Doc) and Lunet E. Luna (undergraduate student). *I thank them for their efforts without which this work would not have been possible.*

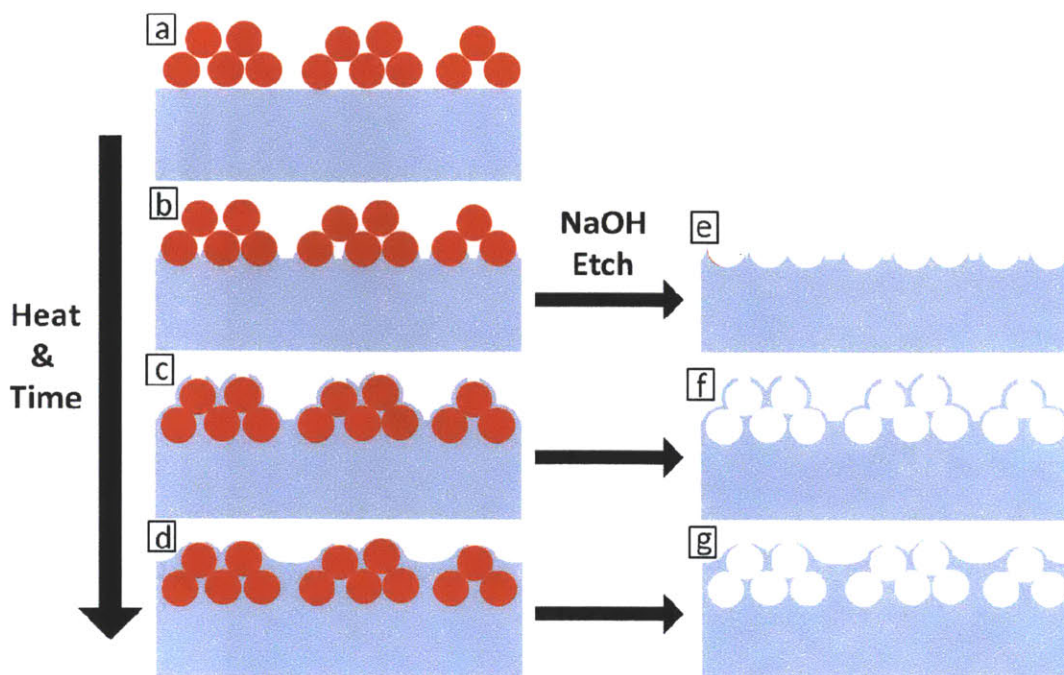


**Figure 6-13.** Illustration of the “sink and etch” approach to surface nanoporosity generation: (a) shows the as assembled nanoparticle coating, while PMMA wetting of the silica nanoparticles and the sinking of [PAH(6)/SiO<sub>2</sub>(9b)]<sub>2</sub> coating into the PMMA surface with heat treatment and time is shown from (b) to (d). Etching away the silica nanoparticles at different stages results in nanoporous PMMA surface layers with different morphologies ((e) to (f)).

As shown experimentally in Figure 6-14, the silica nanoparticles of the LbL assembled coating can be thermally driven into the surface of the PMMA substrate. The morphological evolution with annealing time at 90 °C seen in Fig. 6-14b and Fig. 6-14c, correspond to the schematic representations in Figs. 6-13c and 6-13d respectively.

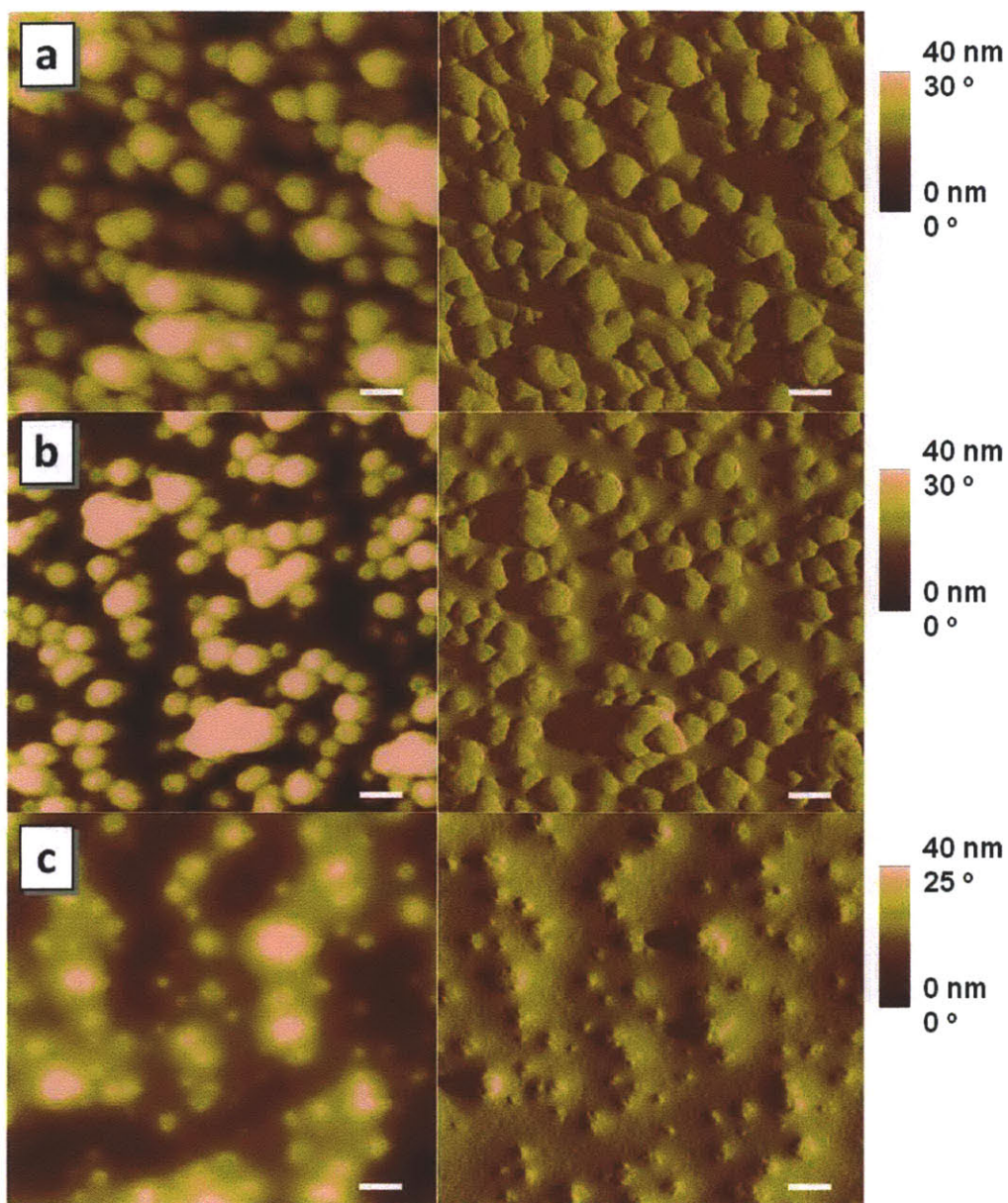


**Figure 6-14.**  $(\text{PAH}(6)/\text{SiO}_2(9b))_2$  (a) as assembled, (b) after annealing for 1 hr at 90 °C and (c) after annealing for 2 hrs at 90 °C. The images on the left are height images while the images on the right are corresponding phase images. Vertical scale bars are shown to the right of each row. Scale bars in the bottom right corner of images represent 100 nm.

Upon etching with NaOH, the surface embedded silica nanoparticles can be removed to create inverse hollow surface features as depicted in Fig. 6-13 (e) and (f) and experimentally revealed in Figure 6-15.



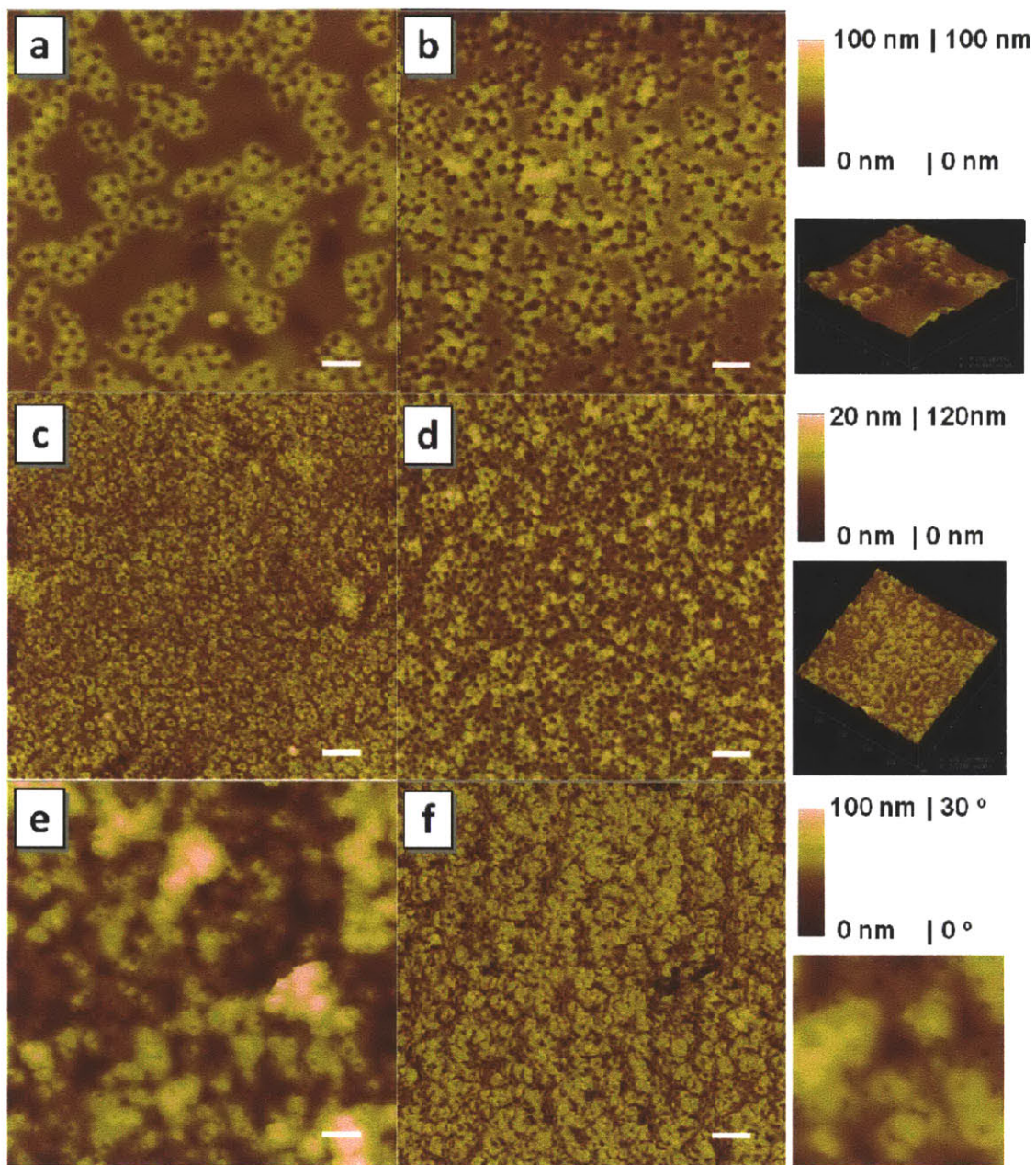


**Figure 6-15.** AFM height images of NaOH etched  $(\text{PAH}(6)/\text{SiO}_2(9b))_2$  on PMMA, (a) annealed at 90 °C for 1 hr (b) annealed at 70 °C for 5 hr (c) annealed at 80 °C for 5 hr, (d) annealed at 100 °C for 5 hr and (e) annealed at 140 °C for 1 hr. (f) is the phase image corresponding to (e). Scale bars at the bottom right of each image represent 300 nm and the vertical scales of images are shown on the right of each row. The small images on the right of each row are (3D) magnified images of the corresponding films in the left most column. These are included to offer a different view of the morphologies.

In accordance with the theory of time temperature superposition, we see that the extent of nanoparticle surface engulfment can be tuned by adjusting the temperature and time allowed for the annealing process. While some degree of sinking is observed upon annealing at 90 °C for 1 hr (Fig. 6-15a), annealing at a lower temperature of 70 °C for a longer time of 5 hrs (Fig. 6-15b) or 80 °C for 5 hrs (Fig. 6-15c) are alternatives for generating surface nanoporosity of different topography. Conversely, annealing can be done at higher temperatures (140 °C, 1 hr) in the same amount of time as that in Fig. 6-15a (90 °C, 1 hr) to achieve a much greater degree of nanoparticle engulfment, as shown in Fig 6-15(e and f). In general, the degree of nanoparticle sinking and engulfment increases with increasing annealing temperature when the annealing time is held constant. This is seen in the progression from Fig. 6-15 (b to c to d) and by comparing Fig 6-15a to Fig. 6-15f. It is interesting to note that the increased PMMA chain mobility at higher annealing temperatures around and above T<sub>g</sub>, results in rather unique structures upon removal of silica. Apart from temperature effects on chain mobility, it is possible that the wetting of silica particles by PMMA is also influenced by temperature. At higher temperatures (e.g. 140 °C), highly mobile surface chains of PMMA could move further upward to wet the silica nanoparticle surfaces more, before the nanoparticles sink into the original PMMA surface. This can possibly explain the empty shell-type morphologies seen in Figures 6-15e and 6-15f.

Samples heated at 140 °C for 1 hr and etched with 5 M NaOH were found to best preserve the AR properties of the original silica nanoparticle coatings. Figure 6-16 shows the reflectivity evolution through the various “sink and etch” processing steps. First, the bare PMMA substrate with ~ 7% reflectance is shown as the curve labeled ‘pristine’. The reflectance of coated PMMA with an as assembled nanoparticle coating is shown by curve ‘aa’. AR properties of this sample arise from the coating of silica nanoparticles that present a low refractive index via inter-particle air spaces. The curve ‘hed’ shows the reflectance from coated samples after heat treatment. When the coated samples are heated and silica nanoparticles sink into the PMMA surface, the preexisting porosity from inter-particle space that provides the low refractive index layer required for AR properties is lost. After NaOH is used to etch away the surface embedded silica nanoparticles, nanoporosity is regenerated in the surface layer of PMMA and AR properties are restored as seen from the excellent AR performance of the coated, heated and etched sample (curve labeled ‘hed’).

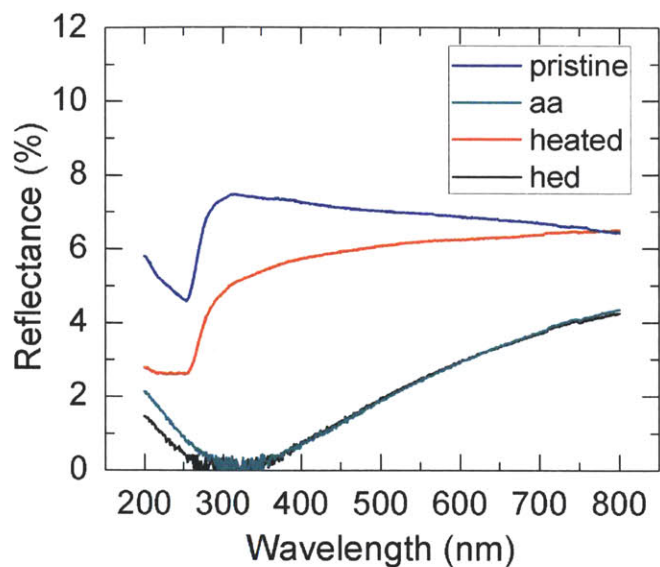


**Figure 6-16.** Reflectance from uncoated PMMA substrates (denoted 'pristine'), PMMA coated with as assembled  $(\text{PAH}(6)/\text{SiO}_2(9b))_2$  (denoted 'aa'), PMMA coated with  $(\text{PAH}(6)/\text{SiO}_2(9b))_2$  and heated at 140 °C for 1 hr (denoted 'heated') and PMMA coated with  $(\text{PAH}(6)/\text{SiO}_2(9b))_2$  and heated at 140 °C for 1 hr and etched in 5 M NaOH for 2 days (denoted 'hed').

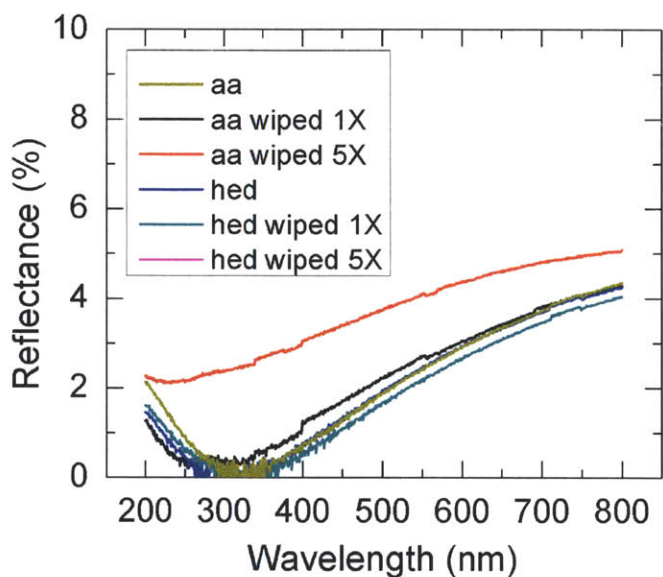


**Figure 6-17.** Reflectance from PMMA coated with as assembled  $(\text{PAH}(6)/\text{SiO}_2(9b))_2$  (aa), PMMA coated with  $(\text{PAH}(6)/\text{SiO}_2(9b))_2$  and heated at 140 °C for 1 hr and etched in 5 M NaOH for 2 days (hed) and the reflectance of each sample after wiping once and after wiping five times. Curves are labeled in the legend.

Both the as assembled polymer/nanoparticle LbL assembly ('aa') and the surface nanoporous layer generated by the post LbL assembly "sink and etch" procedure offer surface nanoporosity that can provide excellent AR properties, with reflection reduction to  $< 0.5\%$  across the targeted 300 – 400 nm wavelength region.

The "sink and etch" procedure replaces the original low RI nanoparticle coating (illustrated in Fig. 6-13a) with a series of holes in the surface layer of PMMA (illustrated in Figure 6-13g). This presents inversely structured porosity composed of a single, continuous piece of PMMA. As demonstrated in Figure 6-17, the resultant nanoporous surface layer of inverse structure offers greater mechanical stability. While a typical lens cleaning procedure (described in the Experimental Section) disturbs the as assembled nanoparticle coating after the first wipe and significantly disrupts the AR coating after 5 rounds of wiping, the inverse porous surface retains its AR properties upon multiple cleaning cycles.

## 6.5 Conclusions

In conclusion, we have shown that LbL assembly of 50 nm Silica nanoparticles and PAH is a facile means to create low index thin ( $\sim 80$  nm) conformal coatings on PMMA. We presented the theoretical framework for the optical design of an AR coating required specifically for transmission of 300 – 400 nm light. Subsequently, we showed that through the choice of component nanoparticles and deposition conditions, we can achieve high AR performance of  $< 0.5\%$  reflection across the 300 – 400 nm wavelength regime of interest. In addition, we explored several methods that could potentially increase the robustness of as assembled porous nanoparticle coatings. We explored (1) improving interfacial adhesion of the coating through deposition and integration of an anchoring block copolymer layer, (2) crosslinking of carboxylic acid surface functionalized silica nanoparticles with PAH to enhance cohesion within the multilayers, and (3) a novel thermoplasticity enabled process that involves sinking of the nanoparticle coating into the PMMA substrate surface, followed etching away of embedded nanoparticles to create a robust, porous, anti-reflective surface layer, continuous with the PMMA substrate itself. Tested with standard lens cleaning procedures, both the dehydration crosslinking with carboxylated silica nanoparticles and the "sink and etch" approach proved effective in enhancing AR coating stability.

## References

- (1) Francon, M. *Modern Applications of Physical Optics*; Interscience Publishers, 1963.
- (2) Dobrowolski, J. A.; Tikhonravov, A. V.; Trubetskov, M. K.; Sullivan, B. T.; Verly, P. *G. Appl. Opt.* **1996**, *35*, 644.
- (3) Epstein, L. I. *J. Opt. Soc. Am.* **1952**, *42*, 806.
- (4) Schallenberg, U. B. *Appl. Opt.* **2006**, *45*, 1507.
- (5) Willey, R. R. *Appl. Opt.* **1993**, *32*, 5447.
- (6) Rancourt, J. D. *Optical thin films: User's handbook*; SPIE Optical Engineering Press, 1996.
- (7) Southwell, W. H. *Appl. Opt.* **1985**, *24*, 457.
- (8) Jacobsson, R. In *Progress in Optics*; Wolf, E., Ed.; Elsevier: 1966; Vol. Volume 5, p 247.
- (9) Schubert, E. F.; Kim, J. K.; Xi, J. Q. *physica status solidi (b)* **2007**, *244*, 3002.
- (10) Rainer, F.; Lowdermilk, W. H.; Milam, D.; Carniglia, C. K.; Hart, T. T.; Lichtenstein, T. L. *Appl. Opt.* **1985**, *24*, 496.
- (11) Laux, S.; Mann, K.; Granitza, B.; Kaiser, U.; Richter, W. *Appl. Opt.* **1996**, *35*, 6216.
- (12) Xi, J. Q.; Schubert, M. F.; Kim, J. K.; Schubert, E. F.; Chen, M.; Lin, S.-Y.; Liu, W.; Smart, J. A. *Nat Photon* **2007**, *1*, 176.
- (13) Zhang, F.; Yang, W.; Pang, A.; Wu, Z.; Qi, H.; Yao, J.; Fan, Z.; Shao, J. *Applied Surface Science* **2008**, *254*, 6410.
- (14) Nagel, H.; Metz, A.; Hezel, R. *Solar Energy Materials and Solar Cells* **2001**, *65*, 71.
- (15) Kennedy, S. R.; Brett, M. J. *Appl. Opt.* **2003**, *42*, 4573.
- (16) San Vicente, G.; Morales, A.; Gutiérrez, M. T. *Thin Solid Films* **2002**, *403-404*, 335.
- (17) Lee, D.; Rubner, M. F.; Cohen, R. E. *Nano Letters* **2006**, *6*, 2305.
- (18) Schirone, L.; Sotgiu, G.; Califano, F. P. *Thin Solid Films* **1997**, *297*, 296.
- (19) Thomas, I. M. *Appl. Opt.* **1992**, *31*, 6145.
- (20) Yanagishita, T.; Nishio, K.; Masuda, H. *Applied Physics Express* **2008**, *2*, 022001.
- (21) Shimomura, H.; Gemici, Z.; Cohen, R. E.; Rubner, M. F. *ACS Applied Materials & Interfaces* **2010**, *2*, 813.
- (22) Gemici, Z.; Shimomura, H.; Cohen, R. E.; Rubner, M. F. *Langmuir* **2008**, *24*, 2168.
- (23) Forrest, J. A.; Dalnoki-Veress, K.; Stevens, J. R.; Dutcher, J. R. *Physical Review Letters* **1996**, *77*, 2002.
- (24) Keddie, J. L.; Jones, R. A. L.; Cory, R. A. *Faraday Discussions* **1994**, *98*, 219.
- (25) Gemici, Z.; Schwachulla, P. I.; Williamson, E. H.; Rubner, M. F.; Cohen, R. E. *Nano Letters* **2009**, *9*, 1064.
- (26) Lee, D.; Omolade, D.; Cohen, R. E.; Rubner, M. F. *Chemistry of Materials* **2007**, *19*, 1427.
- (27) Z. Wu, J. W. A. N. L. Z. R. E. C. M. F. R. *Advanced Materials* **2006**, *18*, 2699.
- (28) Lee, D.; Gemici, Z.; Rubner, M. F.; Cohen, R. E. *Langmuir* **2007**, *23*, 8833.
- (29) Lvov, Y.; Ariga, K.; Onda, M.; Ichinose, I.; Kunitake, T. *Langmuir* **1997**, *13*, 6195.
- (30) Ostrander, J. W.; Mamedov, A. A.; Kotov, N. A. *Journal of the American Chemical Society* **2001**, *123*, 1101.
- (31) Wark, A. W.; Stokes, R. J.; Darby, S. B.; Smith, W. E.; Graham, D. *The Journal of Physical Chemistry C* **2010**, *114*, 18115.

(32) Du, Y.; Luna, L. E.; Tan, W. S.; Rubner, M. F.; Cohen, R. E. *ACS Nano* **2010**, *4*, 4308.

# CHAPTER 7: CONCLUSIONS

## 7.1 Summary of thesis contributions

The studies presented in this thesis have demonstrated that Layer-by-Layer (LbL) assembly of block copolymers can be used as a facile technique to create temperature responsive thin film hydrogel materials. Previous attempts to create temperature driven, large scale, and reversible swelling transitions using LbL assembly of temperature responsive polymers documented in literature proved unsuccessful. Little was known about why temperature responsive polymers, upon incorporation into the multilayer thin films could not drive the same volume phase transitions they exhibit when free in solution. Through systematic studies presented in Chapter 2, we developed a deeper understanding of how key factors, namely the multilayer crosslinking density and ionic crosslink strength have a deterministic effect on whether final multilayer assemblies can function as responsive hydrogels. From Chapter 2, we understand that using a strong polyelectrolyte like PSS tends to generate tightly crosslinked multilayer assemblies that cannot swell in response to low temperature. The use of PSS for multilayer assembly of temperature responsive polymers is likely to be the reason behind the limited swelling ability previously reported by other groups.<sup>1,2</sup> Furthermore, we showed that large scale reversible swelling responses could be achieved by LbL assembly of temperature responsive PDMAEMA-PPO-PDMAEMA triblock copolymers with weak polyacid PAA. In Chapter 3 we synthesized various block copolymers (BCPs) in order to systematically study the effect of block copolymer architecture on the swelling transitions of temperature responsive multilayers of BCP micelles and PAA, as was presented in Chapter 4. From the work in Chapter 4 we learn that block copolymer connectivity in triblock copolymers of PDMAEMA-PPO-PDMAEMA is critical in sustaining the multilayer networks at low temperature. This is important if reversible swelling is desired. While multilayers made of diblock copolymers disintegrate at low temperature, triblock copolymer multilayers exhibit a wide range of reversible swelling behavior. In addition, PPO

block length is a tunable factor that can be used to customize the film swelling transition temperature.

In Chapter 5, we look into various applications of temperature responsive multilayers developed in Chapters 2 and 4. We first demonstrated that conformal coatings of the temperature responsive multilayers developed in this thesis could be used to actively gate membranes pores. In Section 5.4.1, we demonstrated temperature control of transmembrane fluid flux by the reversible closing and opening of membrane pores brought about by temperature driven swelling and deswelling of the multilayer coatings. The ability to conformally coat the interior of pore walls and systematically narrow pore openings both during assembly with the number of deposition bilayers and post assembly with temperature control, offers opportunities to customize membrane pore size selectivity. In Section 5.4.2, we showed that the LbL method of creating temperature responsive hydrogel coatings is amenable to sacrificial template based creation of novel nanostructured entities like nanotube arrays. In Section 5.4.3, the potential utility of our temperature responsive hydrogels as a protein encapsulation and delivery agent is demonstrated. Lastly, in Section 5.4.4, the stability of various temperature responsive block copolymer multilayer systems were studied in detail. In particular, through the choice of block copolymer architecture, anionic binding partner and LbL assembly conditions, we showed that the disintegration of these temperature responsive block copolymer-polyelectrolyte multilayer systems can be customized for triggered release under specific sets of temperature, salt concentration and pH conditions.

Finally, Chapter 6 demonstrates the versatility of LbL assembly as a facile conformal surface modification technique posed to solve a truly diverse set of technological challenges. In Chapter 6, we showed how inorganic nanoparticles can be used in LbL assembly to create porous low refractive index, high quality UV anti-reflective coatings for optical applications. There, key features of thin porous nanoparticle coating assembly via LbL are discussed, including how particle size and deposition pH can be used to effectively tune coating porosity, refractive index and optical thicknesses. In addition, we developed several strategies for the stabilization of inherently weak systems composed largely of air. In particular, a novel means to generate stable 'inverse' surface nanoporosity in thermoplastic materials was developed.



## 7.2 Recommendations for future studies

LbL assembly of temperature responsive thin film hydrogels made possible by the knowledge gained in Chapters 2 to 4 of this thesis opens up a variety of application possibilities, only a few of which were touched upon in Chapter 5. While Chapter 5 itself lay some foundational groundwork for further pursuit of the applications outlined within, these systems are potentially useful other a host of other applications including temperature controlled surface wettability and thermo-mechanical actuation.

Further, while work in this thesis was directed toward understanding and enabling the use of LbL assembly to create temperature responsive hydrogels, for the application of these systems as permanent surface coatings, or for their application in high salt buffers, their stability needs to be improved further. Functionalization of PAA side groups and end-functionalization of the PDMAEMA triblock copolymers with complimentary click chemistry groups would be a viable way to create stable covalent crosslinks in the network that would allow these systems to function as permanently stable, responsive gels.

In addition, the knowledge gained in Chapter 4 can be used to direct improved molecular level designs for better temperature responsive systems. For instance, star block copolymers with temperature responsive core blocks and weak polyelectrolyte end blocks are possibly even better architectures (compared to triblock copolymers) for creating responsive hydrogels with robust, creep-free, reversible swelling transitions.

On a separate note, while the focus in this thesis has been on the temperature response of these assemblies in aqueous media, it is useful to bring attention to the fact that these micelle containing multilayers offer unique nano-compartmentalization of chemical function (as depicted in Fig. 5-10). This could make them be useful materials for catalytic sequestration, inorganic templating, and nano-pattern generation.

Moving on, while nanoporous coatings were studied in Chapter 6 for specific application to short wavelength UV anti-reflection (AR) motivated by NASA's space project, it is important to note that the final "sink and etch" technique developed has possible applications beyond that of AR. LbL assembly followed by the "sink and etch" technique presents a facile, robust route to creating conformal surface nanoporosity that is often difficult to achieve. The high surface area

offered by surface nanoporosity is important in catalysis<sup>3</sup>, chemical adsorption<sup>4</sup>, sequestration and control of bioavailability<sup>5</sup>, cell interfacing<sup>6,7</sup>, and sensing<sup>8,9</sup>. As such, application of this technique to surface modification of PMMA based microfluidic sensor devices and biomedical implants or devices would be well worth exploring.

## References

- (1) Glinel, K.; Sukhorukov, G. B.; Möhwald, H.; Khrenov, V.; Tauer, K. *Macromolecular Chemistry and Physics* **2003**, *204*, 1784.
- (2) Glinel, K.; Déjugnat, C.; Prevot, M.; Schöler, B.; Schönhoff, M.; Klitzing, R. v. *Colloids and Surfaces A: Physicochemical and Engineering Aspects* **2007**, *303*, 3.
- (3) Coppens, M.-O. In *Structured Catalysts and Reactors*; CRC Press: 2005, p 779.
- (4) Kim, Y.; Lee, B.; Yi, J. *Korean Journal of Chemical Engineering* **2007**, *24*, 679.
- (5) Nam, K.; Alexander, M. *Environmental Science & Technology* **1998**, *32*, 71.
- (6) Karlsson, M.; Johansson, A.; Tang, L.; Boman, M. *Microscopy Research and Technique* **2004**, *63*, 259.
- (7) Karlsson, M.; Pålsgård, E.; Wilshaw, P. R.; Di Silvio, L. *Biomaterials* **2003**, *24*, 3039.
- (8) Lin, K.-C.; Kunduru, V.; Bothara, M.; Rege, K.; Prasad, S.; Ramakrishna, B. L. *Biosensors and Bioelectronics* **2010**, *25*, 2336.
- (9) Wittstock, A.; Biener, J.; Baumer, M. *Physical Chemistry Chemical Physics* **2010**, *12*, 12919.



# APPENDIX A: Studies of PDMAEMA and PPO containing BCPs in solution

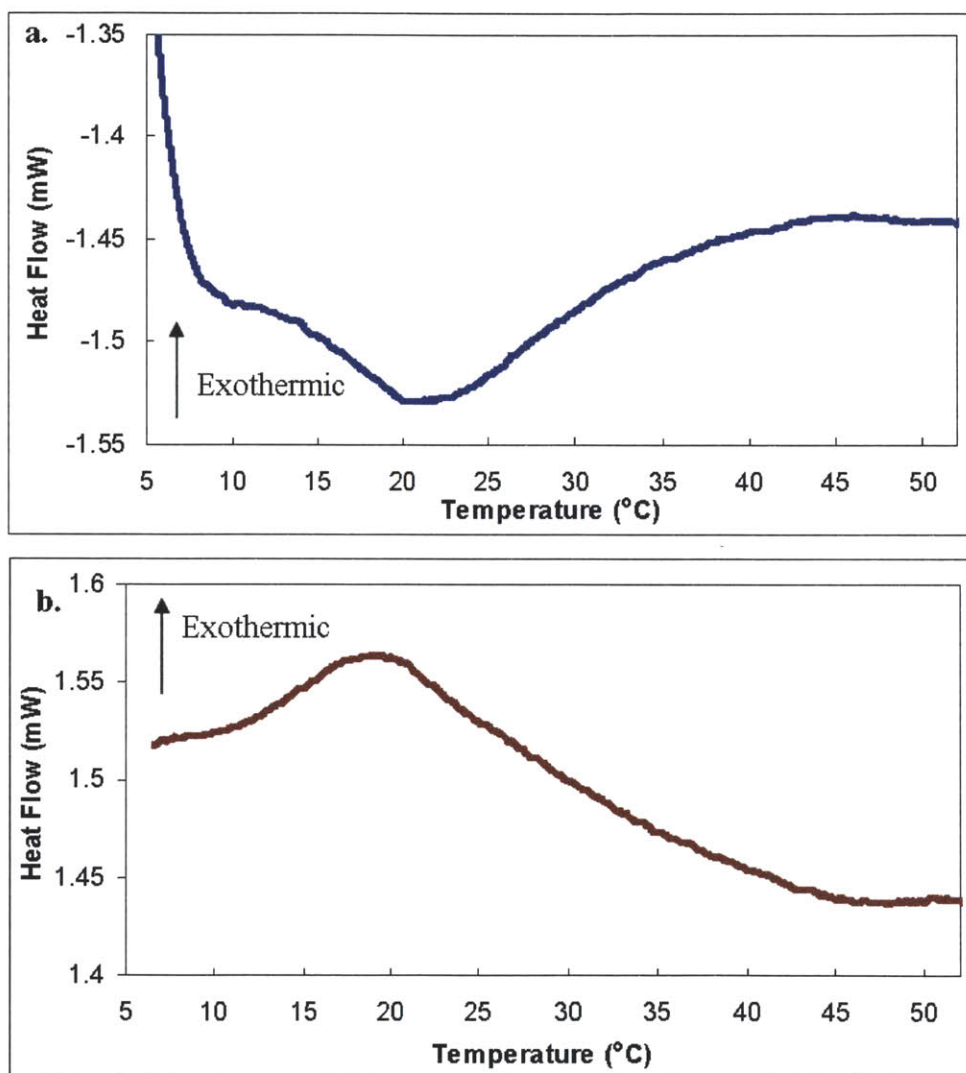


**Figure A-1.** Heat flow as a function of temperature during representative heating (a) and cooling (b) cycles of 3.3 mg/ml PD-PP-PD solution in DI adjusted to pH 7.

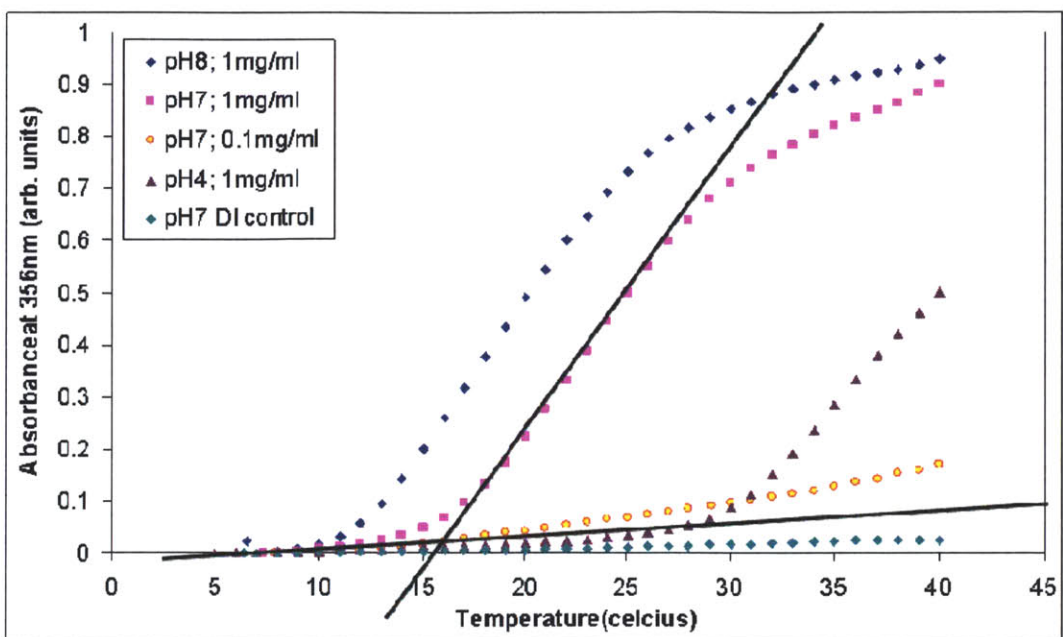


**Figure A-2.** Absorbance, of PD-PP-PD solutions with 0.004 mM DPH, at 356 nm as a function of solution temperature for 1 mg/ml PD-PP-PD solutions adjusted to different pH. Included is a control of DI water adjusted to pH 7 and a dilute 0.1 mg/ml polymer solution adjusted to pH 7. (0.1 mg/ml is the concentration used for multilayer deposition.) Lines illustrate the procedure used to determine the CMT.

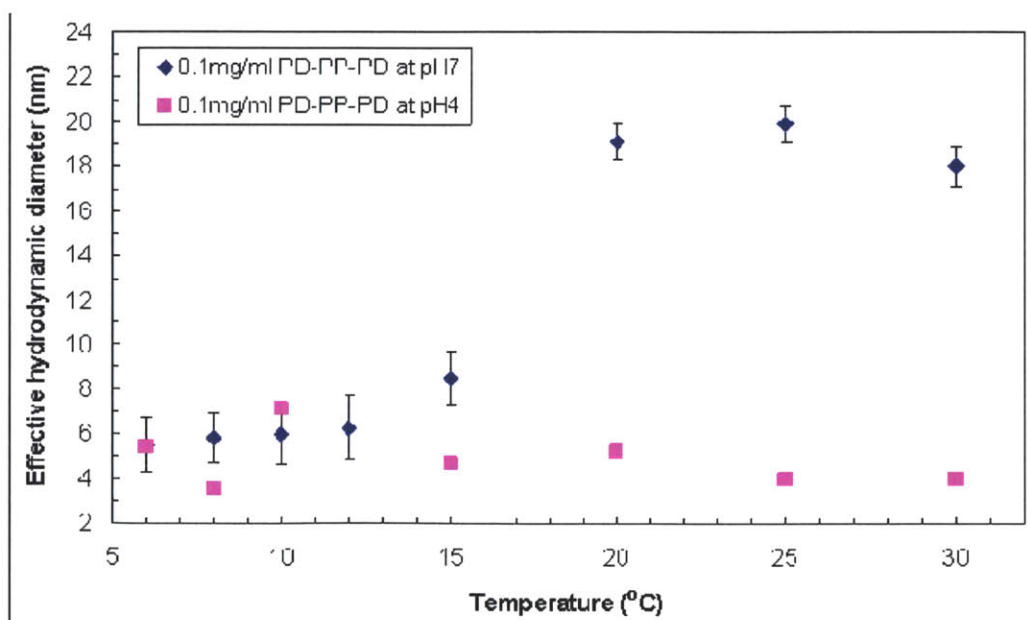


**Figure A-3.** Number average hydrodynamic diameter in 0.1 mg/ml PD-PP-PD solutions at pH 4 and pH 7, as determined by dynamic light scattering.

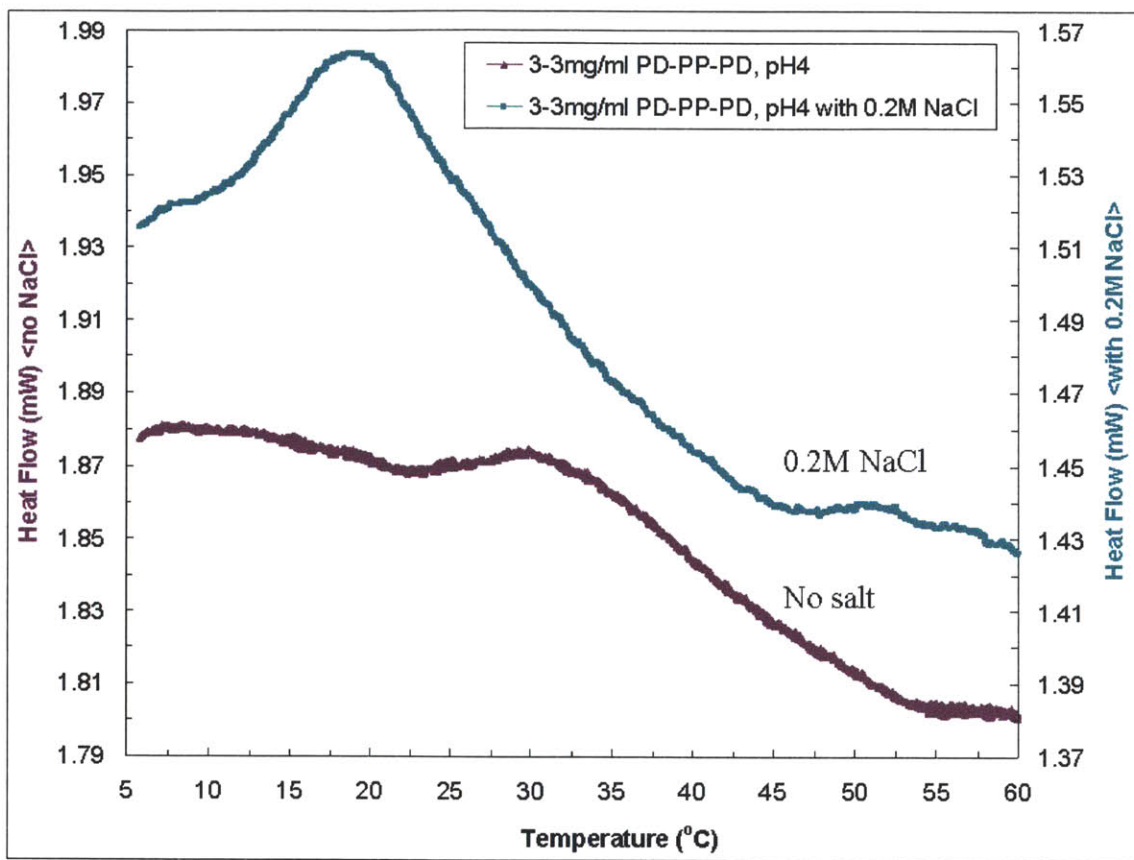


**Figure A-4.** Heat flow as a function of solution temperature during cooling for 3.3 mg/ml PD-PP-PD solution in DI adjusted to pH 4 with and without 0.2 M NaCl added. Titration curve and pKa of triblock

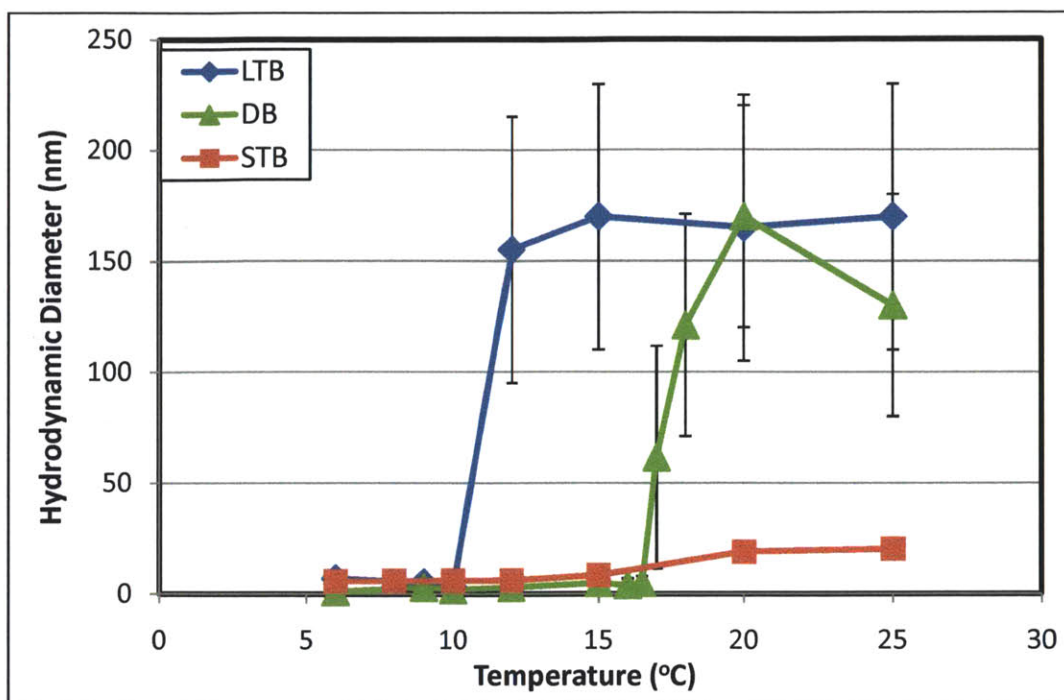


**Figure A-5.** Temperature dependent evolution of effective hydrodynamic diameter of 0.1 mg/ml BCP solutions at pH 7, obtained from dynamic light scattering.

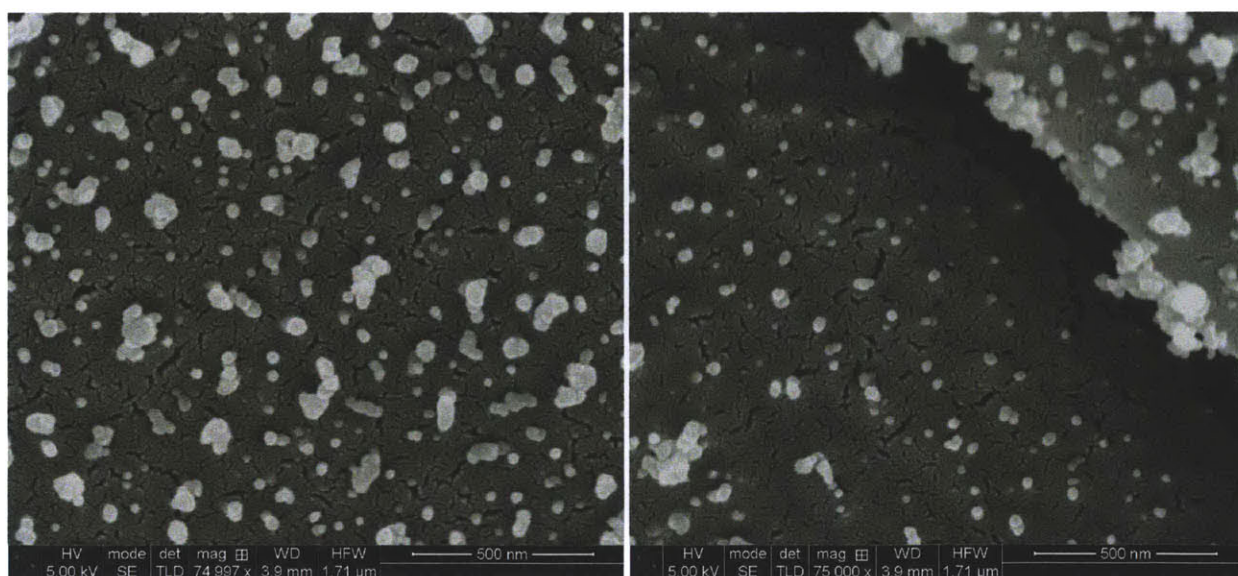


**Figure A-6.** Cryogenic scanning electron microscopy images of 0.1 mg/ml, pH 7 DB solution upon over sublimation and removal of too much water which results in heaping together of micelles.



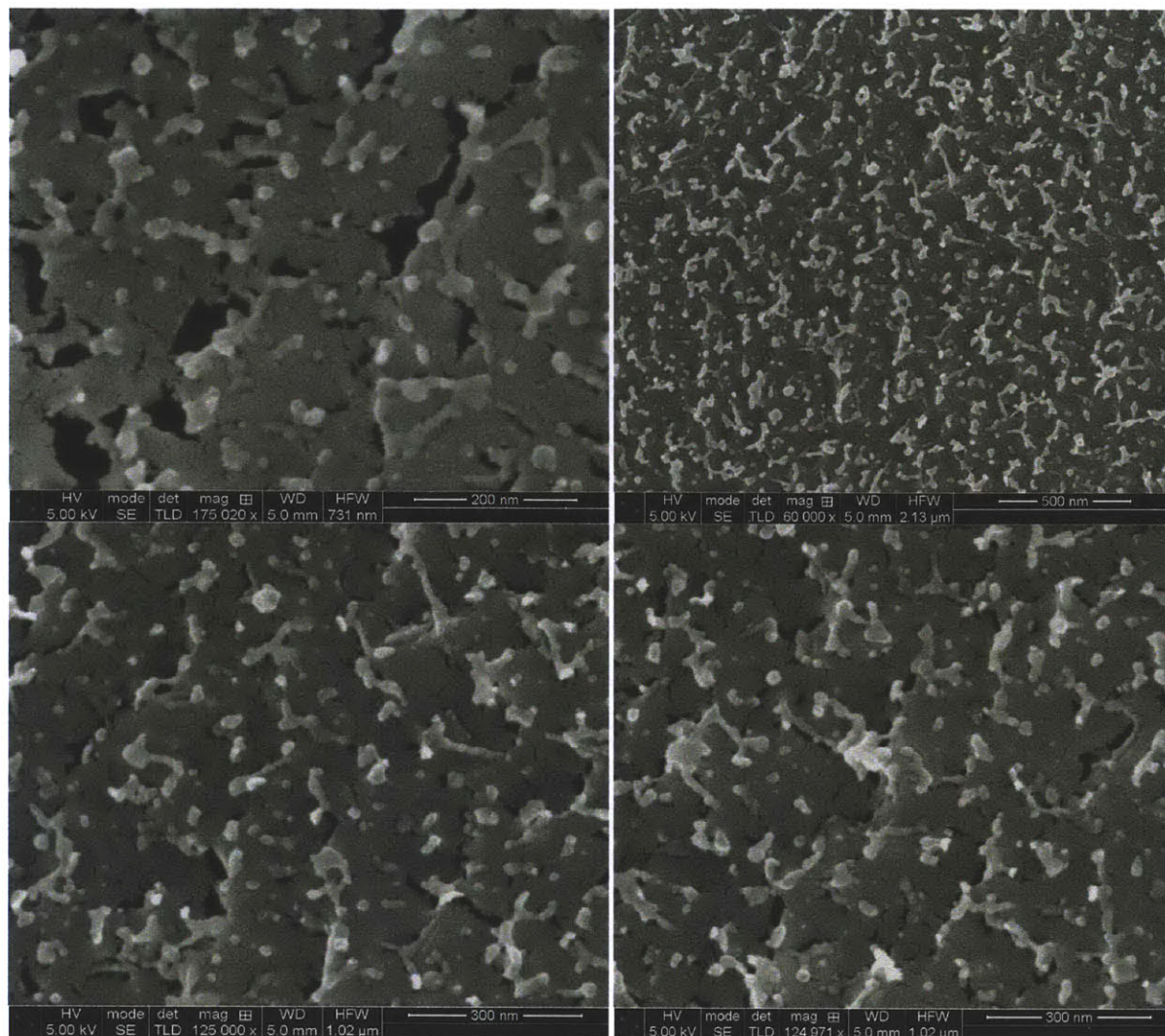


**Figure A-7.** Cryo-SEM images of freeze fractured surfaces of flash frozen STB BCP solutions, concentration 2 mg/ml and adjusted to pH 7, taken after sublimation to expose BCP structure.

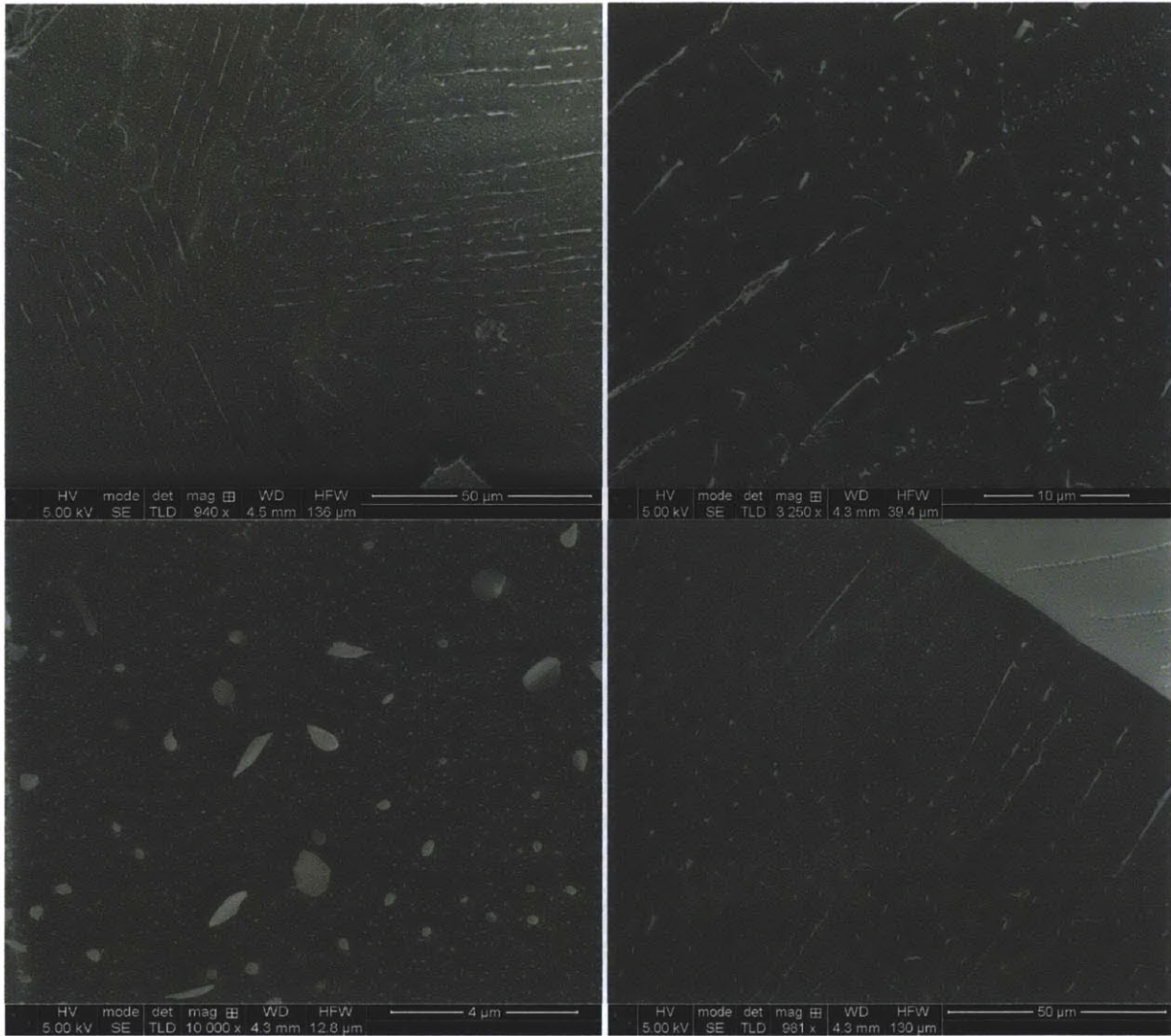


**Figure A-8.** Cryo-SEM images of freeze fractured surfaces of flash frozen LTB BCP solutions, concentration 2 mg/ml and adjusted to pH 7, taken after sublimation to expose BCP structure.

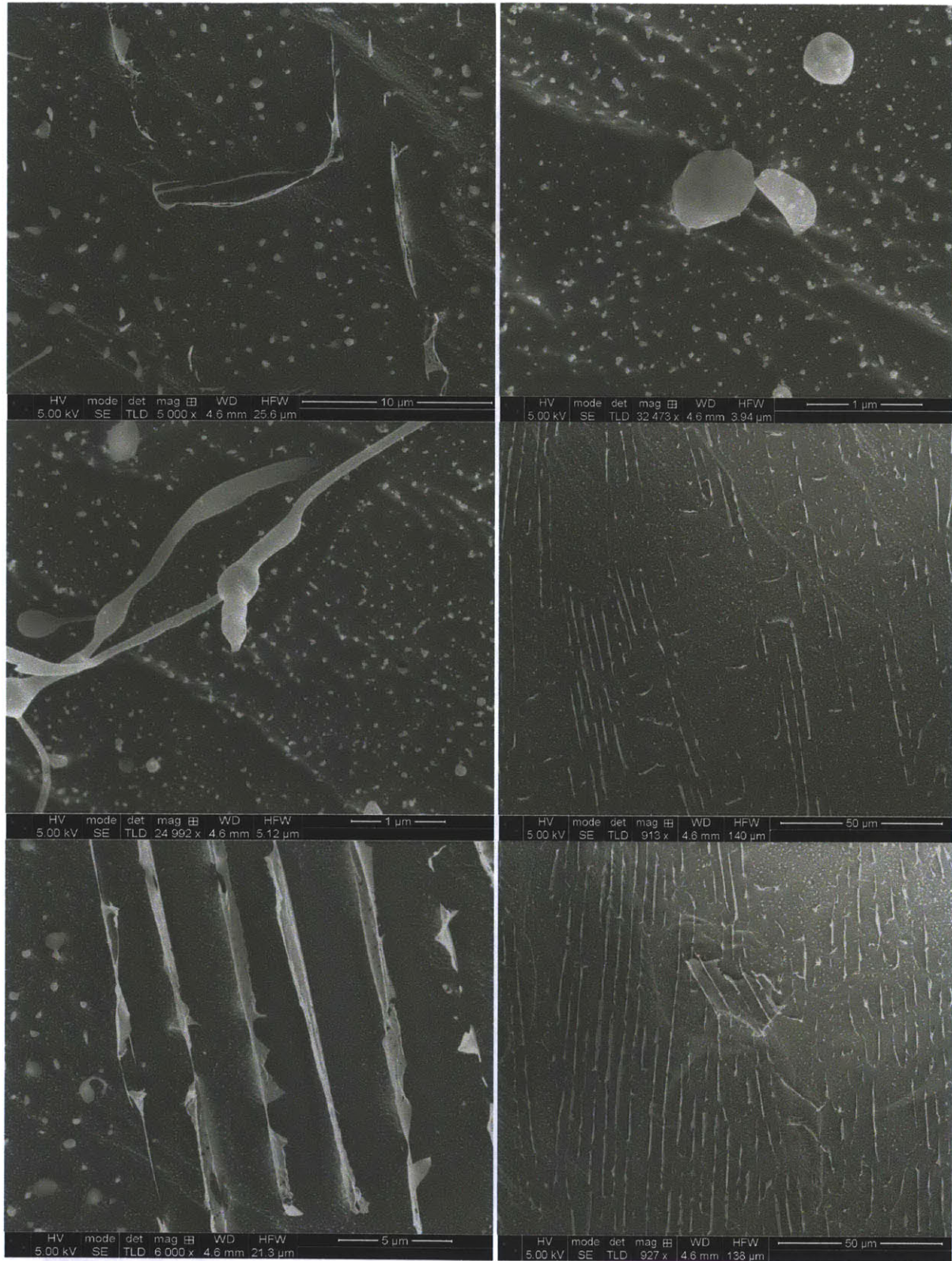


**Figure A-9.** Cryo-SEM images of freeze fractured surfaces of flash frozen DB BCP solutions, concentration 2 mg/ml and adjusted to pH 7, taken after sublimation to expose BCP structure.

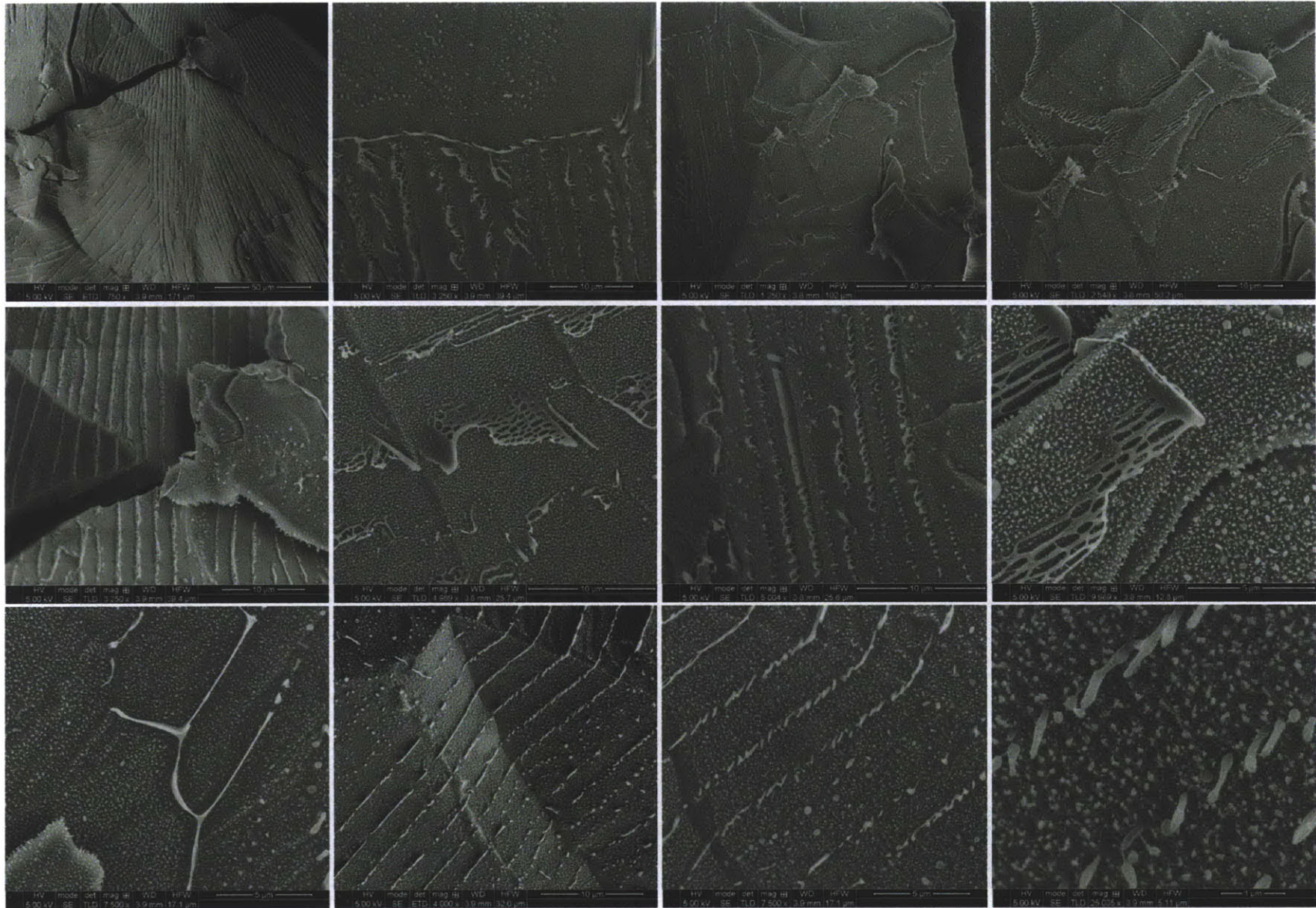


**Figure A-10.** Cryo-SEM images of freeze fractured LTB BCP solutions, concentration 5 mg/ml adjusted to pH 7.

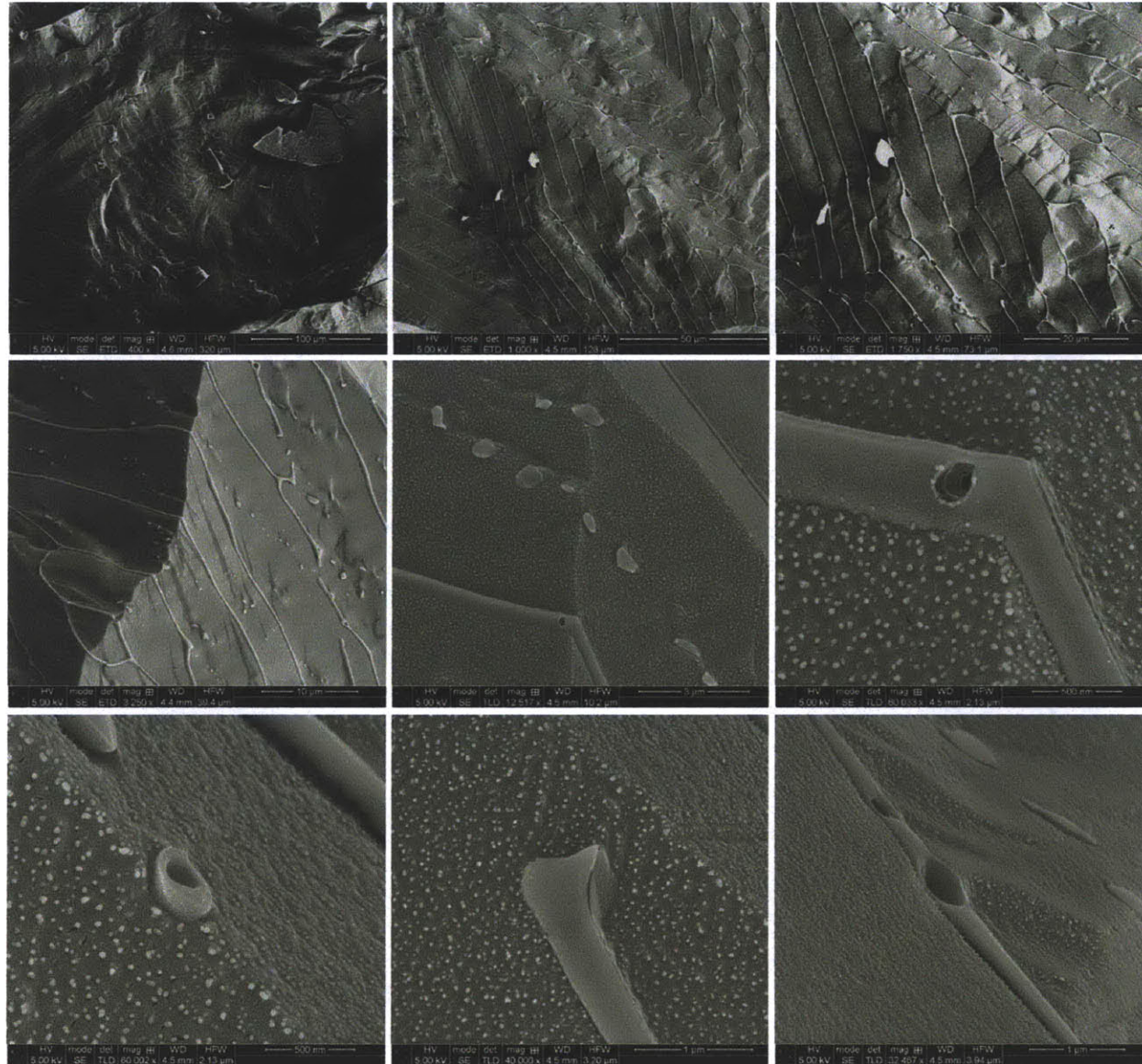


**Figure A-11.** Cryo-SEM images of freeze fractured surfaces of flash frozen DB BCP solutions at 2 mg/ml concentration with 0.2 M of NaCl added and adjusted to pH 7, taken after sublimation to expose BCP structure.

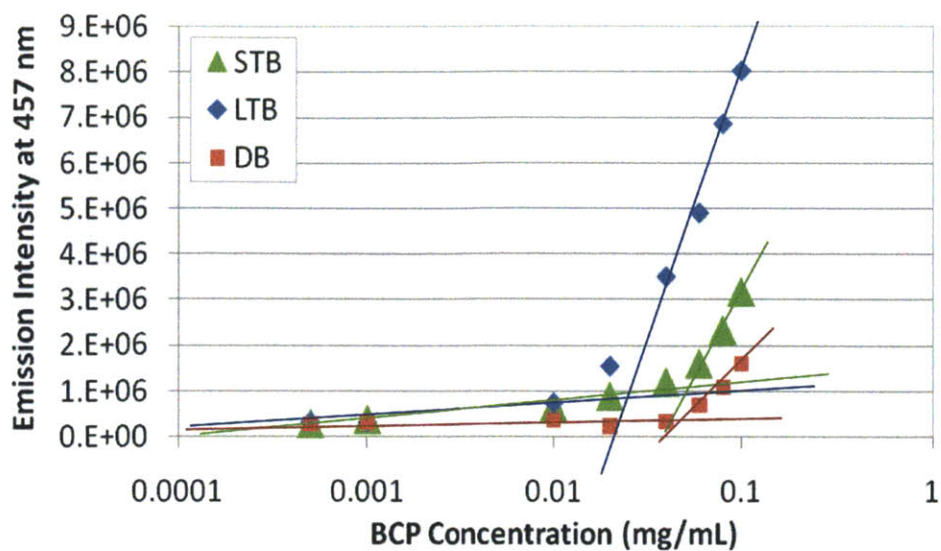


**Figure A-12.** Variation of 0.004 mM DPH fluorescence ( $\lambda_{\text{ex}} = 350 \text{ nm}$ ,  $\lambda_{\text{em}} = 457 \text{ nm}$ ) with BCP concentration, determined after allowing 5h for DPH solubilization. Lines illustrate the procedure used to determine the critical micelle concentration at 22 °C.

## APPENDIX B: Morphology of BCP multilayers; additional AFM insights

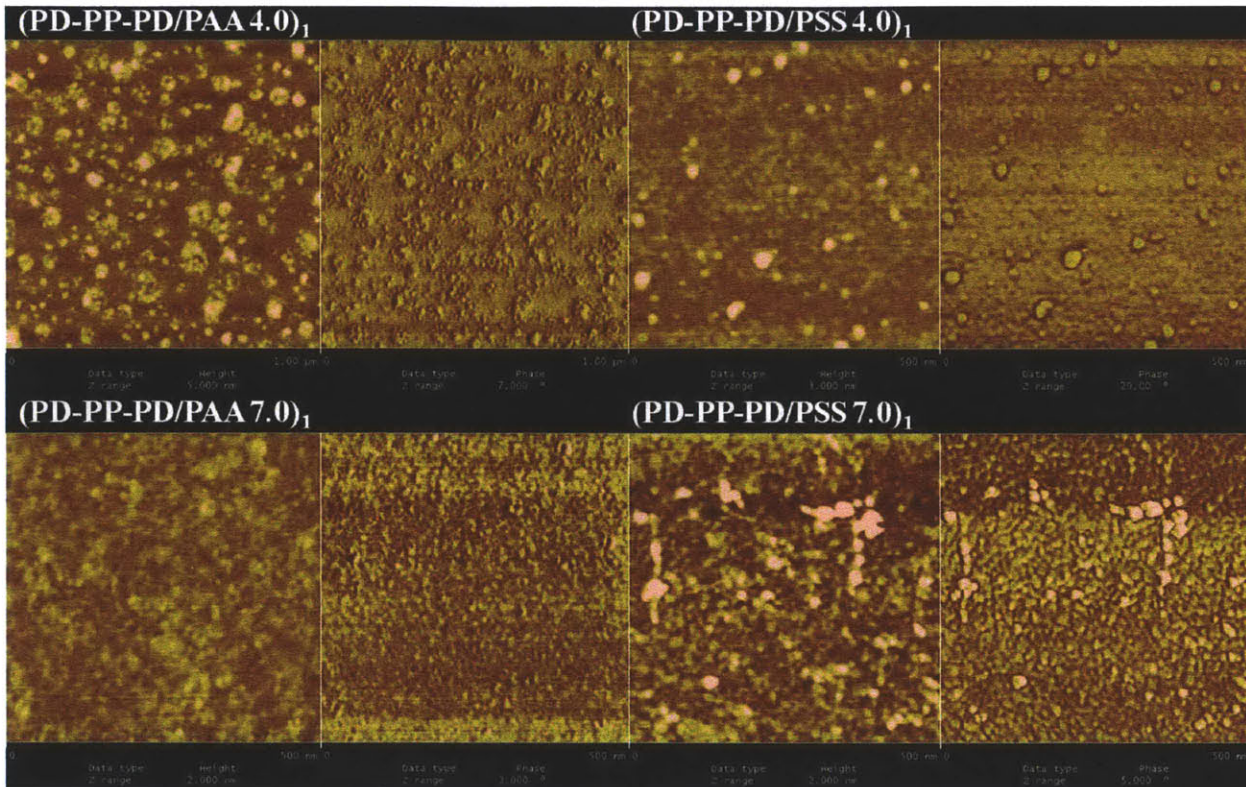


**Figure B-1.** AFM of PD-PP-PD assembled with PAA or PSS at pH 4 or pH 7 after the 1<sup>st</sup> bilayer deposition reveal different initial film growth mechanisms. Confluent films are formed for assembly with both PAA or PSS at pH 7 but assembly at pH 4 shows the tendency for blob formation on the surface, more toward island type growth (though it is likely that the areas between the ‘blobs’ are not bare silicon, especially in the case of PD-PP-PD/PSS).

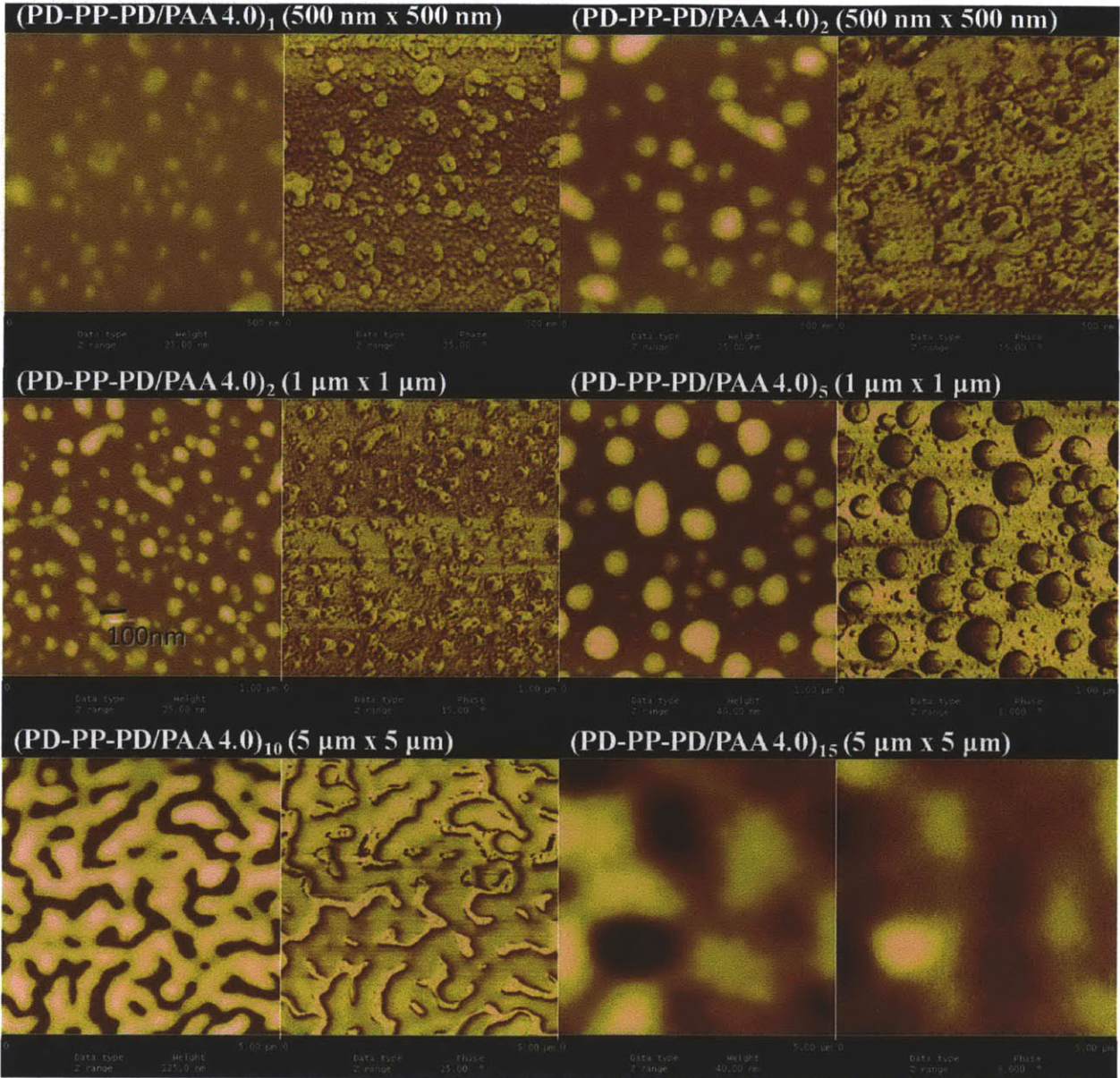


**Figure B-2.** The morphological evolution of PD-PP-PD/PAA multilayers assembled at pH 4; AFM images of 1, 2, 5, 10 and 15 bilayer films, reveal an island growth mechanism of initial film formation during LbL assembly, where islands nucleate, grow and merge to form a conformal film during the first 15 bilayer deposition cycles.



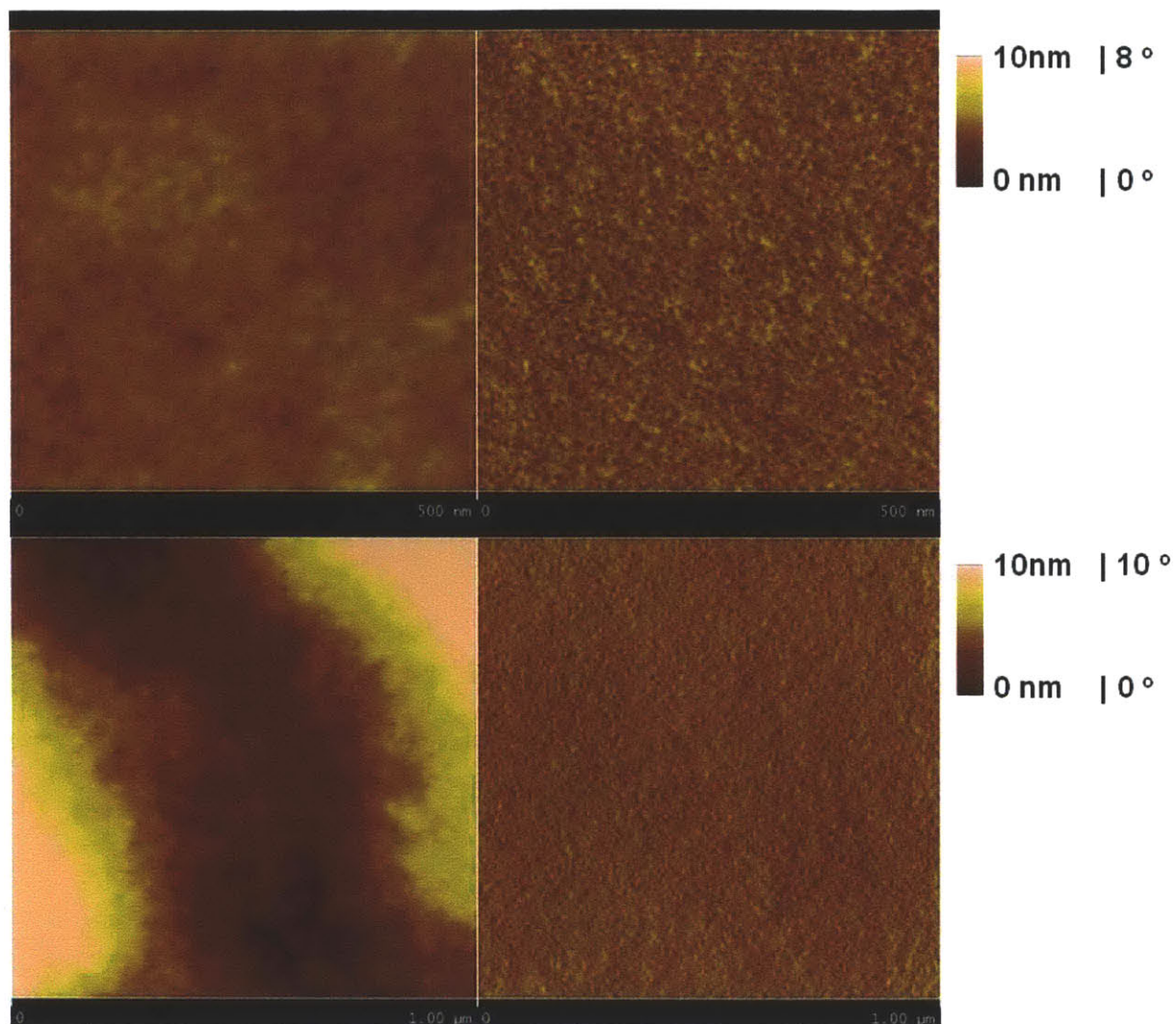


**Figure B-3.** AFM tapping mode images of dry  $(\text{PD-PP-PD/PAA } 4.0)_{15}$  shows fully conformal films are formed after 15 bilayers of deposition. PP-PD-PP in pH 4, 0.1mg/ml solutions used for LbL assembly exist in a unimeric state as opposed to micelles at pH 7. The dry film surface morphology of multilayers of PP-PD-PP assembled with PAA at pH 4 are starkly different from films assembled from the same constituents at pH 7 seen in Figure B.3.

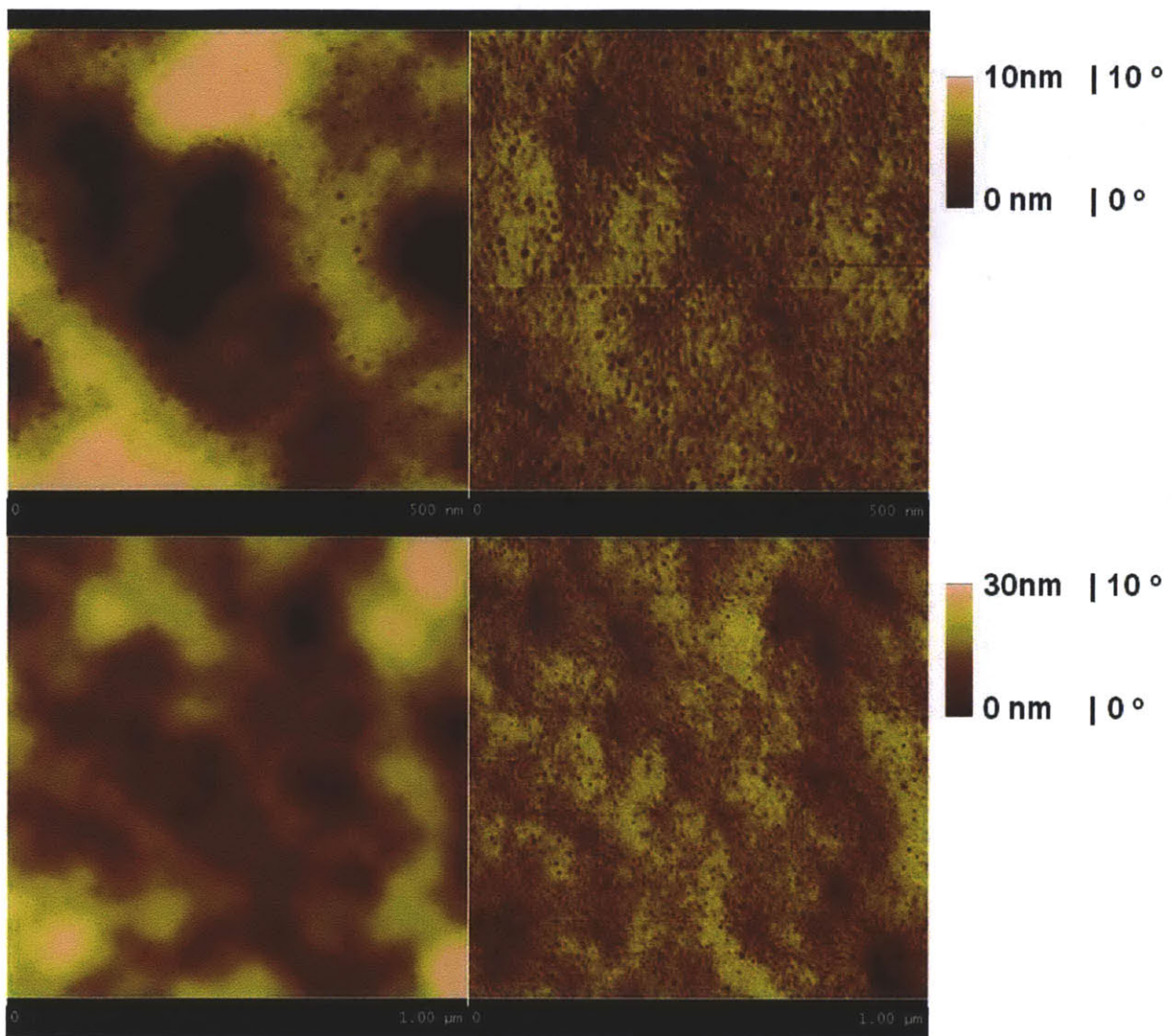


**Figure B-4.** AFM tapping mode images of dry  $(\text{PD-PP-PD/PAA } 7.0)_{15}$  reveals interesting dimpled structures that originate from micelle deposition.

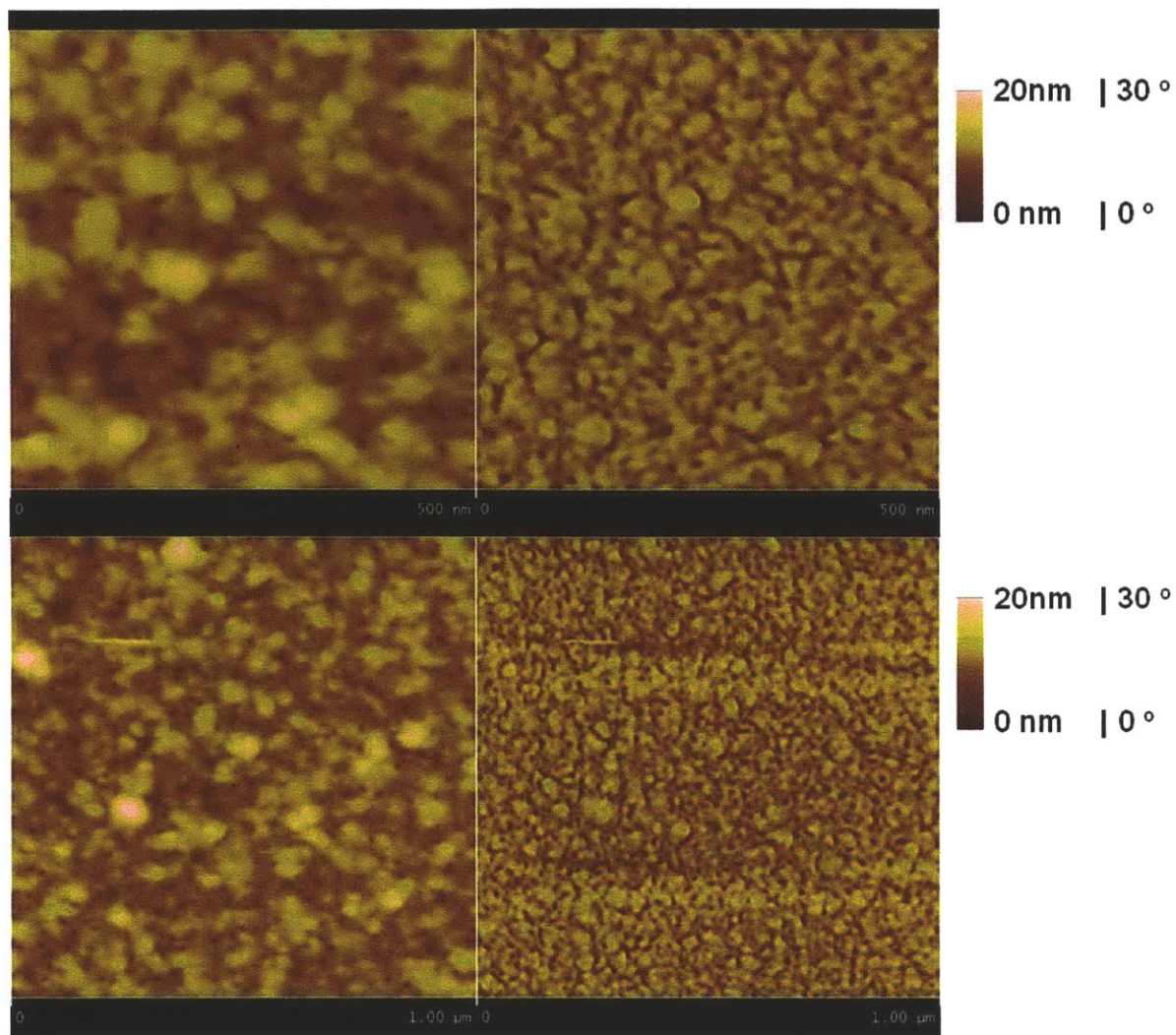


**Figure B-5.** AFM tapping mode images of dry  $(\text{PD-PP-PD/PSS } 7.0)_{10}$  shows that the dry film surface morphology of multilayers of PP-PD-PP assembled with PSS at pH 7 also show evidence of dimple-type structure but have a different (more granular) surface as compared to PP-PD-PP assembled with PAA at the same pH of 7.

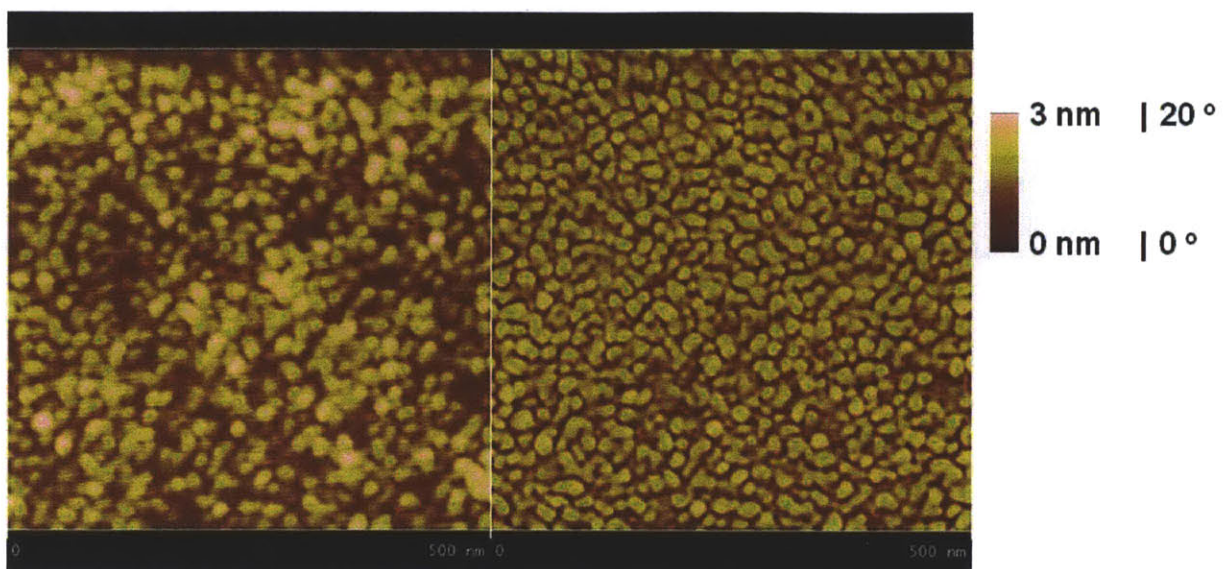


**Figure B-6.** AFM tapping mode images of dry  $(\text{PD-PP-PD/PSS } 4.0)_2$  shows rather unique the dry film surface morphology. It is interesting to recall from Chapter 1 that  $(\text{PD-PP-PD/PSS } 4.0)$  grows extremely slowly with less than 30 nm of film formed after 60 bilayer deposition cycles, the morphology shown here of a 2 bilayer film does not vary much from that of a 60 bilayer one. An image of a 41 bilayer film is shown in Figure B.7.

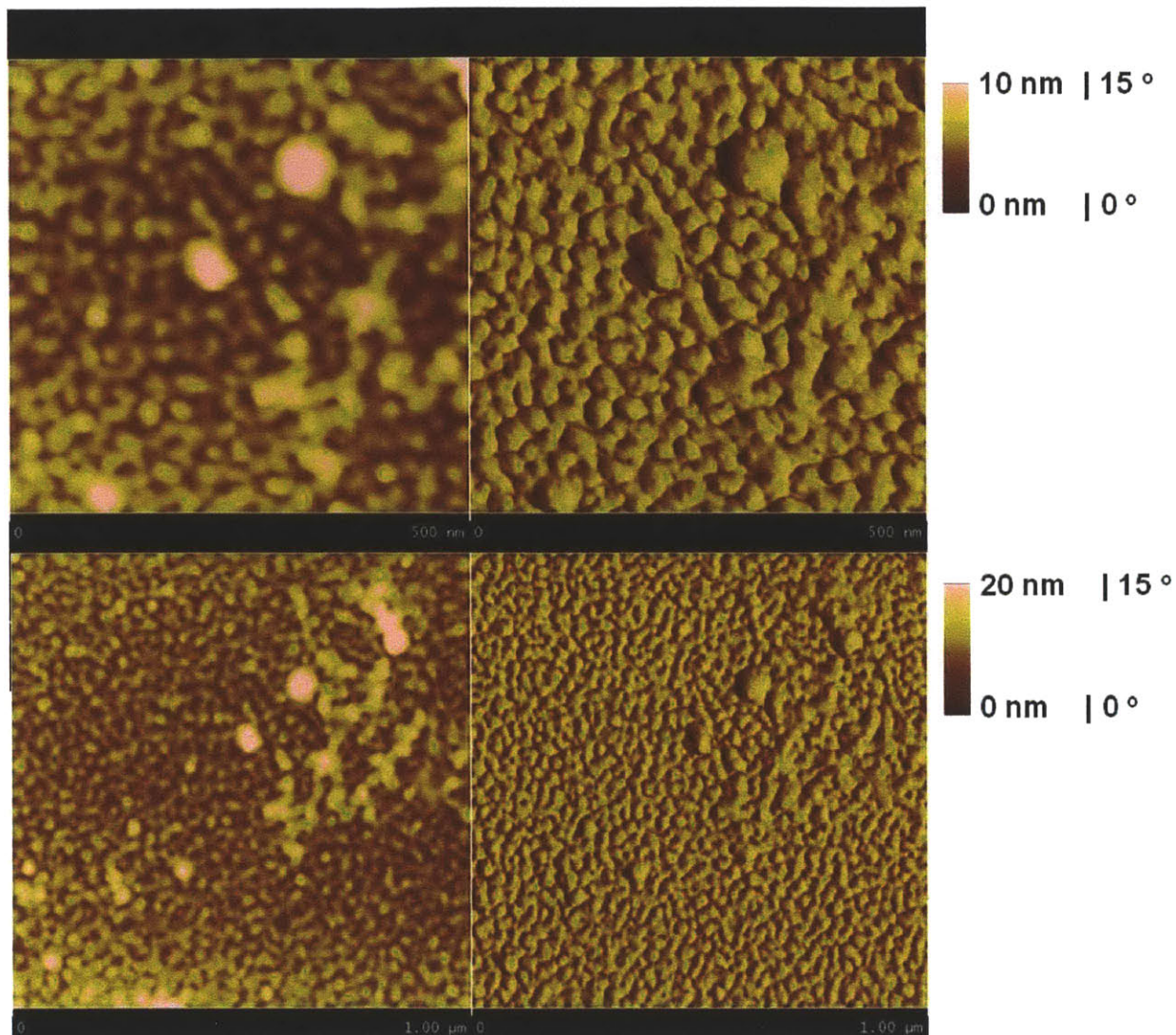


**Figure B-7.** AFM tapping mode images of dry (PD-PP-PD/PSS 4.0)<sub>41</sub>

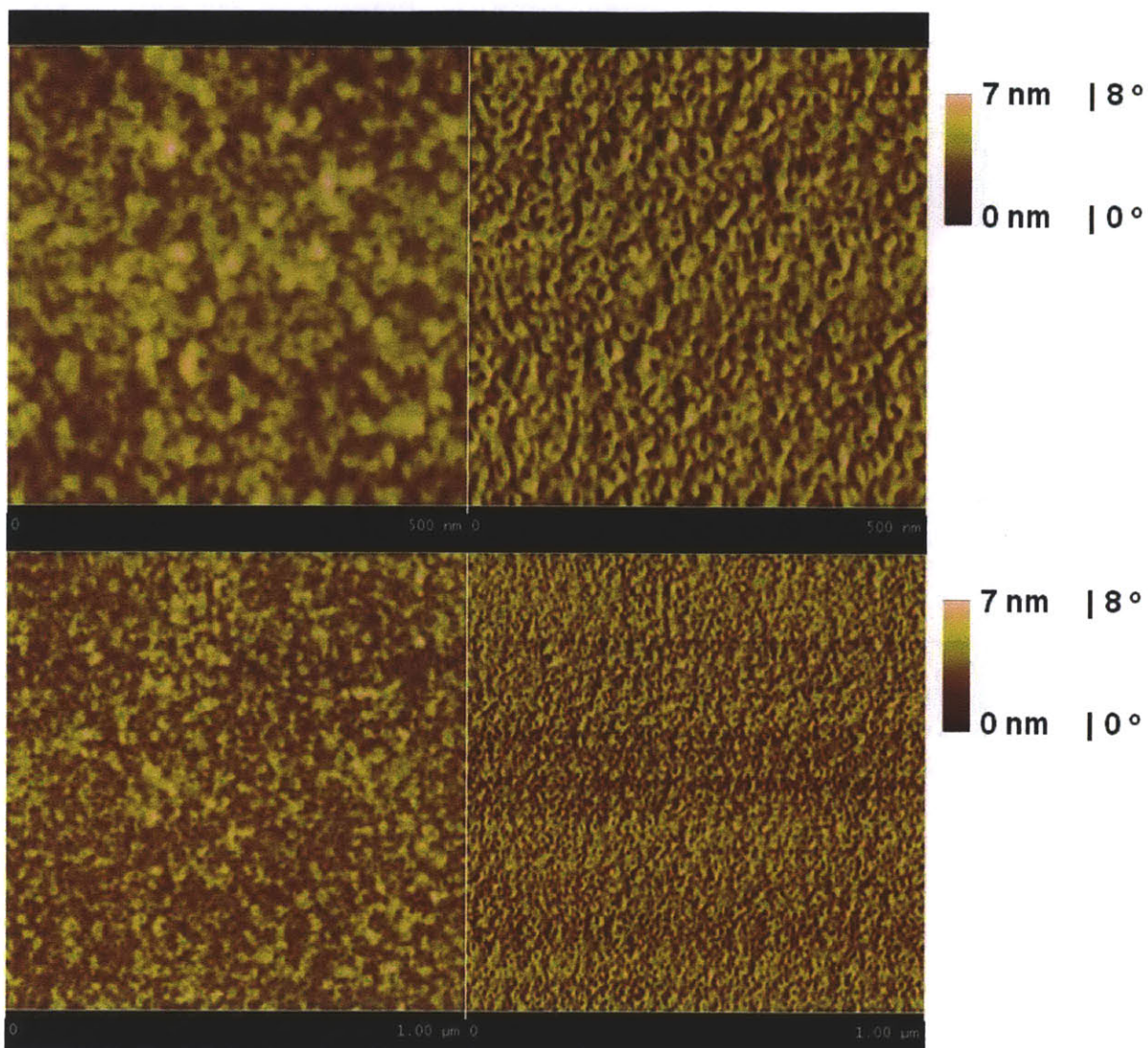


**Figure B-8.** AFM tapping mode images of dry  $(\text{PD-PP-PD/PAA})_1$  assembled from PBS buffer. While the addition of salt to solutions of amphiphilic BCP solutions could change the solution morphology of aggregates, e.g. transitions from spherical to rod or worm-like micelles, such effects were not reflected in the dry film morphology of PD-PP-PD assembled with PAA from pH 7 PBS buffer solutions. Interestingly, these films assembled from buffer solutions resemble  $(\text{PD-PP-PD/PSS } 7.0)$  more than  $(\text{PD-PP-PD/PAA } 7.0)$ . It is unknown what exact individual and combined effects PBS buffer has on BCP solution morphology, PAA solution configuration as well as the ionic associations within the film. A combination of these effects is likely the cause for morphological differences in the final film formed.

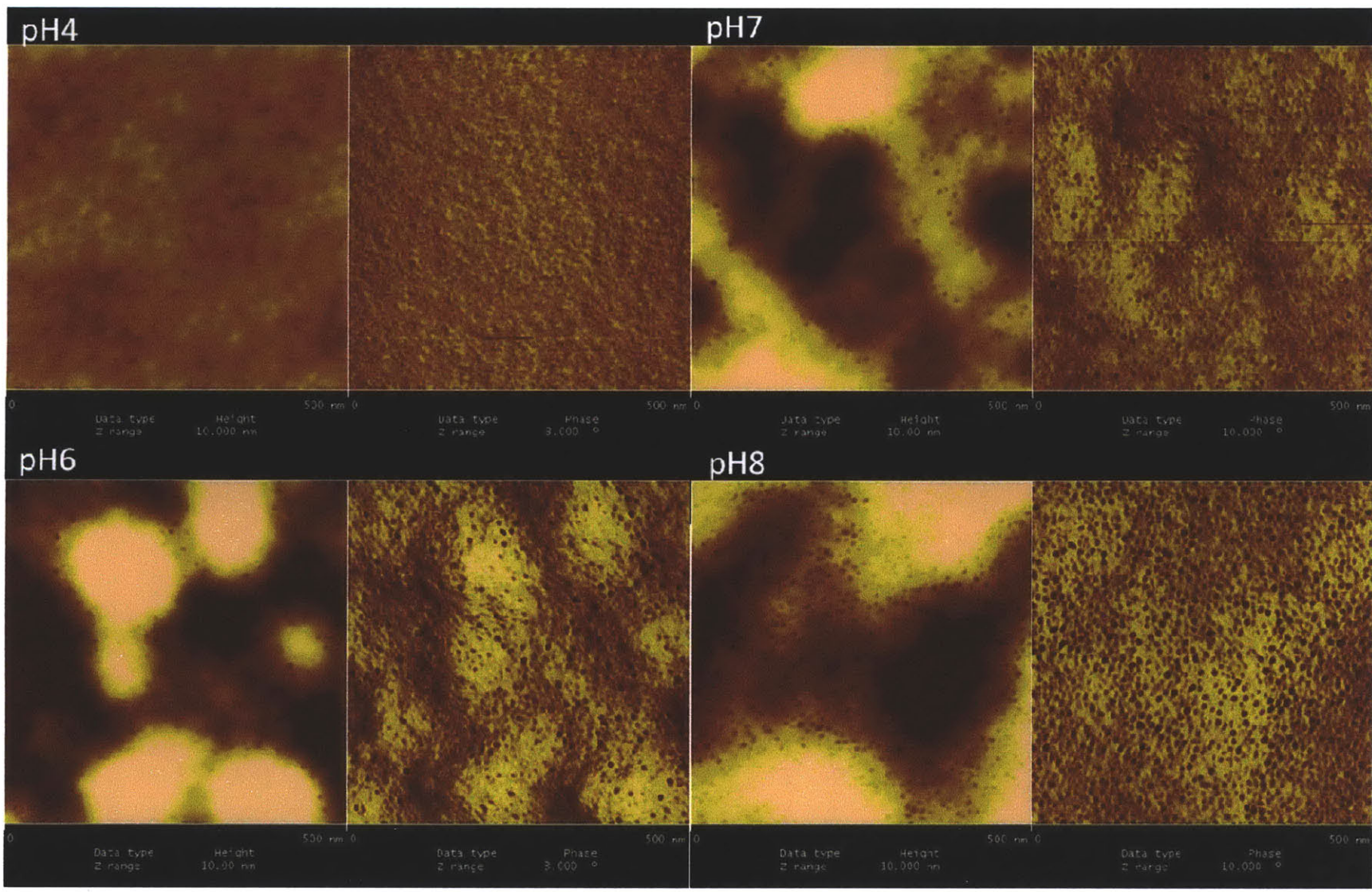


**Figure B-9.** Effect of assembly pH on PD-PP-PD/PAA surface morphology. AFM images of PD-PP-PD/PAA assembled at pH 4, pH 6, pH 7 and pH 8.

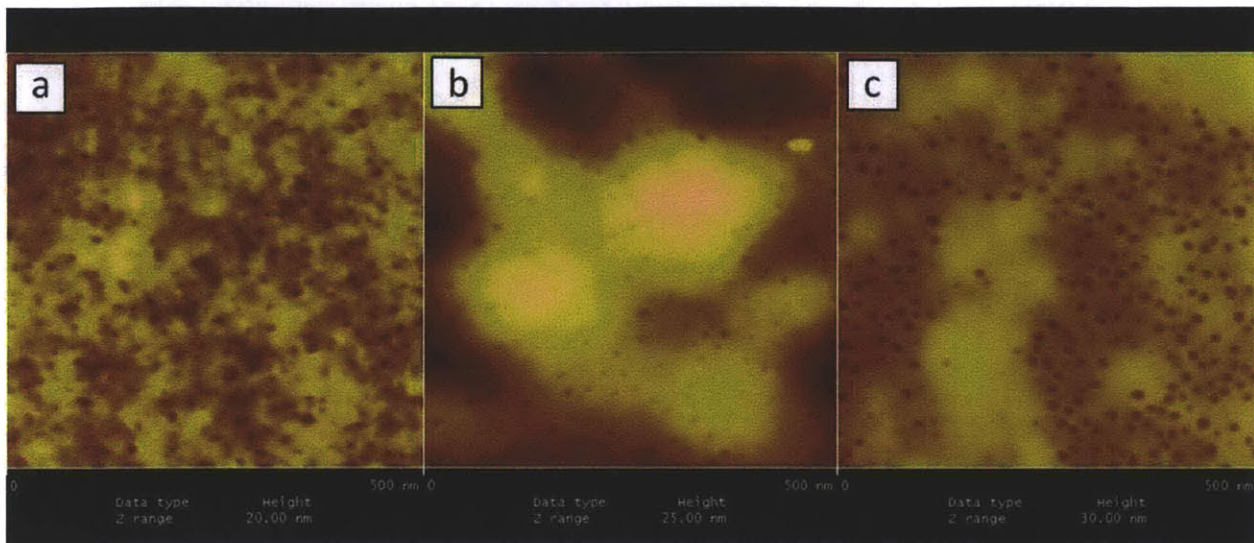


**Figure B-10.** (PD-PP-PD/PAA 7.0)<sub>9</sub> assembled at room temperature dried at (a) 6 °C (b) 24 °C and (c) 40 °C. The films were transferred in the wet state (covered with a film of water from the last rinse preventing drying before film equilibration at each temperature) transferred to a petri dish in the fridge (6 °C) or an oven at 40 °C, or left to dry as usual at room temperature. At 6 °C water becomes a good solvent for PPO. As seen in (a) the morphology of the films dried from a state where the PPO micelle cores are expanded results in a more open ‘holey’ structure than that resulting from films dried at 24 or 40 °C where water is a poor solvent for PPO.



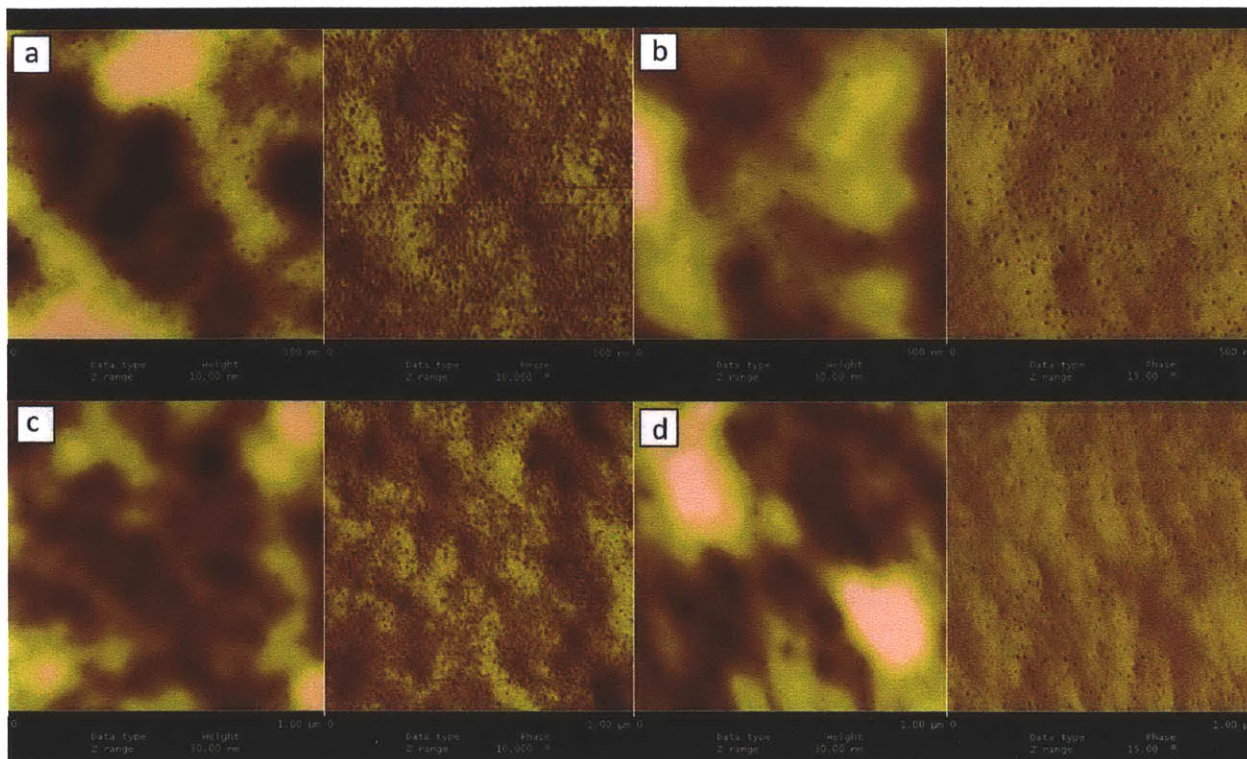


**Figure B-11.** AFM tapping mode images of dry (PD-PP-PD/PAA 7.0)<sub>16</sub> multilayer films before ((a) and (c)) and after more than 5 swelling and deswelling cycles between 6 and 20 °C in DI water adjusted to pH 7. Images (a) and (b) are 500 nm X 500 nm while (c) and (d) are 1 μm X 1 μm. Images show evidence of film smoothing upon repeated swelling deswelling cycles apart from which films remain relatively intact and unchanged. It is interesting as large scaled swelling and deswelling in typical hydrogels tend to result in surface ‘wrinkling’ due to instabilities that originate from the large volume changes and lateral constraints imposed by adhesion to the substrate below the film. This could be an interesting result of the nanostructured character where swelling is confined to localized nano-scaled domains of the micelle cores, interspersed with a continuous ionically linked domain that is pliable but does not swell more at low temperature.

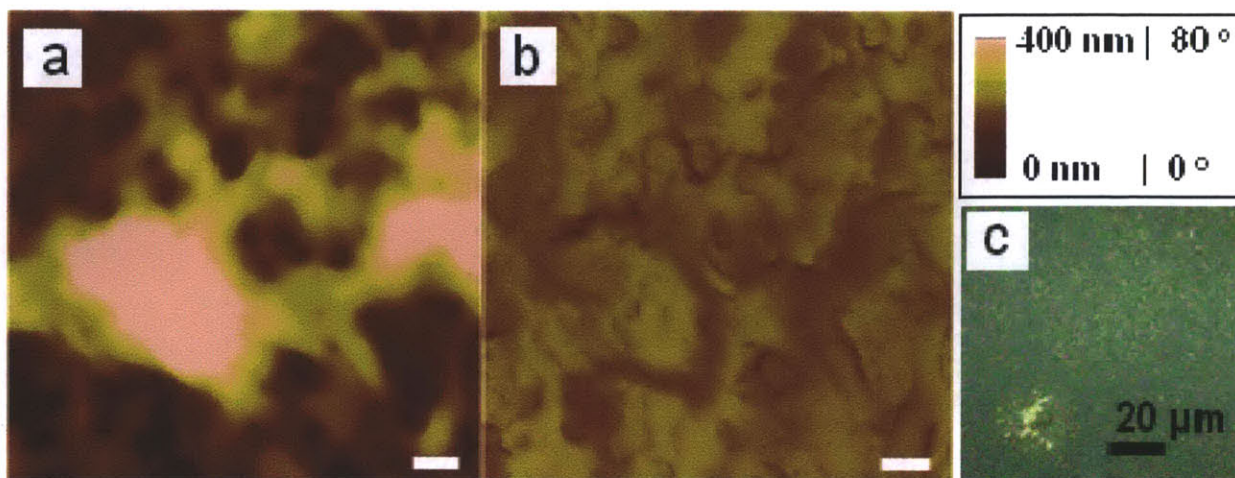


**Figure B-12.** AFM  $5\ \mu\text{m} \times 5\ \mu\text{m}$  height image (a) and corresponding phase image (b) of a dried DB/PAA multilayer post swelling in pH 7 DI water for 30 mins at  $6\ ^\circ\text{C}$ . White scale bars on the bottom right of each image represent 250 nm and the height and phase scales are shown on the right. An optical micrograph (c) is included to provide a large scale overview.

As seen in Figure B-11, massive reconstruction throughout the originally 200 nm thick flat film occur when (DB/PAA 7.0) multilayers are exposed to  $6\ ^\circ\text{C}$  for 30 min. Optical images like Fig. B-11.c, show exposed parts of the underlying silicon wafer and other regions where height variation of over 400 nm can be observed by AFM (Fig. 7a). This is indicative that film loss is bulk disintegration process whereby continuous uptake of water into P domains resulted in the opening of voids that merge and tear the PEM apart.

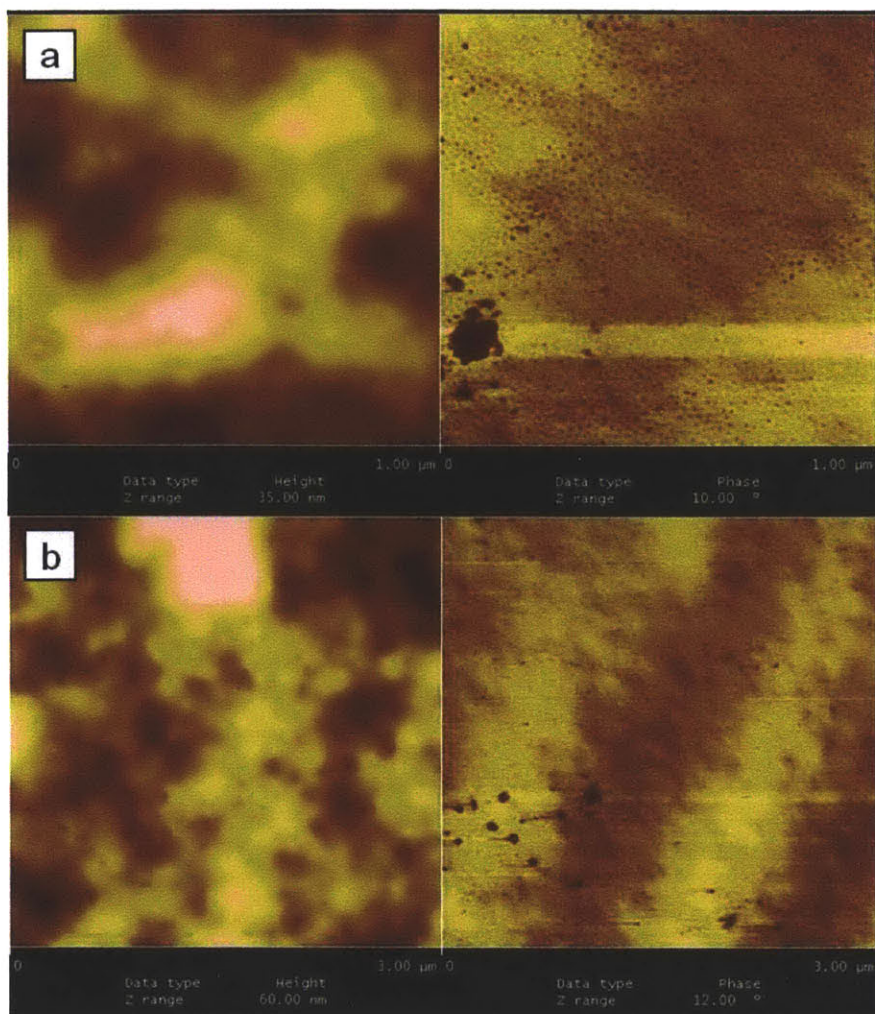


**Figure B-13.**  $1\ \mu\text{m} \times 1\ \mu\text{m}$  (a) and  $3\ \mu\text{m} \times 3\ \mu\text{m}$  (b) atomic force microscope (AFM) images of dried  $(\text{DB/PAA } 7.0)_{35}$  after 2 min swelling ( $T = 6\ ^\circ\text{C}$ ) and deswelling ( $T = 20\ ^\circ\text{C}$ ) cycles in pH 7 DI water. The left column consists of height images while the right column consists of phase images. This image reveals the beginning of instability and defect formation in the diblock copolymer multilayers when cycled at  $\Delta T = 9\ ^\circ\text{C}$  as opposed to reversible cycling at  $\Delta T = 6\ ^\circ\text{C}$  as seen in Chapter 4 Fig. 4-8.



## APPENDIX C: Additional data related to LbL assembly for AR coatings on PMMA

**Table C-1.** List of refractive index, thickness and thickness/bilayers (bL) values of a variety of LbL coatings deposited on unmodified and modified PMMA substrate surfaces.

Multilayer components	Substrate modification	$N_c$	Thickness (nm)	Thickness/bL (nm)
TM40(3) PAH(4.5)	none	1.252	207.2	13.8
TM40(3) PAH(4.5)	bcp coated	1.252	223.2	14.9
SM30(5) PAH(5)	none	1.262	199.9	16.7
SM30(5) PAH(5)	bcp coated	1.261	216.2	18.0
HS40(4.5) PAH(4.5)	none	1.262	198.3	16.5
HS40(4.5) PAH(4.5)	bcp coated	1.261	216.2	18.0
PAA(3) ZrO(3)	none	1.554	37.4	1.9
PAA(3) ZrO(3)	-NH <sub>3</sub> PMMA	1.529	49.4	2.5
PAA(3) Apsilica* (3)	none	1.531	25.2	2.5
PAA(3) Apsilica(3)	on bcp	1.558	18	1.8
SPS(3) Apsilica(3)	none	1.328	41.4	4.1
SPS(3) Apsilica(3)	-NH <sub>3</sub> PMMA	1.318	32.8	3.3

\* Apsilica is an abbreviation for amine functionalized, hence positively charged silica nanoparticles.

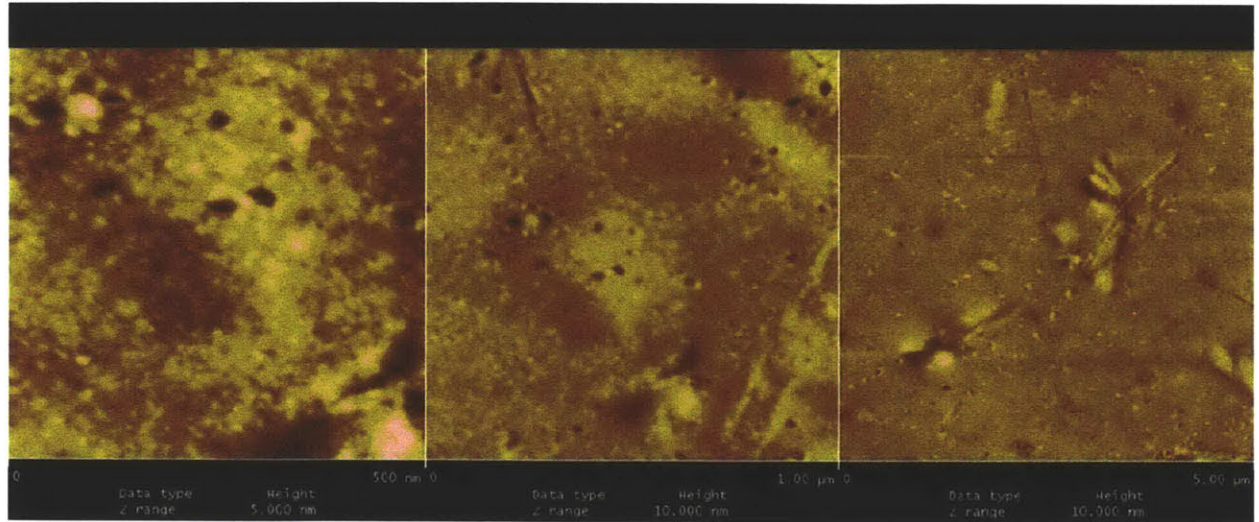


**Figure C-1.** AFM height images of uncoated PMMA substrate surfaces showing nanometer to micron scaled surface defects like potholes and scratches that can scatter light incident on these substrates.

**Table C-2.** List of refractive index and thickness values of a variety of LbL coatings before and after hydrothermal treatment (htd) at 90 °C in saturated water vapor for 4 hours.

Multilayer components	Treatment	$N_c$	Thickness	% change in $N_c$	% change in thickness
TM40(3) PAH(4.5)	none	1.252	207.2	+7.5	-22.3
TM40(3) PAH(4.5)	htd	1.346	160.9		
HS40(4.5) PAH(4.5)	none	1.257	131.4	+9.7	-21.4
HS40(4.5) PAH(4.5)	htd	1.379	103.2		
HS40(4.5) PDAC(4.5)	none	1.266	101.3	+10.9	-41.4
HS40(4.5) PDAC(4.5)	htd	1.404	59.3		
HS40(4.5) PDAC(4.5)	none	1.263	159.2	+7.4	-20.3
HS40(4.5) PDAC(4.5)	htd	1.356	127.0		
SM30(5) ZrO(3)	<i>on glass</i>	1.351	41.3	+5.3	-9.1
SM30(5) ZrO(3)	<i>on glass htd</i>	1.423	37.5		
HS40(4.5) ZrO(3)	none	1.300	143.7	+7.0	-10.9
HS40(4.5) ZrO(3)	htd	1.392	128.0		
TM40(3) ZrO(3)	none	1.266	77.4	+14.9	-39.7
TM40(3) ZrO(3)	Htd	1.454	46.7	+10.6	-60.4
TM40(3) ZrO(3)	htd	1.400	30.7		
TM40(3) ZrO(3)	none	1.264	425.9	+0.9	-2.6
TM40(3) ZrO(3)	htd	1.275	415.0		



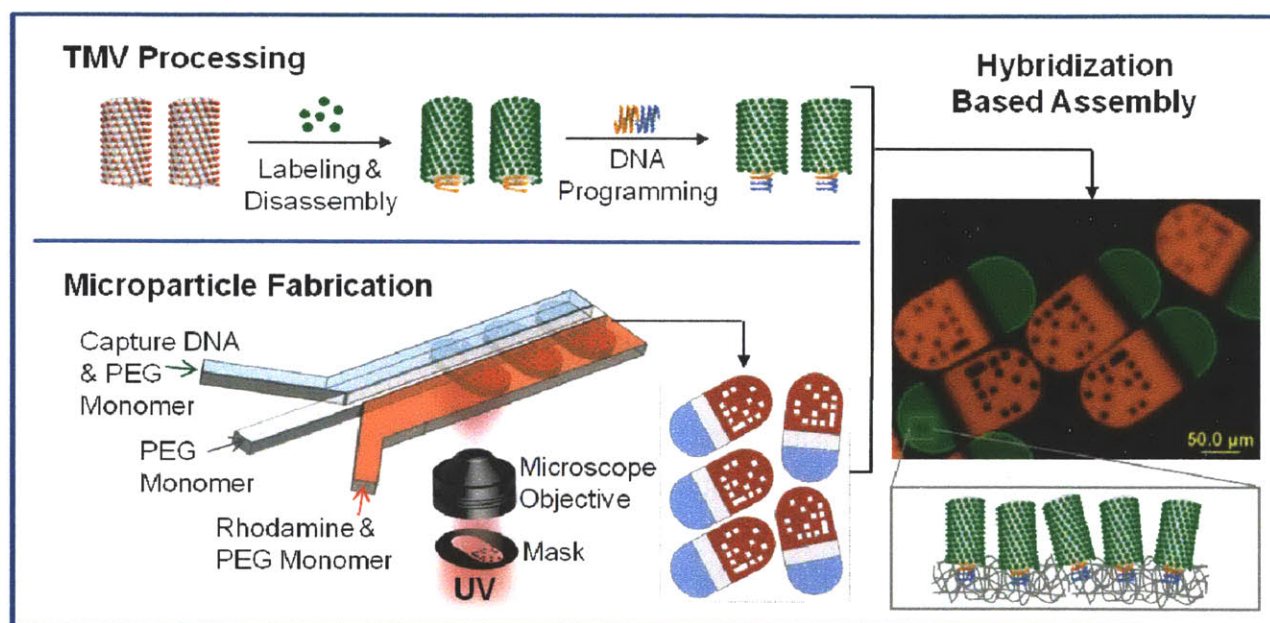


# APPENDIX D: Hierarchical Assembly of Viral Nanotemplates with Encoded Microparticles via Nucleic Acid Hybridization

*This appendix is reproduced in part with permission from Wui Siew Tan<sup>1,†</sup>, Christina L. Lewis<sup>2,†</sup>, Nicholas E. Horelik<sup>2</sup>, Daniel C. Pregibon<sup>1</sup>, Patrick S. Doyle<sup>1,\*</sup>, and Hyunmin Yi<sup>2,\*</sup>, Langmuir, 24, 12483-12488, 2008. Copyright 2008 American Chemical Society.*

<sup>1</sup>Department of Chemical Engineering, Massachusetts Institute of Technology, Cambridge, MA 02139

<sup>2</sup>Department of Chemical and Biological Engineering, Tufts University, Medford, MA 02155



While the research discussed in chapters 2 to 5 of this thesis centered around thin film conformal coatings of responsive hydrogels, my interest and first work on hydrogel materials started with micron sized covalently crosslinked poly(ethylene glycol) colloidal particles. This work was done in the time (between 2006 and 2008) that I spent in Prof Patrick S. Doyle's laboratory in the Dept of Chemical Engineering at MIT. Stop flow lithography (SFL) is a fascinating microfluidic method of producing 3D-hydrogel particles of unique shape and functionality as will be apparent in the work that follows.

This work was done in collaboration with Christina L. Lewis and Prof. Hyunmin Yi from Tufts University. I thank Prof Doyle for the opportunity to work on this interesting project in his lab and also thank Daniel C. Pregibon, native SFL expert from the Doyle lab for showing me the ropes.

## Abstract

We demonstrate hierarchical assembly of Tobacco Mosaic Virus (TMV) based nanotemplates with hydrogel based encoded microparticles via nucleic acid hybridization. TMV nanotemplates possess a highly defined structure and a genetically engineered high density thiol functionality. The encoded microparticles are produced in a high throughput microfluidic device via stop-flow lithography (SFL), and consist of spatially discrete regions containing encoded identity information, an internal control, and capture DNAs. For the hybridization based assembly, partially disassembled TMVs were programmed with linker DNAs that contain sequences complementary to both the virus 5' end and a selected capture DNA. Fluorescence microscopy, atomic force microscopy (AFM), and confocal microscopy results clearly indicate facile assembly of TMV nanotemplates onto microparticles with high spatial and sequence selectivity. We anticipate that our hybridization based assembly strategy could be employed to create multifunctional viral-synthetic hybrid materials in a rapid and high-throughput manner. Additionally, we believe that these viral-synthetic hybrid microparticles may find broad applications in high capacity, multiplexed target sensing.

## Introduction

Structurally and chemically complex hybrid materials are needed for high end applications in renewable energy, electronics, computing, diagnostics, medicine and analytical chemistry<sup>1-6</sup>. To create materials with properties that transcend those of individual components, hierarchical assembly of units tailored across nanometer and micrometer length scales is highly desired<sup>7</sup>. Methods used to synthesize hierarchically assembled materials include direct or synergistic templating, self-assembly, photochemical patterning, electrodeposition, microcontact printing, and nanolithographic techniques<sup>7-9</sup>. These methods often involve a series of complex steps or have limited ability in controlling spatial resolution while maintaining full integrity of the individual components. Therefore, a facile method for hierarchically assembling hybrid materials under mild conditions in a selective manner is needed.

Recently, viruses have gained substantial attention as nanoscale templates for material synthesis<sup>10-18</sup>. They are structurally well defined, monodisperse, robust, nanoscaled units that have proven to be versatile substrates for the creation of novel materials by coupling to synthetic chemistry or genetic manipulation<sup>12,19-25</sup>. Site directed mutagenesis on viruses enables surface display of amino acids, which may be coupled to downstream chemical conjugation or used for direct display of peptides like antibodies or enzymes in well defined spatial arrangements on the nanometer scale<sup>26-28</sup>. Tobacco Mosaic Virus (TMV) offers an attractive nanotemplate that provides high density covalent coupling sites with precise nanometer scale spacing. As shown in the Atomic Force Microscopy (AFM) image of Figure D-1(b), a wild type TMV virion consists of approximately 2130 identical coat proteins helically wrapped around a 6.4 kb positive strand of genomic mRNA, making it an 18nm diameter and 300 nm long rigid nanotube with a 4nm diameter inner channel<sup>29</sup>. Particularly, TMV possesses several unique properties as nanotemplates such as simple mass production<sup>30</sup>, a well defined structure<sup>29,31-33</sup>, and

extraordinary stability. For example, TMV has been shown to be stable under various harsh conditions: temperatures up to 90°C, extreme pHs (2-10) and organic solvents (80% ethanol, methanol, and DMSO)<sup>30,34,35</sup>. Furthermore, the ability to confer surface functionalities via genetic manipulation<sup>36</sup> makes TMV an attractive choice compared to inorganic nanotubes. Due to the reasons mentioned above, TMV has been successfully exploited in creating a wide range of organic-inorganic hybrid materials<sup>37,38</sup> and has also been applied in functional digital memory devices<sup>39</sup> and battery electrodes<sup>40</sup>. Patterning the assembly of functionalized TMVs<sup>41,42</sup> in a hierarchical manner is imperative to fully harness TMV's unique potential as a nanotemplate.

We have previously demonstrated continuous fabrication of poly(ethylene glycol) (PEG) based microparticles with custom designed geometries and tunable chemical anisotropy via stop-flow lithography (SFL)<sup>43</sup>. Benefits of the SFL technique include rapid and continuous production of monodisperse and biocompatible microparticles in a high throughput manner. This simple microfluidic technique affords the ability to create microparticles consisting of spatially discrete regions containing encoded identity information and covalently attached capture DNAs. The encoded region may be used to distinguish the microparticles from one another with over a million different codes available allowing immense multiplexing capability<sup>44</sup>. The region containing covalently attached capture DNAs provides a platform for selectively patterning TMV. Combining the two technologies of TMV nanotemplates and encoded microparticles to create multifaceted hybrid materials may have significant potential in a broad range of applications including high throughput sensing.

Here, we demonstrate hierarchical assembly of fluorescein-labeled TMV1cys nanotemplates onto encoded microparticles, as shown in Figure D-1. As shown in the schematic diagram of Figure D-1(a), genetically modified TMV1cys nanotemplates possess one cysteine residue on the outer surface of each coat protein that serve as covalent coupling sites for fluorescein-maleimide, a fluorescein derivative that forms a covalent thioether linkage with cysteine's thiol group<sup>41,42</sup>. These labeled TMVs were then partially disassembled to expose the 5' end genomic RNA via sucrose gradient ultracentrifugation under alkaline pH. Since coat protein-RNA interactions are weakest at the 5' end of the viral RNA, mild alkaline treatments and centrifugation can be used to mimic cellular conditions in order to partially disassemble the virus and expose the 5' end of its genome<sup>42</sup>. Figure D-1(c) shows that these fluorescently labeled TMVs form a discrete band while unreacted fluorescein dye remains at the top of the sucrose gradient. Next, these TMVs were programmed via hybridization with linker DNA consisting of two regions: one complementary to TMV's 5' end RNA and the other complimentary to the microparticle's capture DNA sequence. This confers the capture DNA sequence-specific assembly address to the TMV (Table 1).

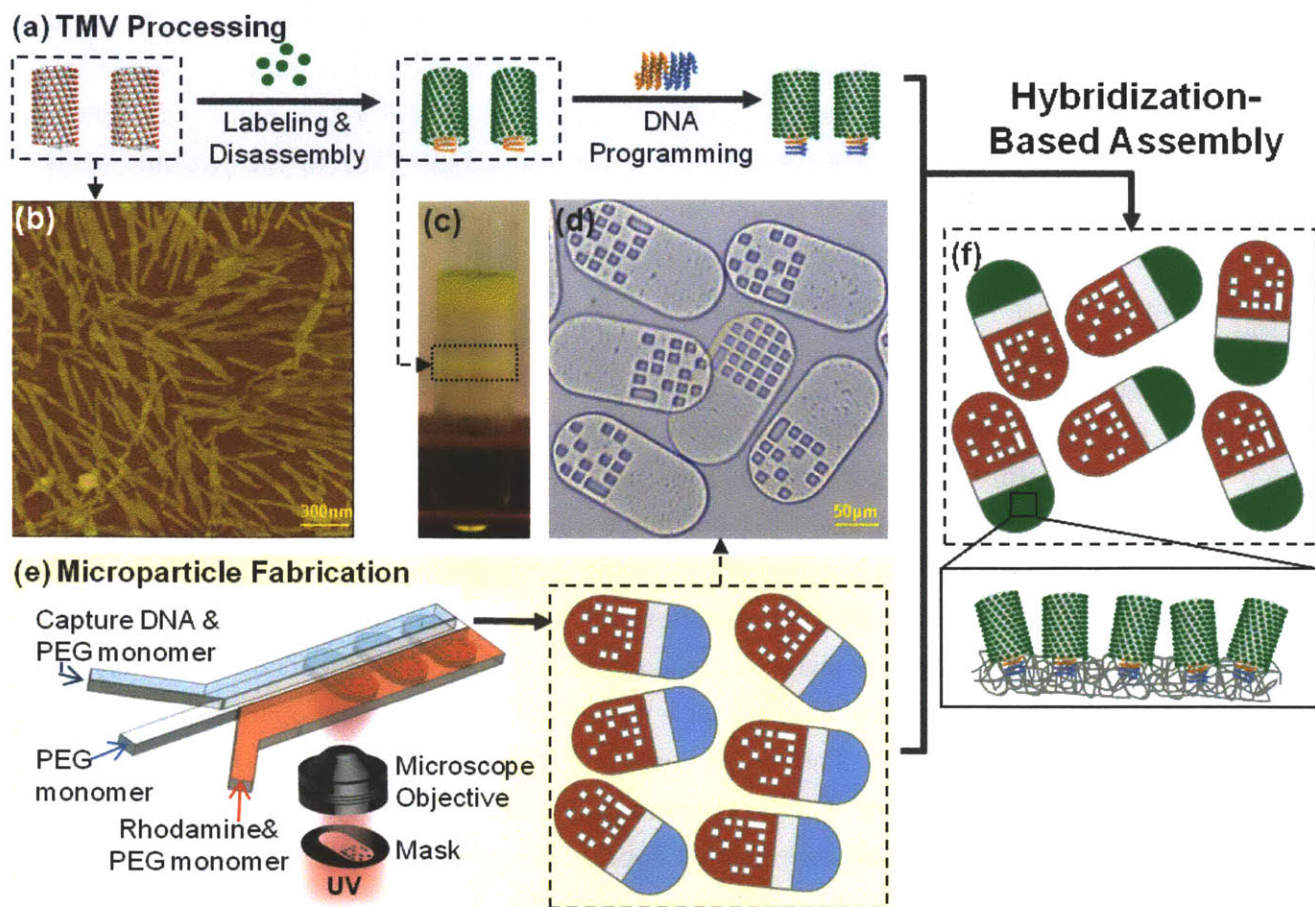


**Figure D-1.** Hierarchical assembly of fluorescein-labeled TMV1cys nanotemplates onto encoded and capture DNA embedded PEG-based microparticles. (a) Schematic diagram depicting the labeling, disassembly, and programming of TMV1cys. The TMV models are generated from UCSF Chimera software (Experimental Section) and represent approximately one tenth of the total TMV virion. The red dots represent cysteine residues genetically displayed on the outer surface of each coat protein (~2130 identical proteins per virion), adding precisely spaced thiol functionality for covalent conjugation of fluorescent markers. Partial disassembly followed by hybridization with linker DNA confers capture DNA-sequence specific assembly address. (b) Atomic Force Microscopy (AFM) topographical image of TMV1cys. The yellow bar represents 300nm. (c) Sucrose gradient containing fluorescently labeled TMVs as a discrete band (boxed) separated from unreacted fluorescein dye at the top of the sucrose gradient. (d) Brightfield micrograph of encoded microparticles. The yellow bar represents 50µm. (e) Schematic diagram of stop-flow lithography (SFL) for production of encoded and DNA embedded microparticles. (f) Formation of nanobio-synthetic hybrid microentities following hybridization based assembly of TMVs with microparticles.

The PEG based microparticles consisting of the encoded, control, and capture DNA regions were fabricated in a microfluidic device via SFL, as shown in the schematic diagram of Figure D-1(e). The regions of different functionality are copolymerized seamlessly within each microparticle by a single

UV exposure through a photomask with the desired microparticles shape. This photolithography based microfluidic technique of SFL enables rapid and continuous production of various shaped microparticles using diacrylate chemistry and patterned UV crosslinking through a photomask containing the desired microparticle shape. A brightfield micrograph of these microparticles is shown in Figure D-1(d). Hybridization based assembly of the labeled and programmed TMVs with the encoded microparticles containing capture DNA creates nanobio-synthetic hybrid microentities, as shown in Figure D-1(f). Fluorescence microscopy, AFM, and confocal microscopy results clearly illustrate facile assembly of TMV nanotemplates onto microparticles with high spatial and sequence selectivity. Since proteins and antibodies can be covalently linked to TMV via its high density thiol surface functionality, we envision that our facile assembly strategy, that allows the creation of complex functionalized TMV-PEG structures, can be readily exploited for a variety of biotechnological applications such as high throughput, multiplexed protein sensing<sup>45,46</sup>.

## Experimental Section

*TMV1cys and Fluorescent Labeling.* TMV1cys was provided as a generous gift from James Culver, University of Maryland Biotechnology Institute, Center for Biosystems Research. Purified TMV1cys was incubated at room temperature for 2h with 10-fold molar excess of fluorescein-5-maleimide (Biotium, Hayward, CA) in 100mM Tris-buffer, pH 7.0. Fluorescein-labeled virus was separated by centrifugation in a 10-40% sucrose gradient<sup>41,42</sup> at 48,000g for 2h while the pH was adjusted to 8.0 to partially remove coat protein subunits from the 5'ends of the viral genome. Partially disassembled virions were pelleted by centrifugation for 40min at 106,000g. Pelleted viruses were resuspended in 5xSSC buffer (75mM sodium citrate, 750mM sodium chloride, pH 7.0).

*Microparticle Fabrication.* PEG microparticles were synthesized as previously described<sup>44</sup>. Briefly, a poly(ethylene glycol) diacrylate (PEG-DA Mn=700, Aldrich) monomer was mixed with 2.5 vol% of 2-Hydroxy-2-methylpropiophenone photoinitiator (Darocure 1173, Aldrich), 33 vol% of TE buffer (10 mM Tris pH 8.0 (Rockland Immunochemicals, Inc., Gilbertsville, PA), and 1mM EDTA (OmniPur)) containing 0.01 vol% of 10 wt% sodium dodecyl sulfate (SDS, Invitrogen). This base monomer mixture was in turn mixed in a 9:1 volume ratio with 1 part of TE solution containing DNA-Acrydite capture DNAs, blue food dye (to visualize the co-flowing monomer streams using bright-field microscopy), or Rhodamine B (Polysciences Inc., Warrington, PA). DNA probes (IDT Technologies, Coralville, IA) were modified with a reactive Acrydite group and an 18-carbon spacer. Three different capture DNA sequences were used in this study, as shown in Table 1. Final prepolymer mixtures contained either (a) 50 $\mu$ M DNA-Acrydite capture DNA (C1, C2 or C3) (b) 1 vol% blue food dye or (c) 0.1mg/ml of Rhodamine B. The prepolymer mixtures were co-flowed through microfluidic PDMS devices made by traditional soft lithographic methods. Channels were designed with one to three 100 $\mu$ m wide channels that converged into a single 200-400 $\mu$ m wide channel allowing co-flow of up to three different monomer streams to create microparticles with up to three distinct regions. The thickness of each stream was controlled by adjusting the relative pressure on each of the inlet channels,

which were connected to a pressure source (regulated by a pressure valve, Controlair Inc., Amherst, NH). Using an inverted Zeiss Axiovert 200 microscope with a 100W HBO mercury lamp and photomasks inserted in the field-stop position, PEG microparticles were polymerized by 75ms bursts of wide-excitation ultraviolet (UV) light from a 11000v2 UV filter set (Chroma Technology Corp., Rockingham, VT). A computerized stop-polymerize-flow sequence of ~1sec was cycled to obtain 1000's of microparticles in less than 20mins. The resulting microparticles were 30 $\mu$ m thick and of shapes projected from the photomask. Using a 20 $\times$  optical objective, photomasks were designed to form the 180 $\times$ 90 $\mu$ m encoded microparticles shown in Figure D-1(d). These microparticles (3 types) were made using three co-flowed streams, shown in Figure D-1(e) with capture DNA C1, C2, or C3, each containing a different encoded region. Microparticles were cleaned of unreacted monomer with three different rinse solutions: TE buffer containing 0.1% Tween 20 surfactant, PEG-DA monomer, and TE buffer containing 1% Tween 20 surfactant. The rinses were completed with ~1ml of rinse solution, vortexing, centrifugation, and aspiration of supernatant. Microparticles were stored in TE buffer containing 1% Tween 20 surfactant at 20 $^{\circ}$ C before use in hybridizations.

*Hybridization Based Assembly of TMV Nanotemplates.* For address specific programming of labeled and partially disassembled TMV, 10-fold molar excess of linker DNA (IDT Technologies, Coralville, IA) was added to fluorescein-labeled TMV solutions and incubated at 30 $^{\circ}$ C for 2h. The linker DNA consisted of two regions: one complementary to TMV's 5'end RNA and the other complimentary to the microparticle's capture DNA sequence, as shown in Table 1. To remove the unbound linker DNA, mixtures were centrifuged at 106,000g for 40min in 5xSSC buffer. The fluorescein-labeled single stranded (ss) DNA, described in Table 1, was purchased from Gene Probe Technologies Inc. (Gaithersburg, MD). For assembly of TMV, fluorescein-labeled ssDNA, and microparticles, both the programmed TMV pellets and fluorescein-labeled ssDNA were resuspended in 5xSSC buffer containing 0.01% Tween 20 and hybridized with the microparticles overnight at 37 $^{\circ}$ C. The final TMV and ssDNA concentrations in the hybridization solution were circa 50-100nM. The microparticles were then rinsed several times with 2xSSC buffer containing 0.01% Tween 20.

*Analysis.* The hybridized microparticles were visualized using standard filter sets U-N31001 and U-N31002 (Chroma Technology Corp., Rockingham, VT), compatible with fluorescein and rhodamine fluorophores, respectively, in an Olympus BX51 microscope. Still images were captured using a DP70 microscope digital camera. The fluorescence images were evaluated with the fluorescence intensity profile function from ImageJ software (<http://rsb.info.nih.gov/ij/>). AFM images were obtained using a Dimension 3100 AFM (Digital Instruments, Santa Barbara, CA) with a Nanoscope IV Controller operated in dry tapping mode with a scan rate of 0.5Hz and moderate amplitude setpoints. Tap300 silicon probes (Budget Sensors, Sofia, Bulgaria) were used at approximately 300Hz. The AFM images were analyzed using Nanoscope software version 6.00. Confocal images were acquired on a Leica DMIRE2 microscope with a TCS SP2 scanner (Wetzlar, Germany). The system was equipped with a 63 $\times$  (NA 1.2) water immersion objective, which was used in this study. Samples were placed on

number 1.5 cover glass within a PDMS well and excited at 488nm. Fluorescence emission spectra were detected from 500-530nm. The depth scan increment was 1µm with a scan thickness of circa 155nm. Analysis was performed with the Leica Confocal Software (Wetzlar, Germany).

**Molecular Modeling.** The TMV molecular graphics images were produced using the UCSF Chimera package (<http://www.cgl.ucsf.edu/chimera>)<sup>47-49</sup> from the Resource for Biocomputing, Visualization, and Informatics at the University of California, San Francisco (supported by NIH P41 RR-01081). The base structure of TMV (PDB ID: 2tmv)<sup>50</sup> used in the molecular graphics images was obtained from the Research Collaboratory for Structural Bioinformatics Protein Data Bank (RCSB PDB, <http://www.pdb.org/>)<sup>51</sup>.

**Table D-M1.** Single Stranded DNA Sequences

Name	5'end	Sequence	3'end
<b>Capture DNA Embedded within the Microparticles</b>			
C1	Acrydite-C18	ATGATGATGATGATGATG	---
C2	Acrydite-C18	TTTTTCGGCAGGTCGGTAAAC	---
C3	Acrydite-C18	CACTACCGATACGTACTIONCAG	---
<b>Fluorescently Labeled Single Stranded DNA Hybridized with Microparticles</b>			
C3'	FITC <sup>1</sup>	CTGAGTACGTATCGGTAGTG	---
<b>Linker DNA Hybridized with TMV and Microparticles</b>			
C2'	---	<u>GTTTGTGTTGTTGGTAATTGTTGTTTTGTTACCGACCTGCCGAAAAA</u> <sup>2</sup>	---

1. FITC: fluorescein isothiocyanate.

2. The detailed sequence description entails: TMV 5'end Complementary Sequence *Spacer* Address-specific Sequence.

## Results and Discussion

**Hierarchical Assembly of TMV Nanotemplates with Encoded Microparticles.** As shown in Figure D-2, we first demonstrate hierarchical assembly of fluorescein-labeled TMV1cys nanotemplates onto microparticles via nucleic acid hybridization. The microparticles were fabricated in a microfluidic device via stop-flow lithography (SFL)<sup>43</sup>, as shown in Figure D-1(e), and consist of three discrete regions: an encoded region containing Rhodamine B, a middle negative control region, and a capture DNA region. TMV1cys nanotemplates were labeled with fluorescein maleimide, which forms a covalent thioether bond with the genetically displayed cysteine's thiol groups. These labeled TMVs were partially disassembled to expose the 5'end genomic RNA then programmed with linker DNAs via hybridization to confer the capture DNA sequence-specific address. These labeled and programmed TMVs were incubated with microparticles for hybridization based assembly and examined with a fluorescence microscope, as shown in Figure D-2.

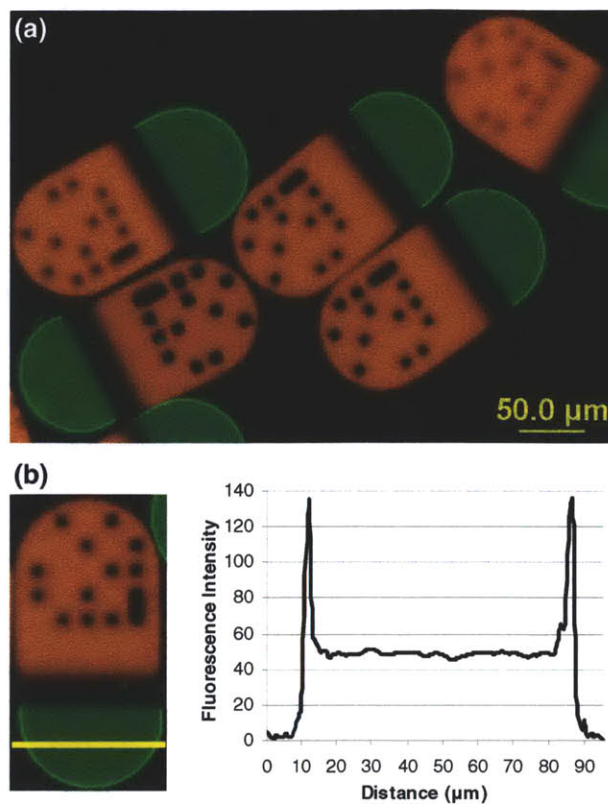


**Figure D-2.** Hierarchical assembly of fluorescein-labeled TMV1cys nanotemplates onto microparticles via nucleic acid hybridization. (a) Overlay fluorescence image of fluorescein-labeled TMV1cys onto Rhodamine B labeled and encoded microparticles. Three regions define the  $180 \times 90 \times 30 \mu\text{m}$  microparticles: an encoded region containing Rhodamine B, a middle negative control region, and a capture DNA region. (b) Fluorescence intensity plot across the TMV assembled region shown by the yellow line.

As shown in the fluorescence micrograph of Figure D-2(a), fluorescein-labeled TMVs readily assembled onto the capture DNA region of the microparticles. Importantly, the encoded and middle control regions of the microparticles showed minimal non-specific binding (from TMV1cys-conjugated fluorescein), demonstrating high spatial selectivity. Figure D-2(a) also shows the reproducibility of both the particle fabrication process and TMV1cys assembly. The fluorescence intensity profile plot in Figure D-2(b) shows a uniform TMV assembly density on the microparticles, as the fluorescence intensity is nearly constant across the TMV region of the microparticles, excluding the edges. Since the TMVs are unable to penetrate far into the microparticles, their localization near the surface of the capture DNA region is expected and results in the bright edges seen when microparticles are lying flat and viewed top-down as shown in Figure D-2(a). Combined, these results demonstrate the highly uniform and multifunctional nature of the microparticles, and the creation of viral-synthetic microentities via hybridization-based assembly of TMV nanotemplates with encoded microparticles.



**Sequence Specific Assembly of TMV with Multiple Microparticle Types.** To directly demonstrate the sequence specificity of our assembly procedure, we incubated the fluorescein-labeled and linker DNA (C2') programmed TMV1cys nanotemplates with a mixture of microparticles, as shown in Figure D-3. This microparticle mixture contained three types, as shown in Figure D-3(a), each with different codes and capture DNA sequences (C1, C2, and C3). The fluorescence micrograph of Figure D-3(b) clearly shows that TMVs assembled only onto the microparticles containing the matching capture DNA sequence (C2). Importantly, minimal fluorescence in the capture DNA area of the non-specific microparticles demonstrates the highly selective nature of the hybridization-based assembly. This result confirms that the assembly event occurs via sequence specific hybridization, suggesting the feasibility of simultaneous “one-pot” assembly of multiple TMV conjugates with a large number of microparticle types, each containing a different barcode and capture DNA sequence. Additionally, the encoded region enables identification of the DNA sequence derived functionality, suggesting the potential for a high throughput screening capability. Similarly, site-specific assembly of TMV conjugates carrying multiple functionalities to multiple regions on a single particle could also be envisioned. The latter could readily be achieved using the versatility of the SFL process that allows production of microparticles with more than one DNA capture region containing different capture DNA sequences.

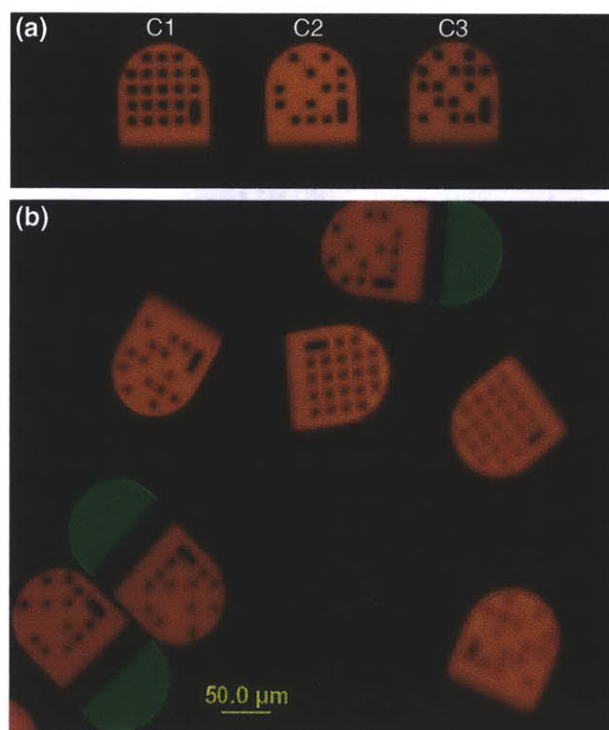


**Figure D-3.** TMV templates hybridized with a mixture of three different microparticle types. (a) Three microparticle types, all differing by the barcode and capture DNA sequence embedded within the microparticles. (b) Fluorescence overlay image showing fluorescein-labeled TMV1cys assembled onto only the microparticles containing the matching DNA sequence, C2.

**Atomic Force Microscopy (AFM) of TMV Nanotemplates on Microparticles.** AFM has been extensively employed in studying biological materials, especially TMVs on solid substrates. These efforts have led to the elucidation of various fundamental properties including mechanical strengths<sup>52</sup>, conductivity<sup>39</sup>, and flexoelectricity<sup>53</sup> to list a few. Here, we have used AFM to physically confirm the presence of TMV nanotemplates on the microparticles and examine the structural integrity of assembled TMVs. For this, the TMV decorated microparticles were extensively rinsed, dried under ambient conditions for 5 days, and examined with tapping mode using a standard silicon tip. The phase contrast AFM image of Figure D-4 clearly shows that TMV1cys nanotemplates are assembled on the microparticles with high density and full structural integrity. We have been able to vary the surface density of TMV assembled onto microparticles through variation of the TMV hybridization concentrations and denser coverage of TMV has been achieved (image not shown). Figure D-4 represents a sample with lower TMV surface density but shows the structural integrity of individual TMVs most clearly. The encoded and negative control regions were also examined via AFM, and did not show a significant number of TMVs (images not shown). Additionally, despite the extensive rinsing and drying conditions necessary for AFM sample preparation, the microparticle-assembled TMVs retained their structure, demonstrating the stability of these hybridized TMV1cys nanotemplates. Overall, this result clearly confirms the presence and structural integrity of TMV nanotemplates assembled on microparticles.

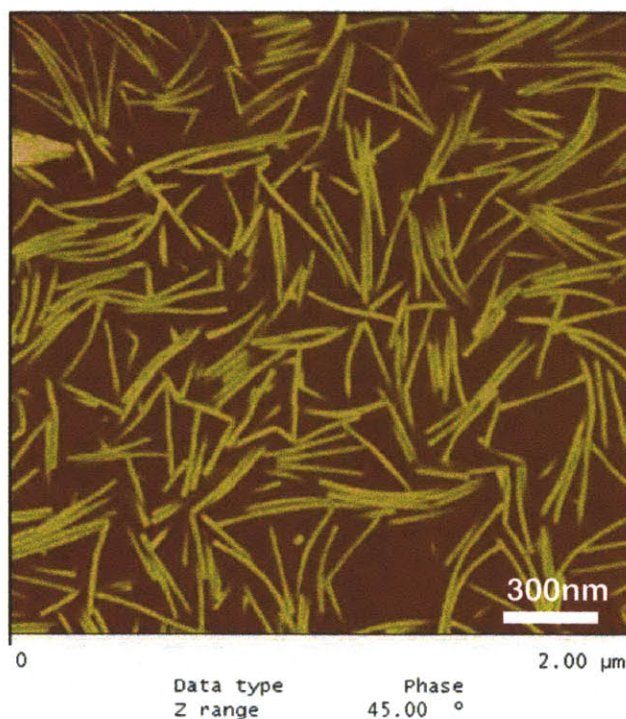


**Figure D-4.** AFM phase contrast image of TMV assembled onto encoded microparticles.

**Confocal Microscopy of TMV Assembled Microparticles.** As shown in Figure D-5, we employed confocal microscopy to examine detailed 3-D assembly features of the TMV- and fluorescein labeled ssDNA-assembled microparticles. As shown in the schematic diagram of Figure D-5(a) and the

brightfield micrograph of Figure D-5(b), the microparticles used for this evaluation contained two spatially discrete capture DNA regions coding different sequences and separated by a negative control region. These microparticles were incubated in a solution containing two fluorescein labeled species: fluorescein labeled TMV programmed with linker DNA complementary to the round region (C2) and fluorescein labeled ssDNA complementary to the rectangular region (C3).

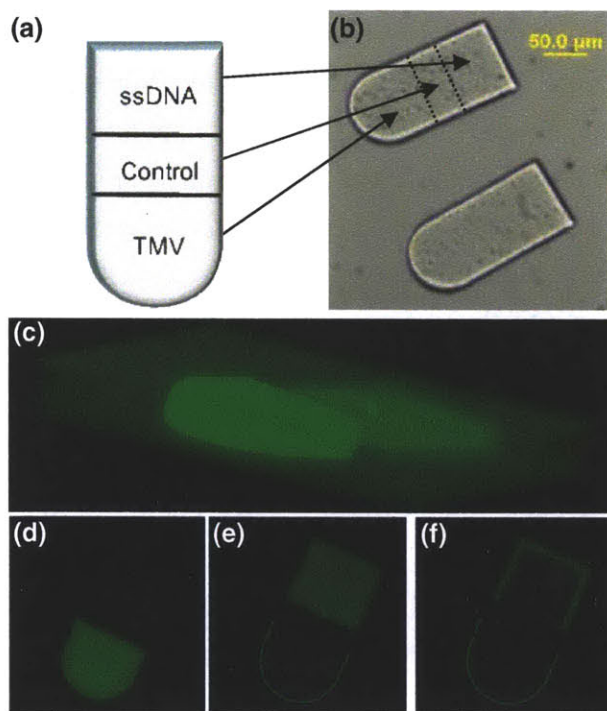


**Figure D-5.** One-pot assembly of fluorescein-labeled TMV and ssDNA onto discrete regions of multifunctional microparticles: (a) Schematic diagram showing the three regions of the multifunctional microparticles: the TMV-complimentary (round edge) and ssDNA-complimentary (straight edge) regions are separated by a middle negative control region. (b) Brightfield image of the multifunctional microparticles. The yellow bar represents 50 $\mu$ m. (c) Reconstituted 3-D confocal image of a multifunctional microparticle following hybridization with the fluorescein-labeled TMV and ssDNA. (d-f) Confocal z-scan images of TMV and ssDNA hybridized microparticles at the surface (d) several micrometers below the surface (e), and center (f).

A z-scan analysis on these microparticles clearly shows the difference in the 3-D assembly feature between the two regions, as shown in Figures D-5(c)-(f). First, the three-dimensional reconstituted image of Figure D-5(c) shows the difference in spatially selective assembly and in material characteristics between the TMV-assembled and DNA-assembled regions. The TMV-assembled region shows bright fluorescence at the very outer surface of the microparticles, and minimal fluorescence within the microparticle volume. This is likely due to the large size of the TMV that prevents deep penetration into the hydrogel matrix of the particle. In contrast, the DNA assembled region shows more

dispersed fluorescence near the particle surface. This is likely due to the smaller size of the fluorescein labeled DNA that allows it to diffuse further into the hydrogel, and correlates well with our previously reported results<sup>44</sup>. This difference in the penetration depth is further demonstrated in the z-scan images of Figures D-5(d)-(f) at the surface (d), several micrometers below the surface (e), and at the center (f). Figure D-5(d), taken at the top surface of the microparticle shows that TMVs are assembled only onto the circular region with high fluorescence intensity, while the rectangular ssDNA region shows minimal fluorescence. As the z-scan layer moves a few micrometers toward the microparticle center, Figure D-5(e) shows that the TMV layer is confined to the very outer surface whereas the fluorescein labeled DNA layer just starts to appear. Finally, Figure D-5(f), taken at the microparticle center, shows that the TMVs are mainly assembled within the outer circa 2 $\mu$ m region of the microparticles with high fluorescence while DNA penetrates several micrometers deeper. Importantly, these confocal microscopy results illustrate the high fluorescein-templating density of the TMV nanotemplates given the same fabrication condition and thus capture DNA density in the two regions. The difference in fluorescence intensities of the TMV bound region versus the ssDNA bound region reflects the high fluorescein-templating density of the TMV nanotemplates. Since numerous fluorescein molecules are conjugated to each TMV while only one fluorescein molecule is attached to each ssDNA, the amount of fluorescence pre DNA binding even is multifold for TMV compared to ssDNA. Furthermore, the two capture DNA regions do not show any overlapping assembly characteristics, strongly suggesting the sequence specificity of the sequence design and assembly procedures. Together, these results illustrate the potential for integrating TMVs and SFL in creating multifaceted hybrid materials.

## Conclusions

Hierarchically assembled materials structured across nano and micrometer length scales provide the ability to exploit features on submicron scales in macroscopic devices as well as form materials with new properties tailored for specific applications. A major challenge among the current methods for creating hierarchically assembled materials is the limited ability in controlling spatial resolution while maintaining full integrity of the individual components. Thus, a facile method for hierarchically assembling hybrid materials under mild conditions in a spatially selective manner is needed.

The fluorescence microscopy results reported in this study illustrated both the spatially selective and sequence specific nature of the assembly process. High spatial selectivity is afforded by the fidelity of the sequence specific DNA hybridization used in our assembly process and holds potential for one-pot assembly of multiple TMV conjugates to different encoded microparticles or to different regions on a single microparticle. In addition, the assembly and particle fabrication processes were shown to be very reproducible. The AFM images clearly showed that the TMV nanotemplates are assembled on the microparticles with high density and full structural integrity despite the extensive rinsing and drying required to prepare samples for AFM analysis. The confocal microscopy results demonstrated the feasibility of one-pot assembly between multiple TMV conjugates and a large number of microparticle types, each containing a different barcode and capture DNA sequence. The confocal microscopy

images also showed the high fluorescein-templating density of the TMV nanotemplates and that these nanotemplates are assembled on the microparticle surface. Combined, these results represent a novel high throughput route to create multiplexed and multifunctional viral-synthetic hybrid microentities in mild aqueous conditions. We expect that the integration of viral nanotemplates and the rapid SFL technique will have significant potential in creating complex structures for a broad range of applications. For example, one could envision protein sensing with antibody conjugated TMVs assembled onto encoded microparticles. The multiplexing capability of such protein-viral-synthetic hybrid materials would enable high throughput analysis of analytes<sup>44</sup>.

**Acknowledgements:** We thank Dr. James Culver at the University of Maryland Biotechnology Institute, Center for Biosystems Research, for providing the generous gift of TMV1cys. We also thank Jonathan Levitt at Tufts University, Biomedical Engineering Department, for assistance with the confocal microscopy analysis. This work was supported in part by Tufts Faculty Research Award (FRAC, H.Y.) and by NSF grant CTS-0304128 (P.S.D.).

## References

- (1) Chomski, E.; Ozin, G. *Advanced Materials* **2000**, *12*, 1071-1078.
- (2) Correia, A.; Perez, M.; Saenz, J. J.; Serena, P. A. *physica status solidi (a)* **2007**, *204*, 1611-1622.
- (3) Lehn, J.-M. *Science* **2002**, *295*, 2400-2403.
- (4) Ozin, G. A. *Chemical Communications* **2000**, 419-432.
- (5) Ungar, G.; Liu, Y.; Zeng, X.; Percec, V.; Cho, W.-D. *Science* **2003**, *299*, 1208-1211.
- (6) Zuo, L.; Wei, W.; Morris, M.; Wei, J.; Gorbounov, M.; Wei, C. *Medical Clinics of North America* **2007**, *91*, 845.
- (7) Whitesides, G. M.; Grzybowski, B. *Science* **2002**, *295*, 2418-2421.
- (8) Lakes, R. *Nature* **1993**, *361*, 511-515.
- (9) Sanchez, C.; Arribart, H.; Giraud Guille, M. M. *Nat Mater* **2005**, *4*, 277-288.
- (10) Dujardin, E.; Peet, C.; Stubbs, G.; Culver, J. N.; Mann, S. *Nano Letters* **2003**, *3*, 413-417.
- (11) Fowler, C. E.; Shenton, W.; Stubbs, G.; Mann, S. *Advanced Materials* **2001**, *13*, 1266-1269.
- (12) Lee, L. A.; Wang, Q. *Nanomedicine: Nanotechnology, Biology and Medicine* **2006**, *2*, 137.
- (13) Niu, Z. W.; Bruckman, M. A.; Li, S. Q.; Lee, L. A.; Lee, B.; Pingali, S. V.; Thiyagarajan, P.; Wang, Q. *Langmuir* **2007**, *23*, 6719-6724.
- (14) Balci, S.; Noda, K.; Bittner, A. M.; Kadri, A.; Wege, C.; Jeske, H.; Kern, K. *Angewandte Chemie-International Edition* **2007**, *46*, 3149-3151.
- (15) Huang, Y.; Chiang, C. Y.; Lee, S. K.; Gao, Y.; Hu, E. L.; Yoreo, J. D.; Belcher, A. M. *Nano Letters* **2005**, *5*, 1429-1434.
- (16) Yoo, P. J.; Nam, K. T.; Qi, J.; Lee, S.-K.; Park, J.; Belcher, A. M.; Hammond, P. T. *Nat Mater* **2006**, *5*, 234.
- (17) Chiang, C. Y.; Mello, C. M.; Gu, J.; Silva, E.; Van Vliet, K.; Belcher, A. *Advanced Materials* **2007**, *19*, 826-832.
- (18) Steinmetz, N. F.; Findlay, K. C.; Noel, T. R.; Parker, R.; Lomonossoff, G., P.; Evans, D. J. *ChemBioChem* **2008**, *9*, 1662-1670.

- (19) Fischlechner, M.; Donath, E. *Angewandte Chemie-International Edition* **2007**, *46*, 3184-3193.
- (20) Fischlechner, M.; Toellner, L.; Messner, P.; Grabherr, R.; Donath, E. *Angewandte Chemie International Edition* **2006**, *45*, 784-789.
- (21) Douglas, T.; Young, M. *Advanced Materials* **1999**, *11*, 679-310.
- (22) Manchester, M.; Singh, P. *Advanced Drug Delivery Reviews* **2006**, *58*, 1505.
- (23) Merzlyak, A.; Lee, S.-W. *Current opinion in chemical biology* **2006**, *10*, 246.
- (24) Singh, P.; Gonzalez, M. J.; Manchester, M. *Drug Development Research* **2006**, *67*, 23-41.
- (25) Gazit, E. *FEBS Journal* **2007**, *274*, 317-322.
- (26) Smolenska, L.; Roberts, I. M.; Learmonth, D.; Porter, A. J.; Harris, W. J.; Wilson, T. M. A.; Santa Cruz, S. *FEBS letters* **1998**, *441*, 379.
- (27) Schwyzer, R.; Kriwaczek, V. M. *Biopolymers* **1981**, *20*, 2011-2020.
- (28) Werner, S.; Marillonnet, S.; Hause, G.; Klimyuk, V.; Gleba, Y. *Proceedings of the National Academy of Sciences of the United States of America* **2006**, *103*, 17678-17683.
- (29) Culver, J. N. *Annual Review of Phytopathology* **2002**, *40*, 287-310.
- (30) Zaitlin, M. *AAB Descriptions of Plant Viruses* **2000**, 370.
- (31) Klug, A. *Philosophical Transactions of the Royal Society of London Series B-Biological Sciences* **1999**, *354*, 531-535.
- (32) Lebeurier, G.; Nicolaieff, A.; Richards, K. E. *Proceedings of the National Academy of Sciences of the United States of America* **1977**, *74*, 149-153.
- (33) Namba, K.; Stubbs, G. *Science* **1986**, *231*, 1401-1406.
- (34) Knez, M.; Sumser, M.; Bittner, A. M.; Wege, C.; Jeske, H.; Martin, T. P.; Kern, K. *Advanced Functional Materials* **2004**, *14*, 116-124.
- (35) Stubbs, G. *Seminars in Virology* **1990**, *1*, 405-412.
- (36) Dawson, W. O.; Beck, D. L.; Knorr, D. A.; Grantham, G. L. *Proceedings of the National Academy of Sciences of the United States of America* **1986**, *83*, 1832-1836.
- (37) Liu, W. L.; Alim, K.; Balandin, A. A.; Mathews, D. M.; Dodds, J. A. *Applied Physics Letters* **2005**, *86*, 253108-3.
- (38) Fonoberov, V. A.; Balandin, A. A. *Nano Lett.* **2005**, *5*, 1920-1923.
- (39) Tseng, R. J.; Tsai, C.; Ma, L.; Ouyang, J.; Ozkan, C. S.; Yang, Y. *Nat Nano* **2006**, *1*, 72-77.
- (40) Royston, E.; Ghosh, A.; Kofinas, P.; Harris, M. T.; Culver, J. N. *Langmuir* **2008**, *24*, 906-912.
- (41) Yi, H.; Rubloff, G. W.; Culver, J. N. *Langmuir* **2007**, *23*, 2663-2667.
- (42) Yi, H. M.; Nisar, S.; Lee, S. Y.; Powers, M. A.; Bentley, W. E.; Payne, G. F.; Ghodssi, R.; Rubloff, G. W.; Harris, M. T.; Culver, J. N. *Nano Letters* **2005**, *5*, 1931-1936.
- (43) Dendukuri, D.; Gu, S. S.; Pregibon, D. C.; Hatton, T. A.; Doyle, P. S. *Lab on a Chip* **2007**, *7*, 818-828.
- (44) Pregibon, D.; Toner, M.; Doyle, P. S. *Science* **2007**, *315*, 1393-1396.
- (45) Sapsford, K. E.; Soto, C. M.; Blum, A. S.; Chatterji, A.; Lin, T.; Johnson, J. E.; Ligler, F. S.; Ratna, B. R. *Biosensors and Bioelectronics* **2006**, *21*, 1668-1673.
- (46) Scheck, R. A.; Francis, M. B. 2007; Vol. 2, p 247-251.
- (47) Pettersen, E. F.; Goddard, T. D.; Huang, C. C.; Couch, G. S.; Greenblatt, D. M.; Meng, E. C.; Ferrin, T. E. *Journal of Computational Chemistry* **2004**, *25*, 1605-1612.
- (48) Couch, G. S.; Hendrix, D. K.; Ferrin, T. E. *Nucleic Acids Research* **2006**, *34*, e29.
- (49) Goddard, T. D.; Huang, C. C.; Ferrin, T. E. *Structure* **2005**, *13*, 473-482.
- (50) Namba, K.; Pattanayek, R.; Stubbs, G. *Journal of Molecular Biology* **1989**, *208*, 307-325.

- (51) Berman, H. M.; Westbrook, J.; Feng, Z.; Gilliland, G.; Bhat, T. N.; Weissig, H.; Shindyalov, I. N.; Bourne, P. E. *Nucleic Acids Research* **2000**, *28*, 235-242.
- (52) Schmatulla, A.; Maghelli, N.; Marti, O. *Journal of Microscopy-Oxford* **2007**, *225*, 264-268.
- (53) Kalinin, S. V.; Jesse, S.; Liu, W.; Balandin, A. A. *Applied Physics Letters* **2006**, *88*, 153902-3.